1989

Natural Convection Above Heated Inclined Surfaces.

John Anthony King
Louisiana State University and Agricultural & Mechanical College

Order Number 9025315

Natural convection above heated inclined surfaces

King, John Anthony, Ph.D.

The Louisiana State University and Agricultural and Mechanical Col., 1989

U·M·I
300 N. Zeeb Rd.
Ann Arbor, MI 48106

Natural Convection Above Heated Inclined Surfaces

A Dissertation

Submitted to the Graduate Faculty of the
Louisiana State University and
Agricultural and Mechanical College
in partial fulfillment of the
requirements for the degree of
Doctor of Philosophy

in

The Department of Chemical Engineering

by
John A. King
B.S., California Institute of Technology, 1982
M.S., Louisiana State University, 1984
December, 1989

Acknowledgements

First, I would like to express my appreciation to my advisor, Danny D. Reible. The high standards he set for himself provided me with my greatest motivation.

Further thanks are due to the many Chemical Engineering faculty who have assisted me during my years at LSU. I would like to particularly thank Professor R.G. Rice for many stimulating and challenging discussions. Professors Price and Sterling were most generous in loaning me equipment for extended periods of time. I would also like to thank Professor E. McLaughlin for affording me the opportunity to teach several classes in the department during his chairmanship. Financial assistance was received from the Exxon Teaching Fellowship, the Amoco Foundation Doctoral Fellowship and the LSU Chemical Engineering Department and is gratefully acknowledged.

Paul Rodrigues from the machine shop and student workers Dawn Smith, Jeff Porter, Darrell Rivers, Sharon Beard, Teresa Sanford and Karen Bell contributed significantly to the progress of this work. Fellow graduate students John Coon, Mark Malhiet and Gary Focht were always ready to provide a helping hand.

I must also acknowledge the kindness shown to me by Anne and Jack Lord of the First Baptist Church in Baton Rouge who extended the hospitality of their home to me so many times during my years as a graduate student.

Finally, I would like to acknowledge the debt I owe to my parents and to my late grandfather, Anthony Hoogerheyde, who exemplified throughout his life the spiritual values which provide life's firmest foundation. This manuscript is dedicated to them.

Table of Contents

Table of Figures

Table of Tables

Abstract

Motivated by a need to assess pollutant transport by upslope flows, an investigation has been conducted into the fundamentals of natural convection flow over inclined surfaces. Particular attention was focused on the influence of ambient fluid stability.

Field studies were performed using tracer gas releases into the upslope flow over a Southern California mountain range. The field studies served to reveal the presence of a split slope flow recirculation and demonstrated the impact of this recirculation on the transport of pollutants from a valley.

In order to pursue a controlled investigation of the phenomena found in the field work, a laboratory model was developed using water as a working fluid. Extensive dye studies demonstrated the presence of this recirculation to varying degrees in nearly every configuration with a stable layer present.

Heat transfer experiments were conducted with the laboratory model to refine and validate the experimental techniques used. Comparisons are made with existing theoretical and empirical predictions where available. Existing correlations for inclined surfaces are extended two orders of magnitude lower in Rayleigh number. A modification to vertical theory based on simply replacing g with $g\cos\theta$ is shown to be useful for inclinations down to 75° from vertical. Transition ranges and empirical correlations are expressed for inclinations of 0°, 15°, 30°, 45°, 60°, 75°, and 90°. Overall correlations are also reported with apparently far less scatter of data than for any previously reported research with inclined surfaces.

Experimentation with stratified ambient fluid resulted in the observation that, with turbulent flow, stratification could apparently be disregarded and heat transfer simply calculated from local conditions. The observed heat transfer coefficients are essentially independent of position along the slope suggesting that an approximate analytical model of upslope flows developed by L. Prandtl in 1942 is applicable. However, quantitative laboratory results showed that Prandtl's one dimensional theory underpredicted the observed boundary layer depths. The results are in good agreement with observed characteristics of atmospheric slope flows.

Chapter 1

Introduction

The pollution of the earth's atmosphere and seas is presently an issue of great concern to scientists and engineers. Encouragingly, however, the earth has shown a huge capacity to absorb, dilute, and degrade most of the harmful byproducts of our civilization. While it should be recognized that there are certain exceptions such as chlorinated fluorocarbons and carbon monoxide, which are currently receiving attention on a global scale, in general, it can be stated that the toxins we add to our environment usually become dangerous only when circumstances converge to keep these toxins confined to a limited region.

Historically, the worst air pollution episodes recorded (e.g. London 1952 - 4000 deaths; Meuse Valley, Belgium 1930 - 63 deaths; Donora, Pennsylvania, etc.) have been linked to extraordinary atmospheric conditions and geography which cooperated in keeping pollutants from dispersing (Seinfeld, 1975). Recent catastrophes such as the Bhopal release of methyl isocyanate have also been exacerbated by a setting which limited dilution. Los Angeles is an example of a city with persistent air pollution problems due in large part to local dispersion problems. Neiburger (1969) points out that coastal cities such as Casablanca, Capetown, Lima and Los Angeles have developed in the worst possible locations from the standpoint of vulnerability to smog. This assessment is related to large scale ("synoptic") meteorological factors which result in persistent light winds and inversions.

If meso and micro scale atmospheric motions are also considered, topographic influences become more important (detailed discussion below). Deep narrow mountain valleys are thus high risk locations for air pollution episodes because of the topographical sheltering effects. Therefore, there is a significant motivation to study pollutant transport in these sorts of complex flow regimes.

A well accepted technique for studying atmospheric diffusion of pollutants is that of tracer gas experiments. This technique has been developed and successfully applied to investigations of flows in complex terrain in the substantial body of work described by Reible (1982). As Reible (1982) has demonstrated, a properly designed and well executed tracer study is probably the best tool available for assessing atmospheric dispersion in complex real settings. Such studies of pollutant transport by atmospheric flows in complex terrain can nevertheless become logistic nightmares. As a rule, these studies are also quite costly since a great deal of data must be collected to get an accurate picture of the physical phenomena which take place.

In this dissertation, the results of two tracer experiments performed in a mountain-valley region with significant air pollution problems are analyzed and conclusions with general implications presented. In addition, the development of an alternative technique for investigating this complex atmospheric flow using

laboratory scale water modeling is described and conclusions drawn from the laboratory studies. Applications are further drawn from the laboratory measurements pertaining to the related area of natural convection heat transfer and fluid flow.

1.1 Upslope Flows

A recurring flow pattern which is observed to occur in mountain valley systems is the diurnal cycle of upslope and downslope flows. These flows are driven by the temperature difference from mountain slopes to the free air in a valley resulting from solar insolation during the day and radiative cooling at night. The upslope (or anabatic) wind velocities increase in the morning to a maximum in the early afternoon and decrease in the afternoon to zero at soon after sunset. The downslope (or katabatic) wind velocities increase rapidly starting shortly after sunset and maintain a cool drainage flow through the night. A typical profile of daytime upslope winds from the Vikar Valley in Austria (derived from Eatontown Signal Laboratory Group (1945)) is shown below in Figure 1-1.

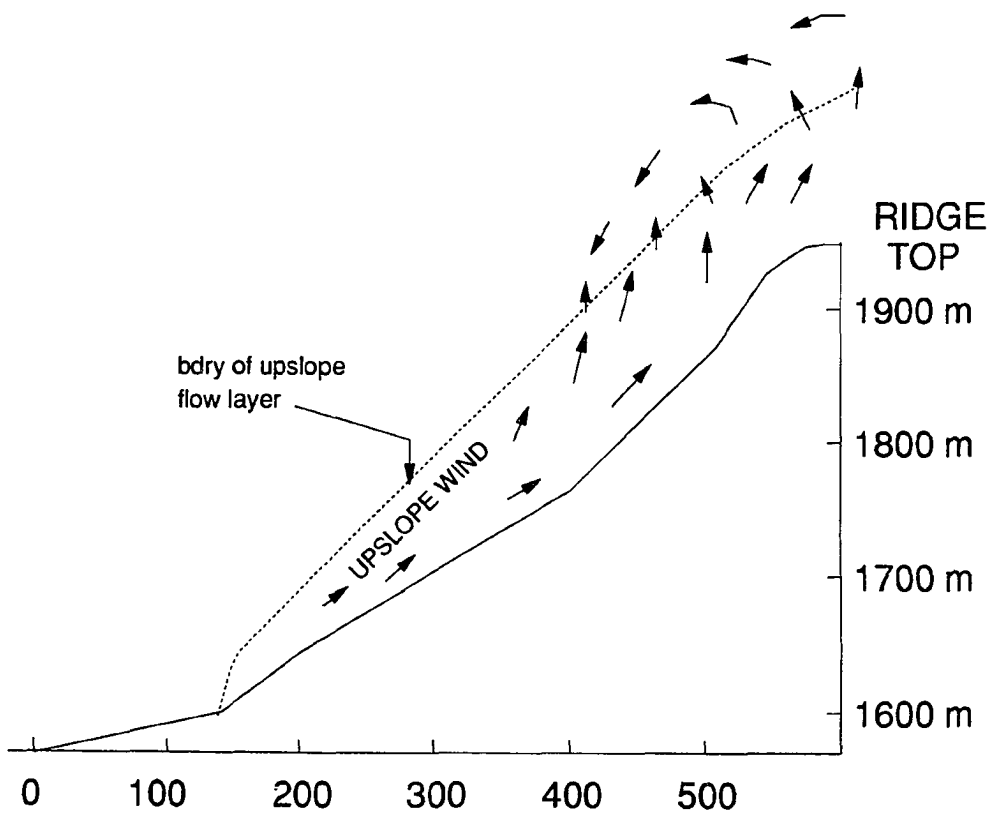

Figure 1-1 Profile of Upslope Winds in the Vikar Valley, Austria (after Eatontown (1945))

Upslope flow velocities usually range from 1.0 to 3.0 m/sec depending on the exposure, inclination of the slope, time and the depth. The typical upslope flow is wedge shaped with observed depths varying from 10 meters at the bottom to anywhere from 100 to 250 meters at the top. The idealized slope wind circulation as described by early investigators is shown diagramatically in Figure 1-2. The characterizing feature of the circulation is the movement of the air toward the slopes at all elevations. The return current is above the ridge top.

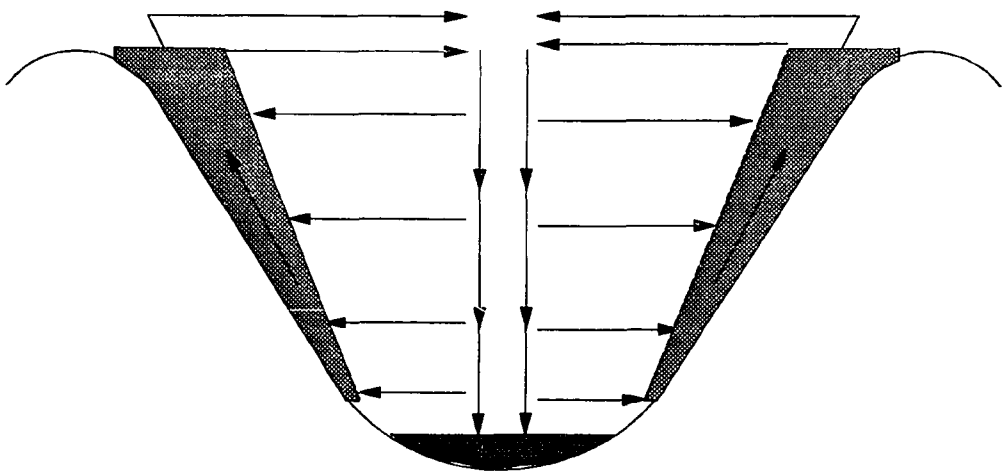

Figure 1-2 Depiction of Idealized Valley Circulation Patterns For Upslope Flows (after Eatontown (1945))

Recent tracer studies have provided evidence of the important role which slope flows can play in pollutant transport. Willson et al. (1983) observed that significant amounts of tracer were entrained by upslope flow out of a Colorado valley they studied. Sivertsen et al. (1983) found that slope winds markedly influenced the concentration pattern downwind of a foundry. Sivertsen et al. observed that the effect of slope winds decreased as the mixing height increased in their study and note that, "Even crude modelling of this flow pattern would improve the dispersion estimates considerably." Reible (1982) and Reible et al. (1983) also present direct experimental evidence that the interaction of the buoyancy driven flow over a mountain slope with the air aloft can be a significant factor in air quality.

The relationship between mixing height and slope winds noted by Sivertsen et al. is consistent with the analysis of Smalley (1970) who determined that San Francisco Bay Area topography tended to channel the marine flow to a greater extent as the depth of the marine layer decreased. Similarly, Carruthers and Choularton (1982) investigated the acceleration of wind up a hill and found that a strong inversion capping a flow can

influence the boundary layer flow markedly, causing lower velocities and even separation of the flow. The effect of a stably stratified capping layer on upslope flows can be expected to be equally if not more important. The results of King et al. (1987) show that atmospheric stability has profound influence on both the flow mechanisms and pollutant transport characteristics of upslope flows. Figure 1-3 shows the slope flow behavior posited by King et al. (1987), who concluded that transport paths are altered by the presence of a strongly stable capping layer.

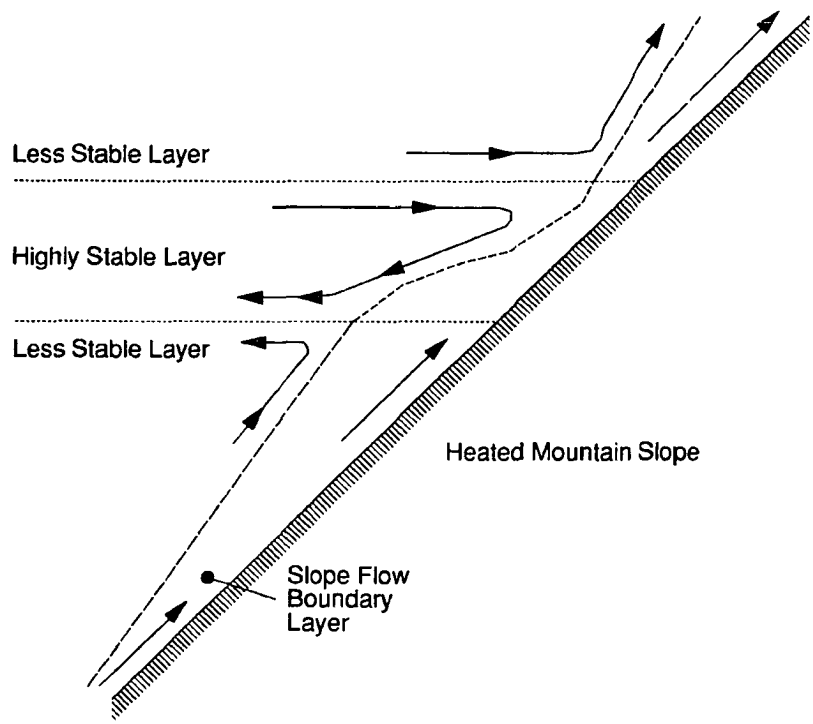

Figure 1-3 Depiction of Slope Flow Structure in the Presence of a Capping Stable Layer

While the tracer experiments mentioned above provide an indication of the problem and direct quantitative information applicable to the design of an appropriate pollution control strategy, the detailed information required to understand and form a priori predictions of the behavior is still lacking. Such predictions require the development of generalized mathematical models capable of being applied under a range of conditions. The role of upslope flows in pollutant dispersion is a little studied one and hence, there have been as yet no models proposed to be used in regions such as the ones studied by Sivertsen et al. (1983), Reible (1982), Willson et al. (1983), and King et al. (1987). McRae (1981) has indicated that the interaction of the

slope winds with the well-mixed layer and the capping stable layer represents a large part of the uncertainties associated with numerical modelling of atmospheric transport, dispersion, and reaction in a mountain valley system such as the Los Angeles Air Basin.

There are presently several analytical and numerical models for simple slope flows developed by atmospheric physicists and meteorologists. While these models do not attempt to address the transport and dilution of pollutants, some progress has been made toward describing the observed profiles of velocity and temperature in a slope flow layer and toward modelling valley air turnover.

One technique which has been used for modelling transport by slope flows is to apply mass balances to the boundary layer flow, treating the layer as a series of contiguous boxes. Such a model is described by Whiteman and McKee (1978) with applications to valley air subsidence. While these models provide a useful framework for describing the gross features of slope flows which have been observed, much work remains to be done in developing a fundamental understanding of the phenomena which occur.

Recently, Vergeiner (1982) has presented a simple box-type model which incorporates features such as entrainment and detrainment to and from the boundary layer. The model provides for the interruption of upslope winds by a strong inversion in the valley atmosphere and a division into two branches, one which is forced to move horizontally away from the slope and the other which continues along the slope. Once again, this model is framed in terms of overall averages for valley air turnover rather than the detailed transport within a slope flow boundary layer.

An early model of slope flows which was developed by Prandtl in 1942 (see Sutton (1953) or Turner (1973)) has been found to provide a useful framework for describing the temperature and velocity profiles which have been observed for upslope flows. The model has the advantage of simplicity but requires the restrictive and possibly unrealistic assumptions of no entrainment of ambient fluid, and a constant temperature difference between the slope and the ambient fluid at a given level. Turner (1973) points out that a more physically realistic surface condition would be that of a constant flux. The Prandtl type models (extended by Defant (1951) and more recently by Egger (1981) and Sorbjan (1983)) predict that the velocity and the depth of slope flows will decrease for higher ambient stabilities. Comparison to observed profiles show that these models generally underpredict the depth of the upslope flow layer. In addition, the response of an upslope flow when interrupted by the presence of a strongly stable capping layer is not addressed by these models.

Egger's (1981) theory does, however, show a thermal circulation spreading outward horizontally from a surface which results from an irregularity of surface temperature (a preferentially heated strip). This circulation was predicted to spread deeply into the atmosphere. The motion was shown to move almost horizontally outward from the slope for the first 1-2 km. Circulations resembling the structure described have

been observed in the atmosphere by other researchers (Brehm, (1981)) and cited by Egger. However, observations showing that surface temperature did not change markedly in the region contradicted and detracted from Egger's initial hypothesis.

1.2 Background for Laboratory Investigation

Although the above models have met with some success in describing the physical phenomena observed, their usefulness in developing pollution control strategies has been limited. At present, the transport of pollutants by slope flows has not been accurately modeled and little data for such transport is available. In addition, due to the difficulty of collecting reproducible data for such flows, it has proven difficult to adequately test the features of the models describing them.

Although it is possible to measure velocity and temperature profiles over just about any type of terrain imaginable, the light winds and intermittence of slope flows in nonuniform mountainous terrain make detailed observations of actual profiles extremely difficult. Egger (1981) notes that even the best, most recent data (from the Inn Valley) is complicated by factors such as winds on an opposite slope, irregularity of terrain, large scale wind fields, and upvalley winds which influence the thermal structure. Nevertheless, Egger goes on to state that the generally simple nature of upslope flows holds out hope that "at least the gross features of flows above a slope can be understood."

A fundamental laboratory scale investigation will permit a carefully controlled investigation of these flows. The establishment of a reliable numerical model for upslope winds along with verification of the predictions made by the model for velocity and temperature profiles will then be more feasible. The data should also facilitate the development of a model which incorporates the key features necessary for predicting pollutant transport and dispersion by upslope winds.

Laboratory scale modeling of larger scale processes and phenomena is a well established engineering tool which is frequently brought to bear on particularly complex or otherwise intractable problems. Laboratory models have been found to be a useful tool in helping to understand the dynamics of mesoscale airflows in the atmosphere as well as in helping to solve problems such as the characterization of pollutant transport and dispersion in such airflows (Erich Plate in Hunt and Fermholz (1975)). Most atmospheric simulation studies have dealt with flows in which there is a mean velocity of some sort superposed on the system. These wind tunnel studies have primarily used air as their working fluid. There is also a significant amount of work dealing with the purely convective flow above a horizontal heated surface. This work, primarily due to G.E. Willis and J.W. Deardorff, has demonstrated the utility of water modelling of atmospheric convection for a variety

of applications including dispersion of pollutants. Water can easily be made to be stratified with a relatively high degree of control over the temperature profile obtained and also results in a time and length scale for the convective motion which permits straightforward application of laboratory measurement techniques.

Laboratory modeling of slope flows can be viewed as an extension and perturbation to horizontal plate studies of mixing layers and penetrative convection. Alternatively, the laboratory model may be thought of as simply a special case of natural convecton over an inclined flat plate for which results may well be available in the heat transfer literature.

Studies of natural convection in fluids adjacent to vertical and horizontal heated plates are numerous and, as a result, these flows have been probed and analyzed in great detail. In contrast to these classic limiting cases, the intermediate case involving natural convection about a heated inclined surface has been the object of relatively few investigations. In particular, it appears that the scope of these investigations has not included the possible effects which a condition of stable stratification in the fluid may have on the convective flow above an inclined plate. Flows resulting from natural convection over inclined plates bounded by an extensive body of stably stratified fluid above would be expected to have many features in common with slope flows generated as a result of daytime heating of mountain slopes.

Examples of convective flows above inclined surfaces also arise in numerous industrial applications such as heating of certain process vessels containing liquids, or heat transfer to sloping containment vessels containing cryogenic liquids. In practice, it would be expected that temperature variations in such fluids would often tend to result in the development of a stable density stratification. An experimental evaluation of the importance of stratification of a liquid upon free convection above an inclined plate should thus be of further interest for its applications to heat transfer calculations.

Chapter 2

Field Experiments

The key features of pollutant dispersion in slope flows can best be identified through field-scale atmospheric tracer experiments. Two such experiments were conducted by the author while an undergraduate assistant at Caltech. Initial analysis was limited to pollutant dispersion rates and mixing height estimates. The key features of the flow and the implifications for pollutant dispersion were identified through analysis of the atmospheric tracer experiments during continued studies at LSU. These results are described in the attached paper published in Atmospheric Environment, v. 21, pp. 53-59, 1987.

ATMOSPHERIC ENVIRONMENT

An International Journal

From the Editor: Dr. J. P. Lodge, Jr.
385 Broadway
Boulder, Colorado 80303, U.S.A.
Tel: (303) 449-7712

27 January 1989

Mr. John A. King
Department of Chemical Engineering
Louisiana State University
Baton Rouge, Louisiana 70803

Dear Mr. King:

I have your letter of 23 January requesting permission to extract figures and text from your paper, "The Influence of Atmospheric Stability on Pollutant Transport by Slope Winds," published in Atmospheric Environment 21, 53-59. Permission is hereby granted to use these items in your Ph.D. dissertation. Proper credit should be given.

Sincerely yours,

James P. Lodge, Jr.

PERGAMON PRESS New York • Oxford • Beijing • Frankfurt • São Paulo • Sydney • Tokyo • Toronto

Atmospheric Environment Vol. 21, No. 1, pp. 53–59, 1987.
Printed in Great Britain

0004–6981/87 $3.00 + 0.00
Pergamon Journals Ltd

THE INFLUENCE OF ATMOSPHERIC STABILITY ON POLLUTANT TRANSPORT BY SLOPE WINDS

J. A. KING, F. H. SHAIR* and D. D. REIBLE†

Department of Chemical Engineering, Louisiana State University, Baton Rouge, LA 70803, U.S.A.
*Department of Chemical Engineering, California Institute of Technology, Pasadena, CA 91125, U.S.A.

(*First received* 16 *September* 1985 *and in final form* 7 *July* 1986)

Abstract—The results of a field investigation into pollutant transport by slope flows are presented. During the study, ozone levels were monitored for eight days at three locations along a mountain slope extending above the Los Angeles Air Basin. In addition, tracer tests were conducted during two afternoons during the study period. The tests were conducted on days with widely varying atmospheric stability and indicate the effect of a strongly stable capping layer on pollutant transport by upslope flows. The experimental results indicated at least two mechanisms for the return of polluted air to the valley below. Under weakly stable conditions, the often noted return of pollutants via night-time downslope winds was observed. In addition, under more strongly stable conditions, a daytime recirculation mechanism consistent with that described by Vergeiner (1982) was observed. The tests also indicated that the slope flow layer depth and speed decreased with increasing atmospheric stability. In addition, the rate of transport and dilution of pollutants in a slope flow appears to be influenced by the entrainment and growth of the boundary layer, limiting the applicability of models that neglect these processes.

Key word index: Slope winds, stability, entrainment, recirculation, ozone, Los Angeles, transport, dispersion.

INTRODUCTION

The effect of air pollution on forests is an issue which is currently of great concern. Although some of the concern is associated with regional air quality degradation (e.g. acid rain), much of the observed damage has been linked to more localized pollution problems which are heavily influenced by the mesoscale meteorology. In a recent review article, for example, McLaughlin (1985) notes that high concentrations of photochemical oxidants have been found in the San Bernardino and San Gabriel mountain ranges due to transport from the Los Angeles air basin. Studies have documented the occurrence of foliar injury, premature leaf drop and decreased growth as well as increased tree mortality in heavily impacted areas of these mountain ranges.

Upslope flows, driven by the buoyancy of the preferentially heated air next to mountainsides, are thought to be an important mechanism whereby pollutants can be transported into forests and wilderness areas located in hilly or mountainous terrain. Miller *et al.* (1972) and Reible (1982) have linked high O_3 concentrations in the Sierra Nevadas to transport via afternoon upslope winds from the adjacent San Joaquin Valley. Williams *et al.* (1977) and Pronos *et al.* (1978) have observed significant damage to sensitive tree species in the National Park and Forest areas in the Sierra Nevadas as a result of this oxidant transport.

It is well known that the stability of the overriding air largely controls the depth and strength of the upslope flow. Simple models of slope flow developed by Prandtl [1942, see Turner (1973)] and extended by Defant (1951) and more recently by Egger (1981) predict that the velocity will vary with the inverse of the Brunt-Vaisala frequency, i.e. $1/N$, while the depth varies as $1/N^2$. However, the response of an upslope flow when interrupted by the presence of a strongly stable capping layer is not well understood. McRae and Seinfeld (1983) have indicated that the interaction of the slope winds with the capping stable layer represents a large part of the uncertainties associated with modeling atmospheric transport, dispersion and reaction in a mountain valley system such as the Los Angeles air basin. One model of the influence of a capping layer on slope winds (Vergeiner, 1982) provides for a flow division into two branches, one which is forced to move horizontally away from the slope and the other which continues along the slope. However, this phenomenon has not been studied extensively and the implications of such flow patterns on pollutant levels have not as yet been investigated.

This paper reports the results of a study undertaken during July 1980 to probe the phenomena of pollutant transport by the buoyancy driven upslope winds from the Los Angeles air basin in Southern California. O_3 measurements were made from 15 to 22 July at two locations in the San Gabriel mountain range and in the city of Pasadena, at the base of the mountains. In conjunction with the O_3 measurements, two atmospheric tracer experiments were performed during the afternoons of 16 July and 22 July 1980. The prevailing

†Author to whom correspondence should be addressed.

atmospheric stability varied widely during the course of the studies. In particular, these tests allowed conclusions to be drawn concerning the effect of a strongly stable capping layer on upslope flows and the role this interaction plays in determining pollutant levels in the mountains.

EXPERIMENTAL

O_3 levels were monitored continuously for eight days from 15 July to 22 July using Dasibi ozone monitors which had been calibrated by the manufacturer immediately before this study. O_3 levels for Pasadena (elev. 247 m) were obtained from the local Air Quality Management District (AQMD) which maintains monitoring stations throughout the Southern California area. The first location in the mountains, Henniger Flats (elev. 800 m), was located at a ranger station 6.0 km NNE of the AQMD station in central Pasadena. The second location was at the Mt Wilson observatory (elev. 1725 m), located 10.2 km NNE of the AQMD station. These locations are identified in Figs 2 and 3 which will be presented during the discussion of the tracer experiments.

The tracer studies involved the release of sulfur hexafluoride, SF_6, an inert, nontoxic gas, from a building on the campus of the California Institute of Technology (Caltech). Caltech is located 1.4 km S of the Pasadena AQMD station. The releases were made at ground level through a high volume rotameter which was used to monitor and maintain a constant release rate. About 25 kg of SF_6 was released during each experiment.

Approximately 350 air samples were collected during each test using 30 cm^3 disposable plastic syringes. Instantaneous grab samples were collected from crosswind automobile traverses at varying distances downwind. Sample intervals ranged from 0.16 to 1.6 km depending on the distance downwind. Grab samples were also collected every 5 min at Henniger Flats and Mt Wilson and represented about 1/3 of the total number of samples. A small number of additional samples were collected during the nights following the experiments using an automatic 1-h averaging sampler located at Caltech.

The tracer samples were analyzed by electron capture gas chromatography. Drivas (1975) and Lamb (1978) have described the details of the analytical procedure and experimental apparatus. Concentrations could be detected to within about 15% at concentrations as low as 10 parts SF_6 in 10^{12} parts air (ppt).

RESULTS

Ozone

Figure 1 presents the O_3 data which were collected during the study period. The measured peak levels are also summarized in Table 1. On most days, for example the period 15–20 July, the arrival time and peak levels in the mountains were consistent with a linkage to valley air through the slope flow. On 21 and 22 July, however, Mt Wilson levels appeared to be decoupled from the other two sites. In addition, on 15–20 July secondary evening peaks appeared in Henniger Flats, apparently the result of the nocturnal drainage winds which are associated with the more rapid cooling of the air near the surface at high elevations during the night. The absence of this evening resurgence in Pasadena O_3 levels can be attributed to NO_x scavenging in the city. A secondary peak also appeared at Henniger Flats at about 1730 on 21 July but this occurred too early to be related to drainage winds and must be attributed to other factors. The source of this peak and the variation in mid-day O_3 behavior between 15–20 July and 21–22 July can be explained as a result of the tracer experiments.

Tracer Test 1, 7/16/80

Initial traverses showed that the tracer was transported in the NNE direction directly towards Henniger Flats and Mt Wilson, as depicted in Fig. 2. Significant concentrations appeared in both places with levels reaching an average of 450 ppt at Henniger Flats and 70 ppt at Mt Wilson. Based upon the tracer arrival times, the mean transport speed was about 2.7 $m\,s^{-1}$ to Henniger Flats and 2.0 $m\,s^{-1}$ from Henniger Flats to Mt Wilson.

Crosswind traverse data, as shown in Fig. 2, and the rate of along-wind dilution of the tracer indicated that the terrain induced turbulence enhanced the rate of dilution over that which would be expected over flat terrain in the observed meteorological conditions. This is consistent with past studies of pollutant dilution in mountainous terrain (e. g. Start *et al.*, 1974). These data also indicated significant entrainment and growth of the slope flow layer along the slope. Mass balance calculations showed a slope flow depth of about 75 m along the traverse route shown in Fig. 2, 100 m at Henniger Flats, 150 m at Mt Wilson and greater than 500 m on Angeles Crest Highway beyond Mt Wilson.

On the night following the tracer release, the 1-h average samples collected at Pasadena indicated an abrupt increase to 72 ppt SF_6 at 8 p. m. which was followed by significant but lower levels throughout the night. The timing of this peak is consistent with a return of a mass of tracer laden air via the nocturnal downslope flow suggesting that this was the mechanism for the secondary O_3 peak observed simultaneously at Henniger Flats. Note that SF_6, as a conservative tracer, would not be subject to the NO_x scavenging which apparently removes the secondary O_3 peak at Pasadena.

Tracer Test 2, 7/21/80

The general path followed by the air mass during Test 2 is indicated by the arrows in Fig. 3. During this experiment, the bulk of the tracer was channeled westward and limited to elevations below 1400 m. Automobile traverses indicated mean transport speeds in excess of 1.8 $m\,s^{-1}$ close to the release site but 1.2 $m\,s^{-1}$ or less at elevated locations. The arrival of small amounts of tracer at Mt Wilson suggested a mean transport speed of only 0.7 $m\,s^{-1}$. Thus the effective along-slope transport speed of the upslope winds decreased significantly with elevation during the second experiment, even though Pasadena winds showed little variation between the two tests.

During the afternoon following the release, SF_6 concentrations as high as 132 ppt were observed at the

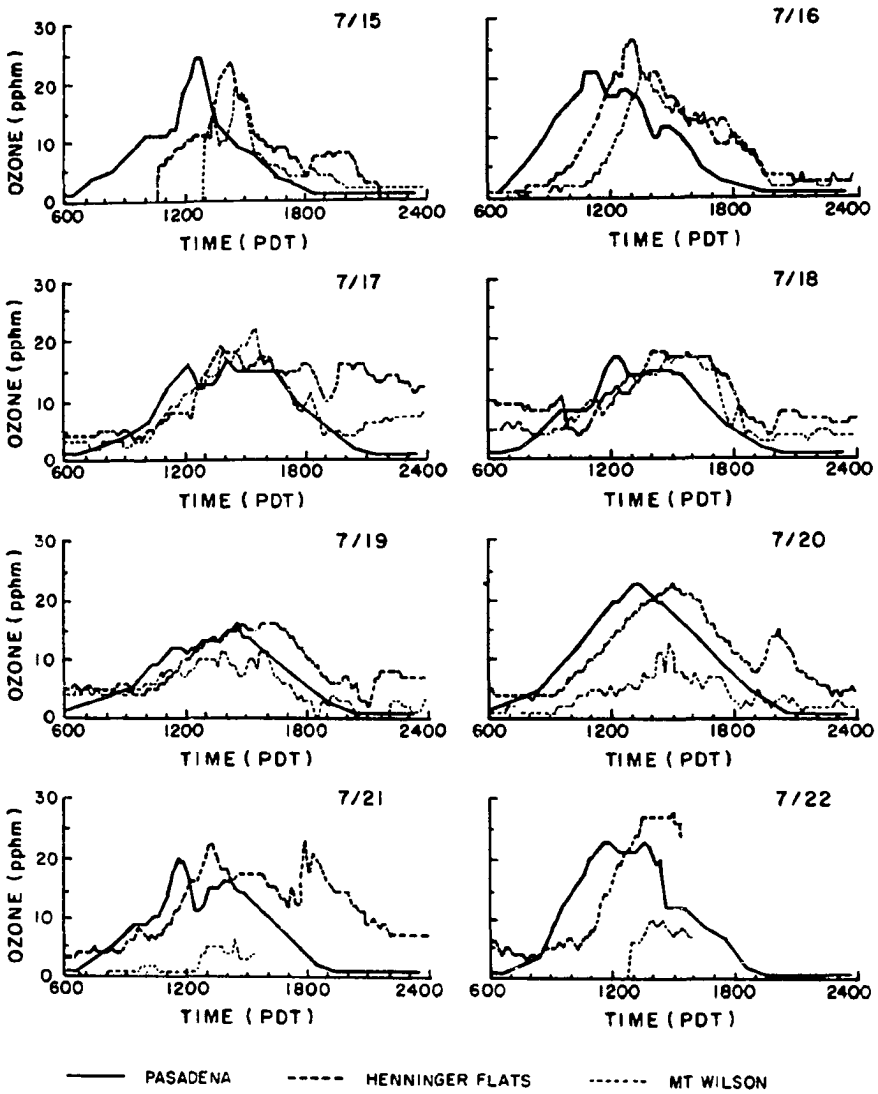

Fig. 1. Ozone concentrations at Mt Wilson, Henniger Flats and Pasadena AQMD during the study period.

Table 1. Peak ozone levels and times

Date	Primary Peak (pphm) and Time (PDT)			Secondary Peak
	Pasadena	Henniger Flats	Mt Wilson	Henniger Flats
7/15	23 (1355)	24 (1425)	20 (1505)	8 (1910)
7/16	22 (1115)	27 (1300)	21 (1330)	4 (2120)
7/17	18 (1425)	20 (1357)	26 (1535)	16 (2000)
7/18	18 (1215)	19 (1405)	20 (1554)	8 (2010)
7/19	16 (1440)	17 (1627)	13 (1544)	8 (2140)
7/20	23 (1325)	23 (1458)	19 (1422)	15 (2000)
7/21	21 (1140)	24 (1330)	7 (1424)	23 (1750)
7/22	24 (1345)	28 (1450)	11 (1355)	*

* Data unavailable.

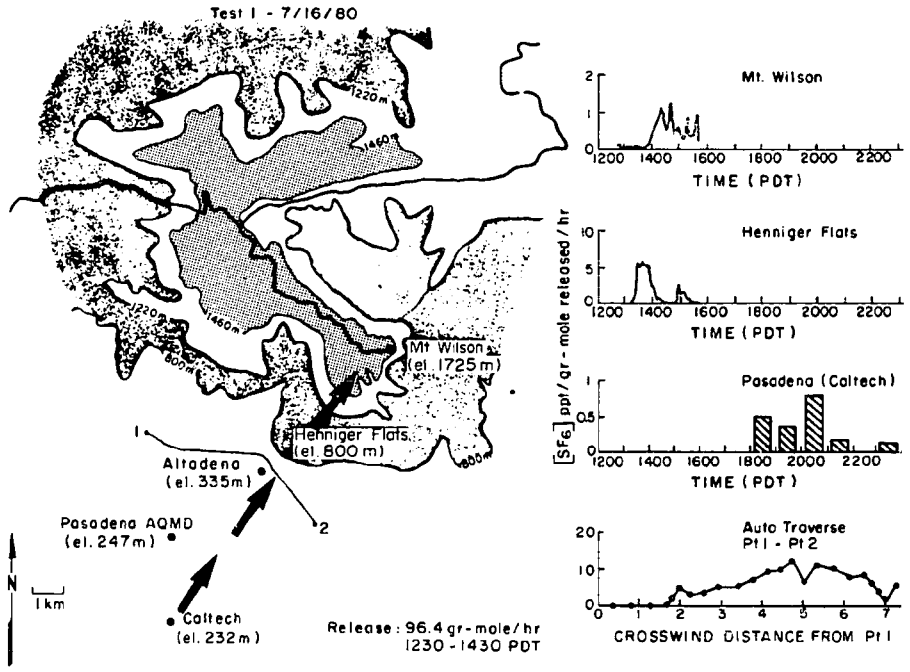

Fig. 2. Overview of Tracer Test 1 on 16 July 1980. Arrows on map indicate general path of tracer plume.

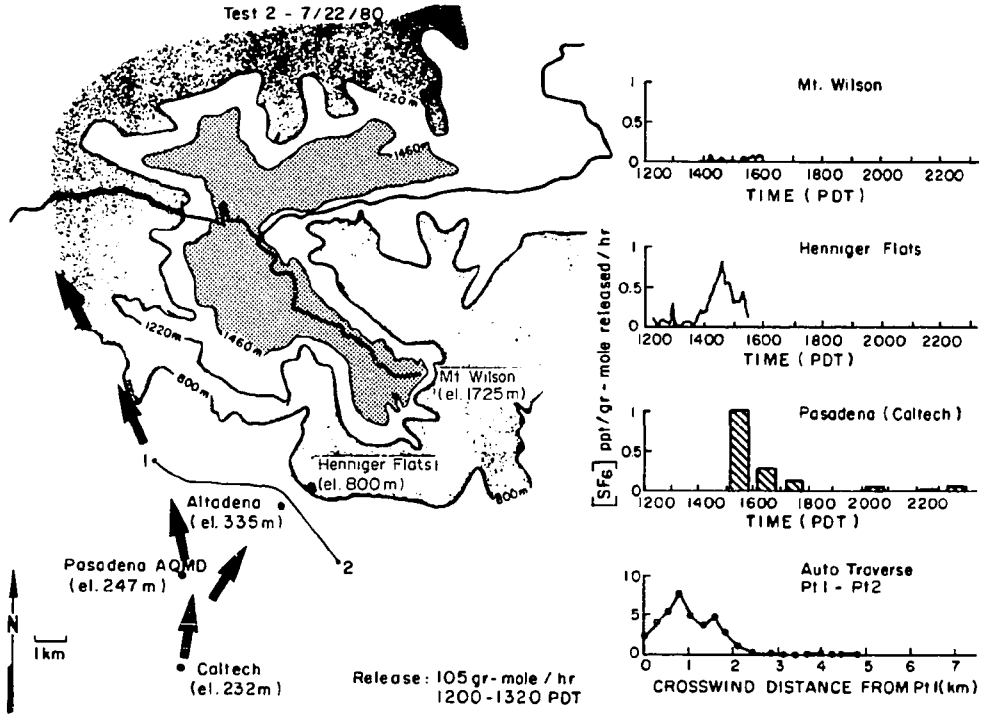

Fig. 3. Overview of Tracer Test 2 on 22 July 1980. Arrows on map indicate general path of tracer plume.

Caltech campus in Pasadena. The arrival of SF_6 occurred too early in the day (1500 PDT) to be the result of return by the nocturnal drainage and is consistent with the mid-afternoon O_3 peaks observed in Pasadena on the test date and also observed in Henniger Flats and Pasadena on the previous day. These results indicate that a shallow mountain-valley circulation directed upslope at the surface and away from the slope aloft was present on 21 July and 22 July and resulted in a direct return of the contaminated air to the valley basin. It should be emphasized that the return of tracer or O_3 to the valley basin was not consistent with surface winds at Pasadena which were directed upslope throughout the afternoon.

DISCUSSION

The two test dates were chosen with the intention of examining slope flows under very similar worst case type conditions. As a result the conditions on the two days were quite close although there were key differences.

On 16 July 1980, the day of the first test, a strong inversion with weak transport winds was established during the morning. During the day surface heating strengthened the sea breeze and lifted the inversion. The unfavorable dispersion conditions associated with this meteorological pattern produced poor air quality and resulted in a stage two O_3 episode (O_3 exceeded 35 pphm) in San Bernardino county (80 km to the E). The second test date of 22 July 1980 was one of the worst air quality days in the Southern California Air Basin for the entire year. Peak O_3 values of over 35 pphm occurred again, this time in Fontana (65 km to the east).

But although both test days had generally poor air quality and similar synoptic conditions, the strength of the inversion was much stronger during the second test. Atmospheric stabilities were evaluated from vertical temperature gradients measured by radiosonde and aircraft. As can be seen in Table 2, the stability as evaluated at El Monte, 10 km SE of the release site, showed a significantly more stable atmosphere on 21 and 22 July when compared to the other days evaluated. Since weekend data is unavailable for El Monte, we also include data from Los Angeles Airport, located on the Pacific Coast 35 km SW of the release site. Although quantitative differences are observed between the stability measures at the two sites, the more stable days of 7/20–22 are clearly separated from the less stable period 7/15–19 in both sets of data.

Thus, the first tracer experiment and the first five days of O_3 monitoring were conducted in the presence of a weak inversion. The lack of significant stability aloft allowed the upslope flows to penetrate deeply into the mountains and resulted in high tracer/O_3 at elevated sites such as Mt Wilson. The tracer data indicated that the depth of the penetrating slope flow layer also increased significantly with elevation, consistent with entrainment of the overriding stable air. Entrainment has been identified as the single most important factor in pollutant plume dilution in slope flows (Willson *et al.* 1983) but most models of upslope flows such as those advanced by Prandtl (1942) and Egger (1981) can only be valid when the effects of entrainment are small. At night, the onset of the normal drainage flows resulted in a return of some of the polluted air to the foothills and the basin.

During the final two days of O_3 monitoring and during the second tracer experiment, a strong inversion restricted the penetration of the upslope flow and significantly reduced the concentrations observed at elevated sites. As a result of the strong capping effect of the inversion, the weak upslope flow was preferentially channelled to the lower elevations to the W of Mt Wilson. In addition, the early return of tracer to the valley floor and elevated late afternoon O_3 levels suggests a shallow recirculation that returned both tracer and pollutants to the valley floor during the period of the upslope flow. This is consistent with the hypothesis of Vergeiner (1982) that suggests that an upslope flow is split and becomes vertically layered by the presence of a strong inversion. The conceptual model of Vergeiner is depicted in Fig. 4 along with the observed vertical temperature profile on the day of the second test. The figure indicates the growth of the upslope boundary layer in less stable regions and restriction of the upslope layer in regions severely

Table 2. Inversion strength

Date	El Monte (1400 PDT) Inversion strength ($C\,m^{-1}$)	El Monte (1400 PDT) Inversion base (m)	Los Angeles airport (1300 PDT) Inversion strength ($C\,m^{-1}$)
7/15	0.000	*	0.012
7/16	0.003	550	0.014
7/17	0.010	610	0.019
7/18	0.010	640	0.010
7/19	*	*	0.011
7/20	*	*	0.020
7/21	0.015	530	0.031
7/22	0.028	480	0.026

* Data unavailable.

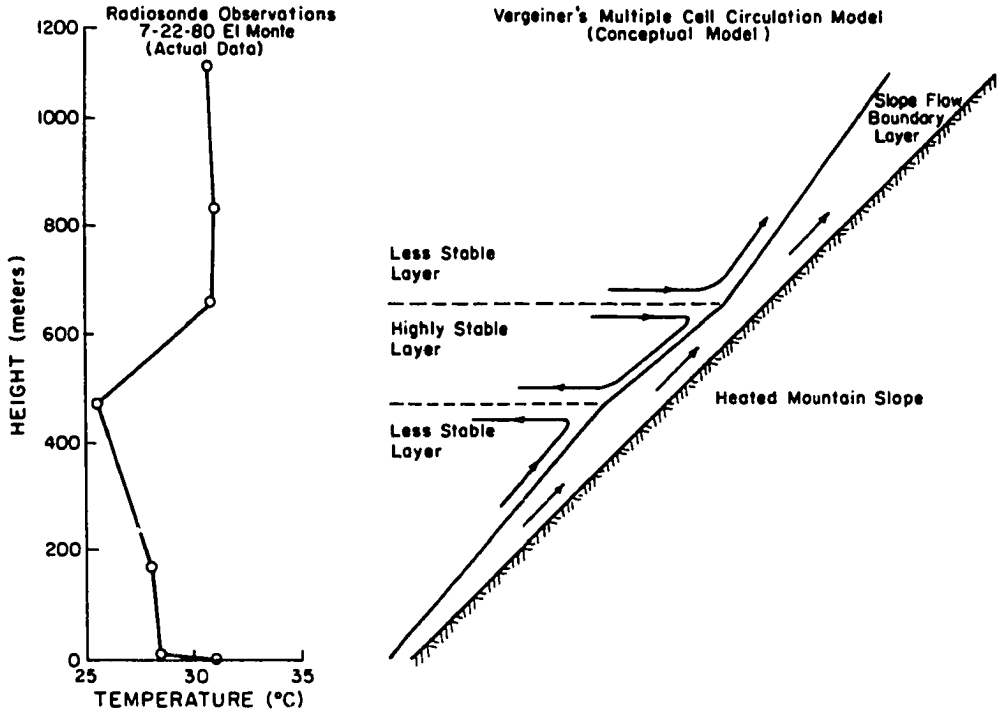

Fig. 4. Conceptual depiction of slope flow structure in the presence of a capping stable layer, after Vergeiner (1982). Note the circulation away from the surface and the relatively deep mixing layer below the temperature inversion and the shallow layer and inflow within. Also included is the observed vertical temperature profile at El Monte on the day of the second tracer test.

damped by the stable inversion. As a result a counterclockwise circulation as shown in the figure is induced below the inversion and an opposing clockwise circulation is shown in the stable inversion. Note that the layering both limits the upslope transport and can result in the development of the shallow recirculation suggested by the tracer experiments.

SUMMARY AND CONCLUSIONS

A study comprised of two tracer tests cannot purport to represent an exhaustive investigation of a class of flows in complex terrain and this limits the scope of conclusions to be drawn from this work. However, the results of the studies are valuable in that they illustrate clearly the response of an upslope flow to a strongly stable capping layer and the impact this can have on pollutant levels. It is perhaps most interesting that while the valley floor experiences its highest pollutant levels under very stable conditions, the highest elevations can be impacted more strongly under more weakly stable conditions when transport is less restricted. In addition, the pollutant levels observed in the valley during strongly stable conditions are apparently enhanced by a shallow recirculation from the surrounding slopes.

Two patterns of recirculation were observed and these were linked to the strength of the capping stable layer. Under strongly stable conditions the data were consistent with a split slope flow recirculating mechanism akin to that described by Vergeiner. Under less strongly stable conditions, a return of tracer via downslope winds was indicated by the data. In addition, it appears that strongly stable conditions resulted in the slope flow being channeled towards the gentler slopes and away from the highest elevations.

The tracer tests indicated that the slope flow layer depth and speed decreased with increasing atmospheric stability, qualitatively consistent with Prandtl type models. Such models, however, neglect entrainment and growth of the slope flow boundary layer which appear to be quite significant. Not unexpectedly, the rate of dilution of pollutant plumes in the mountainous terrain is much more rapid than would be expected over flat terrain.

In summary, these studies have clearly demonstrated the important effect which the strength of the capping layer has upon the transport of pollutants by upslope flows. The results are consistent with most but not all features of slope flows as modeled by Prandtl and others. The studies also point to the importance of incorporating features such as entrainment and the response to a capping stable layer into any model attempting to describe pollutant transport via upslope flows.

Acknowledgements—The authors would like to acknowledge the invaluable cooperation of Chuck Bennett, Mike McCorkle and Chuck Unger of the California Air Resources Board in describing the meteorological conditions and valley air quality during the study period, as well as the assistance of Willie Brown and Anita Jakub of Caltech in conducting the tracer studies. In addition, the support provided by the Caltech SURF program is gratefully acknowledged.

REFERENCES

Defant F. (1951) Local winds. In *Compendium of Meteorology* (edited by Malone T.). American Meteorological Society, Boston.

Drivas P. J. (1975) Investigation of atmospheric dispersion problems by means of a tracer technique. PhD Thesis, Dept. Chemical Engineering, California Institute of Technology, Pasadena, CA.

Egger J. (1981) On the linear two dimensional theory of thermally induced slope winds. *Contrib. Atm. Phys.* **54**, 465–481.

Lamb B. K. (1978) Development and application of dual atmospheric tracer techniques for the characterization of pollutant transport and dispersion. PhD Thesis, California Institute of Technology, Pasadena, CA 91125.

McLaughlin S. B. (1985) Effects of air pollution on forests: a critical review. *J. Air Pollution Control Assoc.* **35**, 511–534.

McRae G. J. and Seinfeld J. H. (1983) Development of a second-generation mathematical model for urban air pollution—II. Evaluation of the model performance. *Atmospheric Environment* **17**, 501–522.

Miller P. R., McCutchan M. H. and Milligam H. P. (1972) Oxidant air pollution in the Central Valley, Sierra Nevada foothills and Mineral King Valley of California. *Atmospheric Environment* **6**, 622–633.

Prandtl L. (1942) Stromungslehre. Braunschweig, Vieweg und Sohn.

Pronos J., Vogler D. R. and Smith R. S. (1978) An evaluation of ozone injury to pines in the southern Sierra Nevada. Report No. 78-1 Forest Insect and Disease Management, 630 Sansomme St., San Francisco, CA 94111.

Reible D. D. (1982) Investigations of transport in complex atmospheric flow systems. PhD Thesis, California Institute of Technology, Pasadena, CA 91125.

Start G. E., Dickson C. R. and Ricks N. R.(1974) Effluent dilutions over mountainous terrain and within mountain canyons. *Symposium on Atmospheric Diffusion and Air Pollution*, American Meteorological Society, Boston, Mass.

Turner J. S. (1973) *Buoyancy Effects in Fluids*. Cambridge Univ. Press, London.

Vergeiner I. (1982) Eine energetische theorie der hangwinde. *Annalen der Meteorologie*, Offenbach a./M., n. s., **19**, 189–193.

Williams W. T., Brady M. and Willison S. C. (1977) Air pollution damage to the forests of the Sierra Nevada Mountains of California. *J. Air Pollution Control Assoc* **27**, 230–234.

Willson R., Shair F. H., Reynolds B. and Greene W. (1983) Characterization of the transport and dispersion of pollutants in a narrow, mountain valley region by means of an atmospheric tracer. *Atmospheric Environment* **17**, 1633–1647.

Chapter 3

Description of Laboratory Model and Equipment

Further investigations of the upslope flow phenomena first observed in the atmosphere were conducted using physical laboratory models. The basic goal was to construct a model capable of generating a buoyancy driven flow over a sloping surface. The model was intended to reproduce key features of slope flows identified from literature reviews and from the field experiments described above.

A primary requirement, therefore, was that stratification of the ambient fluid be incorporated into the model so that the influence of this feature could be assessed in the laboratory model. In addition, it was necessary that the model be capable of measurements in the turbulent regime in order to reproduce the conditions found in the atmospheric flow. Certain aspects of the atmospheric flow were neglected in the laboratory model. In particular, external flow fields (analogous to geostrophic winds) were not considered so that the flow investigated was purely a free convection flow. The basis for physical modeling of atmospheric flows and the validity of this simplifying assumption is discussed in detail in Chapter 5.

In this chapter, the details of the equipment and measurement procedures used for the laboratory experiments will be discussed. The design and construction of the convection tank and associated structures are presented first. Following this, the measurement systems which were developed for temperatures and velocities are discussed. A limited discussion regarding the automation of data acquisition is presented as well. A unified schematic showing the various components used in the laboratory experiments is shown in Figure 3-1.

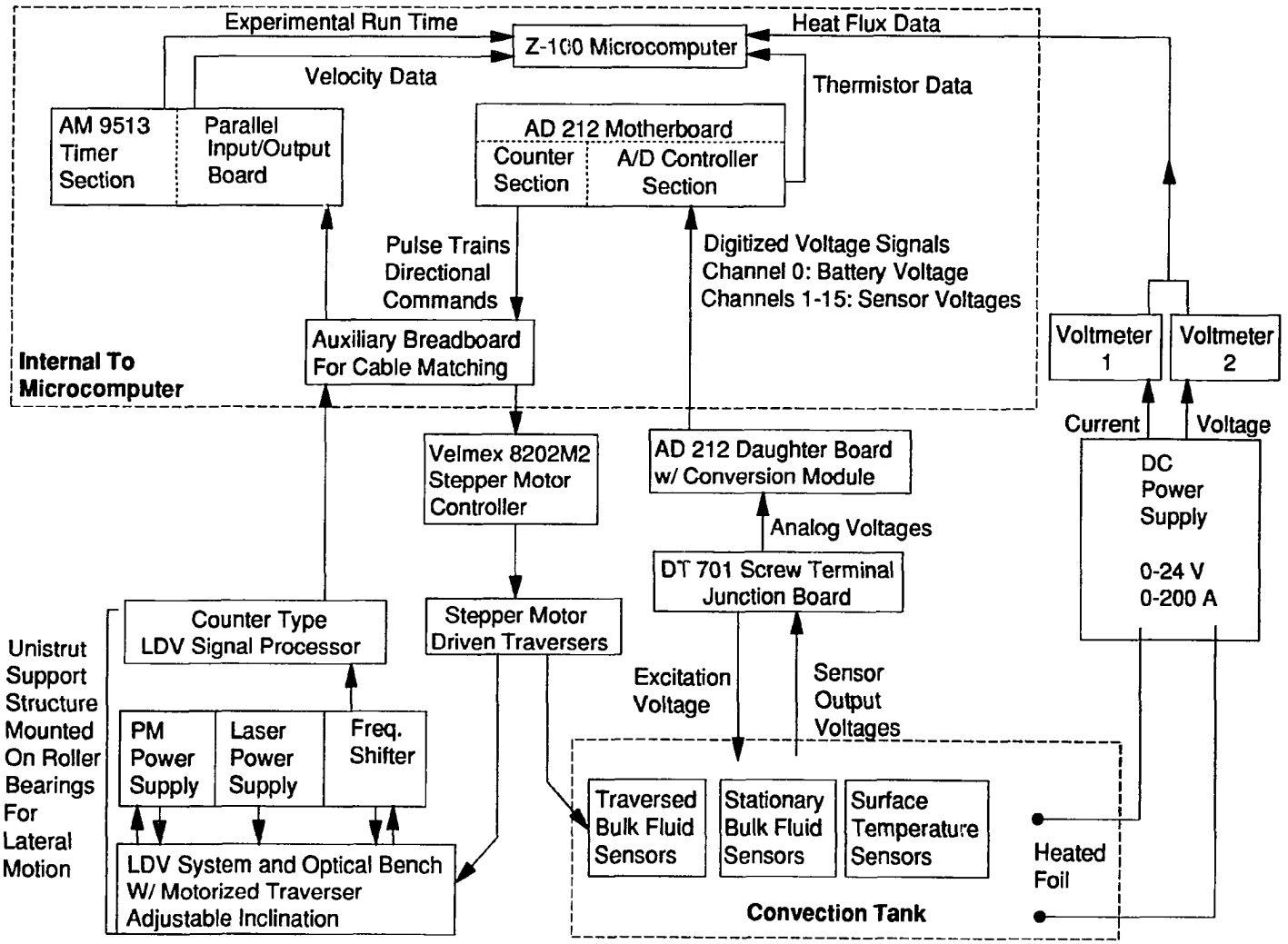

Figure 3-1 Schematic of Experimental Rig

3.1 Design and Construction of Convection Tank and Associated Structures

3.1.1 Bottom Heated Plexiglass® Tank

An early objective of this research was to construct a laboratory model of penetrative convection similar to that of Willis and Deardorff (1974) who simulated atmospheric conditions using a tank of water heated from below. To this end, a large bottom-heated tank was constructed.

The final design of the tank was necessarily a compromise between the desire to minimize wall effects by having a large volume and the need to insure structural integrity and reasonable heating requirements. The result was a cubic tank with a side dimension of 76 cm. The tank sides were constructed of 1.27 cm thick Plexiglass® supported at the corners by 90° angle aluminum pieces. The tank bottom was a 2.54 cm thick aluminum plate which was secured to the sides with closely spaced aluminum bolts and sealed with a rubber gasket and silicon sealant. In order to heat this plate as evenly as possible, a well stirred tray of water heated by immersion heaters was placed directly in contact with the bottom of the tank. The tray was constructed of thin stainless steel sheeting and contained water to a depth of 5 cm, 3 U shaped copper heating rods mounted with watertight bushings through the sides of the tray and a series of mixing jets and recirculating drains. The design goal was a temperature uniformity of ±0.1°C along the span of the heated bottom. A 28 amp variac provided up to 3000 W of power per heater, sufficient to establish turbulent penetrative convection with heat fluxes in the range described by Willis and Deardorff. Further details of the bottom heating and mixing arrangements specific to the penetrative convection problem are not germane to the remainder of this dissertation. It should be mentioned that the aluminum bottom was eventually covered with a cladding of stainless steel to eliminate corrosion problems. The stainless steel sheet was epoxied to the aluminum bottom using thermally conductive epoxy (Omega Catalog# OB-101) and sealed against the Plexiglass® sides with silicon sealant.

The Plexiglass® tank was used primarily for early flow visualization experiments and for the velocity profile measurements described in Chapter 5.

3.1.2 Lexan® Tank

A second tank was constructed before performing the heat transfer experiments (described in Chapter 4). Modifications were made so that this tank could hold the water while heating to deaerate. Silicon sealant was used instead of glue to join the faces of this tank. The corners were strengthened by grooving the edges to be joined and bolting the pieces directly together. The tank bottom was constructed of Lexan®, eliminating contamination of the working fluid by corrosion.

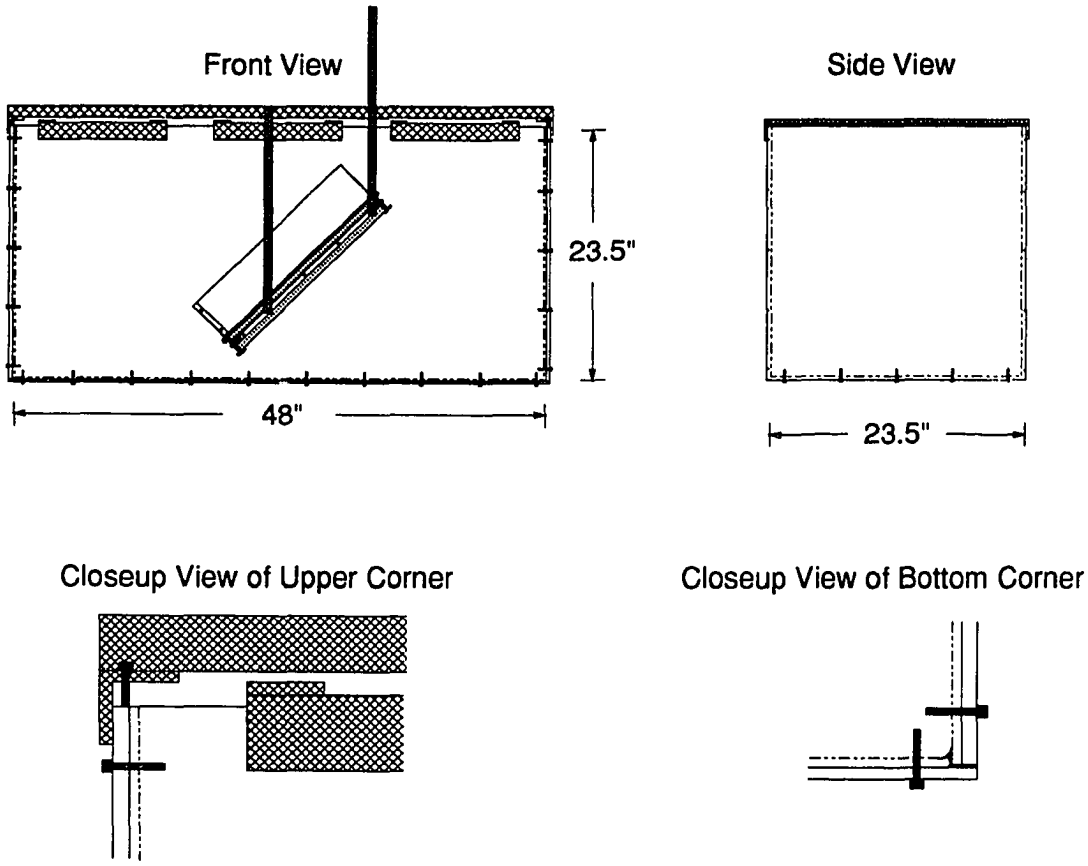

Figure 3-2 Lexan® Water Tank
Rectangular Lexan® tank, dimensions as shown. Styrofoam sheets are floated on the water's surface for insulation. Aluminum braces are placed across width on top of tank to reduce bowing of the front and back faces. Lengthwise aluminum crosspieces (not shown for side view) are used to brace the side faces and also to support the heated surface. Heated surface is held by stainless steel angle bar (0.5"×0.5"×0.125"). Heated plate shown is 20" model, depicted and described elsewhere in greater detail.

The Lexan® tank was constructed from a single 8'×4' sheet of 0.5" thick Lexan®. The inside dimensions of the tank were 47.5"×22.5"×22.5" deep. Corner and bottom joints were made with a 0.125" offsetting groove. Stainless steel socket cap screws (#8-32, 1" long) with lock washers were placed every 6" along the sides and bottom. All joints were sealed with Dow silicon sealant which was allowed to harden into a cured layer before completely tightening the bolts. Drainage was provided by a 1" drain hole threaded and fit with a ball valve leading to a flexible drain hose. To minimize bowing out of the sides caused by the hydrostatic head, the top of the tank was fitted with 4 bracing frames constructed of 1.5"×1.5"×0.25" aluminum angle bar welded to crosspieces made of 1.5"×0.25" aluminum flat bar. The Lexan® tank is depicted in Figure 3-2.

3.1.3 Heating and Stratification of Tank

The water in the tank could be heated by use of a 3000 watt immersion heater. The copper heater rod was enclosed in a stainless steel cladding as shown in Figure 3-3 to keep the water in the tank free of debris produced by corrosion of the rod. Power was controlled by a Powerstat variac providing 0-220V AC and up to 30 A of power.

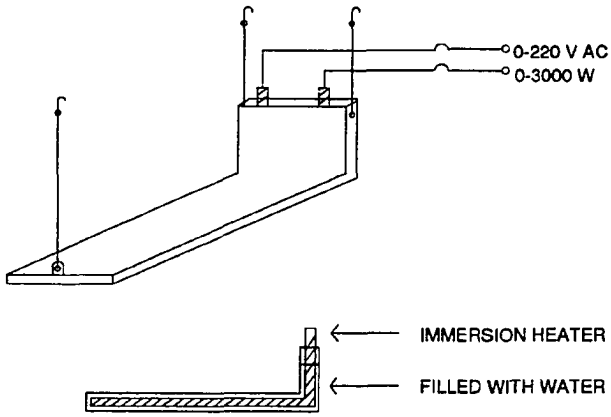

Figure 3-3 Upper Layer Heater

The heater assembly was suspended from a Unistrut® structure above the tank. The heater was positioned about 2 inches below the water's surface to provide upper layer heating for stratification of the tank, and was moved deeper when heating the entire tank for deaeration.

Several methods were tried for stratifying the tank fluid. The first method used was to fill the tank with successively warmer layers of water. Vertical mixing was prevented by filling slowly through a floating styrofoam pinholed sparging tray with a layer of sponge floating below it. This method was workable but proved to be very tedious and time consuming since water could only be trickled in. Furthermore, this method worked only when filling directly with tap water and if the heated plate was not in the tank during the filling process. This was the stratification method used for early flow visualization and velocity profile studies.

The second method used for stratifying the tank was to fill the tank halfway with hot tap water and then continue by adding successive layers of cooler water. The fill tube was positioned so that the cool water was discharged flush to the tank bottom. The upper layers were thus floated above a layer of cooler water. A stronger temperature differential could be created by further heating the initial layer of hot water and by icing the cold fill water. This stratification method had the advantages of being quicker and requiring less attention

than the method described above and was used for most of the flow visualization studies conducted. Since a dye study could be conducted only once or twice before the tank water became tinged, only a few flow visualization studies were conducted with deaerated water.

Filling of the convection tanks was accomplished through an array of 1" PVC pipes attached to the side of a fume hood in the laboratory. The fill system was arranged so that either hot or cold tap water or an intermediate mixture could be added to the tank. The fill line could be run through a Serfilco cartridge filter which filtered particles down to 0.5 μm. The drain line was set up so that the tank could be siphoned through the same piping if so desired. The fill tube ran through a flexible hose which could be positioned flush to the bottom for stratification purposes.

Neither of the previous methods for stratifying the tank could be conveniently used when the tank was filled with deaerated water. In this case, the tank temperature profile had to be adjusted by heating the upper layers and cooling the lower layers. The immersion heater assembly described above was used for upper layer heating. The bottom layers were cooled by circulating water from the bottom layers through an ice bath. Tank water was drawn out through a drain hose and then pumped through a cooling circuit and returned through the bottom flushed fill tube. To prevent mixing of the tank fluid, the cold water was circulated under a stainless steel sheet placed 1" above the bottom of the tank which provided a false bottom for the tank during stratified experiments.

Deaeration of the tank water was required before heat transfer experiments could be conducted using water in order to prevent bubble formation from altering the wall temperature. The water was deaerated by heating the entire tank volume to a temperature near 100 °C, and then allowing it to cool slowly to room temperature. The tank was initially filled with hot tap water in order to reduce the amount of heating required. During the heating process, which took about 12-16 hours using the immersion heater assembly described above, the tank water was continuously stirred using an impeller attached to the Unistrut superstructure. The impeller was also used to mix the fluid for experiments using uniform bulk temperature.

After the water had been deaerated in this manner it was covered with 2.5 cm thick extruded styrofoam sheeting. The styrofoam sheeting had a thin plastic coating affixed to either side which acted as a moisture barrier. The styrofoam sheet was cut to sizes allowing sheets to float on the surface of the water while fitting snugly in the tank. The styrofoam served the purposes of keeping dust and debris out of the tank, providing a thermally insulated boundary at the surface, and inhibiting reaeration of the water. It was found that with the water deaerated and maintained in this manner, experiments could be conducted for several weeks without encountering any problems from bubble formation under normal operating conditions.

3.1.4 Heated Plates

In the following sections, the construction of the uniform flux heated plates is described. The first plate described is a 12" long model which was used for all of the preliminary studies. A second (20") heated plate assembly which incorporated various improvements is described in the section following.

The heated foil assemblies were constructed with the following design objectives.

1. That heat flux be as uniform as possible.
2. That the surface be perfectly flat.
3. That the back of the surface be well insulated.
4. That the leading edge and trailing edge be sharply defined lines.

The heated surface consisted of a thin metal foil through which a high DC current was passed. The resulting resistance heating of the foil gave an essentially uniform heat flux from the surface. DC power was provided by a Rapid Electric DC Power Supply (0-30V, 0-200A).

3.1.4.1 Twelve Inch Model

Shown in Figure 3-4 is the heated plate design used for most of the preliminary measurements. This plate was constructed using knife edge terminals between which the foil was tightly stretched. This was a basic setup which had been used frequently in heat transfer research. The stretching is intended to pull the foil to a rigid flat surface and to provide good electrical contact between the knife edge terminals and the foil. The terminals were constructed from 0.125" stainless steel which was machined to a uniform sharp edge. The distance between the terminals was directly measured to determine the actual heated area.

The foil was held in position by a length of stainless steel which was bolted to the terminal and sandwiched the foil against the top of the outer side of the terminal. The power cables were attached to the bottom of the inner face of the terminal. Since the power cables were made up of stranded copper wire it was not possible to weld or silver solder them directly to the stainless steel terminal. Instead, each cable was stripped and split into a T. Each side of the T was slipped into a 0.25" diameter copper tube which was pressed flat, then silver soldered to the terminal. The knife edge terminals were in turn attached to 1"×1"×6" Plexiglass® blocks which were bolted to a 0.25" stainless steel plate which had been fly cut to provide a uniformly flat basal surface. The trailing edge terminal was allowed to slide along slots in the base plate and was pulled back using 2" long stainless screws anchored to a third Plexiglass® block. When the foil had been properly stretched, the trailing edge terminal was locked in place by bolting it down.

The heated foil was backed by 1.25" of extruded polystyrene insulation (Dow Styrofoam®). The foil was fixed to the styrofoam using double sided rubber tape. Temperature sensors were imbedded between the

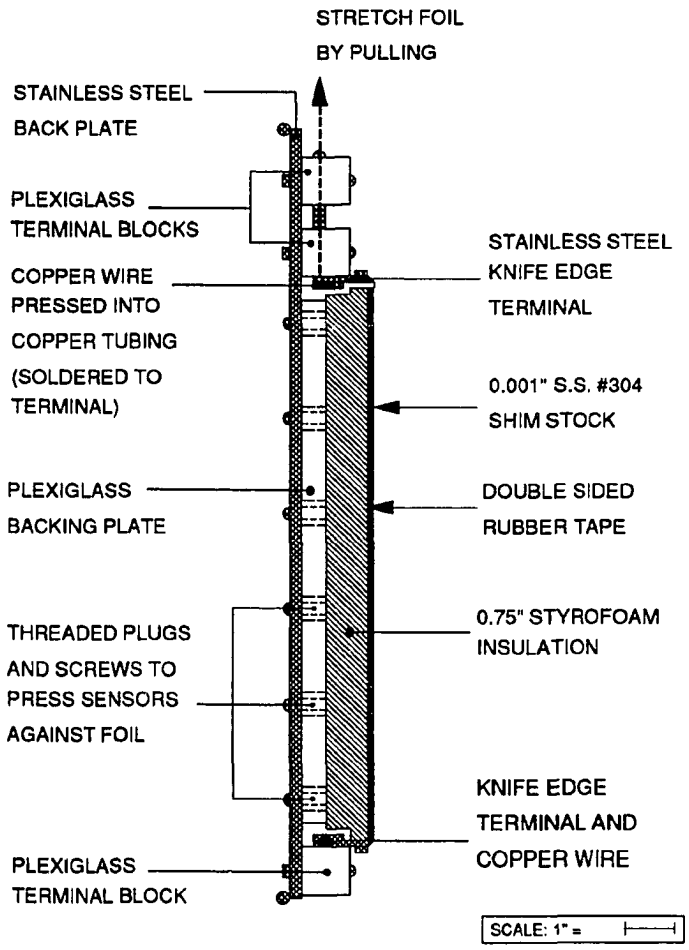

Figure 3-4 12" Heated Plate (Side View)

tape and the heated foil. Shallow grooves were melted into the rubber tape with a piece of hot metal to keep the sensors from being crushed. The grooves were filled with a thermally conductive paste (Omega Catalog# OT-201) which enhanced the thermal contact between the heated foil and the sensors.

Thermistors were used for all surface temperature measurements. An advantage of using thermistors was that electrical insulation was not as critical a factor as for thermocouples since the temperature signal from these is a resistance rather than a low level voltage as for thermocouples. In addition, each sensor was

individually coated with epoxy. Thus the sensors could be placed directly against the heated surface. Thermocouples generally have to be placed behind a sheet of insulating material which causes a significant temperature drop which must be compensated for either with a guard heater (from the back of the insulation) or by correcting the measured temperatures.

The plate assembly depicted in the figure was attached to a frame which allowed the inclination to be varied between 0° and 90°. The base frame was constructed of welded stainless steel with supporting legs of stainless steel angle bolted to it. Plexiglass® sidewalls (12"×12"×0.5") were attached to the base plate to prevent lateral entrainment into the boundary layer.

3.1.4.2 Twenty Inch Model

After conducting a series of experiments using the 12" plate described above, an improved design was formulated and a 20" long plate was constructed. The primary change was to go from stretching the foil to clamping it across the width of each terminal. This change became necessary when experimentation showed that substantial voltage losses occurred when the foil was not so clamped. This is discussed in more detail in Chapter 4. Changes implemented on the 20" plate are listed below.

- Terminals were entirely redesigned so as to get optimal electrical contact by clamping rather than stretching the foil.
- The length of the heated surface was increased to 20" to get more measurements in the turbulent regime. This length was also chosen to make full use of the power available from the DC power supply.
- The base plate was made from 0.5" Lexan® and was made to be the same size as the heated foil. Since the foil was no longer being stretched, bowing of the base plate was not expected to be a problem and Lexan® was substituted for the 0.25" stainless steel. Since the base plate was nonconductive, the clamping terminals were bolted directly to the base plate. Also, since the new base plate was the same size as the foil, the side walls were attached directly to the sides of the base plate. The sidewalls were made of acrylic (0.125"×6"×20"). Six inches was found to be an adequate wall height to contain the boundary layers which typically developed.
- The clamping terminals were slotted so that the foil height relative to the base plate could be adjusted to precisely match the depth of the insulation.
- Power cables were inserted into stainless steel tubes and all exposed copper wire covered with epoxy to reduce corrosion. The stainless tubes were hydraulically pressed flat and sealed with silver solder. The flattened tubes were silver soldered to the bottom edge of the terminals. This arrangement was preferable because it allowed the styrofoam insulation to fit snugly against the terminal's inner face.
- A second wire was spliced to each terminal at the junction of the power cable so that the voltage drop across the foil could be measured.
- All screws used throughout were #8-32 stainless steel and had socket cap heads for easy assembly and disassembly.
- A new frame was constructed to support the plate assembly from above. The frame was constructed of heavy duty aluminum angle stock (1.5"×1.5"×0.25") and rested on the tank walls. Leveling screws permitted the frame to be precisely leveled. The plate was suspended from the frame using stainless steel angle pieces. All lengths and holes were placed to

better than 0.001" tolerance using a milling machine so that the inclination angle was accurate to 0.01° (relative to the horizontally leveled supporting frame). This frame was shown together with the Lexan® tank earlier in this chapter in Figure 3-2.

- A removable wall was added at the leading edge to provide a uniform boundary condition for the leading edge at all inclinations to facilitate comparison of the results to numerical models.

The clamping terminal arrangement described above is shown here in Figure 3-5. Other views of the clamping terminal are included with figures depicting the heated plate. Figures 3-6 and 3-7, following, show the 20" length plate.

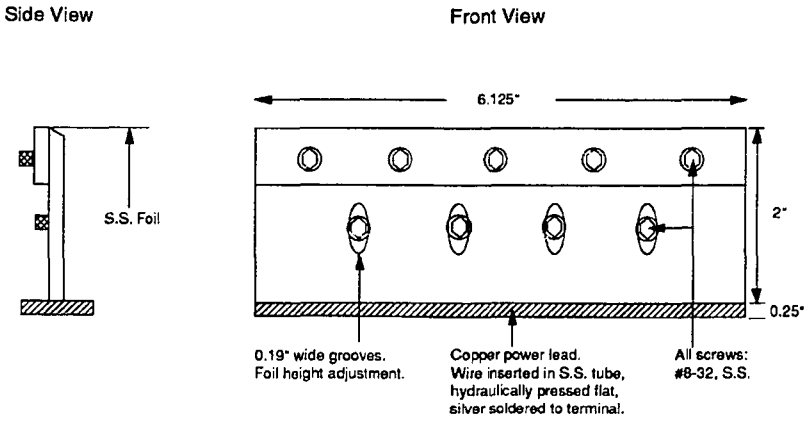

Figure 3-5 Clamping Terminal For 20" Heated Plate

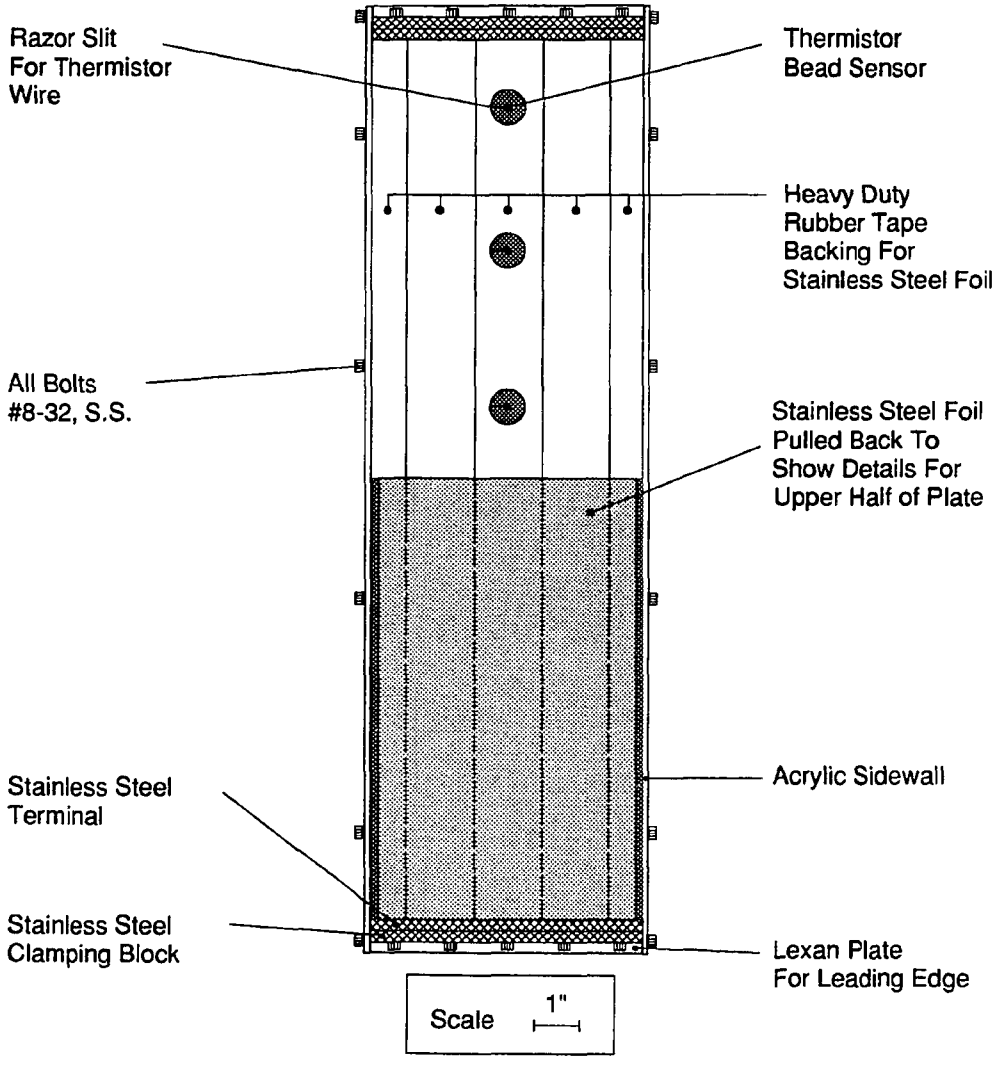

Figure 3-6 20" Heated Plate (Front View)

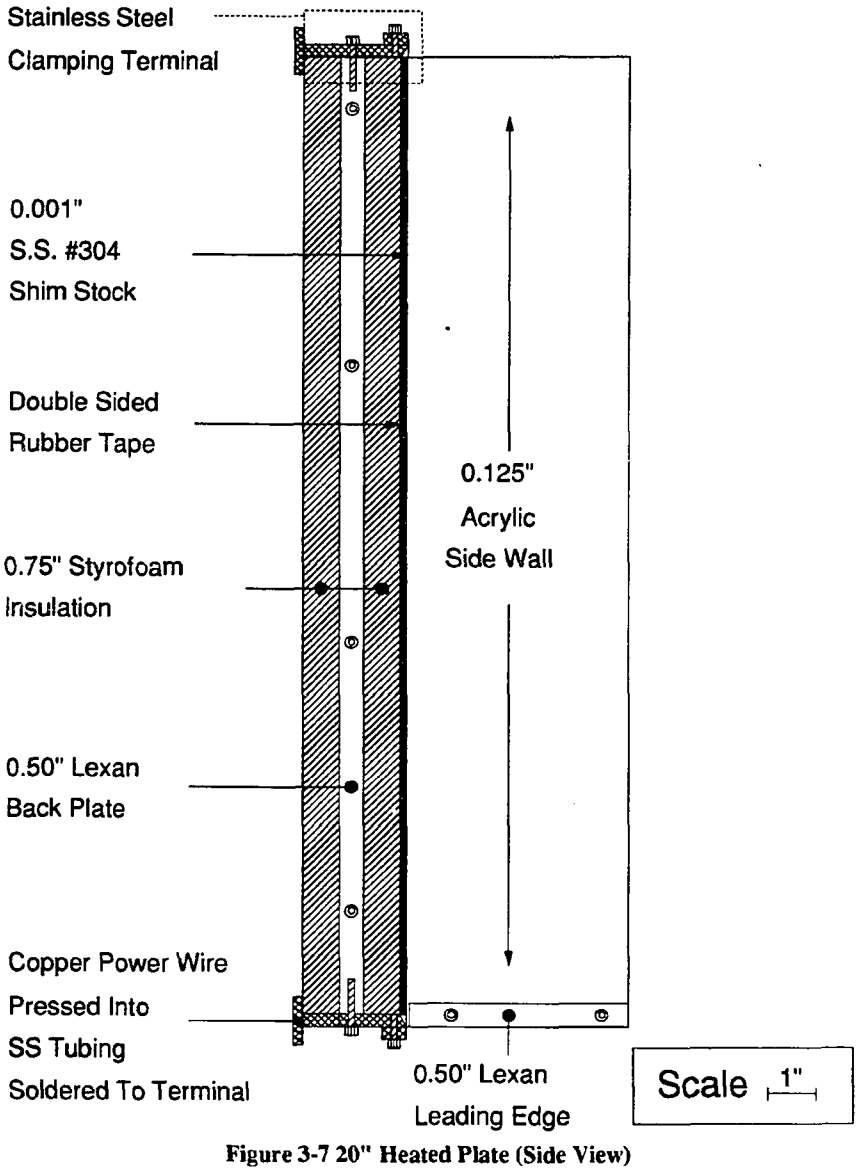

Figure 3-7 20" Heated Plate (Side View)

3.1.4.3 Lateral Uniformity of Temperatures

In order to assess the importance of edge effects, tests were run to measure the lateral variation in temperatures across the plates. Shown below are some of the typical results which were obtained with the 20" plate.

Surface sensors were placed in the plate at a downstream distance of 21.1 cm at lateral positions spanning the plate. Plate temperatures were measured at various heat fluxes encompassing the laminar, transition, and turbulent flow regimes. The temperature difference from the bulk fluid was determined for each point. The normalized temperature differences are plotted in Figure 3-8.

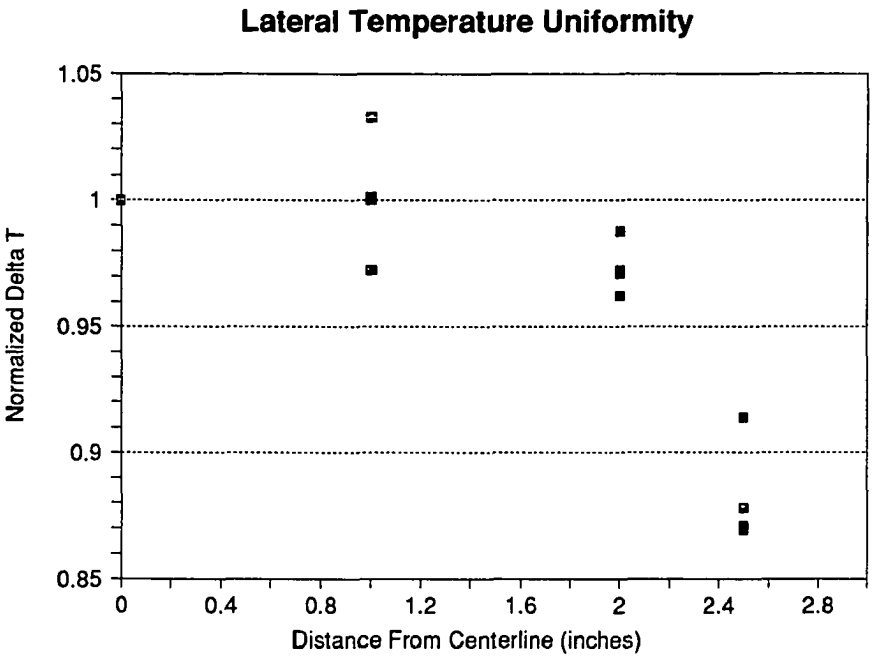

Figure 3-8 Lateral Surface Temperature Profiles

As expected, the maximum temperature difference was usually at the center position so that lateral temperature uniformity was easily assessed by dividing the local temperature rise by the centerline value. As can be seen deviations were never greater than 4% in the center 2/3 of the plate. Measured temperatures indicated a deviation of only about 10% for the outermost sensor which was placed 0.5" from the plate edge. The results shown encompass surface to fluid temperature differences ranging from 0.5°C to 50°C. Measurements were made at various other distances downstream and agreed with these results. Similar results were also obtained for the twelve inch plate but are not shown.

3.2 Temperature Measurement Methods

3.2.1 Development of Temperature Measurement Methods

Over the course of the experimental program conducted for this dissertation, a variety of temperature sensors were evaluated and used for the measurements which were conducted. Initially, it was decided to try using thermocouples since these have the significant advantages of being inexpensive and relatively rugged. Accuracy is rarely better than ~±0.5°C for standard thermocouples. Ultra fine copper-constantan thermocouples were utilized initially for some early measurements. When difficulties were encountered with electrical noise disrupting the low level signals of interest it was opted to switch to using thermistor type temperature sensors. Highly accurate signals which have a large temperature coefficient are easily obtained with thermistors. Thermistors are only capable of measurements over a relatively narrow range of temperatures but this was not a problem in this case since the temperatures of interest here ranged only from 0 to 100°C.

In view of the desire to use a large number of sensors for temperature measurements throughout the heated fluid initial efforts were made to obtain inexpensive thermistors and calibrate them to the high degree of accuracy desired. Unfortunately, the only real result of this process was that a large variety of sensors were evaluated and found to be inadequate for the present application.

Certain of the least expensive thermistors were found to be inherently noisy and unstable. Falling in this category are the Keystone Carbon Co. disk type and rod type thermistors (Catalog # AL1545-6240-73-R1 and AL03006-5818-97-G1) and also the Sintec precision thermistor (Catalog # RL1005-5744-103-D1).

Some of the other thermistors used were found to be stable and accurate, but were difficult to successfully make immersible. Into this category fall the Yellow Springs Instrument Co. thermistors (also sold by Omega Inc.). YSI thermistors used include the bare thermistors with ±0.1°C and ±0.2°C tolerances (Catalog # 44006 and 44031), the above thermistors with teflon casing (Catalog # 44006 and 44131), and the general purpose surface probe (Catalog # 081). We were unable to adequately insulate the bare sensors for underwater or surface temperature measurements although a variety of epoxies and sealants were repeatedly layered on. The teflon encased thermistors could be sealed with a fair degree of success but the sensors were still prone to leak water into the teflon casing and become decapitated. The surface probe sensors were found to be quite rugged, and, with silicon sealant applied to lead junctions, could be reliably used underwater. However, significant problems were encountered when measuring temperatures of the electrically heated surface with these sensors.

The most reliable sensors, from the standpoint of stability and immersibility, were the Thermometrics Series AB6 Thermobead and Thermoprobe assemblies. These sensors had the additional advantage of being extremely small and therefore had a rapid thermal response time. Assemblies which were used include the

AB6C8-BR16KA103, the AB6E3-BR16KA103, and the AB6E8-BR16KA103. Thermistor assemblies with manufacturers specified tolerances from ±5% up to ±40% were utilized successfully, but only after carefully calibrating against the YSI #44131 sensors mentioned above.

The single disadvantage of the Thermometrics assemblies was their fragility. This was due to the small size of the bead sensors and the attached leads. The 'ruggedized' BR16 sensor bead had a nominal diameter of 0.016" with 0.001" platinum leads and was sealed in a glass casing. The assemblies had extension leads attached (38 gauge isomid insulated wire), but great care in handling was still required for these sensors. As an example, electrical insulation of the lead wires using a spray epoxy varnish resulted in an embrittlement of the lead wires which quickly snapped at break points in the epoxy covering. A drawing of the fine gage thermistor assembly described above is included here as Figure 3-9.

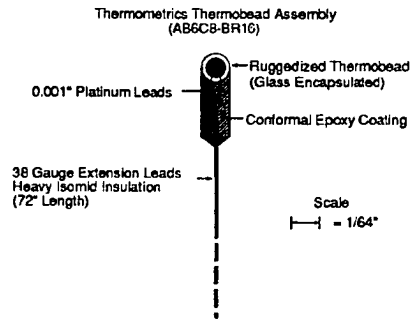

Figure 3-9 Fine Gage Temperature Sensor Assembly (Immersible)

It was most critical to avoid any undue pressure on the sensor itself. In order to be able to move the equipment, the extension leads were bundled together and passed through a 0.25" diameter PVC tube. The bundled leads were tape wrapped within the PVC tube at the point of egress to prevent abrasion against the edge of the tubing. The PVC tube was secured using hose clamps to junction terminals leading to heavier electrical cables.

3.2.1.1 Sensors for Boundary Layer Temperatures

Figure 3-10 shows the type of probes which were used to traverse sensors throughout the fluid for fluid temperature measurements. Various length probes were constructed and kept available for use. The rods could be clamped together into various configurations using commercially available clamps for assembling 0.5" rod support racks. The rods were grooved to provide a protective channel for the fine gage wire. The grooves were coated with electrically insulating Dayton Dem-Kote green epoxy insulating varnish for electrical isolation from the rod. The bottom 6" of the probe was constructed from 1/16" diameter aluminum welding rod (also coated with epoxy) which was pressed into a hole drilled in the tapered aluminum rod. The smaller

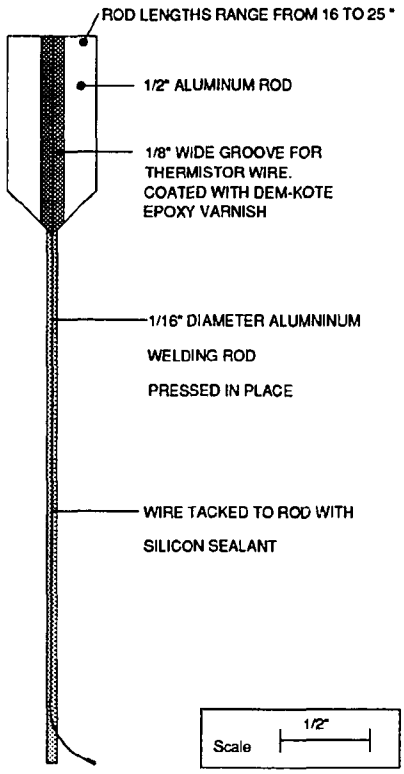

Figure 3-10 Temperature Probe for Fluid Temperatures

diameter served to reduce temperature and velocity disturbances resulting from movement of the probes. In addition, the temperature sensors (Thermometrics fine gage) were positioned about 0.5 cm from the probe. In taking tank temperature profiles, it was found necessary to always traverse downward so that the thermistor preceded the body of the probe into fresh undisturbed fluid. Otherwise, the fluid motion and thermal disturbance caused by the probe rod could affect the measured temperature profile.

3.2.1.2 Sensors for Heated Surface Temperatures

Measurement of heated surface temperatures proved to be a fairly difficult task to accomplish using available thermistors and thermistor probe assemblies. Extensive measurements of surface temperatures with a variety of sensors were necessary before a satisfactory arrangement was attained. The crucial factor was obviously that all sensors be capable of very good thermal contact with the surface. When using thermocouples a typical approach is to bond a large number of fine gage thermocouples into a laminate with the heated foil and some sort of electrically insulating substrate. This method generally destroys many of the sensors and so

was not suitable for use with the fine gage thermistors (which were at once more fragile and more expensive than thermocouples). Another method is to install a guard heater but this was not feasible at this stage of this work.

Because of the difficulty of obtaining sufficiently good thermal contact with any larger sensors it was found that only the Thermometrics fine gage sensors were suitable for these measurements. Since the temperature drops very rapidly from the surface inward, large sensors are exposed to lower temperatures on their downward facing sides. Even with the backs insulated and thermally conductive paste to the front, significant systematic errors were present for any surface temperature measurements which used the larger sensors.

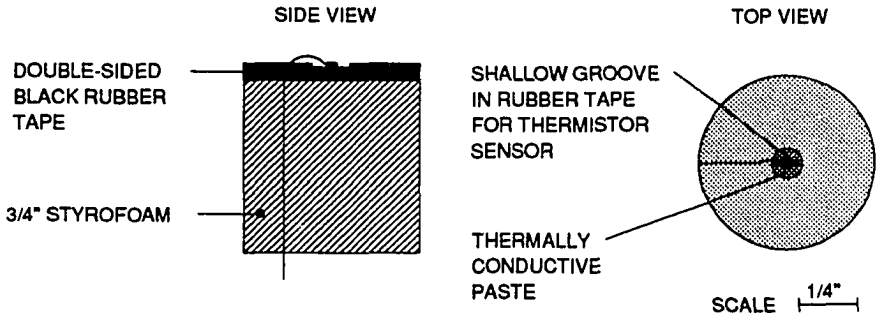

Figure 3-11 Surface Temperature Probe for 12" and 20" Plates

The temperature sensors were placed in contact with the heated surface using the arrangement shown in Figure 3-11. Cylindrical plugs were cut from the backing of the heated foil to allow the sensors to be separately attached after the foil had been pressed together with its backing tape and styrofoam insulation. The sensors were set into a shallow groove which was melted into the tape which affixed the heated foil to the styrofoam backing. The groove was filled with thermally conductive paste (Omega Catalog # OT 201) which wet the sensor and the foil and gave the best possible thermal contact.

3.2.2 Excitation Voltage Circuits For Multichannel Data Acquisition

In using thermistor type temperature sensors, the signals obtained are resistance rather than voltage as with thermocouples. In order to automate the data acquisition process, circuits must be set up to provide excitation voltages to the sensors so that the resistance can be determined. In this case, the excitation voltage was provided by a set of DC batteries (three 1.5v "D" dry cell batteries in series). (The A/D board utilized had available a 5v power source but this feed was found to be unsuitable because of excessive line fluctuations.)

Referring to the circuit depicted in Figure 3-12, the resistance of the thermistor sensor can be calculated from the voltage measured (V_i) if the excitation voltage (V_0) is known using the relation,

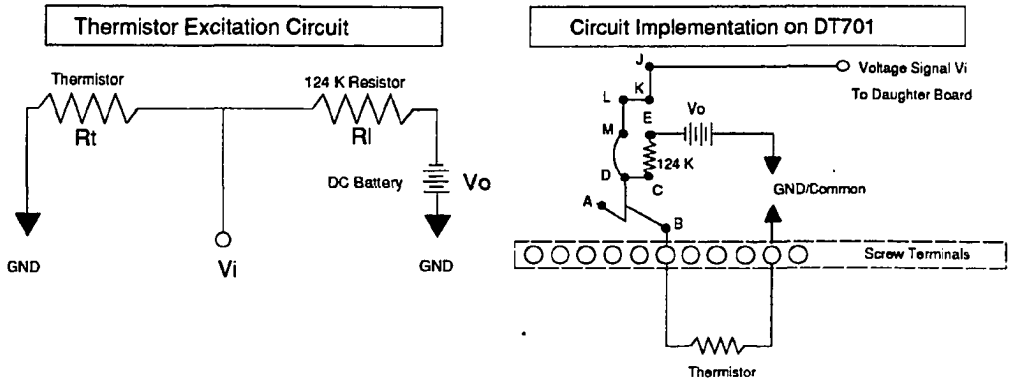

Figure 3-12 Thermistor Excitation Circuit
Circuit schematic and implementation for thermistor excitation. Separate circuits were set up on the breadboard portion of a junction board (the DT701) for each of 15 available channels of input.

$$R_t = \frac{R_l V_i}{V_0 - V_i} \tag{3-1}$$

The resistances to be measured ranged from 1000 Ω to 15000 Ω over the temperature range of interest. In order to reduce self heating effects the thermistors were placed in series with a load resistor which reduced the current flowing through the circuit by 1/10. The load resistance (R_l) was about 124 kΩ. Each of the fifteen load resistors were measured with a precision multimeter and then soldered into signal conditioning circuits on a junction board which merged the voltage signals onto a single ribbon cable for transmission to the data acquisition modules.

The maximum self heating error for the circuits can be estimated as follows. Referring to the circuit drawn in the figure, it can be seen that the current through the thermistor will be given by,

$$I_{circ} = \frac{V_o}{R_l + R_t} \tag{3-1}$$

Typical values were V_o=4.0v, R_l=124 kΩ, and R_t=14930 Ω (T = 15°C). The highest current expected in the circuit was thus 2.88×10^{-5} A. The resulting power dissipated in the thermistor was

$$P_{diss} = I^2 R_t = 0.0124 \text{ mW} \tag{3-2}$$

The power dissipation in still water of the thermistor was 0.33 mW/°C for the calibrating and surface probe type thermistors (YSI/Omega 44006 & 44131) or 0.60 mW/°C for the fine gage thermistors

(Thermometrics BR 16) so that self heating effects should affect the accuracy by less than 0.04°C. Since the sensors are recalibrated against each other this inaccuracy does not affect the precision or repeatability of the measurements.

3.2.3 Minimizing Noise for Thermistor Measurements

In obtaining an accurate calibration of the temperature sensors and utilizing these sensors to measure fluctuations of temperatures it became important to characterize the noisiness of the measured signal. Experimentation directed toward reducing this noise resulted in significant improvements, as shown in this section.

Initially, efforts were made to develop filters for the thermistor signals. Both passive and active filtering of the signal was attempted. For active filtering, low pass 2nd order Butterworth filters (shown in Figure 3-13) were implemented. The use of noise filtering circuits was eventually discontinued because the difficulty of keeping V_{out}/V_{in} strictly equal to 1 made it difficult to ensure accurate adherence to calibrated values.

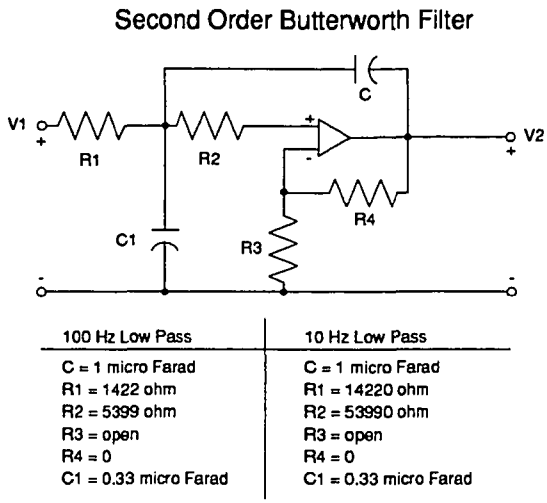

Figure 3-13 Schematic of Second Order Butterworth Filter (Low Pass)

Extensive experimentation was performed to identify and eliminate sources of stray electrical noise where possible. These measures were particularly critical for sensors imbedded in the plate, although problems were found with fluid temperature sensors as well. All cabling, connectors, power supplies, room lights and computer peripherals were separately evaluated for adverse influence on signal quality with sensors both in and out of the water. Various power supply settings were compared, including completely unplugging all the equipment which was in electrical contact with the tank fluid.

Considerable improvement was attained by taking care to identify optimal positioning for the equipment. Particularly important was the isolation of the A/D daughter module as much as possible from sources of R/F noise such as the power supplies, video terminal, and microcomputer. Also, electrically isolating the thermistor wires from any contact with metal probes proved to be very important. A slow rippling of the thermistor signals (sine wave of ±0.3° amplitude, 10 second period) was sometimes noticed. This effect and other electrical noise which appeared only when the thermistors were immersed could be significantly reduced by electrically grounding the tank fluid to building ground.

The measures enumerated above resulted in a significant reduction of noise. However, the most effective step taken for noise reduction was to switch connecting wires carrying analog signals to shielded cabling wherever possible. Since this was the most important step taken for noise reduction, the improvement in signal quality which resulted is shown in some detail.

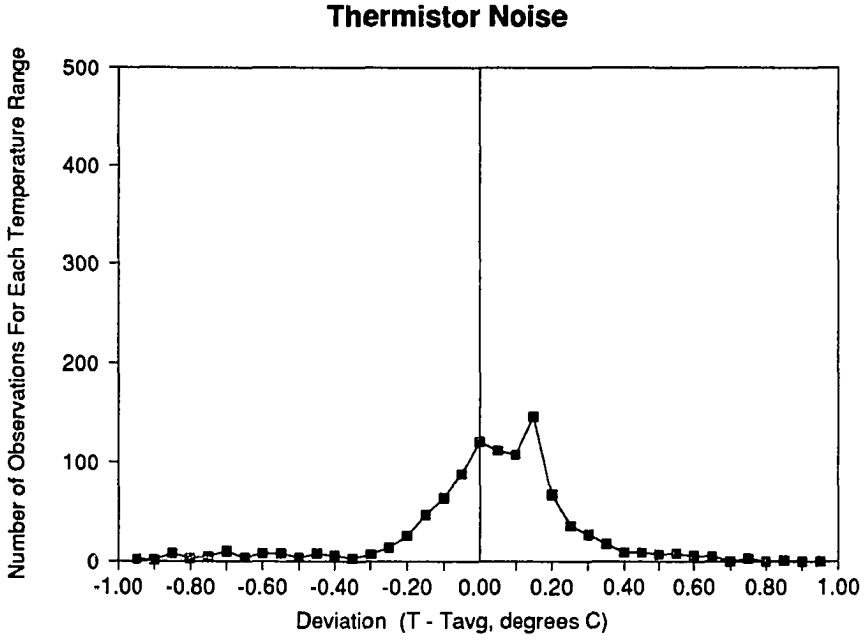

Figure 3-14 Thermistor Signal Noise - Unshielded Cable
Analysis of 1000 individual measurements of thermistor resistance while immersed in a well-mixed water bath at room temperature. Average temperature measured = 26.26°C. Standard deviation of resistance measurement = 99.85Ω (~0.25°C).

Shown in Figure 3-14 is the still fairly noisy signal which was measured before any shielding of the cables was implemented. As can be seen the sensor shows a standard deviation of about 0.25°C with a significant scatter of values over a range of ±1°C around the average temperature. The values plotted were

obtained by taking 1000 individual temperature measurements as rapidly as possible. After averaging the values, the distribution of measurements about the average was determined by counting the number of values falling in 0.05°C increments around the average.

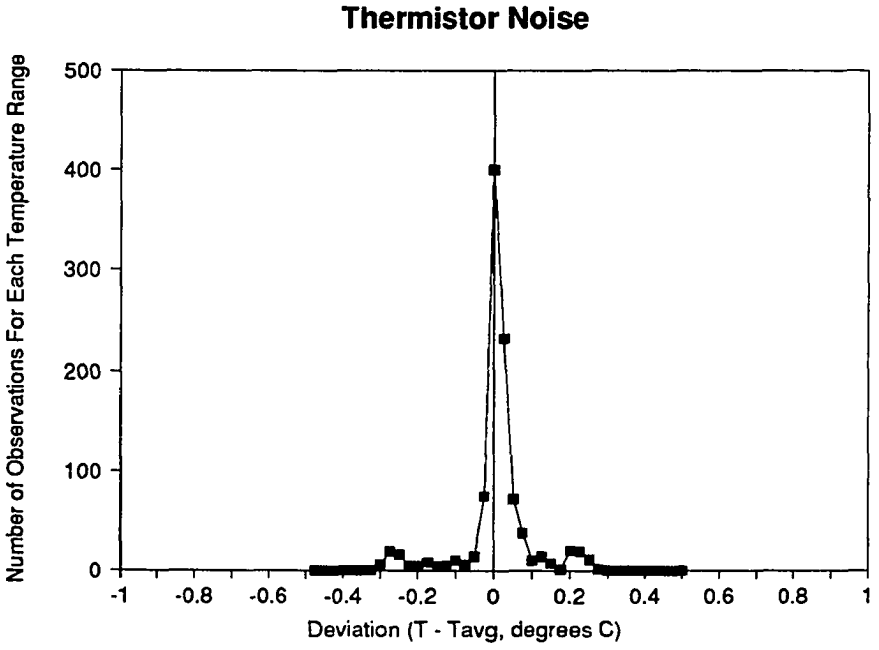

Figure 3-15 Thermistor Signal Noise - Shielded Cable
Analysis of 1000 individual measurements of thermistor resistance while immersed in a well-mixed water bath at room temperature. Average temperature measured = 26.51°C. Standard deviation of resistance measurement = 49.40Ω (~0.13°C).

In Figure 3-15 is shown the significantly improved signal which resulted from careful shielding of all cabling carrying the temperature signal. As can be seen, the shielded cable resulted in a decrease in the standard deviation to about 0.13 °C.

The standard deviation of the measured temperature was further reduced to about 0.03 °C by averaging 20 or more individual voltage measurements to produce a single temperature measurement. This also greatly reduced the number of outlier measurements as can be seen in Figure 3-16.

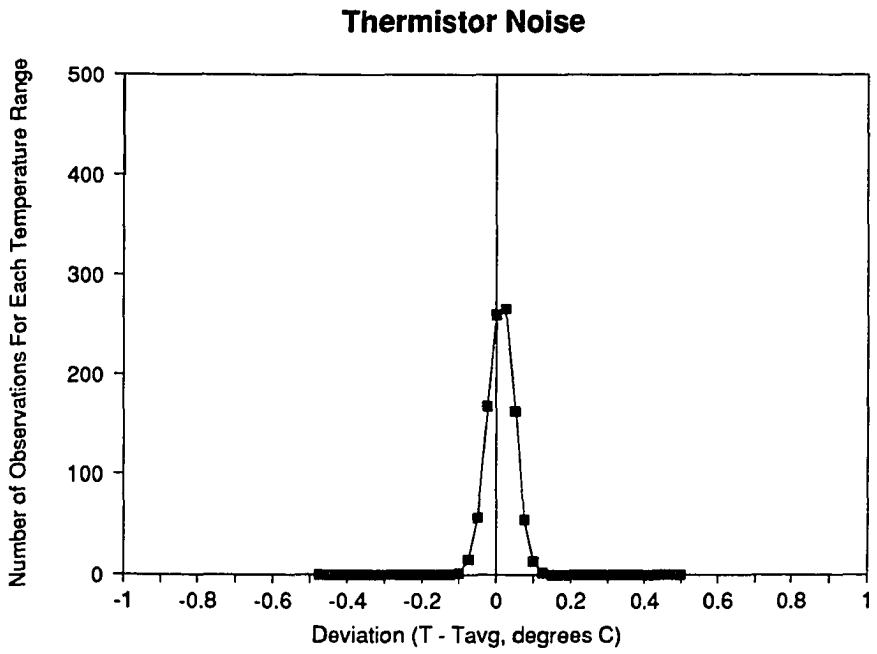

Figure 3-16 Thermistor Signal Noise - Shielded Cable (20 point averaging)
Analysis of 1000 measurements of thermistor resistance while immersed in a well-mixed water bath at room temperature. Each measurement is computed from the average of 20 values of voltage sampled by the AD212. Average temperature measured = 26.67°C. Standard deviation of resistance measurement = 12.74Ω (~0.03°C).

3.2.4 Response Time of Temperature Sensors

In making measurements of fluctuating and time dependent temperatures it is essential that the time response of the sensors be completely characterized. Described below are measurements allowing the determination of thermistor response time τ. Neglecting internal resistance to heat conduction and considering the sensor as a uniform temperature body allows us to write an energy balance equating the rate of heat accumulation to the heat transferred according to Newton's law of cooling. Define sensor temperature T, initial sensor temperature T_0, fluid temperature T_f, sensor surface area A, density ρ, specific heat c_p, sensor volume V, and heat transfer coefficient h. Then,

$$hA(T-T_f) = -\rho c_p V \frac{dT}{dt} \tag{3-3}$$

or

$$hA(T-T_f) = -\rho c_p V \frac{d}{dt}(T-T_f) \tag{3-4}$$

This homogeneous first order differential equation has the solution

$$T - T_f = C_1 \exp\left(-\frac{hA}{\rho c_p V} t\right) \tag{3-5}$$

With the initial condition,

$$T = T_0 \text{ at } t = 0 \tag{3-6}$$

we can write the solution as

$$\frac{T - T_f}{T_0 - T_f} = \exp\left(-\frac{hA}{\rho c_p V} t\right) \tag{3-7}$$

If we define time constant

$$\tau = \frac{hA}{\rho c_p V} \tag{3-8}$$

we can finally write an expression for the sensor temperature in terms of response time as

$$\frac{T - T_f}{T_0 - T_f} = \exp\left(-\frac{t}{\tau}\right) \tag{3-9}$$

The response time τ can be understood to be the amount of time it takes a thermistor to change 63.2% of the difference between its initial temperature and that of its surroundings. Response time is most easily determined by plunging a sensor into a hot water bath. τ is then obtained from the slope of a semilog plot of $(T - T_f)/(T_0 - T_f)$ vs. time. All sensors used were thus characterized. Representative plots are shown in Figure 3-17, 18, and 19. A tabulated summary of response times and best fit slopes for the various sensors used is shown below.

Table 3-1 Temperature Sensor Response Times

Sensor Type	Slope	Time Constant (sec)
Thermometrics Fine Gage (Catalog #BR16AB6C8)	11.974	0.08
Thermometrics Fine Gage (with Devcon epoxy insulation added)	6.328	0.16
YSI Surface Sensor (Catalog #081/44006)	0.38	2.63
YSI Teflon Encased Bead Sensor - Calibrator (Catalog #44131)	0.345	2.90

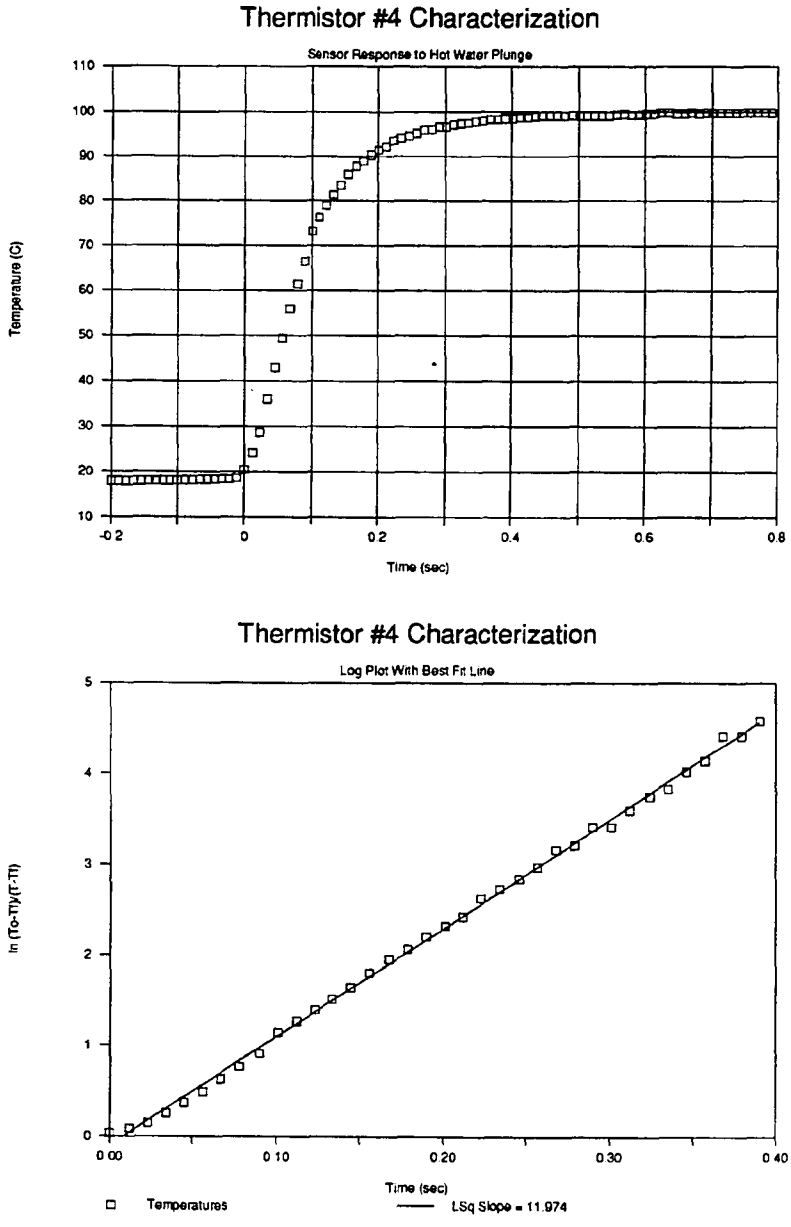

Figure 3-17 Thermistor Response (Fine Gage)
Fine gage thermistor (Thermometrics type BR16AB6C8). Least squares fit slope = 11.974. Response time $\tau = 0.08$ seconds.

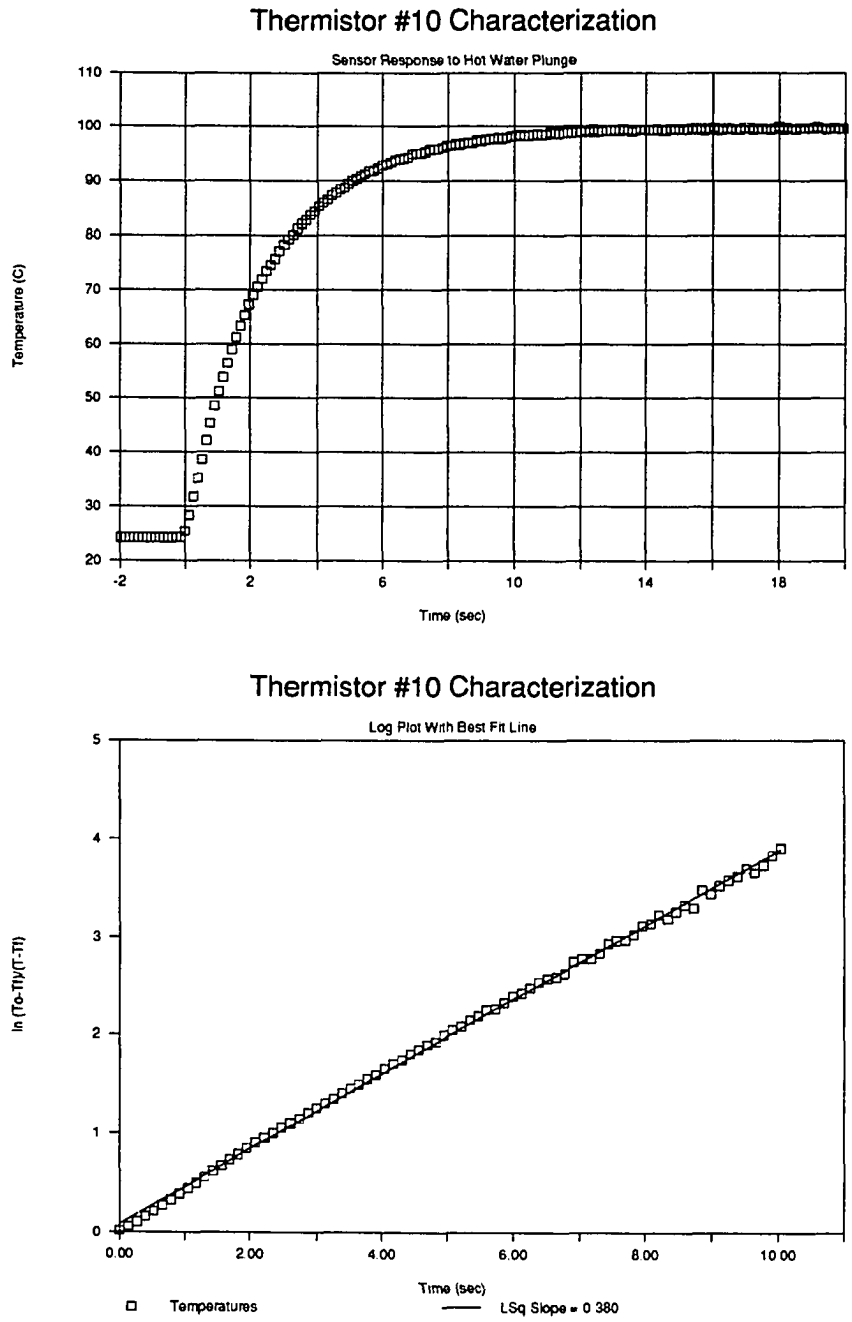

Figure 3-18 Thermistor Response (Surface Sensor)
Surface temperature probe type thermistor (Omega Catalog #ON-909-44006; YSI Catalog #081/44006). Least squares fit slope = 0.38. Response time $\tau = 2.63$ seconds.

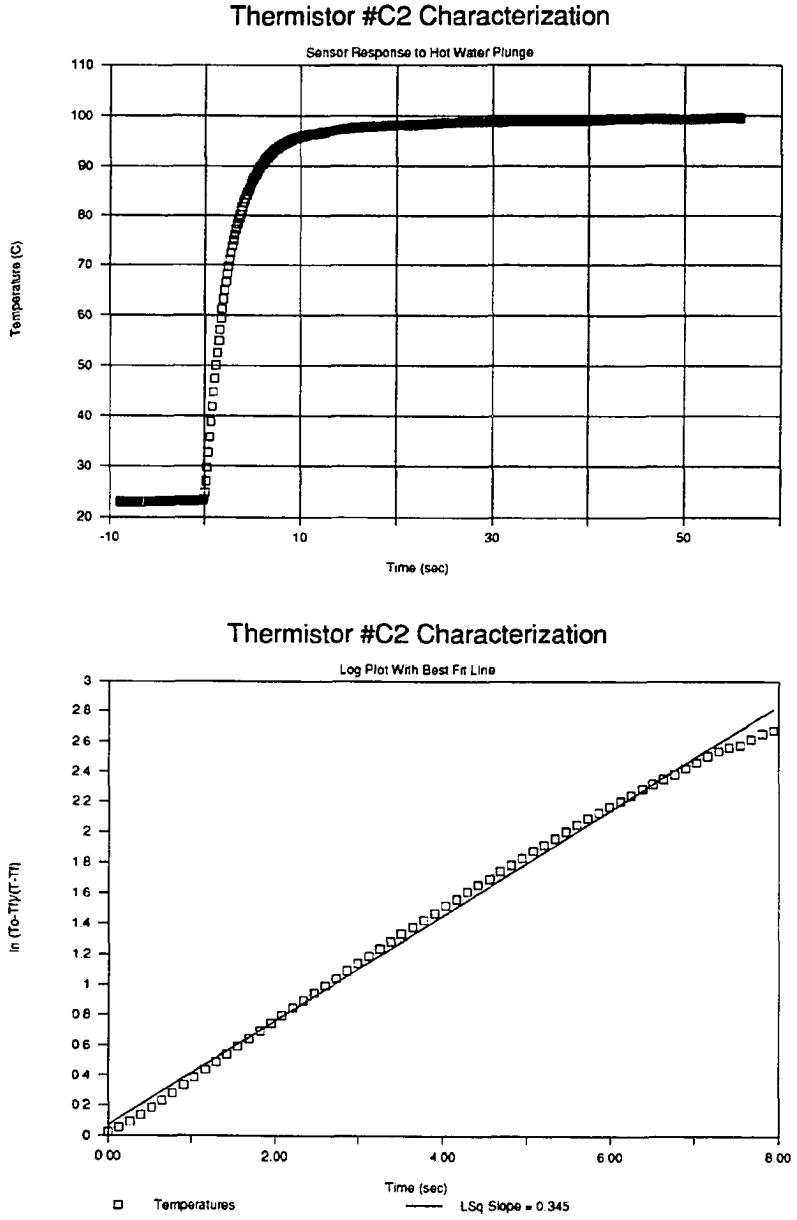

Figure 3-19 Thermistor Response (Teflon Encased)
Teflon encased bead type calibrating thermistor (YSI Catalog #44131). Least squares fit slope = 0.345. Response time $\tau = 2.90$ seconds.

3.2.5 Calibration of Sensors

It was necessary to calibrate the thermistors used in these experiments in order to obtain the accuracy desired (±0.1°C). Sensors which follow a published curve to an accuracy of ±0.1-0.2°C are readily available

commercially. It was, however, prohibitively expensive to obtain such accuracy from the manufacturers of the more specialized fine gage and waterproofed sensors which were used for the bulk of the measurements. Furthermore, a thermistor's characteristic resistance can be affected by strain or shock to the thermistor bead or its connecting leads. Thus it was necessary to calibrate all the temperature sensors before using them for measurements and also to periodically recalibrate any sensors which began to deviate from their originally determined calibration. Recalibration was usually necessary whenever thermistors were detached from an assembly (as happened whenever the heated surface was modified or reassembled).

The basic procedure followed for performing a calibration was to place a number of calibrating sensors together with the sensors to be calibrated in a water bath. Calibrations were performed by obtaining the resistance of the unknown sensors at the water bath temperature as measured by the calibrating sensors. The resistance-temperature data obtained was correlated using the Steinhart-Hart equation. This equation is recommended for use by a number of thermistor manufacturers and has the form,

$$\frac{1}{T} = A + B\ln R + C(\ln R)^3 \tag{3-10}$$

where A,B and C are the constants to be determined.

The calibrating sensors used were specified by the manufacturer to be accurate to 0.1°C (YSI Catalog #44131). The sensors used for the calibrations reported here were encased in a teflon tube by the manufacturer and further sealed with silicon rubber sealant to prevent water from entering from the top of the tube. Still, the sensors were somewhat prone to become deviant after aging. Careful attention was thus paid to the quality of data indicated by the calibrating sensors and 3-5 of these sensors were typically inserted into the water bath to provide redundancy of the measurements. All data from any calibrating sensor which departed from the prevailing values of the other calibrating sensors was discarded.

3.2.5.1 Fitting R-T Data

The three coefficients of the Steinhart-Hart equation can be directly calculated if given three paired values of resistance and temperature covering the range of interest. An improvement in fit can be attained by taking a larger number of R-T values and performing a least squares fit to compute the values of the coefficients. This analysis is fairly straightforward since the Steinhart-Hart equation takes the form of a polynomial in powers of ln(R) which is used to compute inverse temperature values.

To minimize the square of the error for we must attempt to minimize the sum S, where, for n data values we have,

$$S = \sum_{i=1}^{n}\left[\frac{1}{T_i} - (A + B\ln R_i + C\ln R_i^3)\right]^2 \tag{3-11}$$

S is minimized by setting the partial derivatives with respect to each of the coefficients to be zero. Thus,

$$\frac{\partial S}{\partial A}=0 \quad \Rightarrow \quad \sum_{i=0}^{n}\left[\frac{1}{T_i}-(A+B\ln R_i+C\ln R_i^3)\right]=0 \tag{3-12}$$

$$\frac{\partial S}{\partial B}=0 \quad \Rightarrow \quad \sum_{i=0}^{n}\left[\frac{1}{T_i}\ln R_i-(A\ln R_i+B\ln R_i^2+C\ln R_i^4)\right]=0 \tag{3-13}$$

$$\frac{\partial S}{\partial C}=0 \quad \Rightarrow \quad \sum_{i=0}^{n}\left[\frac{1}{T_i}\ln R_i^3-(A\ln R_i^3+B\ln R_i^4+C\ln R_i^6)\right]=0 \tag{3-14}$$

leading to

$$\sum_{i=0}^{n}(A+B\ln R_i+C\ln R_i^3)=\sum_{i=0}^{n}\frac{1}{T_i} \tag{3-15}$$

$$\sum_{i=0}^{n}(A\ln R_i+B\ln R_i^2+C\ln R_i^4)=\sum_{i=0}^{n}\frac{1}{T_i}\ln R_i \tag{3-16}$$

$$\sum_{i=0}^{n}(A\ln R_i^3+B\ln R_i^4+C\ln R_i^6)=\sum_{i=0}^{n}\frac{1}{T_i}\ln R_i^3 \tag{3-17}$$

Expressing the equations in matrix form:

$$\begin{pmatrix} n & \Sigma\ln R_i & \Sigma\ln R_i^3 \\ \Sigma\ln R_i & \Sigma\ln R_i^2 & \Sigma\ln R_i^4 \\ \Sigma\ln R_i^3 & \Sigma\ln R_i^4 & \Sigma\ln R_i^6 \end{pmatrix}\begin{pmatrix} A \\ B \\ C \end{pmatrix}=\begin{pmatrix} \Sigma T_i^{-1} \\ \Sigma T_i^{-1}\ln R_i \\ \Sigma T_i^{-1}\ln R_i^3 \end{pmatrix} \tag{3-18}$$

This set of linear equations is of form $\mathbf{A}\cdot\mathbf{x} = \mathbf{b}$ and can be solved for the unknown vector $\mathbf{x}$ by the Gauss-Jordan elimination technique with full pivoting (see Press et al., (1986)).

3.2.5.2 Sensor Time Lag During Calibration

In the calibration process, a difficulty arises involving the comparison of temperatures measured by sensors with varying time constants. In order to be sure that the same temperature is being indicated by all the different types of sensors it is necessary to hold the bath temperature constant for long enough that all of the temperatures have time to stabilize to the same constant value. This is easily accomplished at boiling and at room temperature. At least one additional intermediate value is required in order to solve for the three unknown constants in the Steinhart-Hart equation. A uniform temperature bath which could hold a set temperature to an accuracy of ±0.1 °C was not available so the calibrations described here were obtained by taking a vessel of hot water and allowing it to cool very slowly while obtaining resistance values for the sensors at various temperatures. The Steinhart-Hart equation's coefficients were then calculated based on a best fit to the R-T data collected over the entire temperature range. One advantage of this method was that the quality

of the calculated curves over the entire temperature range could be checked directly against the data collected. Another advantage was that the range of fit could be narrowed depending on the range of actual interest with an ensuing advantage in the quality of the fit.

Before this slow cooling method for calibration can be used with confidence the difficulty mentioned above with time lag between the fluid temperature and sensor temperature must be resolved. After taking various measures to insulate the vessel used for calibration it was found that the lowest rate of cooling which could be conveniently obtained in our laboratory was in the neighborhood of 0.1°C/min or less over the range of interest. The highest rates of cooling are, of course, obtained at the highest fluid temperatures. As the fluid temperature nears room temperature, this cooling rate is greatly reduced. An analysis of the response times of the various sensors to a given fluid cooling rate can allow the validity of the data to be evaluated.

The basic equation governing heat loss equates the energy lost by the sensor to the heat lost by the sensor according to Newton's Law. Again, define sensor temperature T_s, initial sensor temperature T_0, fluid temperature T_f, sensor surface area A, density ρ, specific heat c_p, sensor volume V, and heat transfer coefficient h.

$$\rho c_p V \frac{dT_s}{dt} = hA(T_f - T_s) \tag{3-19}$$

Now suppose that the fluid temperature is cooling at a constant rate of m (°C/sec). Then,

$$T_f = T_{fo} - mt \tag{3-20}$$

So that,

$$\frac{dT_s}{dt} = \frac{hA}{\rho c_p V}[(T_{fo} - mt) - T_s] \tag{3-21}$$

$$\frac{dT_s}{dt} + \frac{hA}{\rho c_p V} T_s = \frac{hA}{\rho c_p V}(T_{fo} - mt) \tag{3-22}$$

This is a first order ODE with integrating factor,

$$\text{I.F.} = \exp\left(\int \frac{hA}{\rho c_p V} dt\right) = \exp\left(\frac{hA}{\rho c_p V} t\right) \tag{3-23}$$

We note here that the time constant for the system is given by,

$$\tau = \frac{\rho c_p V}{hA} \tag{3-24}$$

so that the differential equation can be expressed as,

$$\frac{dT_s}{dt} + \frac{T_s}{\tau} = \frac{1}{\tau}(T_{fo} - mt) \tag{3-25}$$

$$\left(\frac{dT_s}{dt}+\frac{T_s}{\tau}\right)\exp\left(\frac{t}{\tau}\right)=\frac{1}{\tau}(T_{fo}-mt)\exp\left(\frac{t}{\tau}\right) \tag{3-26}$$

$$\frac{d}{dt}\left(T_s\exp\left(\frac{t}{\tau}\right)\right)=\frac{T_{fo}}{\tau}\exp\left(\frac{t}{\tau}\right)-\frac{mt}{\tau}\exp\left(\frac{t}{\tau}\right) \tag{3-27}$$

Integrate and obtain,

$$T_s=T_{fo}-mt+m\tau+C/\exp\left(\frac{t}{\tau}\right) \tag{3-28}$$

If we assume that the fluid and the sensor start out at the same temperature, we have,

$$T_s=T_{fo} \text{ at } t=0 \tag{3-29}$$

$$\Rightarrow C=-m\tau \tag{3-30}$$

$$\Rightarrow T_s=T_o-m(t-\tau)-m\tau\exp\left(-\frac{t}{\tau}\right) \tag{3-31}$$

We are interested in the temperature difference which develops between the fluid and the sensor.

$$\Delta T=T_f-T_s=(T_o-mt)-T_s \tag{3-32}$$

From the above two equations, then;

$$\Delta T=m\tau\left(1-\exp\left(-\frac{t}{\tau}\right)\right) \tag{3-33}$$

As t→∞, then,

$$\Delta T\rightarrow m\tau \tag{3-34}$$

The fastest cooling encountered during most typical calibrations was about 1.0°C/min or 0.017°C/sec. The largest time constant for thermistors was approximately 3 sec so that the maximum error resulting from the time lag can be expected to be of order 0.05°C. Figure 3-20 shows the development of this temperature deviation for the above worst case conditions. It can be seen that the maximum value is reached within a space of 3 to 4 time constants. The conditions which must be met if it is desired to keep the error in calibration due to time lag to less than 0.01°C are tabulated following the figure.

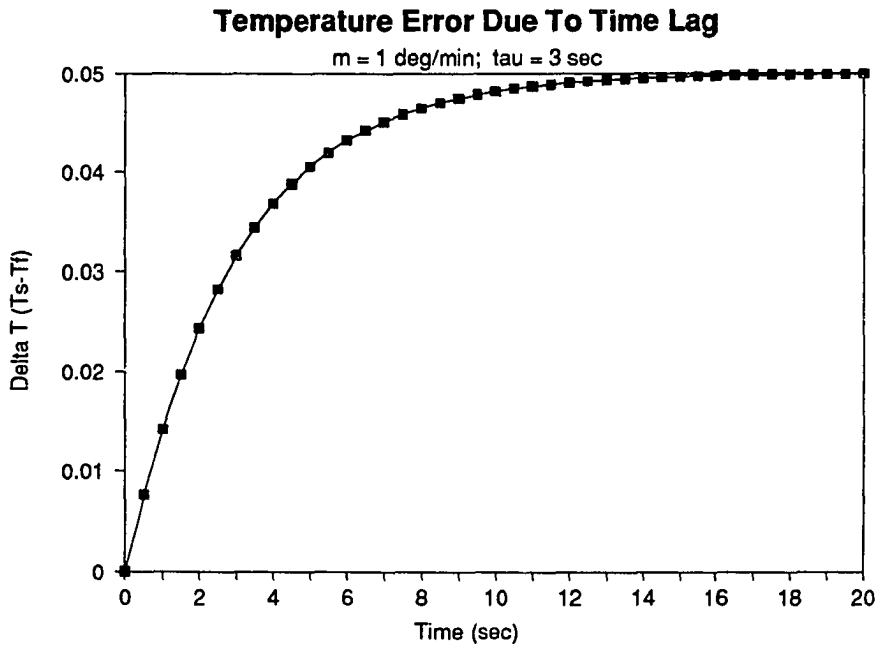

Figure 3-20 Calibration Error Due to Sensor Time Lag
Deviation of sensor temperature from fluid temperature in a steadily cooling temperature bath. Cooling rate = 0.0166°C/sec (1.0°C/min); Sensor response time τ = 3 seconds.

Table 3-2 Maximum Cooling Rate Allowed For 0.01°C Error in Calibration

Sensor Type	Time Constant (sec)	Maximum Cooling Rate (°C / min)
Thermometrics Fine Gage (Bare)	0.08	7.5
Thermometrics Fine Gage (With Devcon Epoxy Insulation)	0.16	3.75
YSI Teflon Encased Calibrator	2.90	0.21
YSI Surface Sensor	2.63	0.23

3.2.5.3 Typical Calibration Procedure

In this section, a typical calibration procedure is described along with the routines used for calibration data sampling and calculation of coefficients. The actual data shown is that of data sets RTEST53.DAT and RTEST55.DAT which were some of the last sets of calibration data used.

Initially, fifteen sensors were attached to the input terminals on the screw terminal junction board. The sixteenth channel of input (Channel 0) was dedicated to monitoring the battery voltage. All available data channels (Channels 1-15) were calibrated with sensors even though it was not anticipated that all these sensors would be needed in subsequent experiments. Careful note was made of the sensor arrangement so that in subsequent use a particular sensor would always be associated with the same input channel. This forestalled the occurrence of inaccuracies resulting from crosschannel nonuniformity in the measurement of resistances.

In this instance, channels 1-7 were occupied by new fine gage sensors which were to be used for surface temperature measurements; channels 8-10 were occupied by fine gage sensors set up for fluid temperature measurements, and channels 11-15 were occupied by calibrating thermistors. Before measurements were made, the 15 sensors were taped together at the lead wires and formed into a tightly spaced bundle. In addition, a final check was run using a routine which checked all input channels to ensure that all sensors were giving realistic resistance values. In the calibration run described here, the precalibration tests showed that sensor 15 (a calibrator) had been damaged and was indicating an open circuit. Since all input channels must be grounded for optimal performance of the A/D board and no other calibrating sensors were available, channel 15 was thus shorted to ground.

The sensors were then suspended in a 1.5 liter beaker filled with water which was heated and mixed from below using a magnetic stirrer. The sides of the beaker were taped with foam insulating tape and the top air space was packed with styrofoam peanuts and sealed with tape. After the water reached boiling, the heater was turned off and the beaker immediately placed in a rectangular styrofoam container with a fiberboard bottom. The airspace within the styrofoam box was also filled with styrofoam peanuts. The box/beaker/sensor combination was then placed back on the magnetic stirrer to provide constant mixing throughout the cooling process.

Data sampling for the calibration was started with the water boiling and continued as the bath temperature declined. The calibration data sampling routine used sampled all channels 100 times and then recorded the average resistance which had been measured for each channel. This data was recorded on disk and also sent to the printer. The battery voltage was measured before each measurement cycle so that any variation due to a slow decay of the battery voltage was eliminated. The run time was also recorded for later use in determining cooling rates for possible sensor time lag errors. Each cycle of 100 measurements on all 15 channels took about 45 seconds. The sampling was set up so that all 15 sensors were measured in sequence before repeating the measurement for the first sensor, thus the maximum time lag between individual sampling of sensors was 0.045 seconds. The temperatures measured by the calibrating sensors were continuously printed to the screen. If the indicated bath temperature had not changed by at least 0.2°C, the program waited until this incremental temperature change had occurred. The result was that data was taken as rapidly as possible at the high end of the temperature scale when cooling was most rapid and was taken much more slowly when cooling rates fell so that repetitive sampling of nearly identical temperatures was eliminated. When the temperature bath approached room temperature, ice was added to lower the temperature below room temperature. The calibration

bath was then allowed to slowly heat back up to room temperature. It was also found to be useful to adjust the room temperature when possible so that the temperature difference would be maximized when calibrating in the temperature ranges near room temperature.

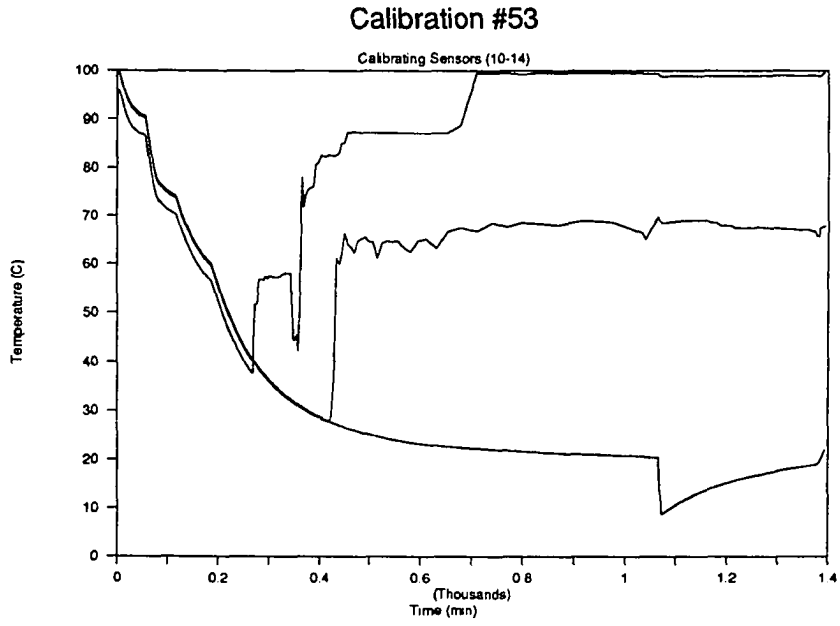

Figure 3-21 Calibration Bath Temperatures (All Calibrating Sensors)
Bath temperature as measured by calibrating sensors (11-14) for data set RTEST53.DAT. This figure includes the two sensors which went off of the manufacturer's specifications and were thus eliminated from the calibration.

As previously mentioned, care must be taken before accepting data from the calibrating sensors. Thus the first step in evaluating the data was to plot the temperatures of the calibrating sensors over the full range of temperatures. The raw data set (RTEST53.DAT) consisting of 15 channels of resistance measurements as a function of time was converted to tentative temperatures based on old calibrations and the manufacturer's specified calibrations. The resulting data from channels 10-14 (the calibrating sensors) is shown in Figure 3-21.

As can be seen, two of the sensors departed radically from the actual temperature during the course of the calibration, leaving only two reliable calibrators to be used for the final calibration calculations. The true calibrating bath temperature is replotted in Figure 3-22 sans deviant data. The nonuniform cooling rate was a result of lowering the heat setting on the magnetic stirrer slowly instead of turning it completely off at the beginning of the run. This resulted in a slower cooling rate at high temperatures for better accuracy.

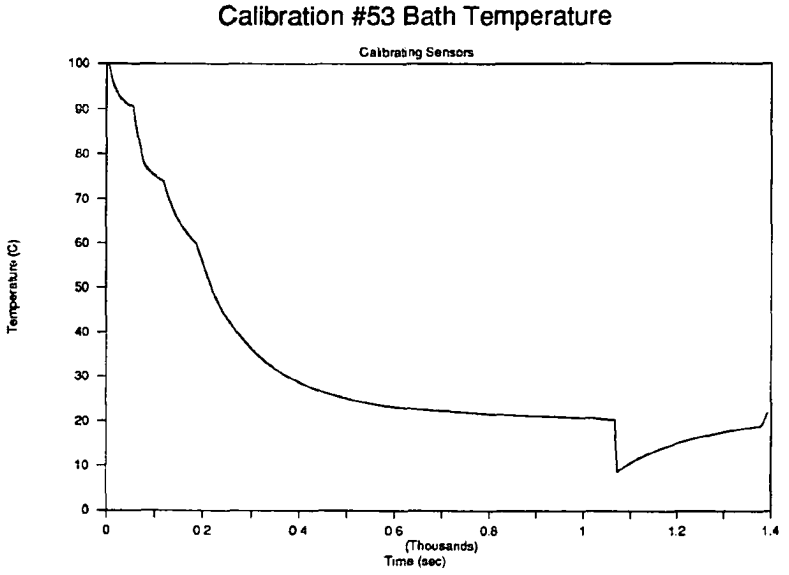

Figure 3-22 Calibration Bath Temperatures (Good Sensors Only)
Bath temperature as measured by calibrating sensors (11 and 12) for data set RTEST53.DAT.

The second step in evaluating the calibration data was to check the data for skewing caused by overly rapid cooling. Figure 3-23 shows the actual cooling rate during the course of the calibration. As can be seen, the fastest cooling occurs for temperatures near boiling. It should be noted that very rapid cooling also occurs when the bath is iced. The data points taken while ice was being used to subcool the bath were excluded from the calibration calculations by the evaluation routines and are not shown on this plot. The estimated error from cooling ($m\tau$) is shown on Figure 3-24.

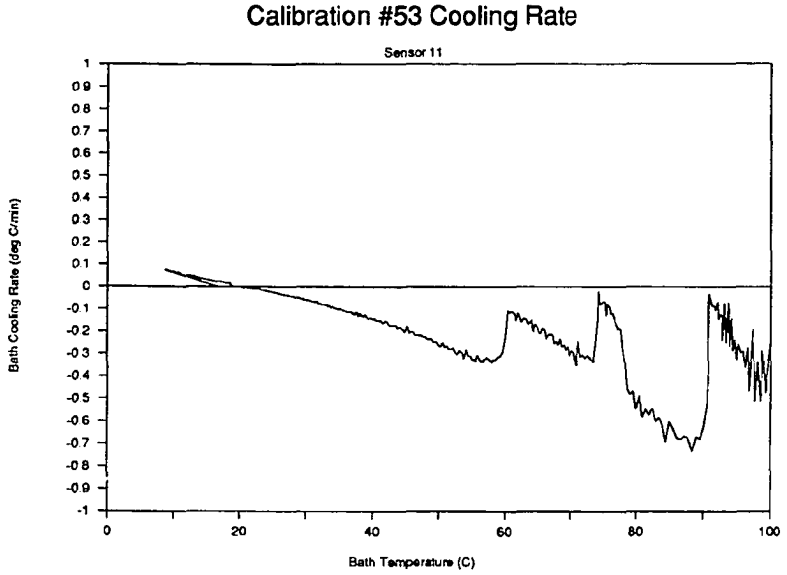

Figure 3-23 Calibration Bath Cooling Rate
Cooling rate for calibration bath. Two data points (during iced cooling) were not used in the calibration and are not shown on this plot.

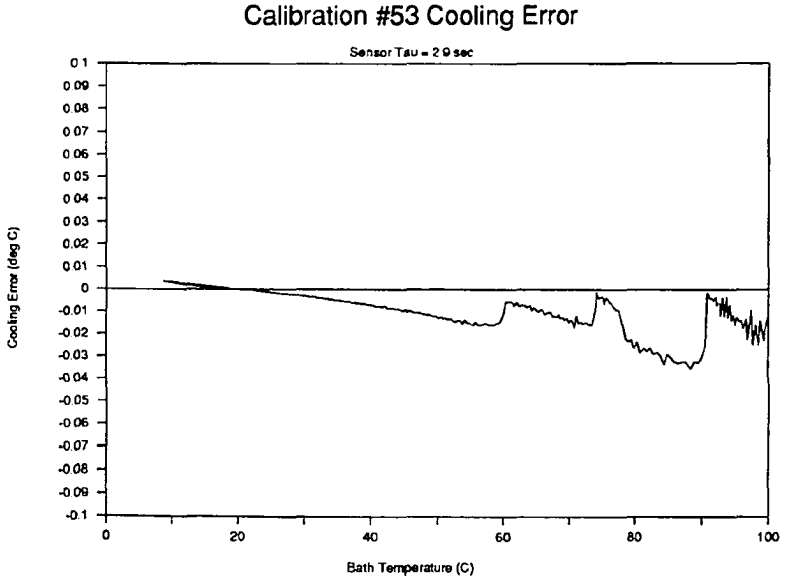

Figure 3-24 Estimated Calibration Error Due to Bath Cooling
Estimated temperature error due to sensor time lag for calibration data set RTEST53.DAT. Temperature error is estimated from the known values of the cooling rate and τ. Plot of estimated value for (T_{sensor} - T_{water}) vs. T_{sensor}.

Having checked the data for consistency and accuracy, the next step was to perform the actual calculation of best fit values for the constants in the Steinhart-Hart equation. The fitting procedure was described previously.

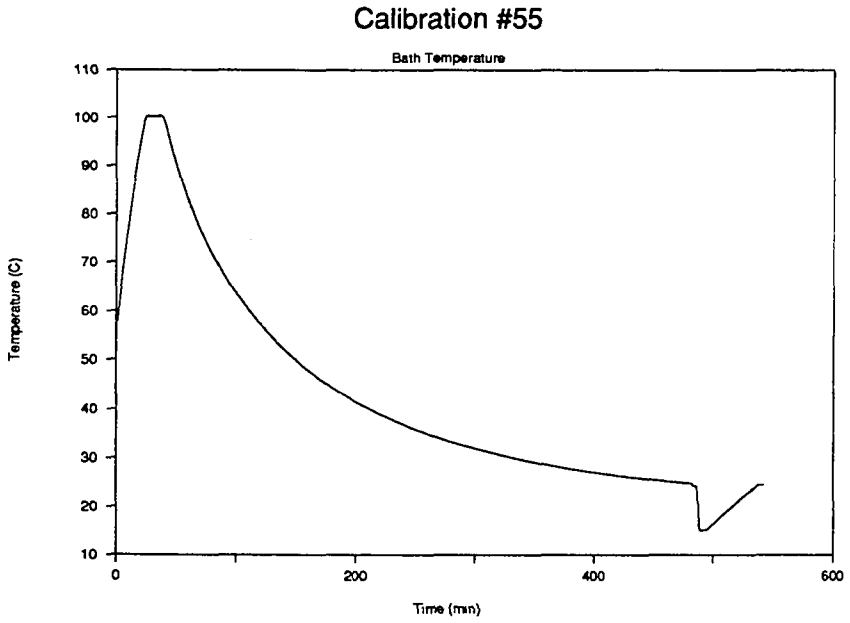

Figure 3-25 Calibration Bath Temperatures (Rapid Cooling Data Set)
Bath temperature as measured by calibrating sensors (1-10) for data set RTEST55.DAT.

This completed the calibration procedure for sensors 1-10. In order to take full advantage of the 15 channels available for temperature measurement during an experiment, the calibration sensors were then detached and five additional sensors calibrated (against the ten newly calibrated sensors) repeating the procedure above. The bath temperature for this final calibration is shown in Figure 3-25. As can be seen, the cooling rate was more rapid for this data set. However, cooling was no longer an issue because all remaining sensors had the same response time (on the order of 0.1 seconds).

We complete this discussion of calibration techniques by presenting a set of figures depicting the overall accuracy of the results. Figure 3-26 shows the standard deviation of each individual sensor from the overall average temperature as determined by averaging all 15 sensors. Standard deviations shown are actually average values over 5°C subranges. It is clear that the newest sensors (channels 1-7) have the cleanest signals with standard deviation never exceeding 0.03°C over the entire range. In the range where measurements were most often made (20-70°C) the standard deviation was even lower, typically being in the neighborhood of 0.01°C or less. Subsequent figures show that the remaining sensors had higher standard deviations overall (particularly

in the range 70-100°C). However, since these sensors were to be used for ambient fluid temperatures, they would typically be measuring temperatures in the range 20-50°C. Thus the typical standard deviation can be expected to be well below 0.05°C for the ambient fluid sensors as well.

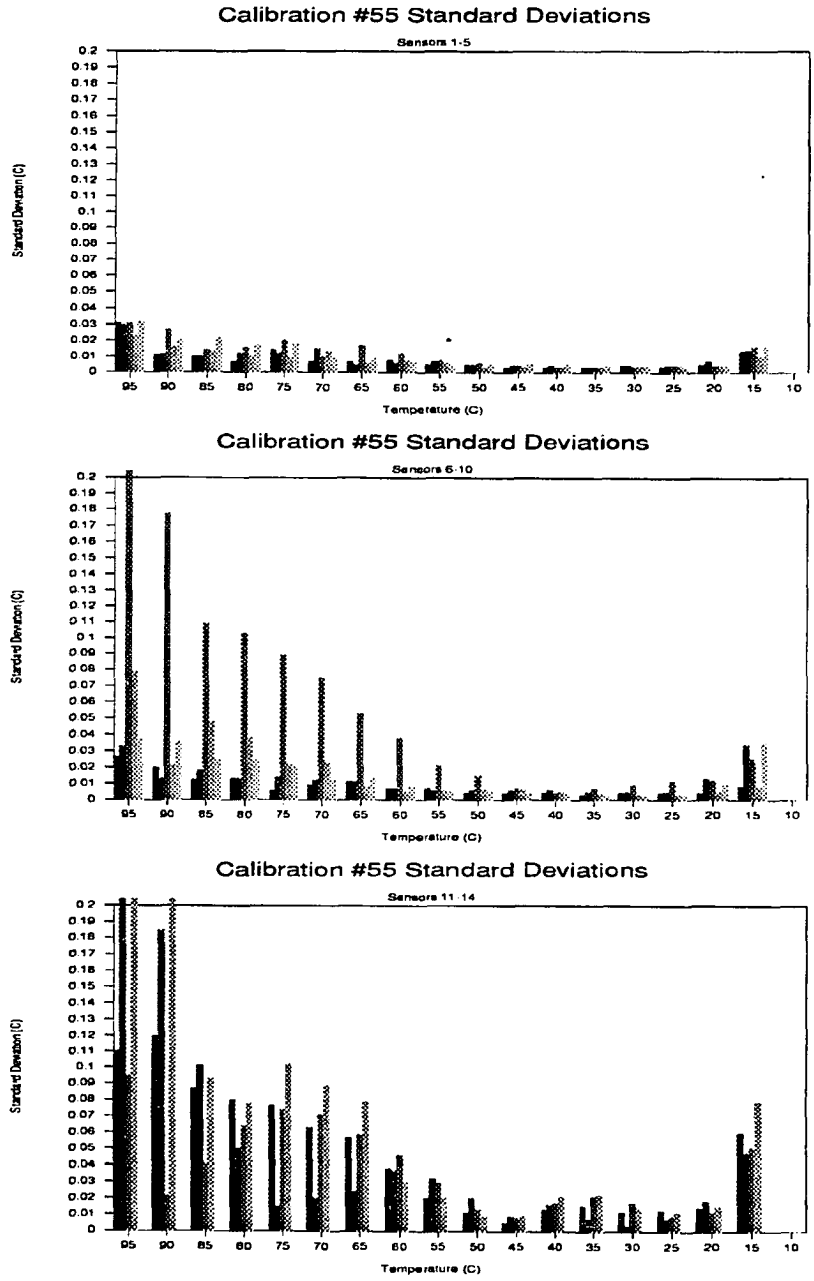

Figure 3-26 Calibration Quality - Sensors 1-15
Plots of standard deviation of sensors 1-5, 6-10, and 11-15 from calibrating temperature through range of temperatures measured. Standard deviations shown are average values over 5°C subranges.

3.3 Laser Doppler Velocimetry Measurements

In addition to the temperature measurements described in the previous section, it was necessary to develop velocity measurement techniques for the experiments which were conducted during this research. Velocity measurements were made using an LDV system (TSI Model 9100-9). In the sections following, the LDV system is briefly described and the configurations which were found to be useful are detailed. The application was a fairly demanding one for this particular system since it required passing backscattered light across a rather large test volume of water. As a result, various particle seeding and signal enhancing measures were required. Aspects of particle seeding are discussed in some detail and some of the other measures are briefly outlined. The methods used for obtaining doppler frequencies and for calculating velocity therefrom are presented as well.

3.3.1 Configurations and Setup of TSI Model 9100-9 LDV System

The TSI Model 9100-9 LDV incorporates frequency shifting to allow accurate determination of the flow reversals and low velocities which predominate in free convection. The LDV was operated in both forward scatter and backscatter modes.

Forward scatter was capable of two component velocity measurements using beam polarization to split the signals from three intersecting beams. Forward scatter measurements were restricted to point measurements. The natural particles present in water scattered sufficient light for good quality forward scatter measurements. However, forward scatter was only suitable for measurements at a fixed point because of alignment considerations. (It was not feasible to traverse the convection tank.)

Most of the velocity measurements reported in this dissertation were made with the LDV operated in backscatter mode. This permitted mounting all the optical components in line on a single optical bench which was then traversed by a mechanical slider. Backscatter measurements were restricted to a single velocity component since backscattered light does not retain its polarization as well as does forward scattered light. In addition, the reduced signal strength makes dual component measurements difficult in backscatter mode.

The entire LDV system was supported by a hinged Unistrut® framework which allowed the traverse direction to be set at any desired angle from 0° to 90°. A further degree of freedom was incorporated by mounting the entire apparatus on precision bearings, allowing several velocity profiles to be determined in quick succession by moving the optical bench and traversers to various distances from the leading edge of the heated plate.

3.3.2 Particle Seeding

The use of backscatter for the velocity measurements forced a number of steps to be taken to reduce noise and increase signal strength. Various particle seeding schemes were tried (including a dilute solution

of milk). When particle seeding was used, the tap water used to fill the tank was filtered down to 0.5 μm particle sizes before seeding. The velocity measurements were eventually made using metallic seeding particles (TSI model 10087: $\rho = 2.6$ g/cm^3, D = 4 μm). Three basic requirements for seeding particles listed by TSI manuals (1980) are:

1) Particles must produce a strong measurable signal.
2) Seeding particles must follow the flow.
3) Particles must be present in proper quantities for good measurements.

The first requirement above is readily satisfied since these particles are manufactured in appropriate sizes intended specifically for seeding flows and are further coated with a highly reflective metallic surface.

In regards to the second requirement listed above, Stoke's Law allows the terminal velocity of the particles to be calculated. Define terminal velocity V_t, particle radius R, solid particle density ρ_s, liquid density ρ_l, gravity g, and liquid viscosity μ_l.

$$V_t = \frac{2R^2(\rho_s - \rho_l)g}{9\mu_l}$$

$$= \frac{2 \cdot (2 \cdot 10^{-4}\text{cm})^2 \quad (2.6 - 1.0)\text{g/cm}^3 \quad 981\text{cm/s}^2}{9 \cdot 0.01 \text{ g/cm s}} \qquad (3\text{-}35)$$

$$= 1.4 \times 10^{-3} \text{ cm/s}$$

This calculation indicates that it would take about two hours for the particles to settle 10 cm (the typical 'head space' above the heated surface). This is well within the time frame of experiments conducted for velocity measurements. In addition, typical convective velocities were in the range 0.1 to 5.0 cm/sec so that the particle velocity can be expected to have little deviation from the actual fluid velocity, thus satisfying the first requirement above. A further calculation can be made to verify the ability of the particles to respond to turbulent fluctuating velocities. The relaxation time for the particles can be calculated from

$$\tau = \frac{\rho_p d_p^2}{18\mu}$$

$$= \frac{2.6 \text{ g/cm}^3 \cdot (4 \times 10^{-4} \text{ cm})^2}{18 \cdot (0.01 \text{ g/cms})} \qquad (3\text{-}36)$$

$$= 2.3 \times 10^{-6} \text{s}$$

The above calculation gives the time constant for the exponential response of the particle to a step change in velocity and shows that little deviation can be expected from the true velocities over the range of fluctuating velocities encountered in natural convection.

The third requirement regarding proper quantities of seeding particles is best satisfied by having one and only one particle present in the measurement volume while maintaining a high data rate. If N_p (particles/cm^3) is the number of particles and V is the volume of the measurement volume, then the probability of having a single particle in the measurement volume is maximized when $N_pV=1$.

The following calculations pertain to the particle seeding requirements for the experiments performed. The equations used are well accepted and thus are not developed here in any detail beyond that needed to make the pertinent calculations. Development of these and many other useful equations as well as a good deal of general background for laser doppler velocimetry are set forth in texts such as Durst and Whitelaw (1979) and are also available in materials published by TSI.

The measurement volume is the volume occupied by the interference fringes created at the beam crossing and can be estimated from the following equation,

$$V_{FR} = \frac{\pi d_{e^{-2}}^3}{6 \cos\kappa \sin\kappa} \tag{3-37}$$

The beam intersection half-angle for the lens used (κ) was given to be 4.701° in air and was recalculated for water using Snell's Law,

$$N_1 \sin\kappa_1 = N_2 \sin\kappa_2 \tag{3-38}$$

Therefore,

$$\kappa_{water} = \sin^{-1}\left(\frac{N_{air}}{N_{water}} \sin\kappa_{air}\right) \tag{3-39}$$

In this equation,

N_{air} = 1 (the refractive index of air)
N_{water} = 1.32 (the refractive index of water)

Therefore,

$$\kappa_{water} = 3.56° = 0.06213 \text{ radians} \tag{3-40}$$

The remaining quantity in the equation, $d_{e^{-2}}$, is the diameter of the e^{-2} contour for the beam crossing, and can be found from,

$$d_{e^{-2}} = \frac{4\lambda f}{\pi D_{e^{-2}}} \tag{3-41}$$

In this equation,

$D_{e^{-2}}$ = beam diameter from laser = 1.1 mm
λ = 632.8 nm (wavelength of light)
f = focal distance of lens = 601.5 mm

From the above, the measurement volume V_{FR} for the configuration used can be calculated to be approximately 7.23×10^{-4} cm^3. It is now possible to estimate the number of optimal number of particles needed (N_p). From the relation $N_pV = 1$ we obtain the estimated number of particles

$$N_p = \frac{1}{7.23 \times 10^{-4}} = 1.384 \times 10^9 \text{ particles/m}^3 \tag{3-42}$$

The mass of a single particle is given by,

$$\rho V = \rho \frac{4}{3} \pi R^3 = 8.713 \times 10^{-11} \text{ g/particle} \tag{3-43}$$

Therefore, the mass of seeding particles needed amounted to about 0.12 g/m^3. This optimal quantity of seeding particles was measured out by weight and added to the tank fluid. The particles were stirred into a suspension in a beaker and then added to the tank during the filling process which has been previously described. The volume of particles to be used amounted to roughly 0.1 cm^3 of for 1 m^3 of water.

It was found by trial and error that using 3-5 times the calculated optimum quantity of seeding particles gave superior results for the velocity measurements. This probably stemmed from a tendency for the particles to adhere into large agglomerations. This was further supported by visual observations which showed visible settling of particles at a rate far exceeding that expected from Stoke's Law considerations.

Because of the importance of particle/flow interaction to the accuracy of the measurements and because of concerns caused by the rapid visible settling out of particles, settling velocity experiments were conducted and are briefly summarized here. Direct measurement of the settling velocity proved problematic due to the fact that the velocities in question approached the limits of accuracy of the setup. However, particle settling velocities could be inferred from the valid data sampling rate since measurements could occur only when a particle passed through the measurement volume.

Experiments were conducted as follows. A beaker of filtered water was seeded with TSI Model 10087 particles and vigorously stirred to disperse and suspend the particles. Velocities were measured using backscatter LDV. The measuring volume was situated 3.5" (8.9 cm) below the surface of the water. Average velocities were recorded after every 100 samples. Standard deviations were calculated as well for each velocity measurement recorded. Velocities were sampled as rapidly as possible. In addition, the time required to obtain 100 measurements was recorded so that any variation in the data sampling rate could be uncovered.

Typical results for velocity and standard deviation are shown in Figure 3-27. As can be seen, velocities start out strongly negative and quickly decay to fluctuate around zero velocity. Standard deviation started out high (same order of magnitude as velocities being measured) and reached a stable level of around 0.07 cm/sec which far exceeded the average velocities being measured. Figure 3-28 repeats the data shown in the previous

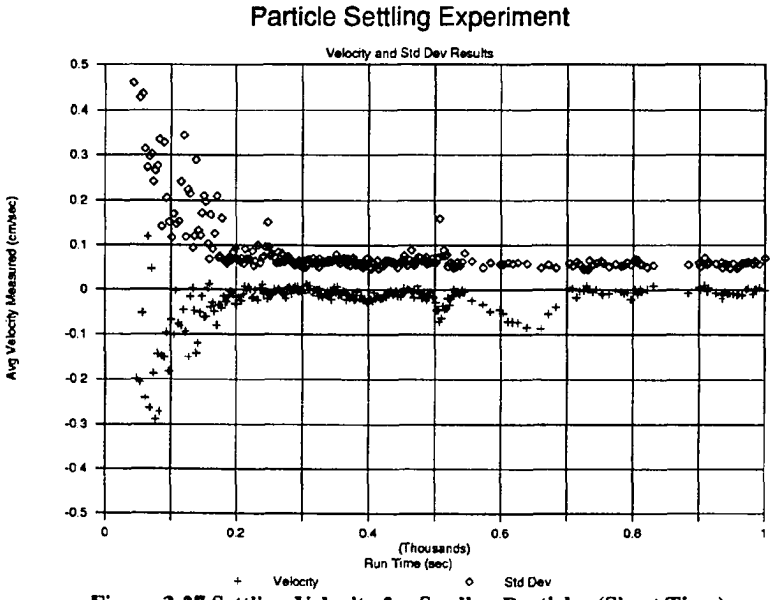

Figure 3-27 Settling Velocity for Seeding Particles (Short Time)

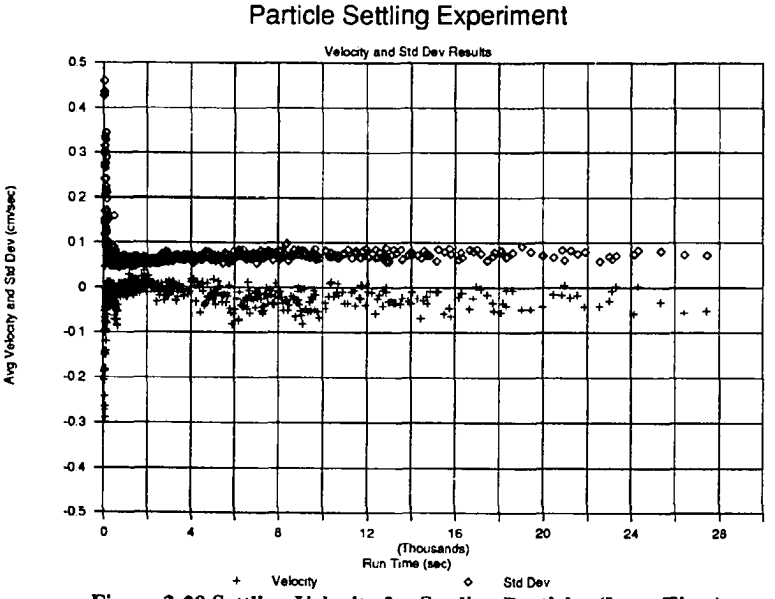

Figure 3-28 Settling Velocity for Seeding Particles (Long Time)

figure but shows velocities out to 28000 seconds (~ 8 hr) after initiating the settling process. It can be seen that data becomes more sparse as time gets very large, due to the decreasing concentration of particles available for scattering.

This effect is separately depicted in the plots shown in Figure 3-29 and Figure 3-30 which show the length of time required to obtain 100 valid data points as a function of the elapsed settling time. The first figure shows a clear break at about 500 seconds, indicating a change in regime at this time. This is the same time scale which had been previously observed for a visual clearing of the suspension to occur and is attributed to settling of undispersed solids. The settling velocity calculated from this time scale would be 1.8×10^{-3} cm/sec, an order of magnitude higher than predicted for these particles.

The second figure repeats the data in the first figure and adds measurements for larger times. As can be seen, a second break in the data is observed at about 6000 seconds. The settling velocity calculated from this time scale would be 1.5×10^{-3} cm/sec which corresponds well to the predicted Stoke's flow terminal velocity of 1.4×10^{-3} cm/sec. We thus conclude that although particle agglomeration occurs and results in a rapid visible settling out of many of the seeding particles, the Stoke's Law flow condition is obeyed by the remaining unagglomerated seeding particles so that adequate data should be obtained by overseeding the flow.

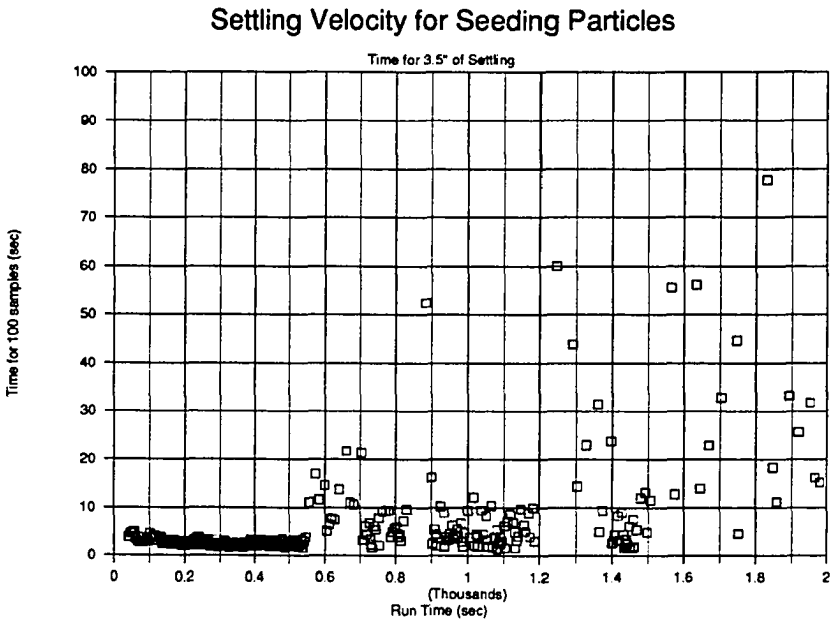

Figure 3-29 Settling Time for Seeding Particles (Rapid Settling)

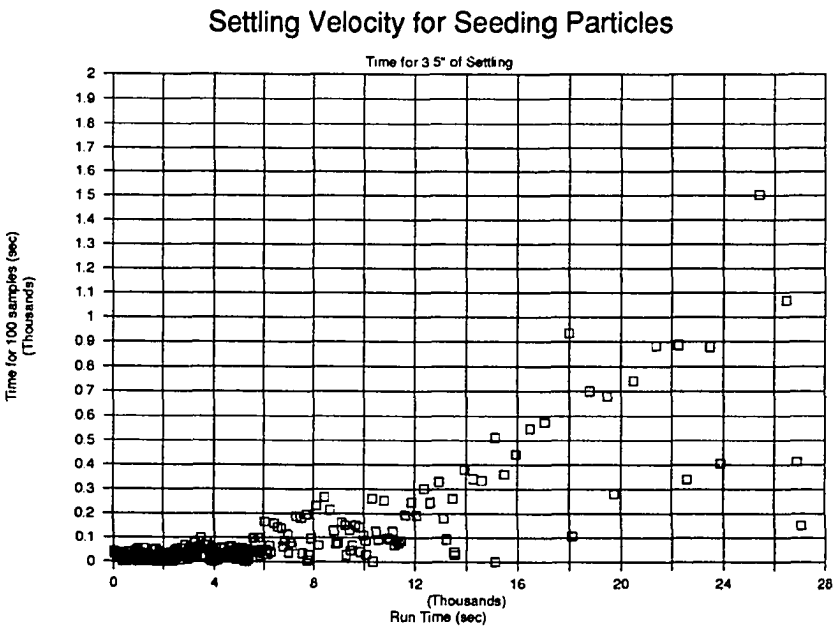

Figure 3-30 Settling Time for Seeding Particles (Stokes Flow Settling)

3.3.3 Additional LDV Signal Enhancing Techniques

In addition to particle seeding, several other techniques for reducing noise and enhancing signal strength are available and are listed by TSI (1980) as follows.

1) Using high quality and clear optics and windows for minimum flare.

2) Eliminating direct reflections by masking.

3) Using a second aperture on the receiving optics as a spatial filter.

4) Turning off room lights and other sources of extraneous light.

5) Using light traps to absorb the light from the incident beams after they have passed the measuring volume.

The TSI manuals point out that in many cases none of these precautions are needed. However, for the velocity results reported in this dissertation, all of the above techniques were found to be necessary and were utilized.

3.3.4 Evaluation of Doppler Frequency and Velocity

The signal from the LDV was evaluated using a TSI Model 1980 counter type signal processor. Initial alignment and signal viewing was accomplished using any one of a number of oscilloscopes which could be purloined from other laboratories for brief periods of time. A storage oscilloscope is recommended for this task but it was eventually found that the signal could be satisfactorily analyzed using a normal oscilloscope with application of great perspicacity.

A fairly straightforward calculation is used to convert the doppler frequency measured by the Model 1980 to the actual velocity. This calculation is implemented in the Turbo Pascal library routine (LDVLIB.PAS) which is included in the appendices to this dissertation. Doppler frequency is first obtained from quantities which are output or preset on the Model 1980. (This processor accepts doppler signals in the frequency range 1 KHz to 100 MHz.) The doppler frequency is calculated from the digital outputs of the processor using the equation:

$$f_d = \frac{N \times 10^9}{D_m \times 2^{n-2}} \tag{3-44}$$

where

N = # of cycles	(set on front panel to be 8)
D_m = mantissa of digital word	(output from processor)
n = exponent	(output from processor)

Velocity is found from the relation:

$$U = f_D d_f \tag{3-45}$$

The distance between fringes d_f can be calculated from the laser wavelength λ and the half angle of the beam intersection κ so that the velocity is finally expressed as:

$$U = f_D \frac{\lambda}{2 \sin \kappa} \tag{3-46}$$

In the above equation, $\lambda = 632.8$ nm and $\kappa = 0.06213$ radians for the laser and focusing lens utilized. Details of the digital interface used for data acquisition appear in section 3.4.2 below.

3.4 Implementation of Microcomputer Based Control of Experiment

In view of the transient nature of the globally established temperature profiles and the large amount of data to be acquired it was necessary to automate many of the data acquisition tasks in order to accomplish them in the short period of time available.

A Zenith Z100 microcomputer (state-of-the-art c. 1983) was made available to the laboratory through the auspices of the LSU College of Engineering. A data acquisition system was assembled on this foundation. The following tasks were automated and controlled through the microcomputer:

- temperature measurements from up to 15 channels of analog signal
- timing of experimental run times to 0.01 second accuracy
- velocity data acquisition through a parallel digital interface to a TSI Model 1980 processor
- traversing of sensors and laser optics through a slaved Velmex subsystem

Software routines were developed in BASIC and eventually assembled into precompiled libraries using the Borland Turbo Pascal (v. 4.0) language package. Subprograms specific to each task were assembled into libraries as follows:

- THERMLIB - temperature measurement routines to measure voltages on selected channels as well as thermistor excitation battery voltages and convert the signals to equivalent resistances and temperatures.
- TIMERLIB - routines to manage timing functions available from the AM9513 timer chips allowing greater precision in timing of data points.
- LDVLIB - routines to sample the doppler frequency output by the TSI processors and convert the signals to velocity.
- TRAVLIB - routines to move traversed sensors up or down at selected speeds using clocking pulses from AM9513 timer chips.

These routines were written so as to be largely self documenting and are included in the appendices to this dissertation.

In the following sections the automated data acquisition hardware subsystems which were developed for this research are briefly described. Minutiae of operation and configuration have for the most part been left buried in the original equipment manuals and circuit diagrams. The particulars included here are intended only to give an overview and to clarify some areas in which the manuals were deemed to be excessively obscure.

3.4.1 Measurement of Temperatures Using Tecmar AD212

In this section the adaptation of the Tecmar AD212 A/D board for the purpose of measuring thermistor temperatures to a high degree of precision and accuracy is discussed. An A/D board functions as a processor which converts an analog signal (eg. a signal which varies from 0-10v DC) to a digital value which can then be stored and manipulated in internal memory locations within the computer. The Tecmar AD212 is a 16

channel, 12 bit A/D board which uses the S100 bus to interface to the Zenith Z100 microcomputer. The AD212 is a powerful and extremely flexible tool for data acquisition. A variety of timing options and software controlled options are available. However, the manuals provided with the board were somewhat incomplete and fairly difficult to draw significant information from. To ensure repeatability of the temperature measurements, key aspects of the configuration and setup process are summarized in the following sections.

3.4.1.1 Specifications and Accuracy of Tecmar AD212

Accuracy of an A/D board is dependent on the conversion module and voltage range employed. On the AD212, the analog voltage range to be measured can be externally selected to optimize accuracy and resolution utilizing a programmable gain feature. Key specifications of the AD212 are summarized in the table below.

Table 3-3 Tecmar AD212 Specifications

Signal Range	Gain	Amp Settling Time	Throughput	System Accuracy
0.0 - 10.0v	1	15μs	40kHz	±0.03%
0.0 - 1.0v	10	15μs	40kHz	±0.03%
0.0 - 0.1v	100	40μs	20kHz	±0.05%
0.0 - 0.01v	1000	250μs	3.8kHz	±0.10%

A 12 bit A/D board converts a given analog signal to a discrete digital signal stored in 12 bits of data. Thus resolution is absolutely limited to 0.024% (1/4096) of a given analog signal range. Inaccuracy can result from the 12 bit limitation on resolution. Thermistor temperature measurements were made using a gain of 10 which provides a range of 0-1 volts. The smallest signal difference which could be resolved was thus 2.44×10^{-4} volts. The following table summarizes the ensuing limitations on temperature resolution. Since the thermistor signals are nonlinear, the temperature resolution is specified for various temperature ranges.

Table 3-4 Temperature Signal Resolution For AD212

Temperature Range	Voltage Signal	Resolution (bits/°C)	Resolution (°C)
25-40°C	~0.0101 volts/°C	41	0.02
40-50°C	~0.0061 volts/°C	25	0.04
50-60°C	~0.0043 volts/°C	17	0.06

3.4.1.2 Communications Between Tecmar AD212 and Zenith Z100 Using S100 Bus

Operations of the AD212 controlled by communication with the host computer are passed through I/O ports dedicated for this purpose. In essence, the host computer presents digital values to the A/D board through output ports and accepts digital values through its input ports. Eight consecutive 8 bit ports are utilized for I/O of data, commands and status. Specific addresses of the ports must be user selected and configured using onboard switches. This aspect of the AD212 is not adequately described in the manuals from Tecmar and so is summarized in some detail below.

In order for the AD212 to recognize when it is being addressed by the S100 bus, DIP switches must be set to correspond to software commands directed to specific ports. In order to set the address, IC's compare incoming signals to the values set on switches. These address lines are designated to be A0 through A23 on the circuit diagrams. A0 is never used. A1, A2 and A3 are left free to provide software capability of specifying eight different destinations for commands and data sent to and received from the board. A4 to A24 are the DIP switches which select the address of the board. A16 to A23 are used only in 24 bit systems. A4 to A7 are utilized in 8 bit systems. In the present instance they were set as follows so that the board will respond to all communications which pass through ports 16 through 31 (binary 00010000 through 00011111).

Table 3-5 Address Parameters for AD212 Assignments

Address	A7	A6	A5	A4	A3	A2	A1	A0
Status	Switch Disabled	Switch Disabled	Switch Disabled	Switch Enabled	Software Controlled	Software Controlled	Software Controlled	Not Used
Value	0×2^7	0×2^6	0×2^5	1×2^4	$?\times2^3$	$?\times2^2$	$?\times2^1$	$NA\times2^0$

The ports function as shown in the table following.

Table 3-6 AD212 I/O Port Functions

Port	Function in WRITE Mode	Function in READ Mode
16 or 17	Set software controlled A/D options	A/D Status
18 or 19	Multiplex Address (Channel Select)	Low 8 bits of A/D value
20 or 21	Start A/D	High 8 bits of A/D value
22 or 23	Clear timer 1	Not used
24 or 25	Clear timer 2	Not used
26 or 27	Clear overrun flop	Not used
28 or 29	Data port of AM 9513	Data port of AM 9513
30 or 31	Command port of AM 9513	Command port of AM 9513

3.4.1.3 Configuration of Tecmar AD212 For Thermistor Temperature Measurements

Many of the options available for configuration of the AD212 are assigned by setting switches and jumpers on the mother and daughter boards. These assignments are summarized in the table below for the configuration used for the experiments performed for this dissertation.

Table 3-7 AD212 Configuration Summary

Configuration or Mode Selected	Setup Switch or Jumper
8 Bit I/O Space	SW 4-7 off, SW 2-7 off
I/O Mapping	SW 5-5 off, SW 1-3,1-4 lower side depressed
Wait State Disabled	SW 3-5 off
CPU Wait For Conversion Disabled	SW 3-6 off
Maximum Channel For Autoincrementing = 15	SW 1-D-1,2,3,4 on, SW 1-D-5,6,7,8 off
Single Ended Input Option	Jumpers 1S to 2S, 3S to 4S, 5S to 6S
Polled Interrupt Disabled	SW 3-7 off

The single ended input option mentioned in the preceding table merits additional discussion. This mode of input must be utilized in order to take advantage of the full 16 channels of input available. However, in order to operate the AD212 in 'single ended' mode, it is necessary that all signals have a common ground. In the alternative 'differential input' mode, input signals need not have a common ground but only eight channels of measurement can be utilized. The circuitry constructed to provide an excitation voltage to the 15 thermistors used was implemented on the DT701 screw terminal junction board and is described in detail in the temperature measurement section above (section 3.2.2).

3.4.1.4 Calibration Procedures for Tecmar AD212 .

A final aspect of the AD212 which is not mentioned in the factory manuals and must be mentioned here is the method used for calibration of the A/D conversion module. Calibration is performed for the gain range which is to be used most frequently. The procedure is as follows:

1. Use proportional gain amplifier potentiometer to zero out the gain amplifier.
   •Ground the input channel.
   •Put a multimeter across the sample and hold pin and the ground pin.
   •Sample and hold pin is pin 13T in the diagram on p. 20 of the AD 212.
   •Ground is located at pin 6 of jumper area A.
   •Adjust potentiometer until multimeter reads 0.

2. Use center potentiometer on conversion module to adjust the software zero setting.
   •Ground the input channel.
   •Adjust potentiometer until screen readout of voltage measured reads 0 volts.

3. Use third potentiometer on conversion module to adjust the software full range adjustment.
   •Put about 80% of full range signal across the input channel.
   •Measure signal with a multimeter and adjust the potentiometer until the screen readout reflects the imposed voltage accurately.

3.4.2 Measurement of Velocities Using Tecmar 4PIO-TOD-Timer-Counter

The Tecmar 4PIO board combines two functions; firstly, a parallel I/O section with two 16 bit parallel input ports and two 16 bit parallel output ports and secondly, a timer section with 5 independent cascadable 16 bit counters. The primary purpose of the parallel I/O section of the board is to provide a high speed parallel channel for communications between two S-100 bus computers. These parallel ports were instead used for receiving data from a TSI Model 1980 counter type LDV signal processor. In order to interface the two devices it was necessary to crossconnect a 37 pin connector on the model 1980 to a 26 pin connector for the input port on the 4PIO board. The cross connection was accomplished using wire wrapped headers on a breadboard which was mounted next to the computer. The following table summarizes the connections which were required.

It should be noted that although a DATA READY signal was available from the TSI model 1980 this signal was not utilized. Instead, data was read in a constant stream as rapidly as possible. The possible skewing problems resulting from counting the same data point twice were circumvented by programming the acquisition

Table 3-8 Connecting TSI Model 1980 to Tecmar 4PIO Board

Output From Model 1980		Input to 4PIO	
Pin	Function	Pin	Function
1	Ground	24	Ground
22	Exponent 2^3	15	data bit 7 (high byte)
23	Exponent 2^2	16	data bit 6 (high byte)
24	Exponent 2^1	17	data bit 5 (high byte)
25	Exponent 2^0	18	data bit 4 (high byte)
26	Data 2^{11}	19	data bit 3 (high byte)
27	Data 2^{10}	20	data bit 2 (high byte)
28	Data 2^9	21	data bit 1 (high byte)
29	Data 2^8	22	data bit 0 (high byte)
30	Data 2^7	2	data bit 7 (low byte)
31	Data 2^6	3	data bit 6 (low byte)
32	Data 2^5	4	data bit 5 (low byte)
33	Data 2^4	5	data bit 4 (low byte)
34	Data 2^3	6	data bit 3 (low byte)
35	Data 2^2	7	data bit 2 (low byte)
36	Data 2^1	8	data bit 1 (low byte)
37	Data 2^0	9	data bit 0 (low byte)

routines to accept a new data point only when the value had changed. Although this is not the preferred method, it proved impractical to implement other possible interface schemes. The ready/resume handshaking protocols are easily understood and programmed but troubleshooting the actual circuit was complicated by the lack of logic probes, pulse generators and the like. In any case, the method used was a workable one since velocities were never found to remain absolutely constant and a valid measurement almost always resulted in some small change in the velocity value.

The 4PIO board is addressed through eight consecutive 8 bit I/O ports as is the AD212. The board address is set in a similar fashion using onboard switches but is more easily accomplished since the 4PIO board has no other configuration switches. The board and switches were set up as summarized below. It can be seen that the board will respond to all communications which pass through ports 80H through 87H (binary 10000000 through 10000111).

Table 3-9 Address Parameters for 4PIO

Address	A7	A6	A5	A4	A3	A2	A1	A0
Status	Switch Open	Switch Closed	Switch Closed	Switch Closed	Switch Closed	Software Controlled	Software Controlled	Software Controlled
Value	1×2^7	0×2^6	0×2^5	0×2^4	0×2^3	$?\times2^2$	$?\times2^1$	$?\times2^0$

3.4.3 Traversing of Sensors for Profile Measurements

Much of the data for the laboratory experiments in this dissertation required that sensors be traversed through the fluid to develop profile type measurements. Traversing of sensors was accomplished using a package comprised of two motorized sliders and a Velmex 8202M2 stepper motor controller. One of the sliders was dedicated for traversing of the LDV optical bench while the other was used for traversing temperature sensors. The Velmex 8202M2 controlled both motors simultaneously yet individually. Direction,

speed, and ramping (acceleration rate) could be controlled manually via push button toggle switches and dial settings. The 8202M2 was also equipped with two digital readouts of distance traveled via counts of stepper motor steps (1000 counts = 1 cm).

3.4.3.1 Passive Monitoring of Position Using AM9513 and Velmex 8202M2

Initially, the traversers were set up in a scanning mode, cycling up and down continuously at constant speed. The setup depended on limit switches at either end of the sliders which signaled the 8202M2 controller to reverse the motors. The Z100 was set up to count the pulse stream generated by the 8202M2 so that sensor position could be recorded automatically while sampling data.

The AM9513 timer/counter chip was used for counting pulses. External devices can be interfaced to the AM9513 using the 40 pin connector P3 on the AD212. The Velmex 8202M2 has a 25 pin D connector for I/O purposes. The only output available on this connector was a 5v or 12v pulse train. In order to follow a change of direction by the traversers, unused pins on the 8202M2 interface were internally connected to the direction controlling logic within the 8202M2. Since the 8202M2 operated on a 12v true logic it was necessary to buffer the signals down to 5v using an inverting hex buffer before sending them on to the AM9513. An additional chip (Quad 2 input NAND Gate) was incorporated so that pulses originating from the limit switches at either end of the traverser (or the manual control buttons) could be output as a counter reset pulse on the 8202M2's 25 pin connector. The AM9513 was then set up so that the counters operated in a single shot mode which was retriggered by an active pulse edge passing through a special gate on board the AM9513. The counter reset pulse from the 8202M2 was hardwired to the input for the AM9513's special gate.

The additional logic circuitry described above was attached to a separate breadboard and installed in the 8202M2. Figure 3-31 gives a schematic representation of this circuitry.

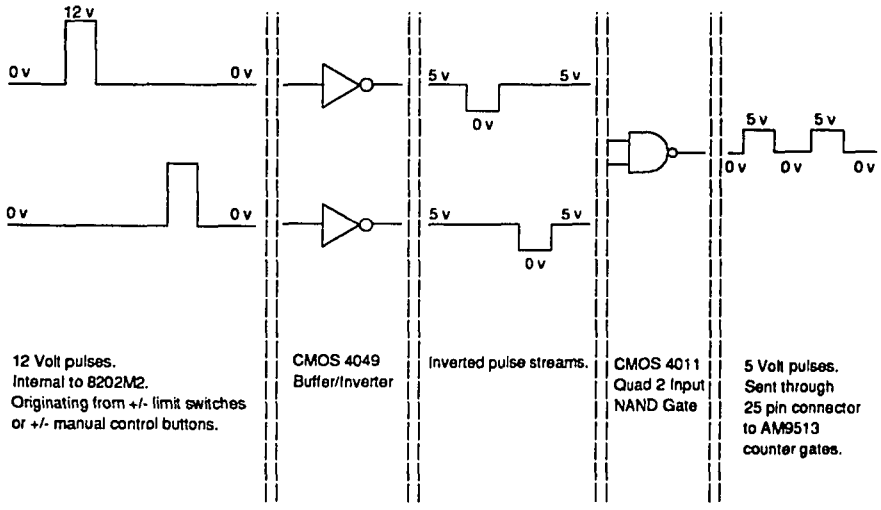

Figure 3-31 Digital Interface Schematic for Velmex Controller

3.4.3.2 Fully Software Controlled Traversing Using AM9513 and Velmex 8202M2

In the configuration described above, the Z100 microcomputer does not in any way control the position of the sensors. Instead, the positioning is controlled manually using the front panel switches of the 8202M2. The counter circuit described above serves basically as a passive monitor of the sensor position.

It was eventually decided to take this automation one step further and generate the clocking pulses and directional signals from the Z100. The AM9513 was again adapted for this purpose. The AM9513 contains five 16 bit counters which can be configured with a great deal of flexibility to count or create pulse trains conditioned on various inputs. In the final setup, counters 1 and 2 of the AM9513 on the PIO board were used to measure the run time of experiments. This is a standard function accomplished by taking a 1 MHz frequency available from an onboard crystal oscillator, gating it so that the signal is divided by 10,000 and then simply counting the resulting 100Hz signal with counter 1. Counter 1 is set to pulse on a terminal count of 6000. Counter 2 is set to count on the pulse from counter 1 and thus accumulates the time in minutes. Configuration methods of the AM9513 are adequately described in the manufacturer's manual which appears as an appendix to the (less orderly) Tecmar manuals, and so will not be discussed in depth here. Subroutines dealing with traversing functions and timing functions (TRAVLIB and TIMERLIB) are included in the appendices to this dissertation and are quite liberally commented so as to be easily understandable by referring to the AM9513 manual.

Counters 1, 2 and 3 of the AM9513 on the AD212 were used to provide the signals controlling the 8202M2. The onboard 1 MHz frequency source was divided by 10 and then used as a 100,000 Hz driver for counter 3. Counter 3 was set to count down repeatedly and pulse each time its terminal count was reached. For example, if a terminal count of 100 was specified counter 3 would pulse at a frequency of 1000 Hz. This signal (OUT3) was sent to the 8202M2 and used as a pulse train which specified the traversing speed. OUT3 was also shunted through SRC1 to counters 1 and 2 which were used to control the direction of travel. With counters 1 and 2 inactive both outputs would be low so that any pulse train coming into the 8202M2 was ignored. To move the traverser, one of the counters would be activated to count down to a terminal count (corresponding to distance traveled). The output from an activated counter was a continuous high signal which went low and stopped movement when the counter reached its terminal value. The output from counter 1 was hardwired to the RUN+ signaling pin on the 8202M2 while counter 2 was hardwired to the RUN- signal pin.

The table below summarizes the wiring arrangement.

Table 3-10 Wiring Required For Z100 Interface to 8202M2

Signal	Location		Received By	Location
OUT1	Pin 8 on AD212 P3	→	RUN+	Pin 17 on 8202M2
OUT2	Pin 7 on AD212 P3	→	RUN-	Pin 16 on 8202M2
OUT3	Pin 6 on AD212 P3	→	CLOCK #2	Pin 20 on 8202M2
OUT3	Pin 6 on AD212 P3	→	SRC1	Pin 19 on AD212 P3

Chapter 4

Heat Transfer Experiments

In addition to being able to probe flows similar to the atmospheric upslope flows, the experimental system could also be used to improve the understanding of natural convection heat transfer. The influence of stable stratification, which was of particular interest here, is one area which has received little attention from experimenters and only very limited attempts at modeling. Inasmuch as this investigation built on an existing body of work, it was deemed necessary to make measurements which could be compared directly with previous experimentation and theoretical predictions where available. These experiments provided a good means of verifying the validity of the new techniques and materials which were used and added a measure of credibility to subsequent experiments which explored virgin territory.

In this chapter we start out by briefly discussing the heat transfer correlations to be found in the literature. The pertinent dimensionless quantities are presented and some justification given for the choice of dimensionless variables. Following this, a literature review is presented summarizing the progress which has been made over the past decades in this area.

The experimental procedures and techniques which were used for heat transfer measurements are then described. Results for heat transfer to a fluid with uniform ambient temperature are presented in the section following this. Finally, results for heat transfer in the presence of a stable stratification are presented. Detailed descriptions of velocity profiles and transport under stratified conditions approximating atmospheric flows are deferred to the following chapter which specifically addresses the modeling of atmospheric behavior.

4.1 Background

4.1.1 Dimensionless Quantities for Heat Transfer Correlations

Before entering the body of this chapter, it is worthwhile to briefly describe the forms in which heat transfer data from plates are typically correlated. As will be shown in the table below, heat transfer textbooks generally present the correlations for heat transfer from plates in the form,

$$Nu_x = C(Gr_x Pr)^m \tag{4-1}$$

In this equation, C and m are constants, Pr is the Prandtl number and Nu_x and Gr_x are the local Nusselt and Grashof numbers respectively, where

$$Pr = \frac{\nu}{\alpha} \quad Nu_x = \frac{hx}{k} \quad Gr_x = \frac{g\beta(T_w - T_\infty)x^3}{\nu^2} \tag{4-2}$$

Physical properties used in the above quantities include the thermal diffusivity α, the kinematic viscosity ν, thermal expansion coefficient β and thermal conductivity k. Expressions for these quantities are set forth in Appendix 1. Ordinarily, physical properties are evaluated at the film temperature T_f where,

$$T_f = (T_w + T_\infty)/2 \tag{4-3}$$

and this practice will be followed in this dissertation unless otherwise noted.

The following table (extracted from Holman (1976)) gives the empirical constants recommended from various sources for use in equation (4-1) with isothermal surfaces.

Table 4-1 Empirical Constants for Use With Equation (4-1): Isothermal Surfaces (after Holman (1976))

Geometry	Gr_fPr_f	C	m	Reference
Vertical - laminar	10^4-10^9	0.59	0.250	McAdams (1954)
Vertical - turbulent	10^9-10^{13}	0.021	0.400	McAdams (1954)
Vertical - turbulent	10^9-10^{13}	0.10	0.333	Warner and Arpaci (1968)

In the case of heat transfer from a uniform flux surface, T_{wall} is no longer a constant and it is more convenient to utilize a modified Grashof number, Gr^*, which includes the heat flux, q_w, instead of the temperature difference. Gr^* is the product of the ordinary Grashof number and the Nusselt number,

$$Gr_x^* = Gr_x Nu_x = \frac{g\beta q_w x^4}{k\nu^2} \tag{4-4}$$

Uniform heat flux correlations are then presented as

$$Nu_x = C(Gr_x^* Pr)^m \tag{4-5}$$

A table similar to the one above can be constructed for uniform flux heat transfer correlations.

Table 4-2 Empirical Constants for Use With Equation (4-5): Uniform Heat Flux Surfaces

Geometry	Regime	Gr_x^*Pr	C	m	Reference
Vertical	laminar	3×10^7-10^{12}	0.60	0.20	Vliet and Liu (1969)
	laminar	2×10^6-10^{13}	0.587	0.200	Qureshi and Gebhart (1978)
	laminar[1]	$<10^{11}$-10^{12}	0.509	0.200	Miyamoto et al. (1982)
	turbulent	2×10^{13}-10^{16}	0.568	0.22	Vliet and Liu (1969)
	turbulent	10^{14}-10^{15}	0.568	0.22	Qureshi and Gebhart (1978)
	turbulent[1]	1.5×10^{13}-1.7×10^{14}	0.104	0.272	Miyamoto et al. (1982)
Inclined	laminar[2]	Varies	0.60	0.20	Vliet (1969)
	laminar[2]	Varies	0.55	0.20	Vliet and Ross (1975)
	turbulent	Varies	0.302	0.24	Vliet (1969)
	turbulent	Varies	0.17	0.25	Vliet and Ross (1975)

[1]Physical properties (except β) were evaluated at $T_r = (3T_w + T_\infty)/4$.
[2]Use g cosθ in place of g for this correlation, range of validity depends on angle of inclination from vertical (θ).

Frequently, the Grashof and Prandtl numbers are combined into a single dimensionless quantity, a Rayleigh number, so that for the Rayleigh number we can write,

$$Ra_x = Gr_x Pr = \frac{g\beta(T_w - T_\infty)x^3}{\nu\alpha} \quad \text{and} \quad Ra_x^* = Gr_x^* Pr = \frac{g\beta q_w x^4}{k\alpha\nu} \tag{4-6}$$

The limits of the laminar, turbulent, and transition regimes are usually defined using the Rayleigh number to define ranges for the various flow modes. The transition occurs earlier as inclination increases from vertical. Vliet (1969) indicated that the midpoint of the transition range, Ra_x^*, varied approximately as,

$$Ra_t^* = 0.3 \times 10^7 \exp(0.18\phi) \qquad (4\text{-}7)$$

with φ measured in degrees from horizontal. Vliet observed a spread between the beginning and end of transition of approximately 1.5 orders of magnitude in Ra_t^*. The table below gives the transition ranges for inclined surfaces observed experimentally by Vliet.

Table 4-3 Transition Ranges for Inclined Plate Heat Transfer

Inclination From Vertical	Transition Range For Ra_x^*
0	5×10^{12}-10^{14}
15	6×10^{11}-10^{13}
30	3×10^{10}-10^{11}
45	10^9-10^{11}
60	6×10^8-6×10^{10}

The dimensionless quantities introduced above arise naturally from the basic equations for fluid flow and heat transfer in applying boundary layer solution techniques and integral method solutions (see for example Holman (1976), Karlekar and Desmond (1977) or Eckert and Drake (1959)). Dimensional analysis is another tool by which these relations can be developed. Below, we briefly present a scale analysis similar to that described by Bejan (1984). This analysis provides a sound physical basis for using the quantities discussed above in correlating the natural convection heat transfer data obtained in this chapter.

We begin with the observation that for the situation shown in Figure 4-1, an energy balance indicates that at steady state the heat conducted out from the plate into the fluid must be approximately equal to the heat which is convected by the flow up along the plate. This energy balance for the boundary layer flow can be expressed as follows,

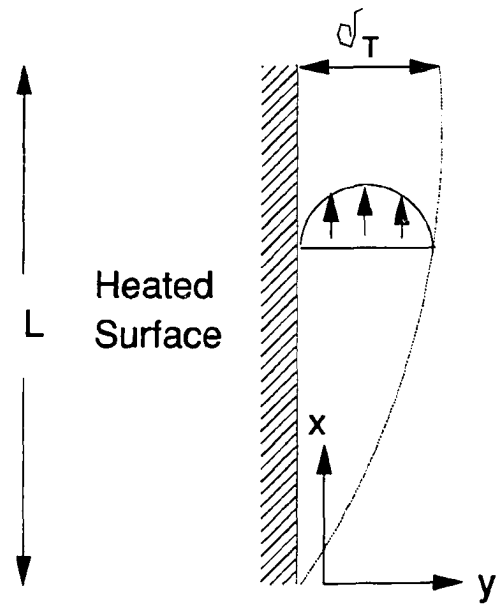

Figure 4-1 Scaling for Vertical Plate Heat Transfer

$$u\frac{\partial T}{\partial x}+v\frac{\partial T}{\partial y}=\alpha\frac{\partial^2 T}{\partial y^2} \tag{4-8}$$

The balance between convective terms and conduction can thus be seen to result in,

$$u\frac{\Delta T}{L},v\frac{\Delta T}{\delta_T}\sim\alpha\frac{\Delta T}{\delta_T^2} \tag{4-9}$$

where δ_T is the thickness of the thermal boundary layer. Now, by conservation of mass in the layer, the two directions of mass flow must be of the same order, that is,

$$u\delta_T\sim vL \Rightarrow \frac{u}{L}\sim\frac{v}{\delta_t} \tag{4-10}$$

Thus, the two terms are of the same order of magnitude and the energy balance reduces to,

$$u\frac{\Delta T}{L}\sim\alpha\frac{\Delta T}{\delta_T^2} \text{ or } u\sim\frac{\alpha L}{\delta_T^2} \tag{4-11}$$

At this point, it is still necessary to specify the size of the thermal boundary layer, δ_T. Starting from the momentum equation,

$$u\frac{\partial u}{\partial x}+v\frac{\partial u}{\partial y}=v\frac{\partial^2 u}{\partial y^2}+g\beta(T-T_\infty) \tag{4-12}$$

we can obtain expressions showing a balance between the inertial, viscous, and buoyant terms,

$$\underset{\text{inertial terms}}{u\frac{u}{L}, u\frac{v}{\delta_T}} \qquad \underset{\text{viscous terms}}{v\frac{u}{\delta_T^2}} \qquad \underset{\text{buoyant forces}}{\sim g\beta\Delta T} \tag{4-13}$$

From mass conservation, again, the inertial terms are both of order (u^2/L). To assess the relative importance of inertial or friction terms versus buoyancy we divide the expressions above by $g\beta\Delta T$ and use the previously obtained relation, $u \sim \alpha L/\delta_T^2$, resulting in,

$$\underset{\text{inertial terms}}{\left(\frac{L}{\delta_T}\right)^4 Ra_L^{-1} Pr^{-1}} \qquad \underset{\text{viscous terms}}{\left(\frac{L}{\delta_T}\right)^4 Ra_L^{-1}} \qquad \underset{\text{buoyant forces}}{\sim 1} \tag{4-14}$$

where,

$$Ra_L = \frac{g\beta\Delta T L^3}{\alpha\nu} \tag{4-15}$$

Therefore, at high Prandtl numbers the thermal boundary layer is governed by the interplay between viscous and buoyancy forces and at low Prandtl numbers the flow is governed by the balance between inertial and buoyancy terms. For $Pr >> 1$, then, we can write

$$\delta_T \sim L(Ra_L)^{-\frac{1}{4}} \tag{4-16}$$

The heat transfer coefficient h will scale according to conduction across a layer of thickness δ_T so that,

$$Nu = \frac{hL}{k} \text{ with } h \sim O\left(\frac{k}{\delta_T}\right) \Rightarrow Nu \sim Ra_L^{\frac{1}{4}} \tag{4-17}$$

Similarly, for $Pr << 1$,

$$\delta_T \sim L(Ra_L Pr)^{-\frac{1}{4}} \tag{4-18}$$

$$\therefore Nu = \frac{hL}{k} \sim \frac{L}{\delta_T} \sim (Ra_L Pr)^{\frac{1}{4}} \tag{4-19}$$

The predicted exponent of 0.25 for large Prandtl numbers agrees well with the laminar experimental correlations for isothermal plates shown in the first table above.

The results of the scale analysis can be easily compared to the experimentally obtained correlations for uniform flux surfaces. The uniform surface temperature data was correlated by,

$$Nu_x = C(Gr_x Pr)^m \tag{4-20}$$

Making the substitution $Gr_x = Gr_x^*/Nu_x$ results in

$$Nu_x^{1+m} = C(Gr_x^* Pr)^m \tag{4-21}$$

$$\Rightarrow Nu_x = C^{\frac{1}{1+m}}(Gr_x^* Pr)^{\frac{m}{1+m}} \tag{4-22}$$

Therefore, an exponent of m=1/4 for the laminar uniform temperature correlation corresponds to an exponent of m/(1+m)=1/5 for the laminar uniform flux correlation. Similarly, a value of m=1/3 (found experimentally) for the isothermal turbulent correlation corresponds to a value of m/(1+m)=1/4 for the uniform flux turbulent correlation. It can be seen that these predicted values fall in line with the exponents which were found for uniform flux in the correlations shown in the second table above.

One further point is of interest here. If we look specifically at the behavior of the heat transfer coefficient which is predicted by the exponents in the correlations, we find the following:

$$h_x \sim \frac{1}{x}(x^3)^{\frac{1}{4}} \propto x^{-\frac{1}{4}} \text{ in laminar range} \tag{4-23}$$

$$h_x \sim \frac{1}{x}(x^3)^{\frac{1}{3}} \propto 1 \text{ in turbulent range} \tag{4-24}$$

The predicted x dependence of the heat transfer coefficient, h, is identical for both the isothermal and uniform flux cases. With a uniform flux surface, since the heat transfer coefficient remains constant with x we conclude that the temperature difference ΔT will also remain fixed along the length of the plate, in the fully turbulent regime.

4.1.2 Literature Review

Before undertaking the laboratory investigation it is clearly necessary to thoroughly review the studies made by previous workers. Therefore, it is appropriate here to briefly summarize the literature surveyed in this area and to describe some of the important results obtained to date by heat transfer researchers.

4.1.2.1 Uniform Bulk Temperature Studies

Schmidt (1932, referenced by Miller and Gebhart (1978)) was apparently the first to study heat transfer from inclined surfaces. This work utilized Schlieren interferometry. Some other early experiments for natural convection heat transfer from inclined plates were described by Rich (1953). Rich reported boundary layer temperature measurements as well as local and overall heat transfer characteristics as determined by Mach-Zehnder interferometry. His experimental work was essentially for the laminar regime. Rich found that heat transfer coefficients were predicted within 10% by vertical plate laminar theory if g was replaced by $g\cos\theta$. Results were thus correlated in the form, $Nu = f(PrGr\cos\theta)$, where θ is the angle of inclination from vertical. Rich's data exhibited a substantial amount of scatter but most subsequent studies in the laminar regime have supported the use of the Grashof number multiplied by the cosine of the angle from the vertical as he suggested.

Rich's study covered the range of inclination angles between 0° and 40° from the vertical. It was intended to be for constant wall temperature, but in actuality lay somewhere between the intended condition and a constant heat flux condition.

Kierkus (1968) used a perturbation analysis to study the flow next to inclined isothermal surfaces and compared his predictions to experimental data taken using interferometric techniques in air. Measurements were confined to a single angle of inclination (45°). The addition of a first order velocity perturbation produced a solution including the parallel gravity component. Kierkus obtained experimental results in good agreement with his calculations, using a Mach-Zehnder interferometer for temperature measurements and dust particles to measure velocity. These were the first data obtained which included velocities.

Vliet (1969) employed air and water at a uniform temperature as his working fluids in conjunction with a constant heat flux surface oriented at several angles of inclination ranging from vertical to 30 degrees from horizontal. His experiments covered the laminar, transition, and turbulent regimes. Rich's conjecture was supported by the results of this study which indicated that the use of $g\cos\theta$ in place of g provided an adequate generalization of the vertical plate predictions to inclined plates in the laminar regime. However, Vliet found no influence of angle of inclination upon the heat transfer coefficients in the turbulent region. Laminar data were fit (with considerable scatter) by,

$$Nu_x = 0.6(Gr_x^* \cos\theta Pr)^{0.2} \tag{4-25}$$

Turbulent data was correlated (with no θ dependence) to

$$Nu_x = 0.302(Gr_x^* Pr)^{0.24} \tag{4-26}$$

Measurements made with air were found to fall about 10% above the data for water. This deviation was attributed to the greater scatter in air data which resulted from the application of heat flux corrections for radiation.

Vliet and Ross (1975) revised the above correlations after performing additional studies for upward and downward facing plates using only air as a working fluid. The resulting correlations were:

$$Nu_x = 0.55(Gr_x^* \cos\theta Pr)^{0.2} \text{ (laminar)} \tag{4-27}$$

$$Nu_x = 0.17(Gr_x^* Pr)^{0.25} \text{ (turbulent)} \tag{4-28}$$

As before, the turbulent correlation was found to be independent of angle, while in the laminar case, the component of gravity along the surface was used in the correlation. Measurements for upward facing plates were made only for θ=30° from vertical and for vertical. The turbulent correlation of Vliet and Ross (1975) falls ~30 percent below the earlier data of Vliet (1969) which was taken with water. Corrections were applied for radiative and conductive losses of heat for the experiments with air. These corrections are probably

substantial enough to be a source of significant error. Vliet and Ross estimated that their conductive losses averaged 2.7 percent while radiation corrections ranged from 18 to 41 percent of the dissipated electrical energy with an average of 26 percent.

Fujii and Imura (1972) presented experiments which agreed basically with the conclusions of Vliet. They reported the following correlation for laminar flows,

$$Nu = 0.56(Gr \cos \theta \, Pr)^{0.25} \qquad (4\text{-}29)$$

Close comparison of this result to other research is difficult since this correlation was based on evaluating all properties except β at a reference temperature $T_r = T_w - 0.25(T_w - T_\infty)$. Perhaps, more importantly, since these experiments used thick (1 cm) brass surfaces heated from the rear by sheath heaters the heating condition was somewhere between uniform flux and uniform temperature. In addition, a temperature stratification was allowed to develop. Thus Nusselt numbers were estimated by selecting a representative bulk temperature and estimating the average wall temperature. Finally, in the reported correlations, the Nusselt number values are for overall heat transfer rather than local heat transfer. Fujii and Imura also reported correlations for data through the transition and turbulent regimes which accommodated the change of regime by adding two additional terms, which depended on critical values for the Grashof number, to the original laminar correlation.

In an extension to the body of work on heat transfer from inclined plates which had primarily focused on the region from 45° to near vertical, Pera and Gebhart (1973) analyzed the effects of a small surface inclination by perturbing the flow over a horizontal surface. Experimental data were obtained for boundary layer flows near the leading edge of nearly horizontal heated surfaces in air. The surface was uniform temperature and the ambient fluid temperature was uniform as well. The trends of the data they obtained were consistent with their computed numerical solutions. This study is of some interest since the authors speculate that the results might have direct application to micrometeorological problems. However, the experiments were made primarily in the laminar flow regime using a constant temperature surface, and there is no mention of any attempt to stably stratify their test fluid before performing experiments. Flow separations were observed but the relationship between this and thermal instability in the atmosphere is not clear.

In another study which used an isothermal plate, Black and Norris (1975) found that the data in the turbulent regime were insensitive to both plate inclination and distance from the leading edge of the plate. Black and Norris also investigated variations in local heat transfer coefficient due to thermal waves traversing the surface of an inclined plate. This investigation utilized interferometric flow visualization techniques and dealt with air and an isothermal plate.

Miller and Gebhart (1978) made a study of the thermal structure of convection above a heated ridge in air. The experiments were conducted using two surfaces, inclined 30° from horizontal and joined at the trailing edges. The surfaces were isothermal and measurements were conducted for uniform ambient temperature air.

One area of major interest for researchers has been the instability and transition in the region between laminar and turbulent flows. Tritton (1963) was the first to investigate the transition from laminar to turbulent flows. This early work utilized the oscillation of a quartz fiber to observe the intensities and fluctuations of the convective motion. Lloyd and Sparrow (1970) investigated the relationship between flow instability and inclination angle for an isothermal plate. Haaland and Sparrow (1973) examined the linear stability of laminar natural convection next to a heated inclined upward facing plate. Their focus was on instabilities caused by disturbances having the form of longitudinal vortices. Shaukatullah and Gebhart (1978) have identified a spanwise variation of heat transfer corresponding to vortices which arise in the transition zone between laminar flow and fully developed turbulent flow. These vortices were observed for an inclined uniform flux heated plate in uniform ambient temperature water. Tzuoo et al. (1985) analyzed convective boundary layer flows for instability using a linear theory. They showed that instability arises from either a wave mode or a vortex mode of disturbance and that the mode of disturbance is related to the angle of inclination.

Experiments for the analogous problem of mass transfer driven convection adjacent to vertical and inclined surfaces have been described by Lloyd et al. (1972). A substantial effect of inclination upon turbulent mass transfer was found using the constant wall concentration boundary condition, disagreeing with Vliet's results for turbulent flow. Lloyd et al. point out that the magnitude of scatter in Vliet's data could have obscured any influence of inclination in the turbulent region. Another possible explanation for the discrepancy is that because of the difference in the magnitude of Schmidt numbers and Prandtl numbers involved in the sets of experiments, the relative sizes of the boundary layers were altered. Patrick et al. (1977) studied instability and transition at a variety of inclination angles for the mass transfer driven flow. They correlated their results successfully using both Ra_L and $Ra_L \cos\theta$, thus hedging their conclusions.

For vertical plate transfer, it is possible to make very accurate heat transfer measurements by using a surface heated on both sides. Since the heat transfer is symmetric, sensors placed between the two heated surfaces can measure surface temperature very precisely without any effect of heat losses due to imperfect insulation. Qureshi and Gebhart (1978) made such measurements for heat transfer from vertical uniform flux plates to uniform temperature ambient fluids. Experimental results agreed well with the correlation

$$Nu_x = 0.587(Ra_x^*)^{0.2} \qquad (4\text{-}30)$$

which they obtained from boundary layer theory for a Prandtl number of 6. Temperature profiles in good agreement with boundary layer theory were also obtained. Turbulent data correlated well with the relation of Vliet and Liu (1969),

$$Nu_x = 0.568(Gr_x^* Pr)^{0.22} \quad \text{for} \quad 2\times10^{13} < Ra_x^* < 10^{16} \tag{4-31}$$

Fully developed turbulent flow was observed for $Ra_x^* \geq 10^{14}$.

Miyamoto et al. (1982) used LDV and thermocouples to make boundary layer measurements near a vertical uniform flux plate in uniform temperature air. They correlated their results by the relations:

$$Nu_x = 0.509(Gr_x^* Pr)^{0.2} \quad \text{for} \quad Gr_x^* Pr < 10^{11} - 10^{12} \quad \text{(laminar)} \tag{4-32}$$

$$Nu_x = 0.724(Gr_x^* Pr)^{0.208} \quad \text{for} \quad 4\times10^{12} < Gr_x^* Pr < 1.5\times10^{13} \quad \text{(transition)} \tag{4-33}$$

$$Nu_x = 0.104(Gr_x^* Pr)^{0.272} \quad \text{for} \quad 1.5\times10^{13} < Gr_x^* Pr < 1.7\times10^{14} \quad \text{(turbulent)} \tag{4-34}$$

4.1.2.2 Studies with Stratification

Since stratification arises naturally in the course of heating a confined liquid, the global fluid temperature profile has been an issue which has required special attention from most of the researchers mentioned above. Fussey and Warneford (1977) went so far as to devise a unique arrangement of baffles and a cooler to deal with the constraints of a finite volume tank during their investigation of heat transfer from a downward facing inclined plate. The results of Fujii and Imura (1972) have been somewhat obscured by the development of a stratification in their containment vessel. More recently, stratification has become an area of specific interest for its implications and influence on heat transfer.

Walin (1971), Rahm (1986) and Hyun and Hyun (1986) present discussions of how best to stratify test fluids efficiently in laboratories by various means designed to allow convective enhancement of the stratifying process.

Jaluria and Gebhart (1974) investigated flows adjacent to a vertical uniform flux surface with ambient stratification. Emphasis was on measurement of stability and transition rather than on heat transfer measurements. Experiments were conducted in a tank of water which was stratified by judicious use of three immersion heaters to obtain temperature profiles amenable to similarity solution.

Chen and Eichorn (1976) describe experiments for natural convection from an isothermal cylinder (7 cm long, 1.9 cm diameter) into a stable thermally stratified fluid. Heat transfer was correlated as a function of Gr, Pr and a stratification parameter S. The temperature gradient was neither constant nor linear so it was simply approximated to be a constant value. Observation of plumes rising along the cylinder indicated that the plume rose to a point near where its ambient temperature was equal to the surface temperature and then flowed horizontally away from the body.

4.1.2.3 Similarity Solutions and Numerical Modeling

The aforementioned studies of heat transfer with stratification are all restricted to the vertical configuration. For vertical plates, similarity solutions provide one avenue of attack whereby solutions have been obtained for certain stable fluid temperature profiles. Similarity solutions were first described by Ostrach (1952) and Sparrow and Gregg (1956) and Yang (1960). Recent extensions to this work have described solutions for a number of nonuniform fluid and wall temperature profiles. Cheesewright (1967) found similarity solutions for some very limited cases of nonuniform temperature profiles. Yang et al. (1972) gave more details for this class of problems. Most recently, Kulkarni (1987), and Henkes and Hoogendoorn (1989) have described solutions in a thermally stratified medium which include cases in which the wall is isothermal and the fluid is linearly stratified.

The predicted heat transfer correlations resulting from similarity solutions have been found to match quite well to experimental data. The predicted correlations for the Prandtl number range of interest for this work were calculated by performing a numerical solution to the transformed boundary layer equations. Details of the similarity transformation and of the solution procedure are included in Appendix 3 of this dissertation. Results were as follows.

Table 4-4 Heat Transfer Correlations Predicted By Similarity Solutions

Reference Temperature (K)	Prandtl Number	Predicted ΔT $-\theta(0)$	Heat Transfer Correlation
293	7.02	0.8321	$Nu_x = 0.590(Gr_x^* Pr)^{0.2}$
298	6.14	0.8585	$Nu_x = 0.587(Gr_x^* Pr)^{0.2}$
303	5.43	0.8806	$Nu_x = 0.587(Gr_x^* Pr)^{0.2}$
308	4.84	0.9083	$Nu_x = 0.582(Gr_x^* Pr)^{0.2}$
313	4.34	0.9327	$Nu_x = 0.579(Gr_x^* Pr)^{0.2}$

Other numerical modelling efforts for thermally stratified fluids include those of Nakayama et al. (1983), who present an approximate solution based on an integral approach for laminar free convection over a non-isothermal plate immersed in a thermally stratified fluid. The results agree well with similarity solutions for the same problem. Venkatachala and Nath (1981) and Surma Devi and Nath (1984) used finite difference schemes to solve for natural convection from uniform temperature vertical plates to stratified fluids.

Solutions for inclined surfaces have at present been limited to cases with uniform external fluid temperature profiles. Schreiber and Singh (1987) used collocation methods to solve the equations of flow around an arbitrarily inclined heated plate in an infinite medium. The ambient temperature was taken to be uniform and the case treated was that of an isothermal plate. Chen and Yuh (1979) solve (using similarity variables) for combined heat and mass transfer on inclined surfaces for constant external temperature T_∞. Chen et al.

(1986) used finite difference methods to study flow and heat transfer of laminar free convection from inclined, horizontal and vertical plates with variable wall temperature and flux. Local heat transfer was found to increase with increased angle from horizontal.

Recent studies have begun numerical modeling of the turbulent natural convection flow adjacent to vertical surfaces with good success. For example, To and Humphrey (1986) have performed a numerical simulation of turbulent natural convection along a uniform temperature vertical plate using two models, a κ-ε model and an algebraic stress model based on approximations for the turbulent fluxes. At present, no numerical studies have been made for the turbulent flow over inclined surfaces.

4.1.2.4 Summary

In summary, a survey of progress made by heat transfer researchers in the field of inclined plate heat transfer reveals several areas which have received limited attention. In early years, most workers concentrated on laminar measurements and correlations, possibly because such flows were more amenable to study by interferometric techniques and also because mathematical descriptions were more forthcoming for the laminar case. Beginning with Vliet (1969), there have been a number of studies which have made measurements in the turbulent regime, of which most have actually concentrated on the behavior at the transition from laminar to turbulent flow. Pera and Gebhart have taken a first step towards examining this problem motivated by possible meteorological applications.

It appears that a study of the convective flow over an inclined plate which includes measurements of velocity profiles, temperature distributions, and turbulent fluctuations in the boundary layer would be of value in advancing the understanding of these flows. Furthermore, the addition of global density stratification should prove of great interest. It seems clear that such a condition will restrict the growth of the boundary layer and influence the heat transfer rates obtained. There has been no work of which we are aware that has purposely addressed the problems involved with the influence of a stably stratified fluid on an unconfined flow over an inclined heated plate.

4.2 Experimental

Heat transfer from plates can be characterized by determining values for the local heat transfer coefficient under a range of conditions. For a uniform heat flux surface, the heat flux is obtained from electrical measurements of the electrical power dissipation. It is then necessary to determine only the local temperature difference between the surface and the bulk fluid at various distances along the heated surface. The local heat transfer coefficient can then determined directly from its defining equation, $q=h_x\Delta T_x$.

To calculate the requisite dimensionless quantities needed for evaluating any heat transfer data it is necessary to have various physical properties of water. As Clausing (1984) points out, errors in interpolation or deviation in the original sources for property data can cause significant variation in the empirical correlations used to fit heat transfer data. Accordingly, the equations used for physical properties of water have been carefully documented in the appendices and referenced to their original sources. The calculation procedures were compiled separately as a unit for easy incorporation into data evaluation routines. These routines can be found in the appendices in the Turbo Pascal unit PHYSPROP.LIB.

4.2.1 Experiments with Uniform Bulk Temperature

The first set of experiments reported were conducted for uniform bulk temperature (room temperature) water. The results described were for the 12" long heated surface and used the Lexan® convection tank. Data was obtained for angles of 0° (vertical), 15°, 30°, 45°, 60°, 75°, and 90° (horizontal). In this section are described the experimental procedures used along with methods used for reducing the raw data to appropriate dimensionless correlations. Summaries of the actual data sets as plotted in the sections following are tabulated in the appendices to this dissertation.

4.2.1.1 Experimental and Data Sampling Procedures

For experiments conducted without stratification of the ambient fluid, it was necessary to first establish a condition of uniform bulk temperature in the tank. This was attained by again mixing the water in the tank with the impeller mentioned above. After mixing the water thoroughly, 10-15 minutes were allowed to pass, permitting all visible motion of the fluid within the tank to cease.

The temperature profile of the tank was then determined. Two temperature probes were traversed vertically through the bulk fluid at a distance of approximately 30 cm from the heated plate (a distance which was found to be sufficiently far from the plate to be representative of the bulk fluid temperature.) The two temperature probes allowed the water's temperature to be measured at two locations separated by a distance of 15 cm but at the same depth, providing a measure of redundancy in the determination of tank temperature profiles. Temperature measurements were taken every 2.5 cm along a 35 cm vertical traverse length. In every case, the traverses were taken in a downward direction, ending at the depth of the leading edge of the heated surface which was designated to be a depth of 0 cm. As a result, the temperature profiles always extended at least 5 cm above the depth of the trailing edge of the heated surface. The direction of the traverse was significant. It was found that traversing upward occasionally led to small anomalies in the temperature measurements, presumably due to the interference caused by the aluminum rods which supported the temperature sensors from above.

After verifying that the temperature profile showed no ambient stratification in the tank, the temperature probes were positioned at the depth of the trailing edge of the heated surface. As an experiment proceeded, the water at the surface of the tank would begin to heat up and a layer of heated water developed which would eventually reach the trailing edge of the heated plate. The temperatures at the depth of the trailing edge were monitored throughout an experiment to ensure that there was no variation in bulk temperature due to heating of the upper layers. It was also important to monitor the bulk temperature throughout the course of an experiment since frequently the bulk temperature would change slowly (typically 0.1 °C per hour) with time. This variation was due to an imbalance between the tank and the laboratory temperatures. It is possible to eliminate such variations by adding a constant temperature bath to jacket the tank used for the experiments (see Ruiz (1986)).

With the above preparations completed, an experiment could be performed. Upon initiating an experiment, the first step was to monitor the temperatures within the bulk fluid and at the surface to make sure that these values remained steady. Surface temperatures were measured at six locations evenly space along the length of the heated plate. Bulk temperatures were monitored using the two sensors located near the vicinity of the trailing edge. Before the power was turned on, the bulk and surface temperature values were examined to ensure that all the values matched each other and that the trends of all temperatures were identical. After 10-15 minutes of initial data, an experiment was initiated by turning the power supply for the heated foil on and adjusting it to the desired voltage. It was found that the surface temperature rapidly (within 2-3 min) reached its final elevated level so that 10-15 minutes of data was more than adequate to establish the average temperature difference for a given heat flux.

Data sampling was accomplished using a routine which sampled all 15 channels of available input sequentially. Average values were recorded on disk for every 50 individual measurements on a channel. Data recorded on disk consisted of the actual resistance measured on each channel. In addition, a hard copy of the data was produced in the form of temperatures. Experimental progress could be monitored by a CRT readout of temperatures on surface and bulk sensors. The original data was retained in the form of resistance to allow corrections to be made to the calibrations if necessary without losing any experimental data. The above sampling procedure resulted in approximately one temperature measurement per minute on each channel. Although faster rates could be attained, this sampling rate reduced the noisiness of the temperature signal by direct averaging and also kept data sets from becoming so large as to become unwieldy. Data sampling was terminated by pressing any key on the keyboard. After a stable condition at the surface temperature sensors had been observed for at least 3-5 measurements, the power level could be altered in order to obtain data at various heat flux levels. At moderate power settings, this technique permitted up to 7 heat fluxes to be utilized

before tank heating began to influence the bulk temperature adversely. At peak power settings (150-200 amps) it was difficult to obtain data for more than one or two heat flux levels. This technique provided a reliable and convenient method of obtaining heat transfer data over a wide range of conditions very rapidly. Since cooling the plate and reestablishing a uniform temperature gradient could be rather time consuming this technique was applied for all measurements presented in this section. In addition, it was important to establish a method whereby a great deal of data could be obtained rather quickly in order to apply the same procedure to obtaining data for the stably stratified case. A stable stratification is not difficult to obtain in the laboratory and in fact tends to develop naturally in a quiescent fluid as a matter of course. However, a fair amount of time and physical effort was entailed in inducing the desired temperature profiles at the correct depths of the water tank.

4.2.1.2 Evaluation of Experimental Data

In order to obtain the local heat transfer coefficient from the temperature data recorded experimentally it is necessary to calculate the local temperature difference and the heat flux.

For the experiments described in this section, the local temperature rise at any time t>0 was computed by taking T_{bulk} from the initial wall temperature data before heating was initiated, thus,

$$\Delta T|_t = T_{wall} - T_{bulk} = T_{wall}|_{heated} - T_{wall}|_{unheated} = T_{wall}|_t - T_{wall}|_{t=0} \qquad (4\text{-}35)$$

This allowed experiments to be performed without monitoring the bulk temperature at each particular sensor's depth. This step was necessitated by the available number of sensors. Another advantage of this method was that the accuracy of the measurements was enhanced by using only one sensor to determine each local ΔT since there was no error contributed by a potential deviation in the calibration of the surface sensor and a separate bulk sensor. Errors were thus reduced since the measurement depended on the precision of an individual sensor rather than its accuracy. This was particularly important in the lowest heat flux ranges when ΔT's as small as 0.05 °C were measured. As noted in the previous section, a slow variation in bulk temperature was unavoidable. This variation was typically about 0.1 °C/hour. To account for this variation, a correction was applied to the ΔT calculated so that the above expression was modified to be,

$$\Delta T|_t = T_{wall}|_t - T_{wall}|_{t=0} - (T_{bulk}|_t - T_{bulk}|_{t=0}) \qquad (4\text{-}36)$$

The variation in bulk temperature was assumed to be uniform throughout the tank and thus data from the fluid temperature sensors located at the trailing edge were used to represent the trends at all depths of the tank. Since experiments were terminated as soon as heating effects were detected at the bulk sensors, this was an acceptable method of typifying bulk temperature variation throughout the tank.

For each flux, an average ΔT was calculated by averaging three to six individual values after the temperature of the heated surface had stabilized. This served to reduce the possibility of errors resulting from rogue measurements of surface temperature. In order to obtain the best possible estimate for the $T_{bulk}|_{t=0}$ term, a linear fit was made for the 15-20 minutes of slowly varying bulk temperature data taken before initiating heating. The computed intercept of this fit line was then used as $T_{bulk}|_{t=0}$. The quantity, $T_{wall}|_{t=0}$ was calculated in the same manner. These minute corrections were required in order to obtain a reasonable degree of accuracy at the lowest heat fluxes where an error of 0.01 °C could cause a 20% error in the calculated value for the Nusselt number.

In order to calculate a local heat transfer coefficient, the heat flux for the plate was required in addition to the ΔT's at the various positions along the plate. The heat flux was determined from electrical measurements which were recorded manually from multimeter measurements. The Rapid Electric DC power supply had vane type gauges for voltage and amperage but these were only accurate to ±5% and were not suitable for a precise determination of the power dissipated. Furthermore, the voltage measured at the power supply was for a circuit which included two power feed cables to the plate. The cables to the plate were 2 meters long, 10 gauge 4 conductor copper wires. The total resistance of the cables (4 meters length) was estimated using CRC wire tables to be ~0.0033 Ω at 20°C or ~0.004 Ω at 75°C. The resistance of the heated surface (for a 12" length) was only about 0.06 Ω so the power loss in the wires would have been ~5% of the total power dissipated. Additional difficulties in measuring the voltage drop across the plate were caused by losses due to contact resistance at the terminals. Consequently, it was decided to measure only the current through the plate and determine the heat flux from this current and the known resistance of stainless steel alloy #304. Current measurement was accomplished by measuring the voltage across a precision current shunt resistor which had an accuracy of 0.5%. The current shunt used was part of the ammeter circuit which was integrated into the Rapid Electric power supply.

The resistivity ρ of stainless steel #304 was found tabulated in various sources as 72 μΩ-cm at 20 °C. The resistance of the 12"×6"×0.001" foil was thus calculated to be

$$R = \rho\frac{L}{A} = 72\times10^{-6}\frac{12}{(0.001)(6)}\frac{1\text{inch}}{2.54\text{cm}} = 0.0567\Omega \qquad (4\text{-}37)$$

This value was used initially to evaluate experimental data and resulted in Nusselt numbers which fell ~20% below those expected. Eventually it was found that the shim stock used had a resistivity which apparently deviated significantly from the tabulated values for this alloy. The true resistivity was estimated by measuring the voltage drop and current through known lengths of the foil. In the course of these experiments it was found that contact resistance at the connecting terminals could be a significant source of error in measuring

the voltage drop across a length of the foil. This observation led eventually to a new design for the terminals with negligible contact resistance which was implemented for a later series of experiments. For the purpose of evaluating the present data, however, it was still necessary to measure the resistivity of the stainless steel shim stock. To accomplish this, various terminals were constructed and tested. Contact resistance was evaluated by the expedient method of comparing the calculated resistivities from measurements with various lengths of foil. The clamping terminals discussed in Chapter 3 were found to have negligible contact resistance since resistivity estimates did not vary for different lengths of foil. A high accuracy Fluke 8050A DMM was used for the best possible precision in these measurements. The resistance of a 12" length of foil was estimated by these measurements to be 0.0644 Ω. This value has an estimated accuracy of ±0.5%. The resistivity of the shim stock alloy (described by the manufacturer as SS #304) is thus seen to be 81.78 μΩ-cm. The variation from normally specified values may be due to some additional processing which is required to manufacture a thin foil for this alloy.

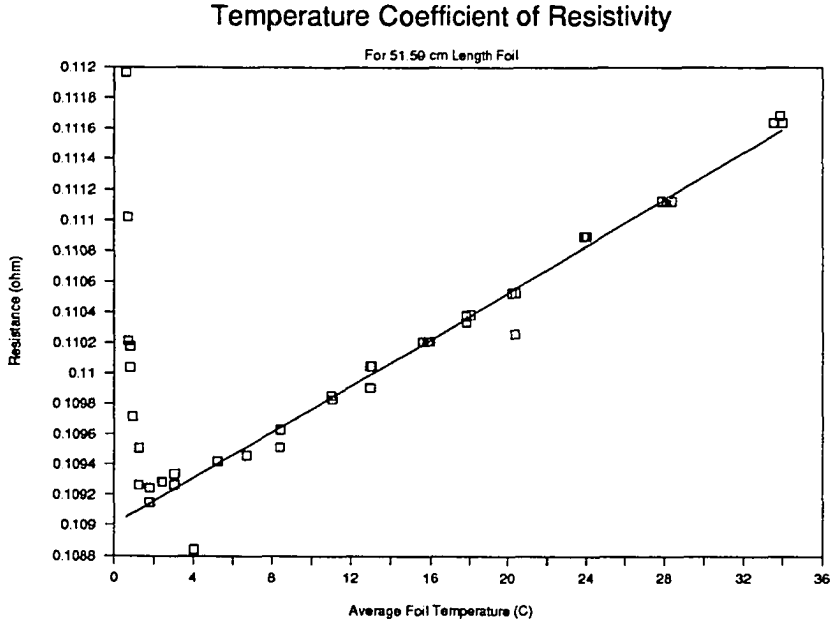

Figure 4-2 Electrical Resistance of Heated Foil: Temperature Dependence
Resistance of 20.3125" (51.59 cm) long foil as a function of surface temperature. Linear variation with temperature indicates temperature coefficient of resistivity = 0.00069 $°C^{-1}$.

One additional consideration was necessary in evaluating the heat flux. Since resistance varies with temperature, a correction must be applied to the foil resistance at high heat fluxes when the temperature is elevated. The temperature coefficient of electrical resistivity for 18-8 stainless steel can be found tabulated as 0.00094 $°C^{-1}$ (see for example, Bever (1986)). This temperature is relatively low and may be compared to

values of 0.0069 (Ni), 0.00651 (Fe), and 0.003 (Cr). In light of the problems encountered with resistivity, it seemed inadvisable to rely on the accuracy of tabulated values of temperature coefficient. Therefore, experiments were made to verify the temperature dependence of resistivity. Shown in Figure 4-2 is a plot of foil resistance (R=V/I) against average surface temperature. Shown on the plot is the best fit to the data which was calculated to have a coefficient of 0.00069 $°C^{-1}$, and a room temperature resistance of 0.109 Ω.

To summarize, the heat flux for these experiments was found by measuring the current using a precision current shunt resistor. The resistance of the foil was estimated from actual measurements of voltage drop and current flow rather than by using tabulated values of SS #304 resistivity. A correction for temperature variation was applied based on literature values of the temperature coefficient of resistivity for this alloy. The resulting expression for heat flux q was,

$$q = \frac{Q}{A} = \frac{I^2 R_{foil}}{A} = \frac{(V_{shunt}/R_{shunt})^2 \rho \frac{L}{A_x}}{A} = \left(\frac{V_{shunt}}{R_{shunt}}\right)^2 \frac{\rho}{WA_x} \tag{4-38}$$

In this expression, R_{shunt} was $2.5\times10^{-4}\Omega$; cross sectional area A_x was 6"×0.001" (3.871×10^{-6} m^2), the plate width W was 6" (0.1524 m), and V_{shunt} was found by directly measuring the voltage drop across the shunt resistor. For temperatures other than room temperature, the resistivity ρ was corrected for temperature dependence using the expression

$$\rho = 1.00069\rho_{20°C}(T_{avg} - 20°C) \tag{4-39}$$

The average plate temperature, T_{avg}, was evaluated from the measured surface temperature values.

The calculations developed above for ΔT and heat flux were performed using the program NEVAL3.PAS which further computed the Nusselt and modified Grashof numbers and calculated best fit line parameters for the laminar range. This program (listed in the appendices) used physical property data for water from the separately written library unit PHYSPROP.LIB, which was described above.

4.2.2 Experiments with Stratified Bulk Fluid

Some modification to the techniques described in the previous section was necessary for measurements made with stratified bulk fluid. Since bulk temperature (and bulk temperature variation) was no longer uniform, additional sensors were positioned in the bulk fluid at the same depths as the surface sensors. Thus, for these experiments, ΔT was calculated as,

$$\Delta T = T_{wall} - T_{bulk} \tag{4-40}$$

A further correction was necessary at small values of ΔT to account for the small initial deviation between the calibrations of the two sensors. With the correction, the calculation used was thus,

$$\Delta T = (T_{wall} - T_{bulk}) - (T_{wall}|_{t<0} - T_{bulk}|_{t<0}) \tag{4-41}$$

The method for heat flux calculations was also altered for this set of experiments. Since the plate used was the 20" model (described in Chapter 3), the connecting terminals were the redesigned clamping terminals which were not subject to the contact resistance problems encountered previously. Thus the voltage across the foil could be obtained directly. Separate leads were run directly to the terminals and soldered in place for voltage measurements to avoid any problems with voltage drop in the power leads. Current was measured using the current shunt resistor as had been done previously. The power dissipated was then obtained directly from the voltage and current without using any resistivity calculations for the plate.

4.3 Results and Discussion

4.3.1 Experimental Results for Uniform Ambient Fluid Temperature

The results from the experiments with uniform bulk temperature are summarized in the sections below. Initial estimates for the empirical coefficients were made in NEVAL3.PAS by linear least squares fits to the logarithmic plots of the data. These coefficients are to be used in the equation,

$$Nu_x = C(Gr_x^* \cos\theta Pr)^m \qquad (4\text{-}42)$$

where θ is the angle from vertical. The lines and correlations which are shown on the plots of the figures in this section correspond are the coefficients by least squares fit to the equation above.

4.3.1.1 Vertically Oriented Surface

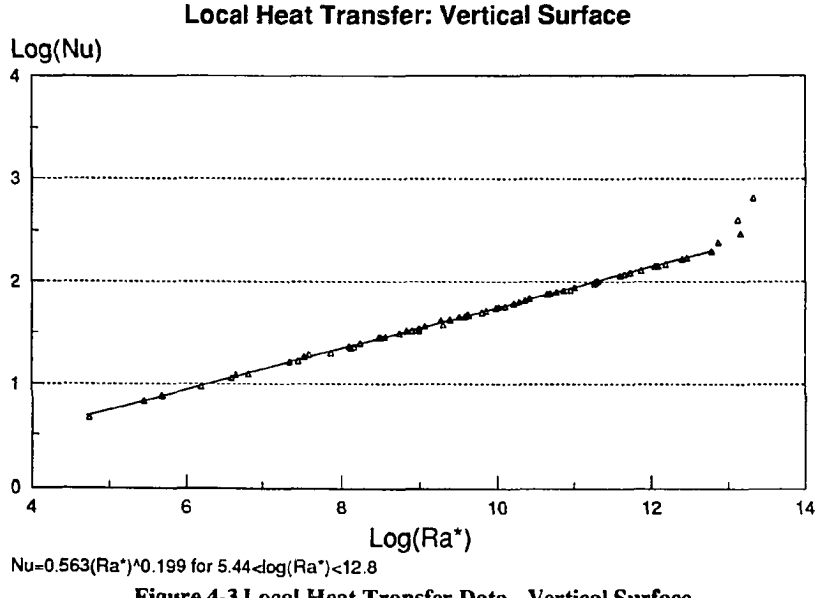

Figure 4-3 Local Heat Transfer Data - Vertical Surface
Vertical uniform flux surface in a uniform temperature bulk fluid. Plot of local Nusselt number vs. modified local Rayleigh number.

The measurements for the vertical configuration were close to those reported by previous researchers. The location of transition to turbulence is comparable to values previously measured. The data is plotted in Figure 4-3 and, as can be seen, the linearity of the log-log fit was excellent. The estimated value of m from a simple least squares fit was 0.199, very close to the predicted value of 1/5. Transition to turbulence began at $\log(Ra_x^*) = 12.8$. The plate length was too short to get any data outside the transition regime.

As can be seen, the behavior appears to stay linear down to the lowest range of Ra_x^* measured. This result is of interest since this data extends as low as 5×10^4, two orders of magnitude further down than any previous measurements. Vliet's (1969) data extended as low as $Ra_x^* \sim 6\times10^6$ while the more recent results of Qureshi & Gebhart (1978) reach down to $\sim 2\times10^6$. Some departure from linearity might have been expected since measurements for uniform temperature plates have shown that for very low Rayleigh numbers ($Ra_L < 10^4$) the correlation becomes nonlinear. This Rayleigh number (Ra_L) is different from the modified local Rayleigh number used above and the numerical values do not correspond. Nevertheless it is worthwhile to note that, with this data, the limits of the linear laminar regime for uniform flux surfaces have been extended to cover the range from $Ra_x^* = 10^4$ to 10^{13}, nine orders of magnitude. For the isothermal case the laminar range is from $Ra_L = 10^4$ to 10^9, for five orders of magnitude in Ra_L.

4.3.1.2 Inclined Surface: 15° From Vertical

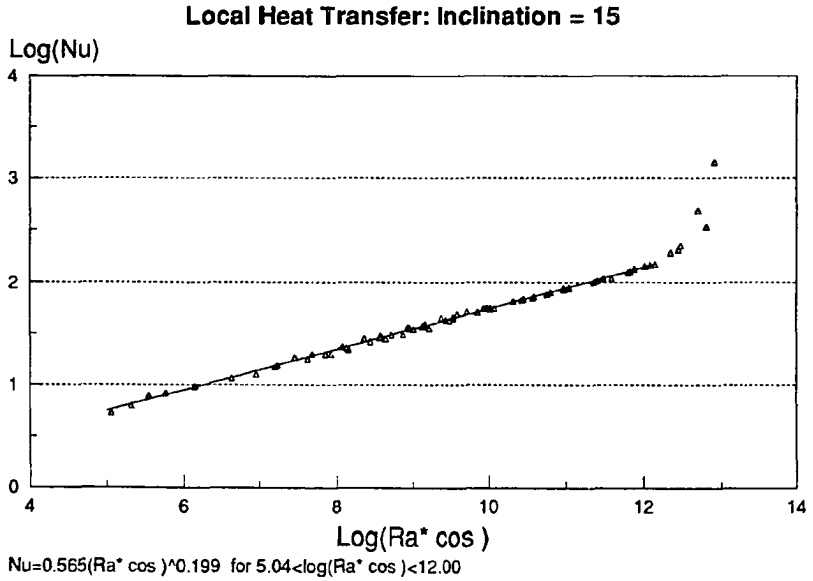

Figure 4-4 Local Heat Transfer Data - Angle = 15°
Uniform flux surface in a uniform temperature bulk fluid. Plot of local Nusselt number vs. modified local Rayleigh number.

The first set of inclined data is for an angle from vertical of $\theta = 15°$. The data for $\theta = 15°$ is shown in Figure 4-4 along with the best fit line. The following characteristics were observed:

- With gravity replaced by $g\cos\theta$ in the correlation, the constants obtained for laminar flow differed very little from those for the vertical plate.
- The transition to turbulence was observed to begin from about $Ra_x^*\cos\theta=10^{12}$ ($Ra_x^*=1.04\times10^{12}$), an order of magnitude lower than for the vertical plate.
- The turbulent data was insufficient to derive any correlation.

4.3.1.3 Inclined Surface: 30° From Vertical

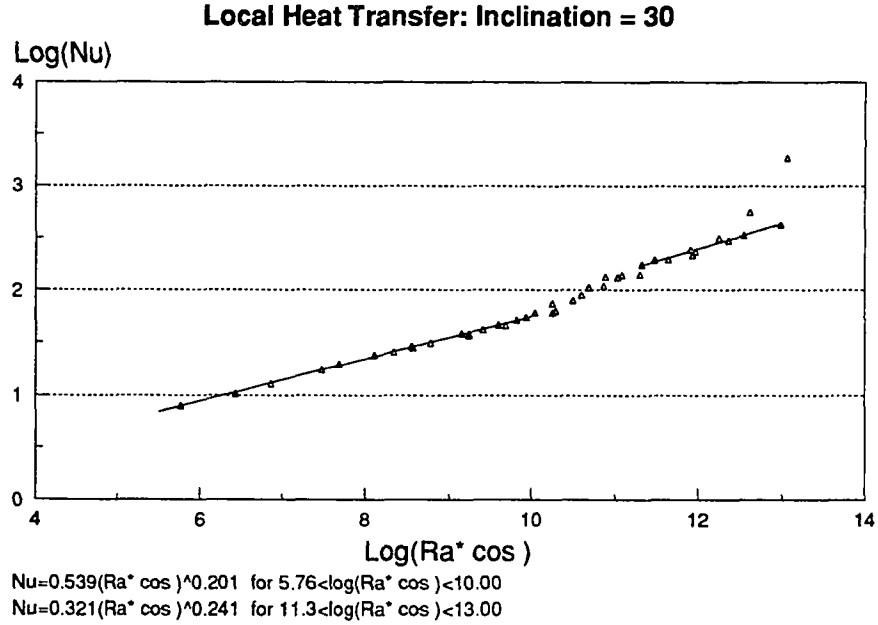

Figure 4-5 Local Heat Transfer Data - Angle = 30°
Uniform flux surface in a uniform temperature bulk fluid. Plot of local Nusselt number vs. modified local Rayleigh number.

Data for an inclination of 30° is shown in Figure 4-5. The following observations can be made:

- The laminar correlation still falls very close to the vertical case adjusted with the correction $g\cos\theta$.
- For $\theta=30°$, the transition to turbulence began at around $Ra_x^*\cos\theta=10^{10}$ ($Ra_x^*=1.15\times10^{10}$).
- Correlations for turbulent data became possible at this inclination. A simple least squares fit to the data over the range $11.3<\log(Ra_x^*\cos\theta)<13$ gave the preliminary result,

$$Nu_x = 0.321(Ra_x^*\cos\theta)^{0.241} \qquad (4\text{-}43)$$

- The exponent of 0.241 for the turbulent data indicates that the heat transfer coefficient was less dependent on distance along the plate for turbulent flow. An exponent of 0.25 would correspond to a situation where the heat transfer coefficient (and ΔT) are completely independent of x.

Beginning with this data set, it can be seen that there appear data points scattered above the turbulent correlating line at the upper end of the plot. These points were for measurements at the sensor closest to the trailing edge (~ 1" from the end) and bear further discussion. Edge effects, or more specifically, a transformation of the turbulent boundary layer to a upward flowing plume near the trailing edge of the inclined surface were blamed for this deviant data. Such a separation would result in the entrainment of cold fluid from the region of the trailing edge and would thus enhance the heat transfer locally. The result would be a skewing upward of the Nusselt number as was observed. Experiments performed with a longer plate (shown in Figures 4-12 and 4-13) verified that this behavior was related to local edge effects. The aberrant data points were therefore excluded from any fitting calculations.

4.3.1.4 Inclined Surface: 45° From Vertical

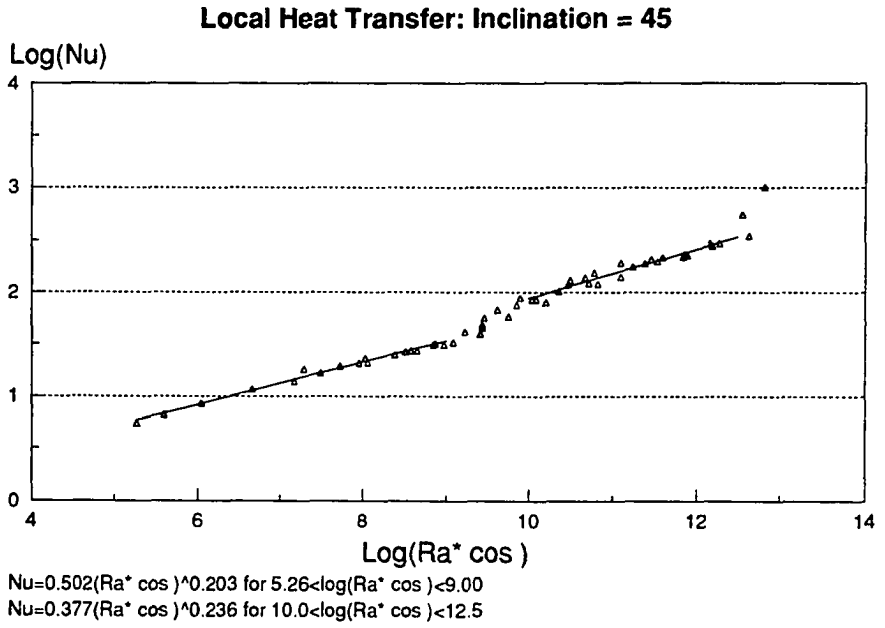

Figure 4-6 Local Heat Transfer Data - Angle = 45°
Uniform flux surface in a uniform temperature bulk fluid. Plot of local Nusselt number vs. modified local Rayleigh number.

In the data for inclinations ≥ 45° (approaching horizontal), starting with the data in Figure 4-6, a trend is seen for the leading constant C to decrease and the slope m to increase. Clearly, the constant C varies in response to a change in m, so these coefficients do not vary independently. Nevertheless, it seems clear that the increasing exponent signifies that the heat transfer coefficient becomes a weaker function of x as the inclination approaches horizontal in the laminar regime. For the 45° inclined plate, the transition to turbulence began at $Ra_x^* \cos\theta = 10^9$ (or $Ra_x^* = 1.4 \times 10^9$), very close to the value observed by Vliet (1969).

4.3.1.5 Inclined Surface: 60° From Vertical

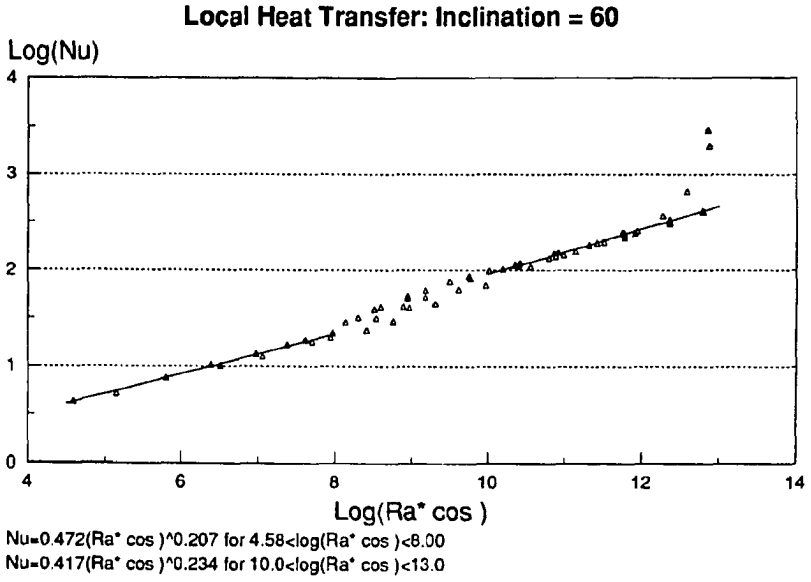

Figure 4-7 Local Heat Transfer Data - Angle = 60°
Uniform flux surface in a uniform temperature bulk fluid. Plot of local Nusselt number vs. modified local Rayleigh number.

Figure 4-7 shows the data obtained for an inclination of 60° from vertical. The following results can be extracted from the data:

- The exponent for the laminar flow has increased to 0.207, with a corresponding decrease in the leading coefficient.
- The transition region began at $Ra_x^*\cos\theta \sim 10^8$ ($Ra_x^* \sim 2\times10^8$), compared to the value of 6×10^8 observed by Vliet (1969).

4.3.1.6 Inclined Surface: 75° From Vertical

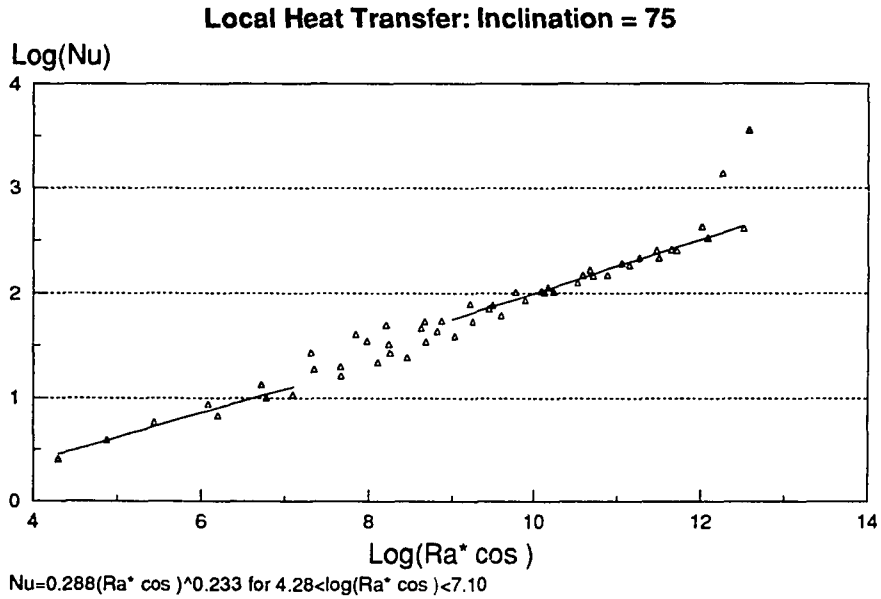

Figure 4-8 Local Heat Transfer Data - Angle = 75°
Uniform flux surface in a uniform temperature bulk fluid. Plot of local Nusselt number vs. modified local Rayleigh number.

Figure 4-8 shows heat transfer data collected for an inclination of 75° from vertical (approaching horizontal). This is the first uniform heat flux heat transfer data taken for upward facing plates at an inclination exceeding 60°.

- An exponent of 0.233 is observed for the laminar regime. This exponent is significantly larger than those found for near vertical plates and indicates a weaker dependence of heat transfer coefficient on distance from the leading edge.
- Transition appeared to begin for $Ra_x^* \cos\theta \geq 1.3 \times 10^7$ ($Ra_x^* \geq 4.9 \times 10^7$). Vliet's empirical correlation for transition ranges for inclinations up to 60° would give a value of $Ra_t^* = 4.5 \times 10^7$, a slightly earlier transition than observed at this inclination.
- The data at this inclination showed departures from the laminar flow behavior of near vertical plates but still appears to be better expressed as a perturbation to vertical plate behavior than as a perturbation to horizontal plate behavior.

4.3.1.7 Horizontal Surface

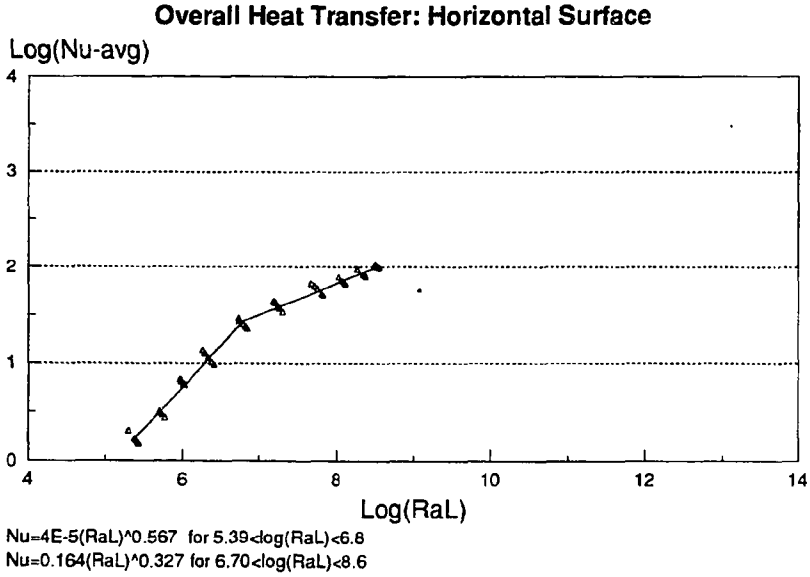

Figure 4-9 Overall Heat Transfer Data - Horizontal Surface
Uniform flux surface in a uniform temperature bulk fluid. Plot of overall Nusselt number vs. modified overall Rayleigh number.

Figure 4-9 shows the data collected for horizontal surfaces. The horizontal plate falls into a different category from the preceding data sets since there is no single leading edge for the convective flow. An overall length scale was thus defined and only overall quantities were calculated.

No correlations were available for horizontal uniform flux surfaces. This data was thus recast in a form allowing it to be compared to correlations which were found for isothermally heated horizontal plates facing upward. Thus, the overall Nusselt number is plotted below against the overall Rayleigh number.

Karlekar and Desmond (1977) give the following correlation for horizontal, isothermal, heated surfaces,

$$\mathrm{Nu}_{av} = 0.54(Ra_L)^{\frac{1}{4}} \quad 2.6\times10^4 < Ra_L < 10^7$$

$$\mathrm{Nu}_{av} = 0.15(Ra_L)^{\frac{1}{3}} \quad 10^7 < Ra_L < 3\times10^{10}$$

Quantities used in this correlation are defined as follows:

$$\mathrm{Nu} = \frac{hL}{k}; \quad \mathrm{Ra} = \frac{g\beta\Delta TL^3}{\nu\alpha}; \quad \mathrm{L} = \frac{\text{surface area}}{\text{perimeter}} = \frac{WL}{2(W+L)} \tag{3-44}$$

The experimental data in the turbulent region was fit by $Nu_{x_v}=0.164(Ra_L)^{0.327}$ which compares well to the correlation above for isothermal plates, suggesting that the isothermal correlation from Karlekar & Desmond may be used in the turbulent region for uniform flux surfaces. Since the uniform flux surface approached an isothermal condition for turbulent flow the agreement between the correlations is not surprising.

The transition point defined by Karlekar and Desmond appears to agree quite closely with the observed transition point for the uniform flux surface. This result is of interest since for vertical and inclined surfaces, the transition for uniform flux surfaces is often as much as an order of magnitude higher than that for isothermal surfaces.

In the low Rayleigh number ('laminar') case there appears to be a large deviation from the predicted isothermal behavior. Apparently, the effects of uniform flux produced nonisothermal effects which were not manifested in the turbulent flow regime.

4.3.1.8 Summary of Experimental Results For Inclined Plate Heat Transfer

As mentioned above, it appears that data from all inclinations from vertical down to 75° from vertical is best treated with variations to the vertical correlation. The least squares fit coefficients shown on the plots of experimental data presented in the sections above are summarized in the table below.

Table 4-5 Experimental Summary for Inclined Plate Heat Transfer Data - Least Squares Fit

Inclination	Laminar			Turbulent		
θ	C	m	$Ra_x^*\cos\theta$ Range	C	m	$Ra_x^*\cos\theta$ Range
90	0.563	0.199	4.73-12.8	NA	NA	NA
75	0.565	0.199	5.04-12.0	NA	NA	NA
60	0.539	0.201	5.76-10.0	0.321	0.241	11.3-13.0
45	0.502	0.203	5.26-9.0	0.377	0.236	10.0-12.5
30	0.472	0.207	4.58-8.0	0.417	0.234	10.0-13.0
15	0.288	0.233	4.28-7.1	0.295	0.253	9.0-12.5

In light of the interdependence of the parameters C and m it was distinctly possible that small variations in the exponent could be overshadowing the behavior of the constant C, and making it appear that the magnitude of this leading term was varying more than the actual variation in the heat transfer coefficient. For a better understanding of the data, further analysis was performed and somewhat more sophisticated fitting procedures were applied. In addition to calculating best fit values of C for specified slopes, procedures were employed which weighted individual data points according to their estimated likely error. This procedure was necessary since the uncertainties of the data points were not all equal.

The variance of the Nusselt number can be expressed in terms of the variances of the variables which were actually measured so that,

$$\sigma^2_{\log Nu} \approx \sigma^2_{\Delta T}\left[\frac{\partial}{\partial(\Delta T)}(\log Nu)\right]^2 + \sigma^2_q\left[\frac{\partial}{\partial q}(\log Nu)\right]^2 + \sigma^2_x\left[\frac{\partial}{\partial x}(\log Nu)\right]^2 \qquad (4\text{-}45)$$

Evaluation of the partial derivatives yields,

$$\sigma^2_{\log Nu} \approx \sigma^2_{\Delta T}\left[-\frac{\log e}{\Delta T}\right]^2 + \sigma^2_q\left[\frac{\log e}{q}\right]^2 + \sigma^2_x\left[\frac{\log e}{x}\right]^2 \qquad (4\text{-}46)$$

The likely errors in the measured quantities were estimated to be given by the following,

$$\sigma_x = 0.0004 \text{ (meters)}; \quad \sigma_{\Delta T} \approx 0.005 + 0.01(\Delta T) \text{ (degree C)}; \quad \sigma_q \approx 0.01q \ (w/m^2)$$

Best fit calculations taking into account the weighting factors described were performed using a general least squares procedure (LFIT) extracted from Press et al. (1986). Results are tabulated below.

Table 4-6 Coefficients for Laminar Inclined Plate Heat Transfer Data - Weighted Least Squares Fit

θ	$Ra_x^*\cos\theta$ Range	Unweighted LSQ		Weighted LSQ		Weighted, m=0.200	
		C	m	C	m	C	m
90	4.7-12.8	0.563	0.199	0.558	0.200	0.552	0.200
75	5.0-12.0	0.565	0.199	0.566	0.199	0.552	0.200
60	5.7-10.0	0.539	0.201	0.540	0.201	0.551	0.200
45	5.2-9.0	0.502	0.203	0.593	0.195	0.542	0.200
30	4.5-8.0	0.472	0.207	0.507	0.203	0.535	0.200
15	4.2-7.1	0.288	0.233	0.225	0.260	0.524	0.200

With the data reanalyzed and presented in this form it becomes evident that the laminar portion of the data can be very well represented by the empirical coefficients C = 0.55 and m = 0.20. For angles of inclination near horizontal, this will overestimate the Nusselt number by ~5%. Since scatter of ±20% is usual for these types of experimental data according to Holman (1976), the degree of accuracy is quite satisfactory. In Figure 4-10, the laminar portions of the data for all inclinations are shown on one plot. For inclinations close to vertical, the scatter of these data were typically less than 2%, providing a significant improvement in quality of data over previously measured data. The recommended fitting correlation (shown on the plot) is

$$Nu_x = 0.55(Gr_x^* \cos\theta Pr)^{0.200} \qquad (4\text{-}47)$$

The turbulent portion of the data also becomes somewhat more coherent when reanalyzed in this fashion. Results are tabulated below. From the weighted best fit slope m, it can be seen that there is only a slight x dependence in the heat transfer coefficient for turbulent flows, with m ranging from 0.233 to 0.243. The turbulent data appears to be best fit then by an exponent of 0.240. The coefficients resulting from a slope of 0.250 are shown as well. The weighted best fit coefficients showed a systematic variation with inclination. Values for C ranged from ~0.32 up to ~0.41 as the inclination went from 30° to 75°.

Table 4-7 Coefficients for Turbulent Inclined Plate Heat Transfer Data - Weighted Least Squares Fit Using $Ra_x^* \cos\theta$

	$Ra_x^* \cos\theta$	Unweighted LSQ		Weighted LSQ		Weighted LSQ m=0.240		Weighted LSQ m=0.250	
θ	Range	C	m	C	m	C	m	C	m
30	11.3-13.0	0.321	0.241	0.363	0.237	0.318	0.240	0.250	0.250
45	10.0-12.5	0.377	0.236	0.398	0.234	0.344	0.240	0.266	0.250
60	10.0-13.0	0.417	0.234	0.421	0.233	0.354	0.240	0.272	0.250
75	9.0-12.5	0.295	0.253	0.377	0.243	0.406	0.240	0.317	0.250

The upward trend in C for fixed slopes gives rise naturally to a question as to whether turbulent data might not be better correlated using the vertical component of gravity, independent of inclination. Recalculating the Rayleigh number and repeating the fitting calculations resulted in the following coefficients.

Table 4-8 Coefficients for Turbulent Inclined Plate Heat Transfer Data - Weighted Least Squares Fit Using Ra_x^*

	Ra_x^*	Weighted LSQ m=0.240		Weighted LSQ m=0.250	
θ	Range	C	m	C	m
30	11.36-13.06	0.318	0.240	0.241	0.250
45	10.15-12.65	0.317	0.240	0.244	0.250
60	10.3-13.3	0.300	0.240	0.229	0.250
75	9.89-13.09	0.292	0.240	0.229	0.250

Clearly the Ra number independent of θ reduced the variation in C and provided a better fit to the data. Although there still remains a weak dependence on θ, this effect is apparently overemphasized when g is modified by the cosθ factor. This can be explained in relation to the observed characteristics of laminar and turbulent flows. For laminar flow, streamlines are parallel to the surface and fluid motion is primarily in the plane of the inclined surface. The relevant buoyant acceleration vector acting on the flow is therefore the along slope component of gravity. In turbulent flow, although the mean velocity is still parallel to the surface, the flow has a fluctuating character with the fluctuations being predominantly in the vertical plane of motion, thus the vertical gravity vector may be more appropriate.

The turbulent portion of the inclined data which was presented above is shown separately in Figure 4-11. Two possible correlations are shown on this plot. A slope of 0.24 was indicated by the best fit slopes for the various data sets. However, as shown by the dashed line on the figure, a slope of 0.25 gives a fit which appears to be within the range of variation for the data sets and may be just as satisfactory.

Summarizing, the following empirical correlations were found and are suggested for use with inclined plates from vertical to 75° from vertical.

Laminar Range: $$Nu_x = 0.55(Gr_x^* \cos\theta Pr)^{0.200} \qquad (4\text{-}48)$$

Turbulent Range:

$$Nu_x = 0.31(Gr_x^* Pr)^{0.24} \quad \text{or} \quad Nu_x = 0.235(Gr_x^* Pr)^{0.25} \tag{4-49}$$

Precise measurements focusing on transition behavior were not a goal of this work. However, the observed ranges of the transition region agreed fairly well with the empirical correlation of Vliet (1969).

The correlation for laminar data is identical to that recommended by Vliet and Ross (1975). Vliet and Ross (1975) made measurements at nine angles, only one of which was for the upward facing "unstable" configuration. The data for upward facing plates appears to be <10 points which deviate by ~20 percent upward in either slope or coefficient relative to the recommended correlation. Vliet and Ross recognized this deviation and attributed the data spread to nonconstant heat flux in the laminar region and bulk temperature variation near the leading edge of their plate. Vliet and Ross thus present only very weak evidence to support using this correlation for upward facing plates.

Vliet (1969) reported data of better appearance using water and mostly upward facing plates but obtained a coefficient of 0.60. The present data indicates that the coefficient of Vliet (1969) was about 10 percent too high. This view is consistent with the results of other recent experiments for the vertical configuration which all show coefficients of less than 0.60. Similarity solutions predict a heat transfer coefficient with coefficients in the range 0.58-0.59.

The data collected extended the experimental measurements of this regime down two orders of magnitude and confirmed linearity in this region.

In the turbulent regime, the correlation developed was close to that of Vliet (1969). Disagreement was noted with the results of Vliet & Ross (1975), obtained for experiments with air. The exponent for turbulent flow indicated that there is at best a slight dependence of the heat transfer coefficient on distance.

It was clearly more appropriate to use the vertical component of gravity in correlating turbulent data at all inclinations. These results agreed with Vliet (1969) in not using the $\cos\theta$ factor for turbulent data. Lloyd et al. (1972) obtained results supporting use of the $\cos\theta$ factor for turbulent mass transfer driven convection and expressed reservations about Vliet's result because of the magnitude of the scatter in Vliet's data. In the present work, empirical coefficients were obtained by correlating the data by both Ra_x^* and $Ra_x^*\cos\theta$. Using $Ra_x^*\cos\theta$ produced a systematic variation of coefficients with inclination. The coefficients obtained using Ra_x^* showed much less variation, suggesting that inclination can properly be disregarded for turbulent flow.

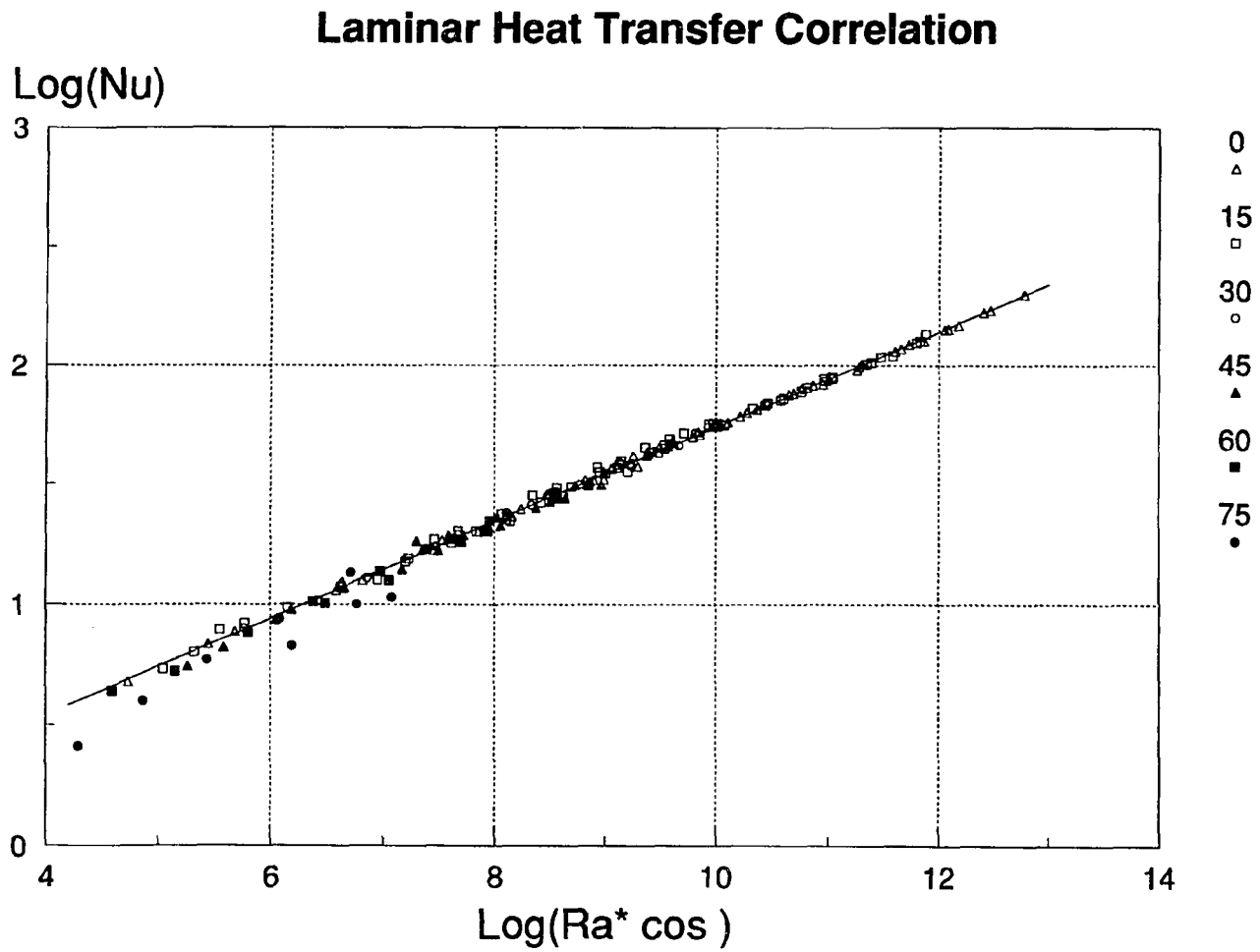

Figure 4-10 Laminar Heat Transfer Data - Angles: 0°,15°,30°,45°,60°,75°
Uniform flux surface in a uniform temperature bulk fluid at various inclinations from vertical. Plot of local Nusselt number vs. modified local Rayleigh number. Solid Line - $Nu_x = 0.55(Gr_x^* \cos\theta Pr)^{0.200}$.

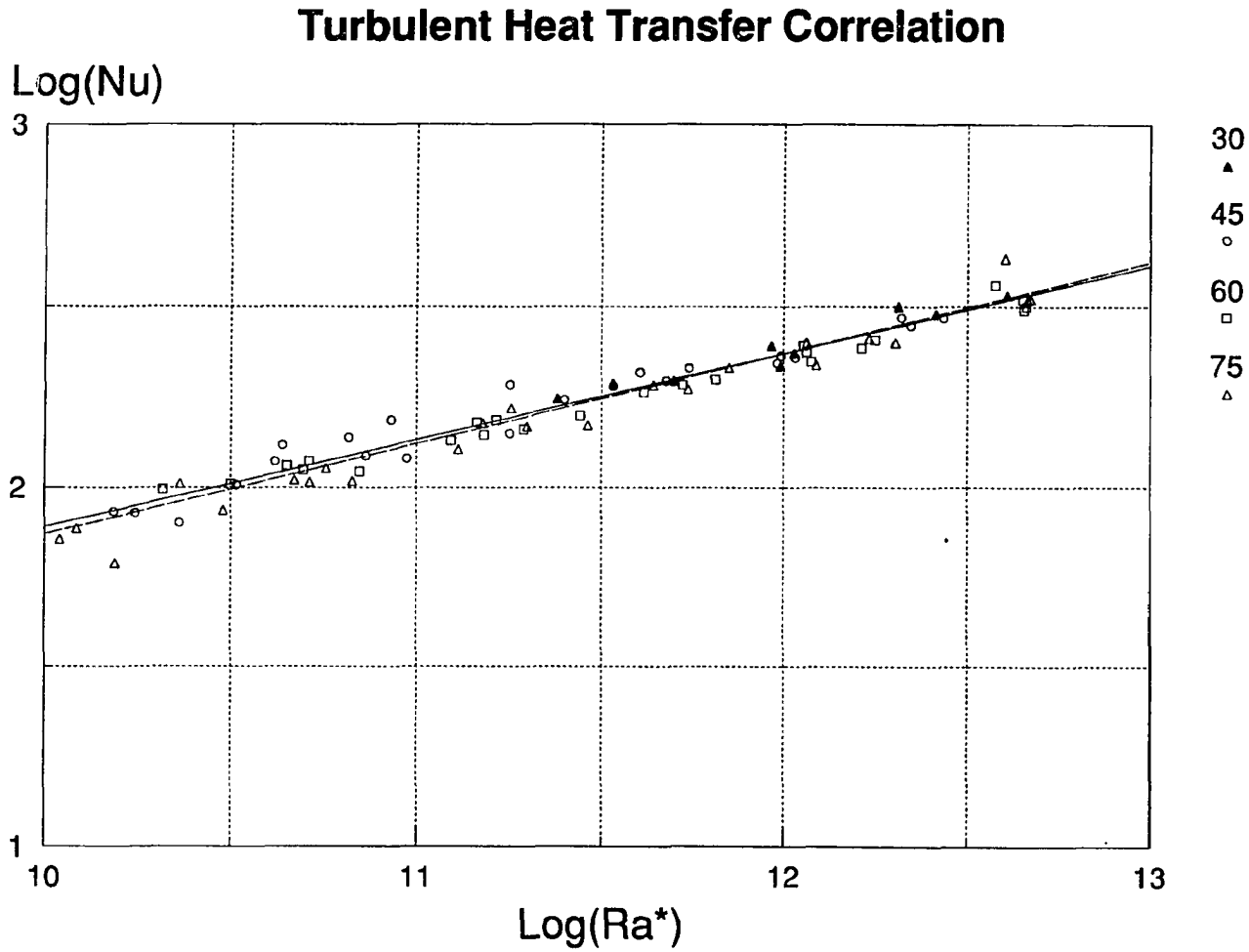

Figure 4-11 Turbulent Heat Transfer Data - Angles: 30°,45°,60°,75°
Uniform flux surface in a uniform temperature bulk fluid at various inclinations from vertical. Plot of local Nusselt number vs. modified local Rayleigh number. Dashed Line - $Nu_x = 0.235(Gr_x^*Pr)^{0.250}$. Solid Line - $Nu_x = 0.31(Gr_x^*Pr)^{0.240}$

4.3.2 Stratified Experimental Results and Discussion

In this section are described measurements of heat transfer coefficients under stratified conditions. In addition to the atmospheric flow simulation measurements, which are described in the following chapter, a number of experiments were conducted in an effort to measure heat transfer coefficients under stratified conditions. There were obviously a great many configurations and variables which could be investigated but the scope of these experiments were limited to a few representative cases for developing and demonstrating the experimental techniques used.

Before conducting any experiments with stratified conditions, a few runs were made without stratification to verify the accuracy of the new measurement techniques and to extend the measurements described above for uniform temperature by repeating them with a longer plate. The new plate enabled the measurements to extend further into the turbulent region because of its greater length. This also allowed measurements to be made in the region where trailing edge effects had been postulated for the earlier experiments.

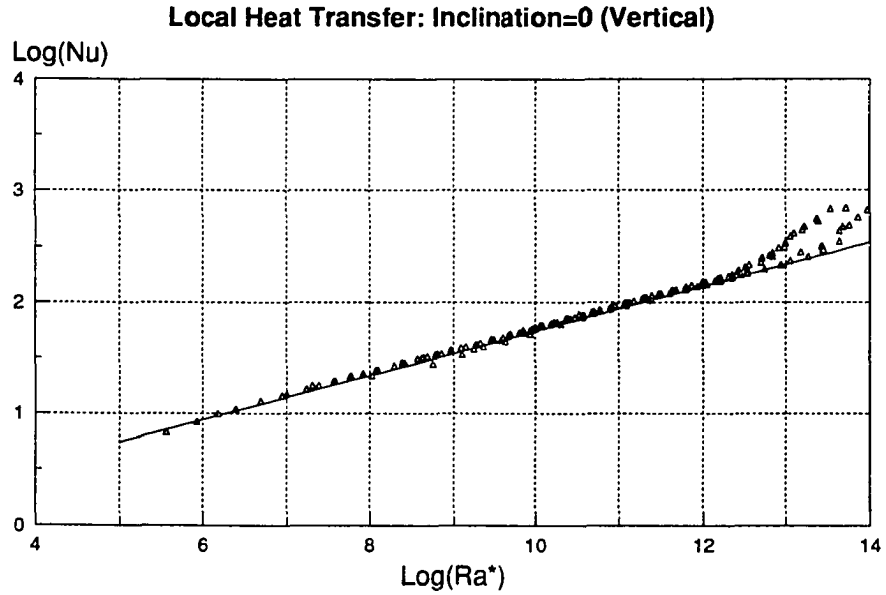

Figure 4-12 Local Heat Transfer Data - Vertical Surface
Vertical uniform flux surface (twenty inch length). Uniform temperature bulk fluid. Plot of local Nusselt number vs. modified local Rayleigh number. Line on plot: $Nu_x = 0.55(Gr_x^* Pr)^{0.200}$

As can be seen in the Figure 4-12, the data obtained were of good quality and the observations extended well into the transition region for the vertical plate. The laminar correlation obtained previously for vertical surfaces is shown for comparison on the plot. The weighted best fit line to the laminar data in the figure was,

$$Nu_x = 0.595(Gr_x^* Pr)^{0.1999} \qquad (4\text{-}50)$$

Forcing a slope of 0.200 resulted in only a minor alteration of the leading coefficient, giving the correlation:

$$Nu_x = 0.594(Gr_x^* Pr)^{0.200} \qquad (4\text{-}51)$$

As can be seen on the figure, the new data are close to but fall slightly above the previous measurements. There are some data for which the transition to turbulence occurred at around $Ra_x^* = 2\times10^{12}$ and other data which indicate a transition at around $Ra_x^* = 2\times10^{13}$.

The early transition was found to occur for data which resulted from taking data while slowly stepping up the heat flux to obtain a large range of measurements. Thus heating had been in progress for ~1 hour and the early transition to turbulence observed may be linked to large scale circulations which probably developed in the tank over a period of time. These circulations could have caused a disturbance to the flow and caused turbulent flow to develop sooner than with a completely quiescent bulk fluid. The data indicating a later transition were obtained from single flux experiments which used a high heat flux for less than 15 minutes. The latter value for transition is in good agreement with other published values from the literature.

Comparison of this figure and the previously obtained data for vertical surfaces verifies that trailing edge effects are probably responsible for the scatter of the last few data points measured with the 12" (30 cm) plate. For the short plate used previously, the trailing sensor was located at 27.5 cm, 2.5 cm from the trailing edge. The measurements here included sensors located at 30.28 cm, 38.10 cm, and 45.40 cm, with the last sensor falling 6.2 cm from the trailing edge. These sensors gave no indication of the scatter observed previously at distances beyond x=27.5 cm for vertical surface measurements.

Similar observations can be made for the data taken with the new plate and sensor configuration at an inclination of 45°, shown in Figure 4-13. The laminar and turbulent data agreed quite well with the previously determined correlations, as shown by the lines on the plot. The location of the transition range fell between $Ra_x^* = 10^9$-10^{10} as it did before.

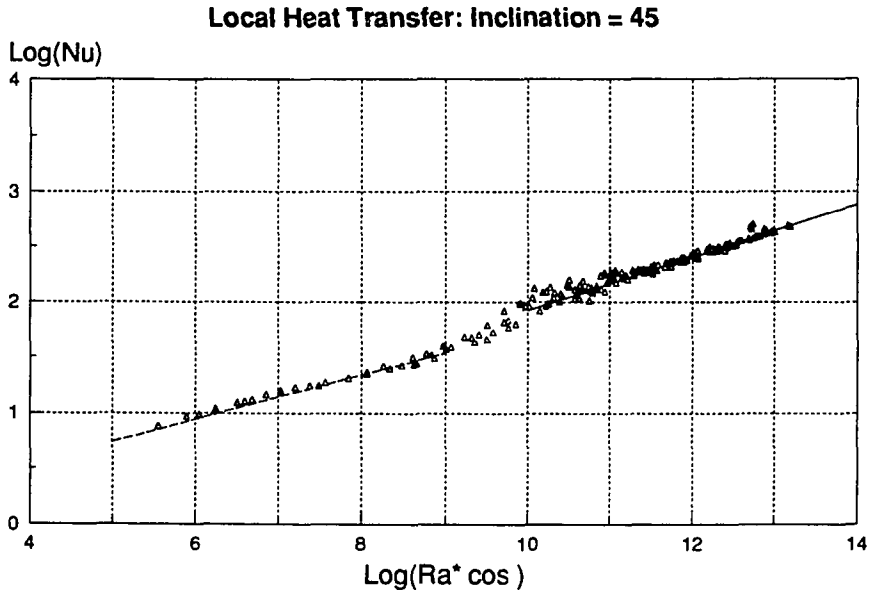

Figure 4-13 Heat Transfer Results - Angle = 45°
Inclined uniform flux surface (twenty inch length). Uniform temperature bulk fluid. Plot of local Nusselt number vs. modified local Rayleigh number ($Ra_x^*\cos\theta$). Lines on plot:
$Nu_x = 0.55(Gr_x^*\cos\theta Pr)^{0.200}$ - Dashed Line
$Nu_x = 0.31(Gr_x^*Pr)^{0.240} = 0.337(Gr_x^*\cos\theta Pr)^{0.240}$ - Solid Line

Heat transfer measurements made with stable stratification are presented here for two cases. The first set of measurements was made with a vertical plate. Figure 4-14 shows the temperature profile for which measurements were made. The temperature is typical of the sort of profile which might develop in an imperfectly insulated tank which is being heated from one of its sides, and is also similar in shape to atmospheric temperature profiles resulting from a stable inversion layer overlying a well mixed surface layer. There is thus a hot upper layer overlying a cold layer at the bottom of the tank with a linear profile region dividing the two regions.

The heat transfer data shown in Figure 4-15 is typical of that resulting from stratified temperature profiles of this type. As can be seen, the heat transfer coefficient is enhanced by the stratification of the ambient fluid. This is a result of the upward transport of cold lower layer fluid in the boundary layer flow which lowers surface temperatures in the upper regions. The result is that the apparent ΔT is lowered, resulting in a higher value of h since the heat flux, q, is constant.

Clearly the behavior of the heat transfer coefficient in the presence of stratified ambient fluid is strongly dependent on upstream conditions and as a result is extremely complex. The values for sensors 1 and 2 fall in the uniform temperature bottom layer and as a result fall right on the expected correlation for uniform bulk temperature. Sensor 3, at a depth of 22 cm begins to show the effects of the stratification. However, the

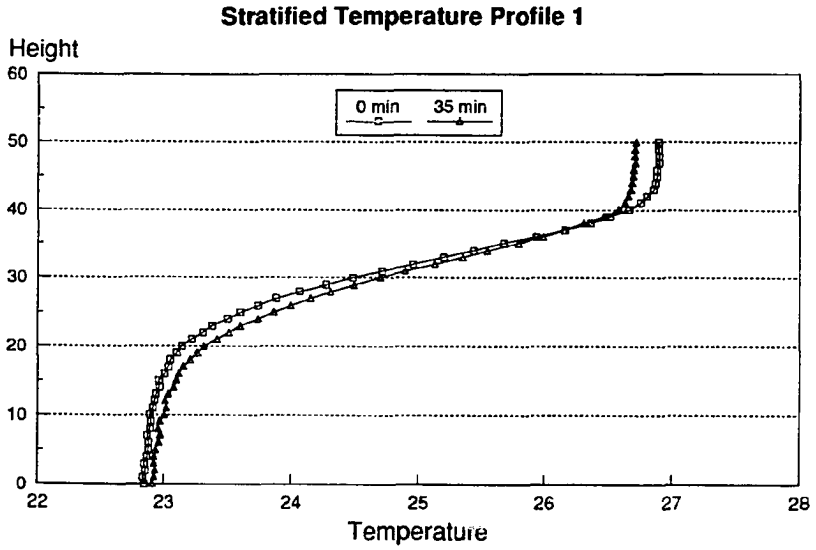

Figure 4-14 Stratified Temperature Profile for Vertical Surface
Corresponding heat transfer data below.

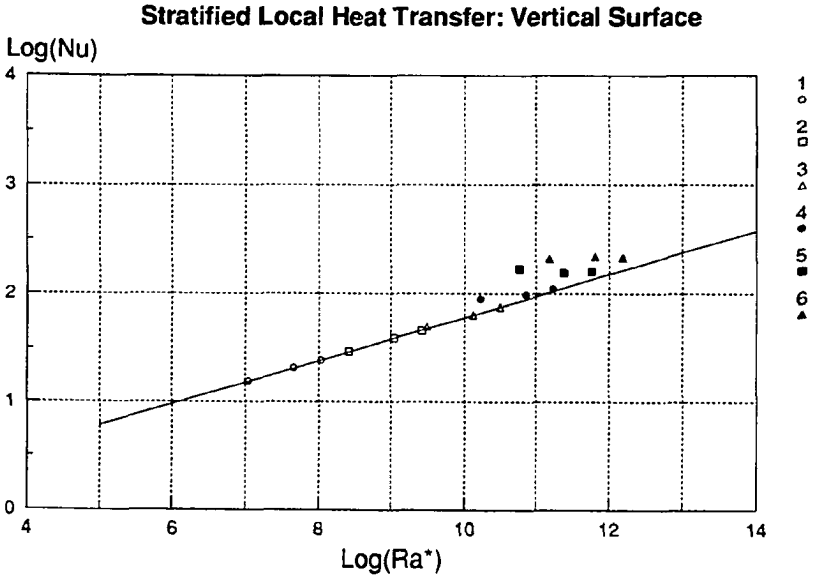

Figure 4-15 Heat Transfer Results - Vertical Surface, Stratified Fluid, Laminar Flow Regime
Uniform flux surface (twenty inch length). Plot of local Nusselt number vs. modified local Rayleigh number (Ra_x^*). Locations of sensors as follows: x_1= 3.02 cm, x_2= 14.45 cm, x_3= 22.07 cm, x_4= 29.69 cm, x_5= 37.31 cm, x_6= 44.93 cm. Line on plot: $Nu_x=0.60(Gr_x^*Pr)^{0.200}$

effects are very weak and are only evident for the lowest of the three heat fluxes measured. The surface to bulk ΔT's for the three heat fluxes were approximately 1 °C, 3 °C, and 6 °C. Since the ΔT is higher at greater heat fluxes, the influence of cold fluid coming up is proportionately lowered. Thus, the lowest flux values show the greatest deviations from the uniform temperature results. This result was repeated for the sensors in the uppermost regions as well.

Several other sets of data were taken for vertical surfaces with stratified ambient temperature profiles but yielded similar results to those described above and are not reported here. The combination of factors mentioned in the previous paragraph produces a complex picture for heat transfer and surface temperature profiles which can generally be explained qualitatively but proved difficult to describe quantitatively. Theoretical predictions are available for stratified fluids but these solutions are based on similarity solution techniques and comparison to the experimental data proved to be difficult due to the extremely limited conditions under which self similar profile would be expected. In any case, a detailed investigation of stratified heat transfer coefficients for either vertical or inclined surfaces was outside of the scope of this dissertation.

The situation of interest for modeling of atmospheric convection in slope flows would be that of an inclined surface with a completely turbulent boundary layer flow. The final data set presented here is for a 45° inclined surface and a stratified temperature profile which was intended to be linear. The heat fluxes measured extended well into the turbulent region in order to specifically explore the heat transfer behavior under turbulent conditions. Figure 4-16 shows the ambient temperature profiles for which this data was obtained. As can be seen, there are deviations from linearity, particularly near the bottom of the plate, but overall the temperature profile is quite close to linear with a temperature gradient of ~0.5 °C/cm. Temperature profiles were taken periodically over the course of making the heat transfer measurements to check for variation due to heating of the tank fluid. The plate extended from depth 0 to about 36.5 cm. It can be seen that variations of the temperature profile were minimal in this region of the tank although the upper layers showed a fair amount of change.

The heat transfer data for this case is shown in Figure 4-17. There is little ambiguity in the results. The heat transfer coefficients in the turbulent regime were hardly influenced by the presence of a global stratification of the bulk fluid. Note that the magnitude of the temperature gradient was in fact much greater in this case than for the previously shown laminar flow case.

The explanation for this behavior is that for turbulent flow the motion of the fluid is largely that of a mixing layer which also has an average direction of motion along the surface of the plate. As a result, upstream conditions become much less important and heat transfer is largely governed by local conditions for the

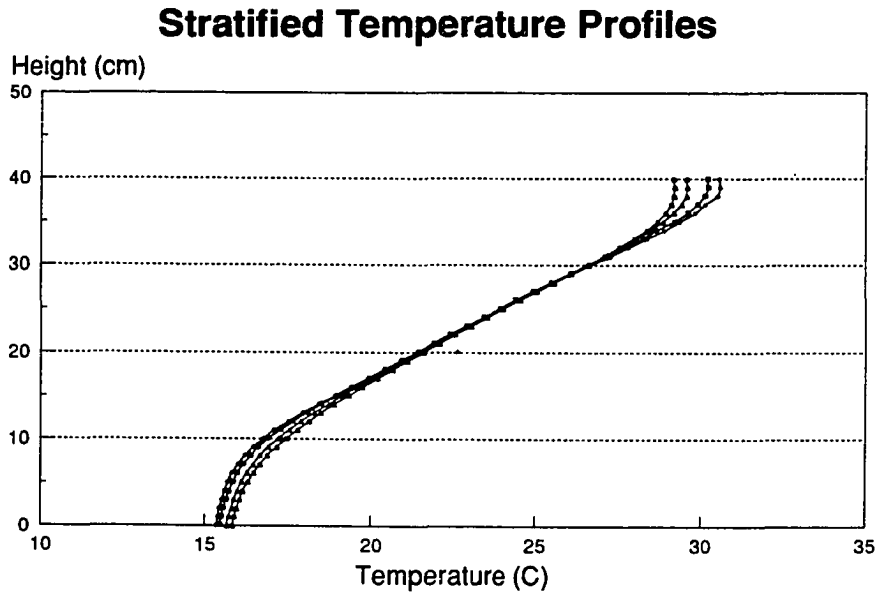

Figure 4-16 Stratified Temperature Profiles for Turbulent Flow

Corresponding heat transfer data below.

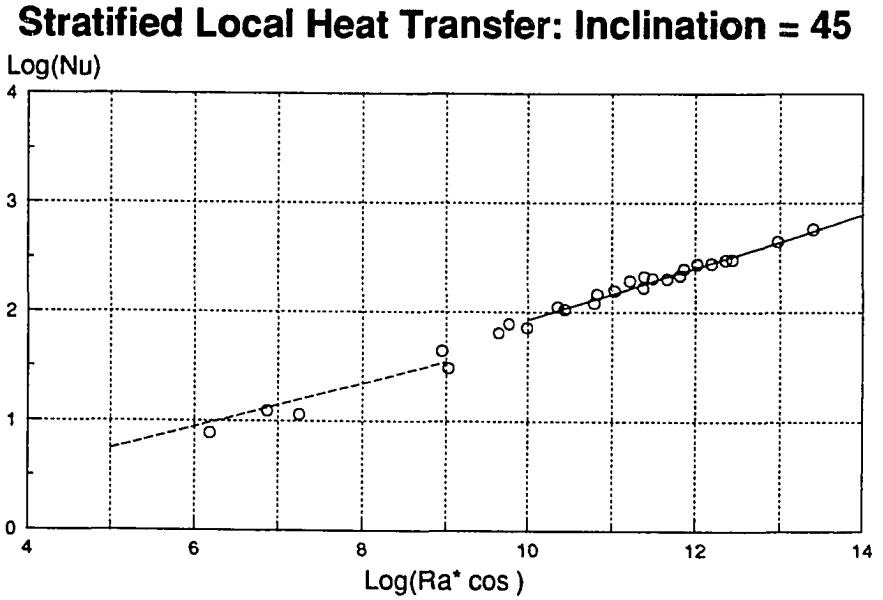

Figure 4-17 Heat Transfer Results - 45° Surface, Stratified Fluid, Laminar and Turbulent Flow Regimes

Inclined uniform flux surface (twenty inch length). Stratified bulk fluid. Plot of local Nusselt number vs. modified local Rayleigh number ($Ra_x^*\cos\theta$). Lines on plot:

Dashed Line: $Nu_x = 0.55(Gr_x^*\cos\theta Pr)^{0.200}$

Solid Line: $Nu_x = 0.31(Gr_x^*Pr)^{0.240} = 0.337(Gr_x^*\cos\theta Pr)^{0.240}$

turbulent flow. This result is not surprising in light of the observed behavior for uniform bulk temperatures. For uniform bulk temperatures the turbulent heat transfer correlated reasonably well to a 0.25 exponent, which indicates a heat transfer coefficient which is independent of distance x. In addition, the uniform bulk temperature results showed that turbulent heat transfer was best correlated by a Rayleigh number which used the vertical component of gravity, regardless of the inclination of the surface, indicating a flow which is predominantly in the vertical plane and thus of a local nature and decoupled from upstream effects.

This result is a significant one since it indicates that the turbulent heat transfer coefficient for uniform flux surfaces can be calculated without regard to stratification of the bulk fluid. Implications for modeling of these flows are also significant since this behavior means that the ΔT from surface to bulk remains constant as well, regardless of stratification of the fluid. Additional measurements would be useful before these conclusions are applied to other stratification temperature profiles and inclinations. However, for conditions close to those in the case shown, it would appear that a considerable simplification can be made in modelling of the flow.

4.4 Summary of Results

Heat transfer experiments for plates at various inclinations resulted in the following correlation for laminar flow:

$$Nu_x = 0.55(Ra_x^* \cos\theta)^{0.200} \tag{4-52}$$

This correlation is identical to that recommended by Vliet and Ross (1975), who fit data from several downward facing inclinations and one upward facing inclination. The present measurements demonstrated the validity of this correlation for a wide range of upward facing inclinations, with much less scatter than typical for these types of experiments. The data further show that the linear laminar regime extends down to $Ra_x^*=5.4\times10^4$, two orders of magnitude lower than previously measured for uniform flux surfaces.

For turbulent flow, the data was well fit by either

$$Nu_x = 0.31(Ra_x^*)^{0.240} \tag{4-53}$$

or,

$$Nu_x = 0.235(Ra_x^*)^{0.250} \tag{4-54}$$

The turbulent data was clearly best fit by using Ra_x^* rather than $Ra_x^*\cos\theta$ for the inclined data, confirming one observation by Vliet (1969). The correlation obtained was close to that of Vliet (1969) but fell 10-20 percent above that of Vliet and Ross (1975) which was obtained using air.

With a stratified bulk fluid, the heat transfer coefficient was generally increased for laminar flows. Heat transfer coefficients were strongly influenced by upstream conditions and by the magnitude of the heat flux for the laminar flow regime. These factors complicated the analysis of data obtained in the laminar regime and made it difficult to generalize the observed results.

In the turbulent flow regime, heat transfer measurements showed that local heat transfer coefficients were not influenced by stratification of the bulk fluid. This result is likely to be of general interest in light of the fact that stratified conditions tend to develop naturally in many situations. The result also implies that the local temperature difference $(T_{wall}|_x - T_{bulk}|_x)$ will remain roughly constant regardless of whether the bulk temperature profile is uniform or stably stratified. This may provide a physical basis for making significant simplifications in the mathematical modeling of turbulent upslope flows in the atmosphere and in the laboratory.

Chapter 5

Laboratory Modeling of Atmospheric Upslope Flows

In this chapter are described measurements of velocity and temperature profiles for laboratory free convection flows which were designed to simulate upslope flows which occur in the atmosphere. Particularly, attention was focused on the effect a capping stable layer has on these profiles.

In the following sections, we begin initially by briefly discussing the specification of appropriate ambient conditions for simulating the turbulent flow which occurs in the atmospheric slope flow.

In light of the tracer experiment results (Chapter 2), it was expected that varying conditions of ambient fluid stability would result in significant variations in the laboratory slope flow. Thus, a primary goal of these measurements was to determine if recirculating flows could be observed in the laboratory flow under conditions expected to be approximately similar to typical atmospheric flow conditions. To this end, dye studies were conducted to permit visualization of the flow and transport patterns.

The nature of any observed recirculation would be of great interest since some opinions had been expressed that a flow outward from the boundary layer would not result from the experiments. Reviewers evaluating a 1984 NSF research initiation proposal to the Division of Mechanical Engineering and Applied Mechanics, Heat Transfer Program suggested that the experiment would either give 'Benard' cells or that the return flow would follow the terrain as shown in Figure 5-1 (reproduced from the proposal review form).

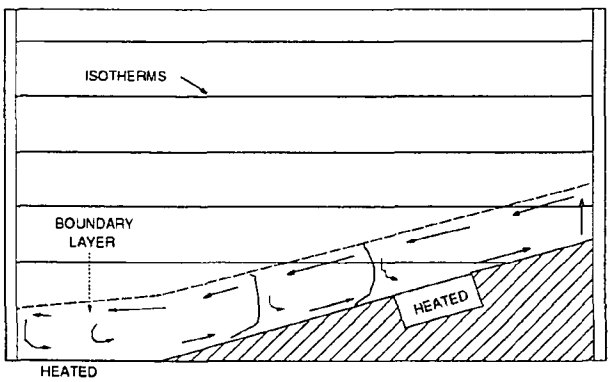

Figure 5-1 Possible Alternative Mode For Return Flow

These studies are discussed in a section describing the qualitative structure of the convective flow along surfaces at various inclinations.

Subsequent sections describe the results of quantitative measurements for velocity and temperature profiles made under conditions appropriate for simulating atmospheric flows. Profile measurements were made for along-slope, horizontal, and vertical components of velocity. The intensity of turbulent fluctuations for the horizontal and vertical components of the velocity are also discussed. Quantitative and qualitative comparisons are made between the phenomena and trends observed and those predicted by the Prandtl model for upslope flows.

5.1 Conditions for Similarity of Laboratory and Atmospheric Flows

In constructing a physical model of an atmospheric flow the conditions governing the flow must be selected carefully in order to best represent the larger scale observed atmospheric conditions.

If L and S are the representative length and velocity scale for the circulation then a nondimensional version of the conservation of momentum can be written, following Pielke (1988);

$$\frac{\partial \overline{u}_i}{\partial t} = -\overline{u}_j \frac{\partial \overline{u}_i}{\partial \hat{x}_j} - \left[\frac{e_{u_i}^2}{S^2}\right] \frac{\partial}{\partial \hat{x}_j} \overline{u''_j u''_i} - \left[\frac{R\delta\theta}{S^2}\right] \hat{\theta}_0 \frac{\partial \hat{\pi}'}{\partial \hat{x}_i}$$
$$- \left[\frac{R\delta\theta}{S^2}\right] \hat{\theta}_0 \left\{ \frac{\partial \hat{\pi}_0}{\partial \hat{x}} \delta_{i1} + \frac{\partial \hat{\pi}_0}{\partial \hat{y}} \delta_{i2} \right\} + \left[\frac{gL\delta\theta}{\theta_0 S^2}\right] \hat{\theta}' \delta_{i3} \qquad (5\text{-}1)$$
$$- \left[\frac{\Omega L}{S}\right] 2\varepsilon_{ijk} \hat{\Omega}_j \overline{u}_k - \left[\frac{\nu}{LS}\right] \frac{\partial^2 \overline{u}_i}{\partial \hat{x}_j \partial \hat{x}_j}$$

To use a physical model to represent the conservation of motion in the atmosphere it is essential that

1. the bracketed terms be equal in the model and in the atmosphere, or
2. the bracketed terms that are not equal must be of much smaller magnitude than the other bracketed terms in the equation.

When these conditions are met the model is said to have dynamic similarity to the atmosphere. Some dimensionless quantities represented by the bracketed terms are defined as follows

$$\frac{\Omega L}{S} = \frac{1}{Ro} \qquad (5\text{-}2)$$

$$\frac{\nu}{LS} = \frac{1}{Re} \qquad (5\text{-}3)$$

$$\frac{gL\delta\theta/\theta_0}{S^2} = Ri_b \qquad (5\text{-}4)$$

where Ro is the Rossby number, Re is the Reynolds number and Ri_b is the bulk Richardson number. $\delta\theta$ is the potential temperature perturbation and is of the same order as the temperature perturbation δT.

To maintain dynamic similarity is can therefore be inferred that

1. the ratio of subgrid scale kinetic energy to the grid volume kinetic energy must be kept constant;

2. reducing the length scale L in the simulated model requires that
   •the rotation rate Ω be increased, the lab scale wind speed S be decreased or both,
   •the viscosity ν be decreased, S be increased or both,
   •$\delta\theta$ (the magnitude of the temperature perturbation be increased, S be decreased or both;
3. an increase in $\delta\theta$ for the pressure gradient term dictates that S must also be increased.

It is impossible to satisfy all of these requirements simultaneously on models constructed on a laboratory scale. For example, if a 10 km high mountain ridge is represented by a 1 m plate, the scale reduction is 10^4. If air is used for the model, the speed S in the model would have to be 10^4 m/s to match a typical atmospheric flow of 1 m/s. For water models, $\nu_{H2O} \sim 0.1\nu_{air}$, so that the model flow speed would have to be 10^3 m/s. Similarly, the model would have to be rotated at a speed 10,000 times faster than the earth or the speed would have to be reduced by a factor of 10^{-4} to maintain Rossby number similarity. The requisite reduction in speed unfortunately, contradicts the increase necessary for matching the Reynolds number.

The only way that laboratory modeling of the atmosphere can be valid, therefore, is if the results are insensitive to large variations within specified ranges for some of the quantities. Cermak (1975), for example, suggests that for large enough values of the Reynolds number, the variations of the resulting flow become independent of Re in simulations of the atmospheric boundary layer. Clearly since it is impossible to obtain exact dynamic similarity between a model and large scale atmospheric phenomena the key becomes evaluating which of the dimensionless terms in the equation must be included for modeling purposes.

A conservation relation for heat results in an equation similar to those expressed above for momentum. Following Pielke (1988) the equation of energy is written

$$\frac{\partial \bar{\theta}}{\partial t} = -\bar{u}_j \frac{\partial \bar{\theta}}{\partial \hat{x}_j} - \left[\frac{e_\theta e_u}{\delta\theta S}\right] \frac{\partial}{\partial \hat{x}_j} \overline{u''_j \theta''} + \left[\frac{k_\theta}{\rho_0 C_p \nu}\right]\left[\frac{\nu}{LS}\right] \frac{\partial^2 \bar{\theta}}{\partial \hat{x}^2} + \bar{S}_\theta \qquad (5\text{-}5)$$

where the ratio $k_\theta/(\rho_0 c_p \nu) = Pr^{-1}$ is the Prandtl number (~1 for air, ~7 for water).

In order to obtain thermic similarity, the Reynolds number must be very large and the partitioning between subgrid scale and resolvable heat fluxes must be approximately equal. $\hat{S}_\theta$ is a dimensionless source-sink term which encompasses a wide range of complex phenomena such as radiative flux divergence, phase changes of water etc. These sorts of terms are typically complex functions of the dependent variables and extremely difficult to evaluate using scale analysis. In practice, most physical modeling excludes this term from the analysis and makes no effort to simulate these behaviors.

A similar equation can be written for conservation of mass on various species such as water vapor, aerosols, and gaseous pollutants. However, since the sources and sinks for these variables are also difficult to evaluate through scale analysis, physical modeling has only addressed the movement of nonreactive, conservative pollutants.

The final relation which must be satisfied is the conservation of mass. Assuming changes in density are relatively small, variations in the specific volume can be ignored for the purpose of this equation and the scaled equation written

$$\frac{\partial u}{\partial x}+\frac{\partial v}{\partial y}+\frac{\partial w}{\partial z}=0 \tag{5-6}$$

so that

$$w\sim\frac{L_z}{L_x}u \quad \text{and} \quad w\sim\frac{L_z}{L_y}v \tag{5-7}$$

This requirement is satisfied if the horizontal to vertical representation of the terrain and ground surface features are not exaggerated so that there is geometric similarity. By keeping the ratio of the horizontal to vertical scales of the circulation constant between the model and the atmosphere, kinematic similarity is therefore obtained.

Additional considerations for modeling include requirements of boundary similarity so that incoming velocity and temperature profiles be scaled properly and surface condition such as surface roughness and bottom temperature be scaled so as to produce similarity in the regions of the model closest to the surface.

The work of Willis and Deardorff has demonstrated that the boundary layer scale turbulence of the convective planetary boundary layer can be realistically simulated by laboratory scale water models. Modeling simplifications occur when it is noted that the convective turbulence has too short a time scale to be affected by the earth's rotation and is little influenced by wind shear which is mainly confined to small heights near the surface. The mean wind is then considered as essentially a mechanism for translating downstream the mixed layer turbulence.

The mechanical generation of turbulence is indeed often confined to a small bottom region of the well mixed layer, so that in many cases, the atmospheric boundary layer has been found to be in a state of free convection for the majority of its depth. Laboratory and field measurements have further established that the properties of the turbulence in the planetary boundary layer are often essentially independent of the friction velocity and of the Coriolis parameter.

The Richardson number expresses the ratio of the buoyant production of turbulent energy to that produced by velocity shear. Since turbulence is overwhelmingly due to buoyant production in a free convection flow, the Richardson number similarity condition will be matched as long as both the atmosphere and the model remain in a state of free convection.

The buoyant production of turbulence equals production due to velocity shear at a height equal to $-L_{MO}$ (the Monin-Obukhov length scale). At heights very much greater than this, the production of turbulence via velocity shear becomes less important. In the atmosphere, $-L_{MO}$ varies from about 1 m under the most unstable conditions to about 200 m under the most stable conditions. Since the atmospheric boundary layer extends to 500 or 1000 m or more, this indicates that buoyancy effects predominate over a large fraction of this layer.

In the specific case of turbulent natural convection over a heated sloping surface local conditions are highly unstable so that the value of $-L_{MO}$ can be expected to be very small (of order 1 m). Typically, the depth of a slope flow layer ranges from 100 to 200 meters so that buoyancy effects should predominate throughout most of this depth.

The Reynolds number based upon the vertical velocity scale and the depth of the mixed layer is of the same order of magnitude (5×10^3) as in the experiments of Willis and Deardorff (1974) who have demonstrated similarity to the free convection layer of the atmosphere. Although the Reynolds number defined in the same manner is much larger in the atmosphere (10^8 - 10^9), the structure of the turbulence is evidently independent of Reynolds number over this range.

Since the free convective flow is not driven by large pressure gradients, we neglect matching of these parameters. Geometric similarity is clearly a function of the particular slope of interest but since the objective of these experiments was not to produce an exact model of a particular mountain ridge but rather to simulate the general characteristics of slope flow, the exact angle selected was not an important factor.

It remains to address the question of partitioning of the transport of heat and momentum between the various scales. Lacking the detailed measurements of turbulence scales and energy spectra for either the atmospheric flow or the laboratory flow it was necessary to take a position that if conditions satisfied the guidelines of Willis and Deardorff for atmospheric free convection modeling of horizontal surfaces, the laboratory slope flow would satisfy this requirement.

Foremost is the condition that the flow be fully turbulent. Willis and Deardorff (1974) report Rayleigh numbers criteria for turbulence in their horizontal model. For the slope flow, similar criteria can be established for various inclinations based on the heat transfer results reported in the previous chapter.

Willis and Deardorff have indicated for a horizontal surface that production of turbulence by buoyancy effects will dominate as long as the horizontal velocity scale is the same order of magnitude as the vertical velocity scale. Deardorff and Willis (1975) give as a guideline the requirement $U < 6w^*$ for penetrative convection which corresponds to a ratio of layer depth H to $-L_{MO}$ of approximately 10 or greater. Typical values for these quantities over flat land on a sunny day are $w^* = 1\text{-}2.5$ m/sec and $U = 2\text{-}10$ m/sec. Thus neglecting shear generated turbulence in the kinetic energy budget appears valid for the upslope flow layer in

which along slope velocities rarely exceed 2-4m/sec. It is apparent that if these conditions are not satisfied in the atmosphere there will generally not be a recognizable slope flow (because the large synoptic scale meteorology would obliterate smaller terrain specific patterns) so the limits of validity for the model apparently correspond closely to the atmospheric conditions which permit slope flows to develop. Note that the theory breaks down at large angles of inclination in that eventually, as the angle of inclination approaches vertical, shear generated turbulence can no longer be neglected.

The selection of the most appropriate values for parameters such as the heat flux, temperature gradient and layer depth for the laboratory model must now be addressed. Having established Rayleigh number criteria for the transition to turbulent flow, ambient conditions and heating rates were selected to match those of Willis and Deardorff for which similarity of the turbulent transport had been demonstrated. Typical heat fluxes used in the experiments of Willis and Deardorff fall between 10,000 and 20,000 W/m^2. Temperature gradients used in the ambient fluid were between 0.2 and 1.1 °C/m. The average surface-to-mixed-layer temperature difference was 12°C. Similar values were used in the experiments described herein.

5.2 Qualitative Structure of Laboratory Upslope Flows

Having posited a set of reasonable parameters for the laboratory simulation investigation we proceed to a description of the ensuing qualitative studies of transport patterns for various geometries and ambient fluid conditions.

5.2.1 Development of Experimental Techniques and Early Results

Flow visualization experiments were used throughout this investigation to gain a better understanding of the physical processes taking place in the flows being investigated. Dye injection techniques were used most often, although some interferometric measurements were made as well. Although interferometric techniques have been widely applied to natural convection problems for both qualitative and quantitative purposes, they are best suited for discerning the flow in unfluctuating laminar boundary layers and for observing the fine structure of disturbances in the transition from laminar to turbulent flow.

For the turbulent recirculating flows which were of foremost interest in this study, dye studies offer the advantages of clarity and ease of use. Much of the utility of interferometric studies is lost when observing turbulent flow layers since the complex structure of the flow is unsteady and not well manifested. In addition, significant effort is required to set up and align a system of mirrors large enough to observe the flows generated here. Finally, interferometric techniques rely on temperature differences to allow the flow profiles to be visualized and may not be useful for observing the horizontally extruded boundary layer shown in the following sections.

Since nothing of significance was learned from the sporadic interferometric studies we describe only the dye studies in the sections to follow.

5.2.1.1 Preliminary Dye Studies Using Bottom Heated Tank

The first dye measurements were made using red dye (food coloring) injected by hand using a syringe and a copper tube. These experiments were initially undertaken using the bottom heated tank described in Chapter 3. The bottom heated tank had been built in the course of developing equipment for a laboratory investigation of transport between two stratified horizontal layers flowing in opposite directions. As a result, the equipment was not very well suited for the experiments and only very sketchy observations could be made. In order to obtain an inclination of the heated bottom surface the entire containment tank had to be tilted. For obvious reasons, angles near vertical were problematic. Furthermore, the endwalls forced development of large scale circulations which obscured the appearance of any sort of stability driven recirculation in the global fluid.

The flow was definitely influenced by the development of roll cells and other large scale circulations in the tank. After taking this into account, these early results were nevertheless deemed to be encouraging inasmuch as the boundary layer growth and elevated negative velocities agreed with observed characteristics of atmospheric slope flows. Results of the experiments were summarized and recorded as sketches in laboratory notebooks. A typical example run during which boundary layer growth and negative velocities (but no separating cusps) were observed is reproduced in Figure 5-2.

The results from these early experiments can be summarized as follows.

1) The slope flow layer depth grew along the direction of flow, indicating the presence of entrainment into the layer.

2) Elevated negative velocities were observed when the ambient fluid was stably stratified. The negative flows were observed just above the main upward (along slope) flow layer. The direction of flow was roughly parallel to the heated surface and appeared to be distinct from larger scale roll cells which also developed in both stable and unstable ambient conditions. This flow can be likened to the alternative recirculation mode shown previously in Figure 5-1.

3) Some cusps of dyed fluid were observed to separate from the main layer flow at the juncture between a hot layer overlying a cold layer of ambient fluid. These separations appeared only for the strongest temperature gradients.

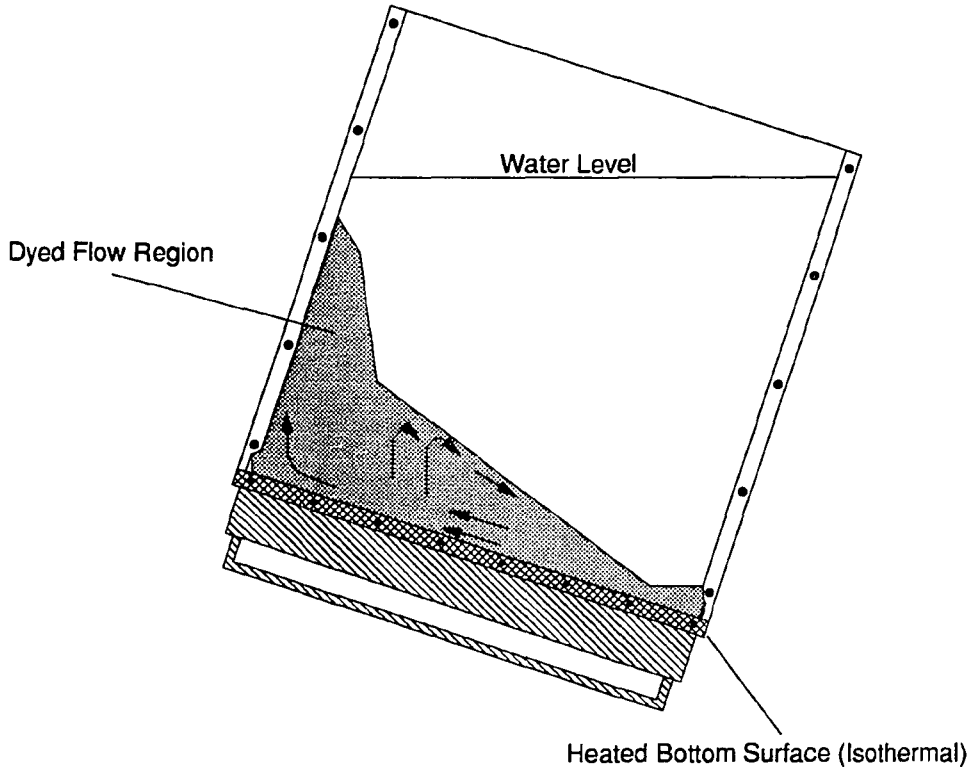

Figure 5-2 Sketch of Typical Dye Study (Bottom Heated Tank)

5.2.1.2 Preliminary Dye Studies Using Uniform Flux Surface

A second set of flow visualization experiments were conducted after obtaining the Rapid Electric DC power supply and constructing a uniform flux surface. These experiments benefited from having a rapidly heated surface and a surrounding ambient fluid of greater extent relative to the heated layer. Red and blue food coloring dyes were used, simultaneously in some cases. Injection was accomplished using a hand operated syringe connected to a length of copper tubing. Power dissipated was about 750 watts for a heat flux of ~16000 W/m^2. Some pertinent results from experiments conducted with a 45° inclined surface follow.

1) Experiments showed that lateral entrainment was significant for an isolated heated surface with no sidewalls. With sidewalls, little lateral variation of streamlines and transport was observed across the surface except for a narrow region within 0.25-0.50 inches of the sidewalls.

2) A horizontal separation away from the surface was observed in the presence of a sharply stable gradient. These flow separations were found to occur at the base of a stable temperature inversion layer.

3) Boundary layer growth by entrainment appeared to be significant over the 30 cm length of the heated plate with uniform temperature fluid.

The experiments described above were hampered and the results obscured by the uneven manual injection of dye. Although an unmistakable flow separation was again observed visually, the results were far from clean and the photographic record of the experiments was somewhat muddled. Any inferences regarding the genesis of this separation were thus subject to some skepticism.

5.2.2 Results for Flow Visualization Experiments

In light of the somewhat ambiguous results obtained and described above, a final, additional, set of experiments was conducted after obtaining the use of a syringe pump which permitted a steadily metered injection of dye into the boundary layer at the leading edge of the plate. Dye was injected through a small diameter Tygon tube fitted to a hypodermic needle on the syringe. The Tygon tube was attached to a temperature probe rods which tapered to a 1 mm diameter aluminum rod at its tip. The Tygon tube extended ~0.5 cm beyond the tip of the aluminum probe to avoid contacting the heated foil with any metal pieces. Experiments were conducted using either food coloring dyes or water colored with small amounts of erioglaucine blue dye (Aldrich Chem Co.). The erioglaucine provided much more intense coloration at very low dye injection rates, allowing sufficient amounts of dye to be carefully metered into the leading edge of the boundary layer without significantly disrupting the boundary layer flow.

5.2.2.1 Vertical Plate Flow

Beginning with the plate at a 90° inclination (vertical) we first show photographs of the laminar and turbulent boundary layer flows with uniform temperature ambient fluid (Figure 5-3). These layers are unexceptional examples of typical boundary layer flows. As can be seen, for the low heat flux case, the laminar boundary layer is very thin and steady so that the dyed fluid runs straight up the plate in a narrow ribbon. The dyed layer is so thin (<1 mm) that the flow must be viewed from a slight angle to be visible. It can be seen that the injected dye has negative buoyancy at the point of injection so that some sinking of excess dye occurs. For the high heat flux case, the boundary layer is much thicker and is easily visible in a side on photograph. Growth along the length of the heated surface due to entrainment is evident. Fully developed turbulence is not attained until the region near the trailing edge.

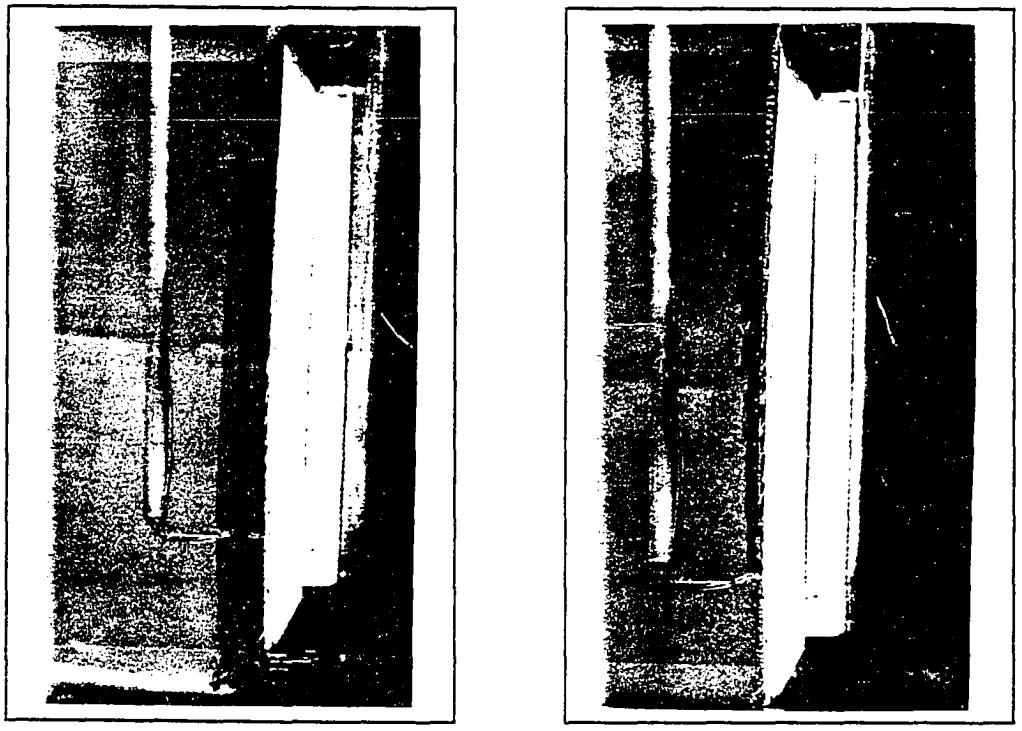

(A) (B)

Figure 5-3 Vertical Plate Dye Studies - Uniform Ambient Temperature

(A) Dye Study Conditions: Laminar flow. For a vertical plate, the transition range begins at $Ra^*_x = 10^{13}$. For this experiment, the heat flux was ~162 W/m^2. Using a film temperature of 25°C, the estimated $Ra^*_L = 4.2\times10^{10}$. [Photo 3-1]

(B) Dye Study Conditions: Transition/Turbulent flow. For a vertical plate, the transition range begins at $Ra^*_x = 10^{13}$. For this experiment, the heat flux was ~65000 W/m^2. Using a film temperature of 40°C, the estimated $Ra^*_L = 3\times10^{13}$. The transition range begins at x=22.5 cm where $Ra^*_x = 1.0\times10^{13}$.[Photo 3-6]

In the next set of photographs we show the effect of adding a strong ambient stability gradient (~1°C/cm) to the vertical plate flow. In the case of low heat flux (laminar flow), a significant departure occurred from the previous behavior. It can be seen that nearly all of the dye flows upward along the plate and then is rejected at the beginning of the stable layer. Only a thin thread of dyed material issues upward at the trailing edge. In a photograph taken several minutes after initiating the experiment, a complex structure of sinking fingers of negatively buoyant dye bulging outward from the plate and then down into the ambient fluid is visible (see Figure 5-4).

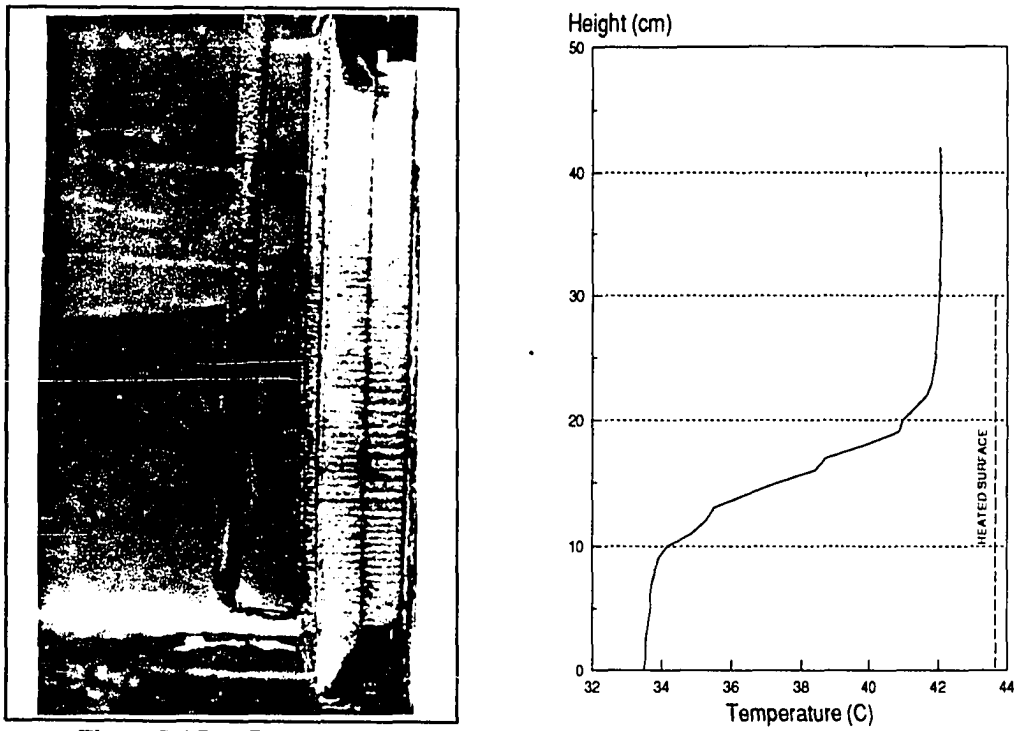

Figure 5-4 Dye Studies: Vertical Plate, Stratified Ambient Fluid, Laminar Flow
Dye Study Conditions: Laminar flow. For a vertical plate, the transition range begins at $Ra^*_x = 10^{13}$. For this experiment, the heat flux was ~1000 W/m^2. Using a film temperature of ~ 25°C, the estimated $Ra^*_L = 2.6 \times 10^{11}$. [Photo 7-10]
Ambient Fluid Temperature Profile: Stable. Maximum gradient = 1.2 °C/cm at 17.5 cm. Overall $\Delta T = 8.6$°C. Plate orientation and position corresponds to dotted segment on temperature profile plot.

For the high heat flux case, the influence of the stable ambient fluid was again visible but flow bifurcation was much weaker. In Figure 5-5, the upper layers above the plate have obviously received by far the greatest part of the dyed flow while only a small percentage has been split off from the boundary layer flow. The flow regime must be regarded as a transition flow (neither laminar nor fully turbulent) since only the last 5 cm or so of the plate reached fully turbulent flow by Rayleigh number transition criteria. It should be noted that this transition criteria is determined from the change in heat transfer characteristics at the surface for the different regimes and can be expected to be a conservative estimate of when the flow has become turbulent. The early stages of transitional flow are unlikely to show marked immediate influence on the local heat transfer coefficient.

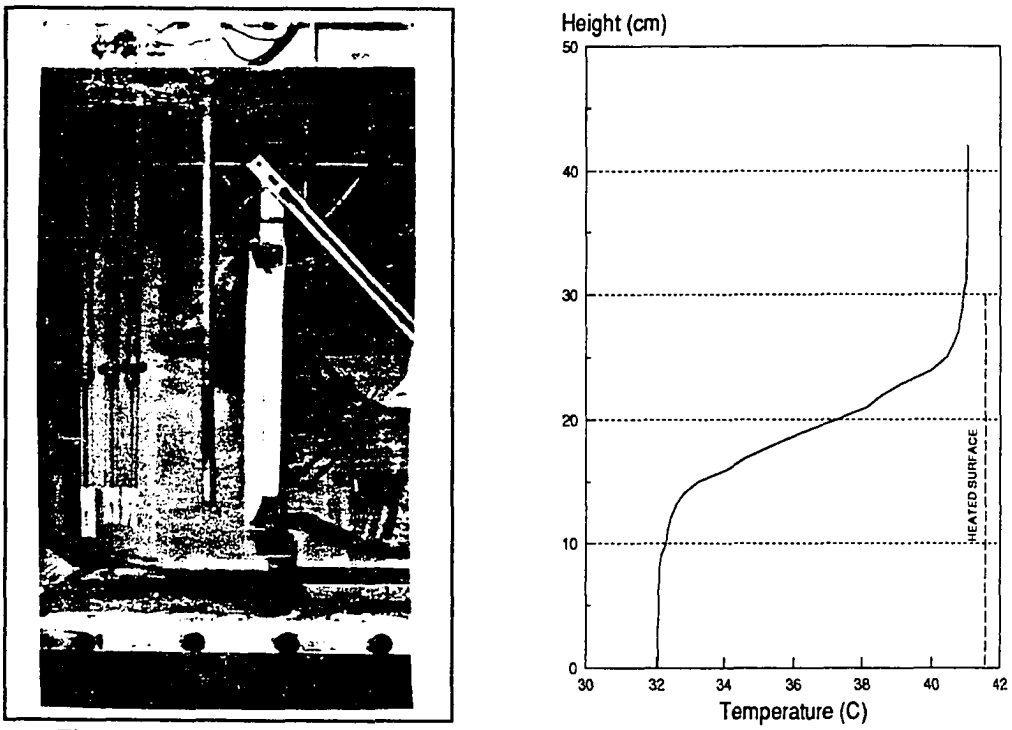

Figure 5-5 Dye Studies: Vertical Plate, Stratified Ambient Fluid, Transitional Flow
Dye Study Conditions: Transition/Turbulent flow. For a vertical plate, the transition range begins at $Ra^*_x = 10^{13}$. For this experiment, the heat flux was ~36000 W/m^2. Using a film temperature of 40°C, the estimated $Ra^*_L = 1.8\times10^{13}$. The transition range begins at x=26 cm where $Ra^*_x = 1.0\times10^{13}$. [Photo 7-16]
Ambient Fluid Temperature Profile: Stable. Maximum gradient = 1.0 °C/cm at 19.5 cm. Overall ΔT = 9°C. Plate orientation and position corresponds to dotted segment.

5.2.2.2 Inclined Plate Flow

Following the results above for vertical plate flow, similar experiments were conducted for various inclinations of the heated plate. Since transition to turbulence occurs more quickly, these results extend into the fully turbulent flow regime as desired.

5.2.2.2.1 Turbulent Boundary Layer Flow (Unstratified)

Figure 5-6 shows the normal boundary layer flow observed for a turbulent flow in a uniform temperature ambient fluid. The flow is not remarkable in any way but is included for comparison with the subsequent runs which were performed with a stratified fluid. It can be seen that the dye is traveling directly up along the heated surface and on into the upper layers of fluid above the plate. Boundary layer growth is also evident.

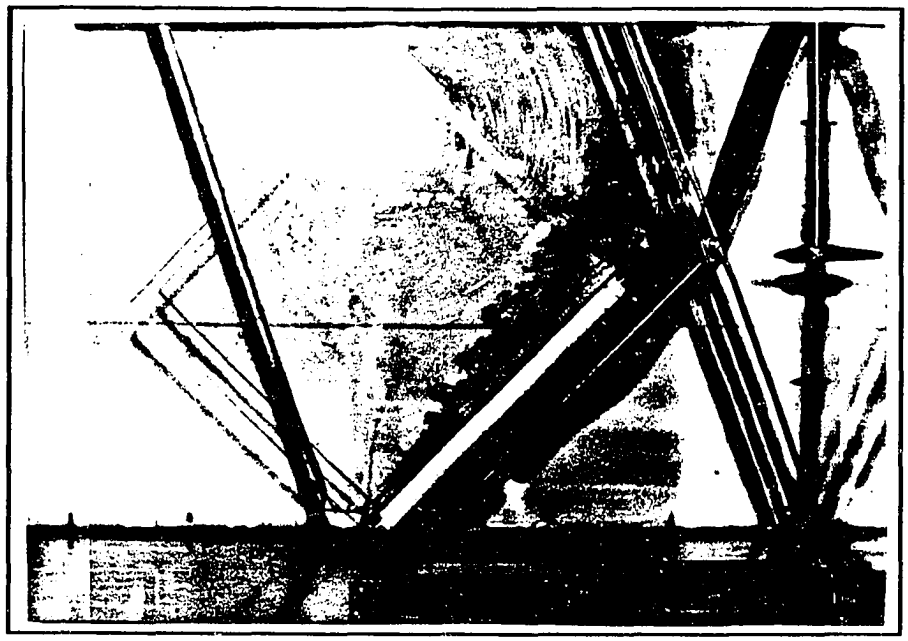

Figure 5-6 Dye Study: Inclined Plate, Uniform Temperature Ambient Fluid, Turbulent Flow
Dye Study Conditions: Turbulent flow. For a 45° inclined plate, the transition range is $Ra^*_x = 10^9 - 10^{10}$. For this experiment, the heat flux was ~36000 W/m^2. Using a film temperature of 40°C, the estimated $Ra^*_L = 1.2\times10^{13}$. The fully turbulent range starts from around x=5 cm where $Ra^*_x = 9.6\times10^9$. [Photo 9-10]
Ambient Fluid Temperature Profile: Uniform, no gradient.

5.2.2.2.2 Turbulent Flow Separation From Inclined Surface

In this section are presented a set of photographs which show the developing recirculation outward from a heated inclined plate subjected to a stable temperature gradient in the ambient fluid. The study was conducted under turbulent flow conditions identical to those for the preceding figure. The single difference in experimental conditions is the stable ambient fluid temperature profile. The temperature profiles are shown in Figure 5-7. Following the temperature profile are shown the time sequence photographs. These pictures show clearly the influence of a strongly stable temperature gradient. As can be seen, a horizontal flow outward from the heated surface develops and runs outward parallel to the isotherms in the fluid.

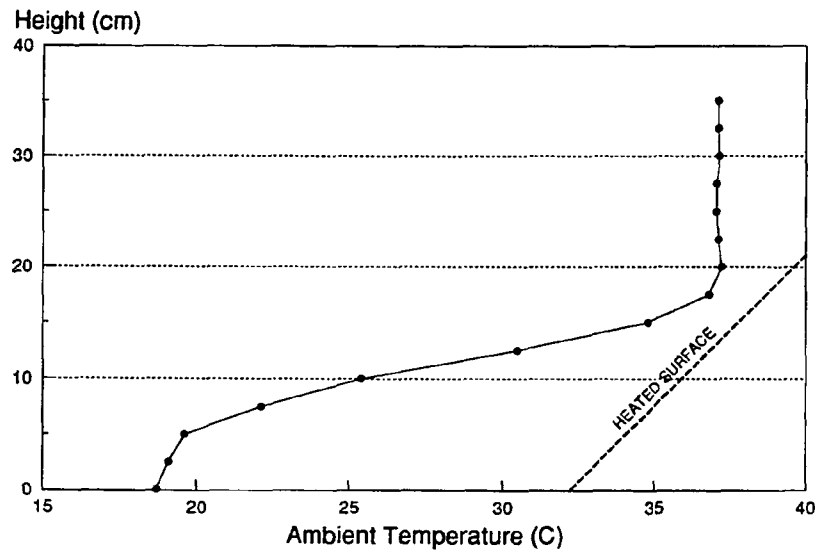

Figure 5-7 Ambient Fluid Temperature Profile For Time Sequence Dye Study
Ambient Fluid Temperature Profile: Stable. Maximum gradient = ~2°C/cm at 15 cm. Overall ΔT = 18.5°C. Plate orientation and position corresponds to dotted segment on plot.

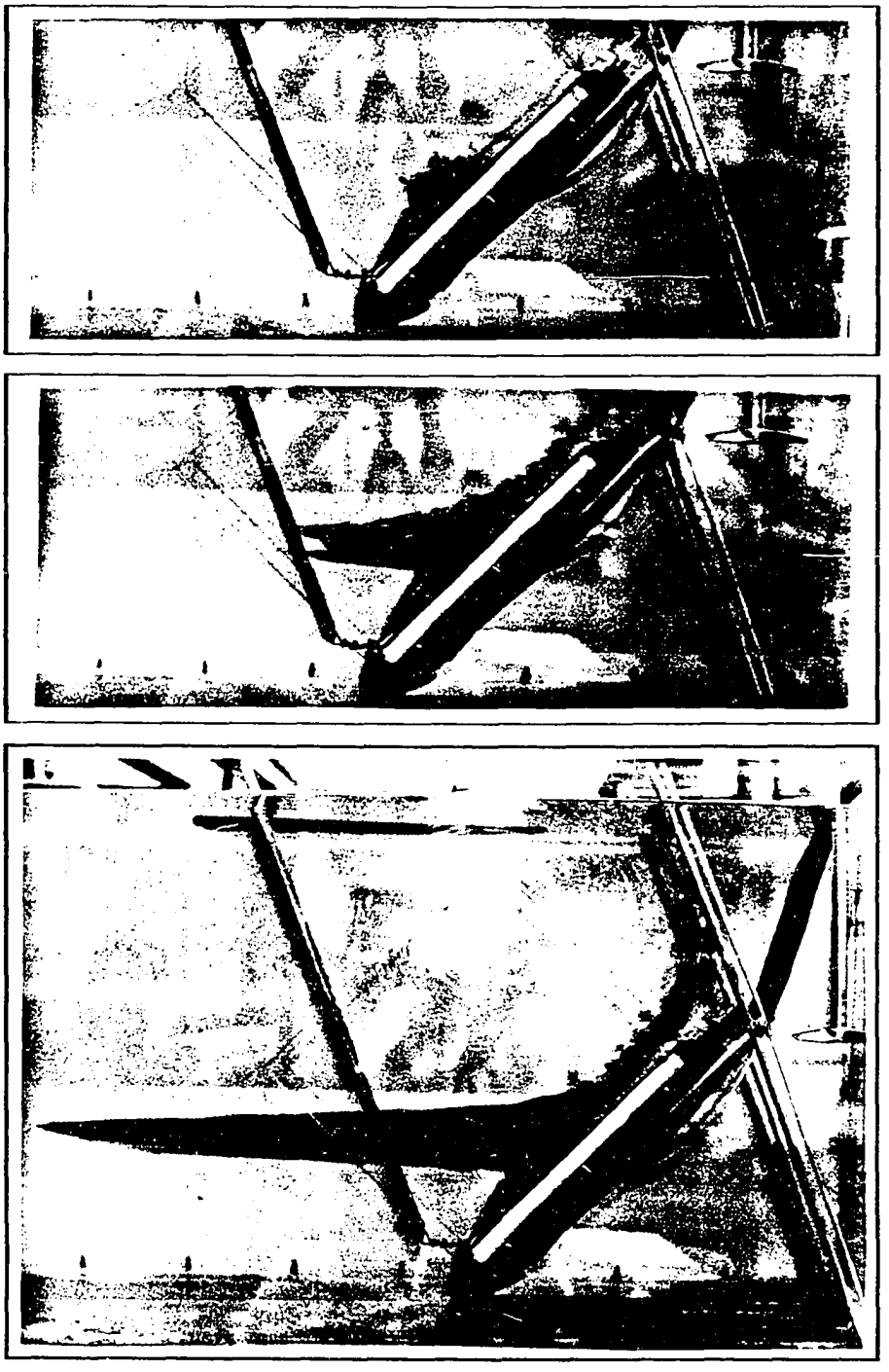

Figure 5-8 Dye Study: Time Sequence for Recirculation from Inclined Plate, Stable Ambient Fluid, Turbulent Flow

Dye Study Conditions: Turbulent flow. For a 45° inclined plate, the transition range is $Ra^*_x = 10^9 - 10^{10}$. For this experiment, the heat flux was ~36000 W/m^2. Using a film temperature of 40°C, the estimated $Ra^*_L = 1.2\times10^{13}$. The fully turbulent range starts from around x=5 cm where $Ra^*_x = 9.6\times10^9$. [Photos 11-4,5,7,10,11,12]
Ambient Fluid Temperature Profile: Stable, as shown in previous figure.

5.2.2.2.3 Dye Study With Concurrent Temperature Profile Measurements

A final dye study is shown in the figures following. Conditions for this study were fairly close to those in the preceding study. The initial ambient temperature profile is shown here on Figure 5-9. In addition, ambient fluid temperature profiles measured midway through the experiment and after completing the experiment are also shown on this figure. Comparing the initial temperature profile to that in the previous section, it is seen that the positions of the stable layers are nearly identical. However, the temperature gradient is only about half as strong in the case of this experiment.

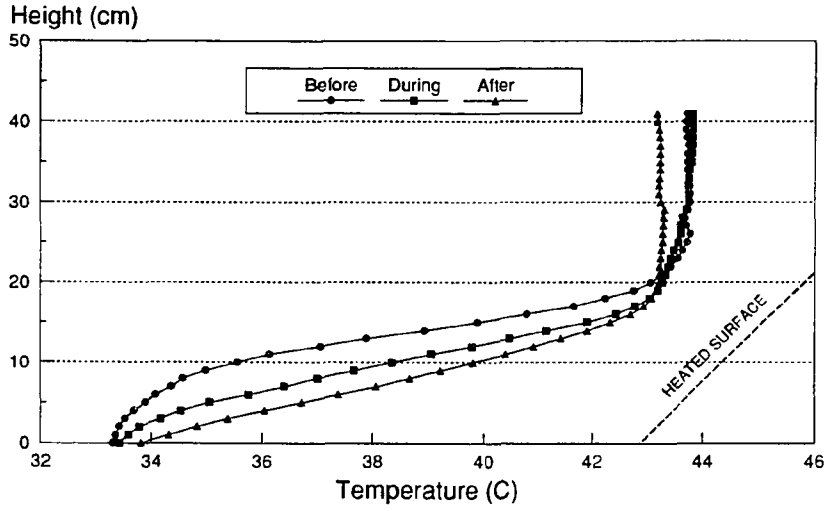

Figure 5-9 Ambient Fluid Temperature Profiles
Ambient Fluid Temperature Profile: Stable. Maximum gradient = ~1°C/cm at 13.5 cm. Overall ΔT = 10.4°C. Plate orientation and position corresponds to dotted segment on plot.

Not surprisingly, the photographic record of the dye flow shows rather similar results to the previous experiment as well. Figure 5-10, taken at 4.5 minutes after initiating the experiment shows a horizontal extrusion of dye closely resembling that shown in the previous section. The extrusion has reached 30 cm from the heated surface in 4.5 min as compared to ~50 cm in 120 seconds for the previous section's experiments. Clearly the strength and velocity of the extruded fluid is enhanced by the increase in ambient stability. (More precise quantitative comparisons are of dubious value here since differences in dye flow rates and lighting conditions probably affected the extent of visibly dyed regions for each experiment.)

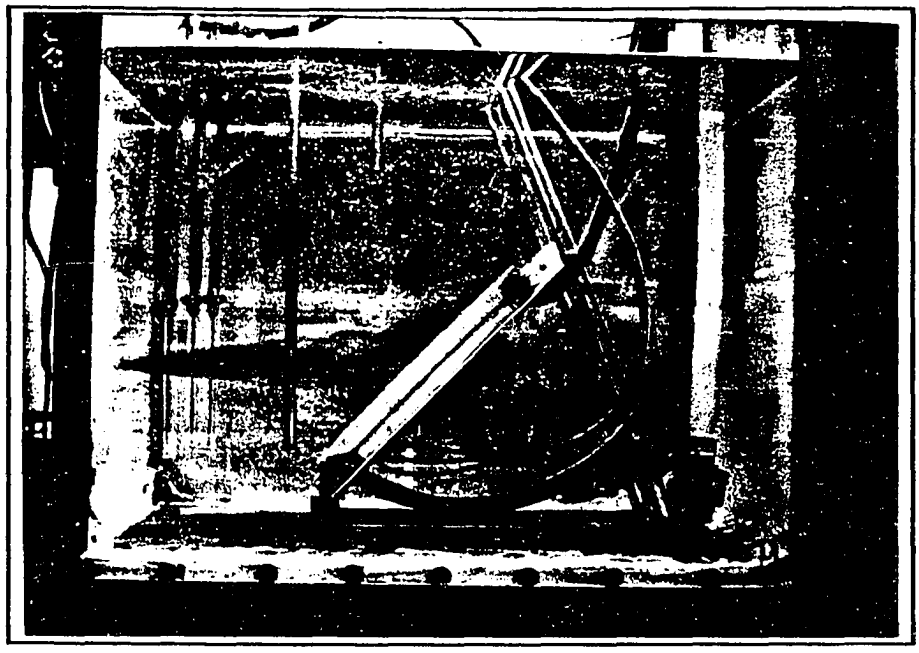

Figure 5-10 Dye Study: Inclined Plate, Stable Ambient Fluid, Turbulent Flow
Dye Study Conditions: Turbulent flow. For a 45° inclined plate, the transition range is $Ra^*_x = 10^9 - 10^{10}$. For this experiment, the heat flux was ~36000 W/m^2. Using a film temperature of 40°C, the estimated $Ra^*_L = 1.2\times10^{13}$. The fully turbulent range starts from around x=5 cm where $Ra^*_x = 9.6\times10^9$. [Photo 7-9]
Ambient Fluid Temperature Profile: Stable as shown on previous figure. Maximum gradient = ~1°C/cm at 13.5 cm. Overall ΔT = 10.4°C.

A closer examination of the temperature profiles taken during this dye study reveals an interesting result. During the course of this particular experiment, the ambient temperature profile was measured three times, once before heating was initiated, once during the course of the experiment, and a final time after the experiment had been concluded. It was noted that the temperature sensors were traversed directly through the dyed fluid for the latter two profiles, which were depicted on the figure above along with the initial temperature profile. It is clear that the profiles are changing as the experiment proceeds. However, although it was noted that the temperature sensors encountered the dyed region at heights between 7 and 10 cm, the profiles appear to be basically linear through this region. At first glance, then, there seems to be no significant disturbance of the temperature field caused by the recirculating flow.

An alternative method of looking at these temperature profiles is to look at the deviation from the initial ambient profile rather than the actual profiles themselves. The resulting temperature deviation profiles, shown in Figure 5-11 (with x axis inverted for visual effect) are quite interesting. The disturbance to the temperature

field covers a much broader vertical scale than is visibly apparent from dye flow. There is, however, a close correspondence between the location of the peak temperature disturbance and the location of the extruded dye flow.

The location of peak disturbance is seen to descend about 5 cm over the course of the latter half of the experiment. This is probably linked to the subsidence of the global fluid due to transport of the lower layers upward along the heated surface. Reduced upper layer temperatures are also observed after the experiment has been completed. This is also consistent with the transport of cool lower layer liquid into the upper layers of the tank. Analogous subsidences have been described in mountain-valley systems by Whiteman and McKee (1977 and 1978). The authors hypothesize that their observed inversion descent is due to upslope flow of a heated surface layer transporting air up the side of the valley out from under the inversion.

It seems clear that if otherwise unremarkable global temperature fields are examined in terms of deviations from their initial state the results can be quite compelling. Given the repeated observation of this horizontal extrusion under a wide range of experimental conditions in the laboratory, it seems possible that a reexamination of valley temperature profiles from previous field studies will uncover data which recorded the presence of this recirculation but passed unnoticed.

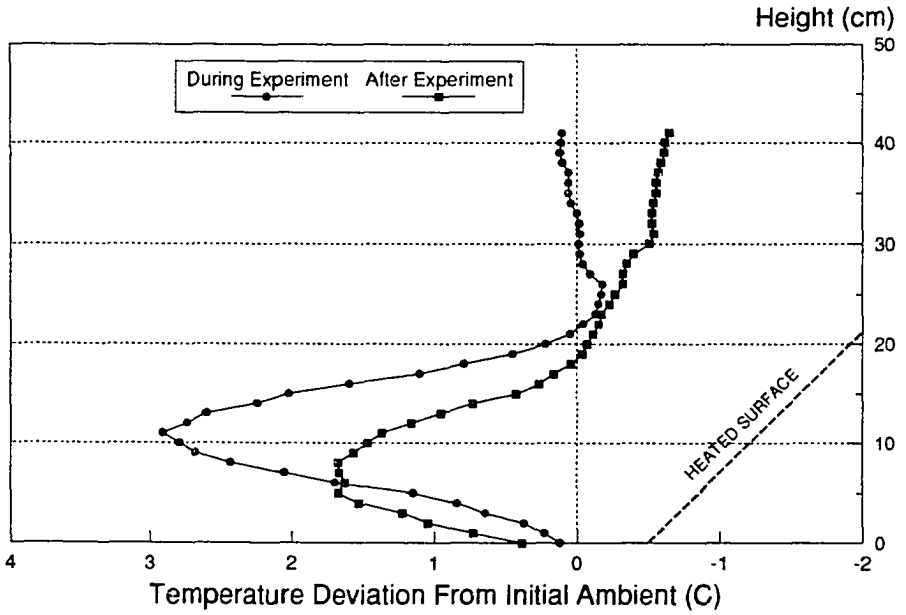

Figure 5-11 Ambient Fluid Temperature Deviation Profiles

5.2.3 Summary

The flow visualization studies provide a valuable and vivid tool in demonstrating the flow patterns and circulations which occur over heated sloping surfaces in the presence of capping stable layers. The postulated

recirculation was observed in one form or another for all inclinations measured between vertical and 15° from horizontal. The pictures showing the behavior of the detrained dye indicate that complex phenomena such as sinking dye fingers and detached cusps can occur for the laminar flow. Numerical modeling of the full range of phenomena observed would likely be extremely difficult.

The dye studies provided a means of verifying that the time scale and length scale of the flows being investigated were such that the development of the flow was not overly affected by constraints from the scale of the laboratory model. In addition, the techniques used present a method by which transport throughout the full velocity field could be assessed as a whole rather than on a profile or point by point basis as obtained from LDV and temperature methods.

The resulting pictures indicate that a flow pattern consistent with the type of atmospheric circulation described by King et al. (1987) was found under a variety of conditions which might be expected to correspond to typical stabilities, heat fluxes, and geometries found in the atmosphere.

The combination of the dye studies with simultaneous temperature profile measurements showed that the flow extrusion may not be immediately apparent from isolated temperature profile measurements. However, the comparison of temperature profiles taken before and during heating indicate that measurable deviations occur, consistent with that which would result from a disturbance to the global temperature field. This may indicate a means by which the presence of these recirculating flows could be inferred from valley air temperature profiles from existing sets of field data.

5.3 Quantitative Structure of Upslope Flows

Before beginning the discussion of the quantitative portion of the measurements, it is necessary to describe in some detail the Prandtl model for upslope flows. Described by Prandtl in 1942, this model provides a simplified set of equations describing slope flows, for which an analytic solution can be obtained. This model has met with some success in describing the observed profiles for upslope and downslope flows in the atmosphere.

A fundamental assumption made by the Prandtl model is that the local temperature deviation (T_{sur}-T_{bulk}) does not change along the length of the slope. A stable, linear temperature gradient is assumed in the bulk. The surface temperature, then is required to increase linearly along with the temperature in the bulk.

The newly obtained heat transfer coefficients for turbulent flow with stable stratification showed that in the water model of the flow, the Nusselt number varied as $\sim Ra_x^{*0.25}$. This implies $Nu \propto x$ which in turn implies a heat transfer coefficient h_x independent of x. The heat transfer data therefore indicates that for a

uniform flux surface the temperature deviation does not vary along the length of the surface for turbulent flow. This new data therefore gives strong support to a key underlying simplification for this model since the apparently restrictive initial assumption has proved to be in agreement with experimental data.

The Prandtl model assumptions result in the predicted profiles,

$$\theta = \theta_0 e^{\left(\frac{-y}{l}\right)} \cos\left(\frac{y}{l}\right) \tag{5-8}$$

$$u = \theta_0 \left(\frac{g\beta K_H}{B K_M}\right)^{\frac{1}{2}} e^{\left(\frac{-y}{l}\right)} \sin\left(\frac{y}{l}\right) \tag{5-9}$$

These solutions are derived and all variables defined in the Appendix 5 of this dissertation. The coordinate system is oriented parallel to the inclined slope so that u is the along slope velocity component, θ is the temperature deviation from bulk and φ is the inclination from horizontal. The length scale l is given by

$$l = \left(\frac{4K_H K_M}{g\beta B \sin^2\phi}\right)^{\frac{1}{4}} \tag{5-10}$$

The slope flow velocity is thus predicted to vary such that $u \propto B^{-0.5}$ while the depth varies as $l \propto B^{-0.25}$. The velocity profile obtained is in the form of a damped oscillation about u=0, the amplitude decreasing with distance normal to the slope. By setting the velocity gradient equal to zero, the maximum velocity is seen to occur at $y=\pi l/4$. In practice, the oscillation is damped rapidly by the factor exp(-y/l) so that the upward wind is effectively confined to the layer $(0,\pi l)$.

Figure 5-12 shows the general shape of the velocity and temperature profiles resulting from Prandtl's analysis.

Observations by Defant described in Sutton (1953) show a maximum velocity at x=27m for both up and downslope winds. This would require a length scale for this flow of l=34.4 m. Thus, the slope flows would be confined to layers of depth πl=108m. This agrees well with observations for downslope flow but is found to somewhat underestimate the observed depth of the upslope flow in the atmosphere.

Subsequent theoretical treatises on upslope flows have built upon the groundwork laid by Prandtl. For example, Defant (1951) extended Prandtl's solution to the unsteady case by simply multiplying the solutions by $\cos\Omega t$. Although the assumptions made by Defant are crude he obtained good agreement with observations for average air transport by slope winds and valley warming rates.

One recent model, the linear two dimensional model of upslope winds presented by Egger (1981), is framed as a perturbation to the Prandtl model for slope winds. Egger emphasizes the response of the flow to a temperature nonuniformity along the surface. His work indicates a deep penetration of the circulation above

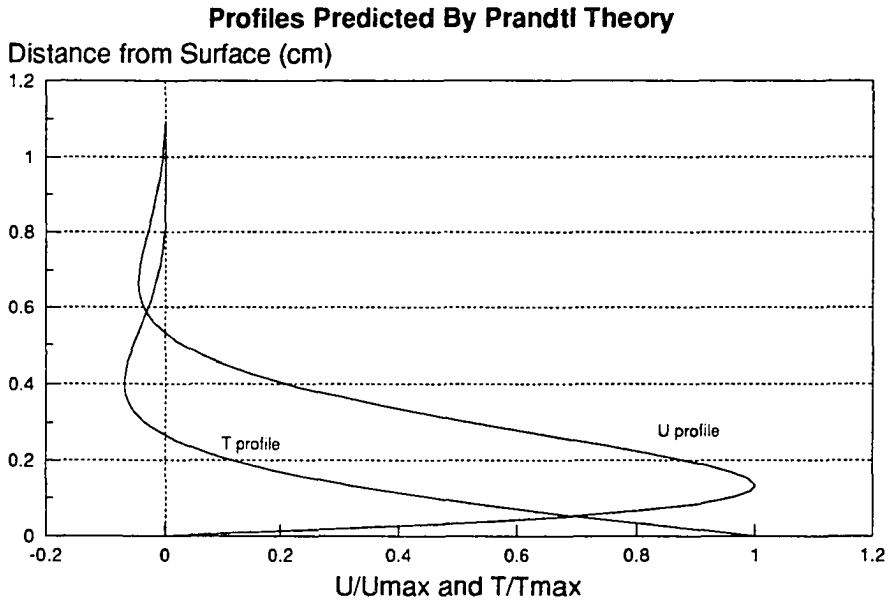

Figure 5-12 Prandtl Model Theoretical Profiles

a temperature irregularity on the surface. Egger's model is similar to Prandtl's in predicting the effect of global or external fluid stability on the slope flow layer. The base slope flow velocity in both models decreases as $B^{-0.5}$ and its depth shrinks with $B^{-0.25}$.

The predicted velocity profile shapes and the behavior relative to global stability predicted by these model are compared to the observed behavior for the laboratory model described below. Described first are an early set of experiments which measured the average along-slope velocity profiles for various stabilities. Following this we describe a more recent set of experiments which probed the nature of vertical and horizontal velocity profiles.

5.3.1 Measurements of Along-Slope Velocity Component

In the sections following are described the results of a series of experiments conducted in order to see if atmospheric phenomena related to upslope flows and in particular the complex recirculations driven by the interaction of upslope flows with inversion layers could be reproduced in the laboratory. These results are extracted from King and Reible (1986a).

5.3.1.1 Experimental

The experimental setup, consisting of an electrically heated foil set at an angle in a large tank of water, has been described in detail in Chapter 3 of this dissertation and is one which has been widely used in the study of the closely related problems of heat transfer and fluid flow about heated surfaces. Flows resulting from natural convection over an inclined plate must, however, be bounded by an extensive body of stably

stratified fluid above if they are expected to be similar to slope flows generated as a result of daytime heating of mountain slopes. Thus, the modeling objective of these experiments necessitated a key modification to the usual condition of uniform fluid temperature.

The experimental investigations were conducted in the Plexiglass® tank described in Chapter 3. Bottom heating was not utilized during these experiments but rather a uniform flux heated plate was used to create the convective flow. The heated plate used was the twelve inch model described in Chapter 3. The foil was set in the tank at an angle of 45 degrees with the bottom edge of the foil 12 cm from the bottom of the tank. The ambient fluid could be made to be density stratified by the addition of successively cooler layers of water through a fill tube located flush to the bottom. Fill water was filtered but not deaerated for these experiments.

During the course of these experiments the current level was kept at 100 amps with a voltage of 7.5 volts, resulting in a heating rate of 750 watts for a surface heat flux in excess of 16000W/m^2. Heat transfer measurements described in Chapter 4 indicated a transition to turbulent flow at a Rayleigh number of ~10^9 with fully developed turbulent flow present at Rayleigh numbers greater than ~10^{10} (for a 45° inclination). Using the appropriate film temperature of 35°C (drawn from Chapter 4 data giving surface temperatures at this heat flux) and physical properties from routines in the appendices, we calculate $Ra^*_x=1.02\times10^{10}$ at a distance of 6.5 cm and $Ra^*_x=1.07\times10^9$ at a distance of 3.7 cm. Thus the flow is laminar for the first 3.7 cm and becomes fully turbulent by around 6.5 cm from the leading edge. Since the total length is 30 cm, the greater part of the flow will be comfortably within the turbulent flow regime as required.

During the experiments reported in this section, two types of measurements were made. First, the "ambient stability" was determined by measuring the temperature gradient in the fluid far away from the plate. Second, along-slope velocities were measured at various heights throughout the free convection boundary layer, allowing the compilation of a set of averaged velocity profiles for various stabilities. Tank temperatures at a series of depths were measured using a multimeter to monitor a thermistor (YSI Catalog# 44031). The temperature sensor had an accuracy of ±0.1°C. The thermistor was insulated from the water by means of a conformal epoxy coating. The multimeter measured resistance with an accuracy equivalent to ±0.01°C maximum error. These temperatures provided a point determination of the ambient temperature profile in the water which was taken to be representative of global conditions throughout the tank. A top to bottom temperature profile took about 10 minutes to perform because of the relatively slow response time of the thermistor. However, the length of time required proved to be of little concern since repeated measurements of the ambient temperature profile showed excellent repeatability in preliminary testing. Since experience proved that ambient

fluid temperature profiles varied slowly and in a predictable fashion during an experimental run it was possible to determine the temperature profile only twice; once before and once after an experiment, without loss of important data.

The remainder of the experimental data presented in this chapter consists of velocity measurements made using the TSI LDV system. LDV measurements were made in backscatter mode with frequency shifting implemented. TSI Model 10087 seeding particles were utilized. The LDV was traversed on a 45° incline.

Because of the turbulent nature of the flow it was necessary to make a large number of instantaneous velocity measurements at each point in order to obtain a reliable average velocity before moving to the next point in the profile. Thus the velocity measured at each height is actually an average of a number of instantaneous values measured over a period of 30-45 seconds. The dominant frequencies of this type of turbulent convective flow have been determined to be of the order of a few seconds or less (Willis & Deardorff, 1974), far lower than the selected averaging time. In all cases the velocity profiles were begun just above the surface of the inclined foil at a point 17 cm from the leading edge and centered horizontally. The LDV was then traversed upwards, perpendicular to the foil, while measuring the velocity component parallel to the foil.

5.3.1.2 Velocity Profiles

Figure 5-13 presents a sample set of results obtained for along slope velocity profiles under the stably stratified conditions described above.

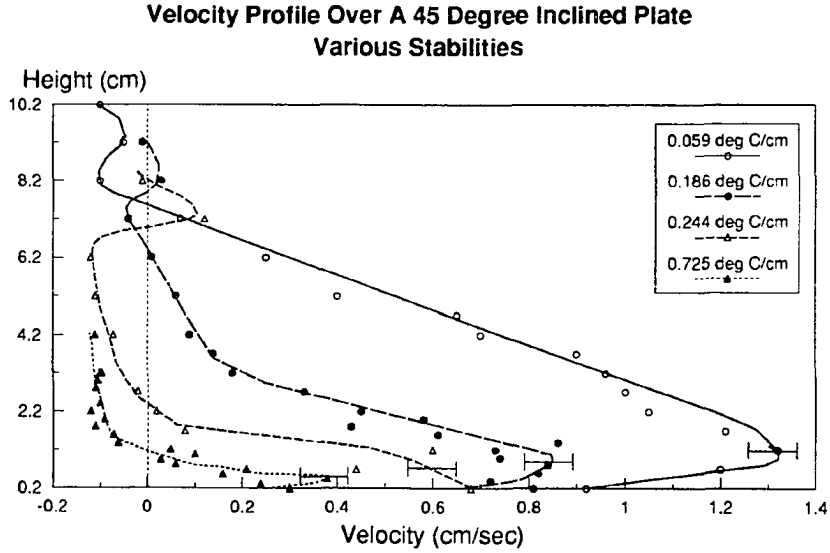

Figure 5-13 Velocity Profiles for Various Stabilities
Component of velocity along plate at distance 17 cm from leading edge. Ambient temperature profiles shown in following figure.

The profiles were obtained for various degrees of thermal stability ranging from 0.075°C/cm to 0.625°C/cm. The temperature profiles in the tank are depicted in Figure 5-14 with two sets of lines for each experiment corresponding to the measurements made at the beginning and end of each experiment.

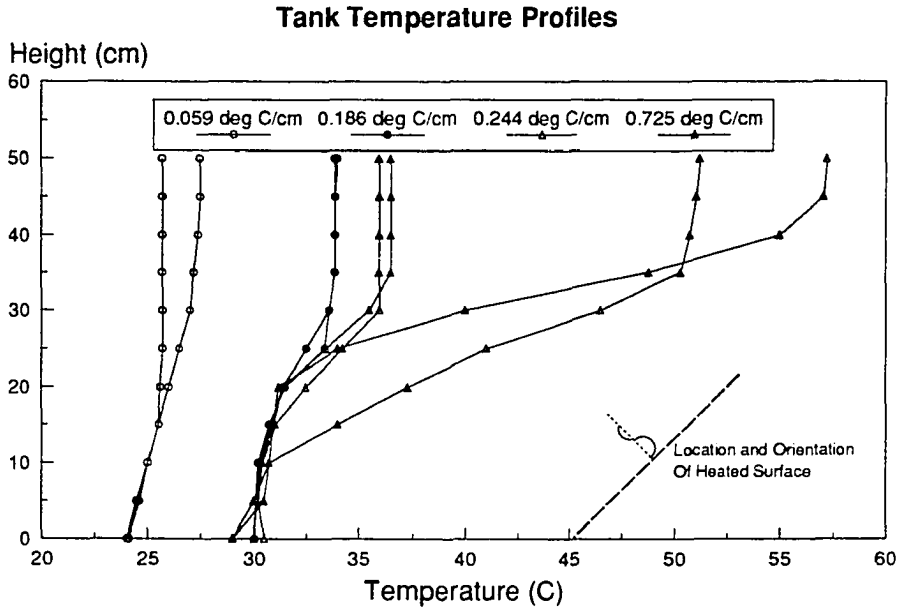

Figure 5-14 Ambient Temperature Profiles
Temperature profiles taken before and after experimental runs. Location of heated plate and velocity profiles depicted by dotted lines on chart.

The strong influence exerted on the layer depth and velocities by the overall stability is readily evident. In addition, the shape of the profiles appears to show the exponentially decaying sine wave form predicted by Prandtl's (1942) model and observed in the atmosphere. It should be noted here that while only 4 of the experiments are shown here for the sake of clarity, the overall trends and behavior are typical of all runs made.

5.3.1.3 Discussion of Results

Due to the time required to perform a complete traverse of the LDV through the flowing layer, it was important to establish that a quasi-steady state was established wherein the average velocity at a given height did not vary significantly over the time scale required to measure velocities throughout the profile. The time required for a velocity profile was in the range of 10 to 20 minutes (since these measurements were performed before data acquisition was automated).

Figure 5-15 shows the results of a set of data demonstrating that while the velocity at a given height will develop somewhat with time, this effect is minimal over 10-20 minutes and can be safely ignored for the present purposes of model validation.

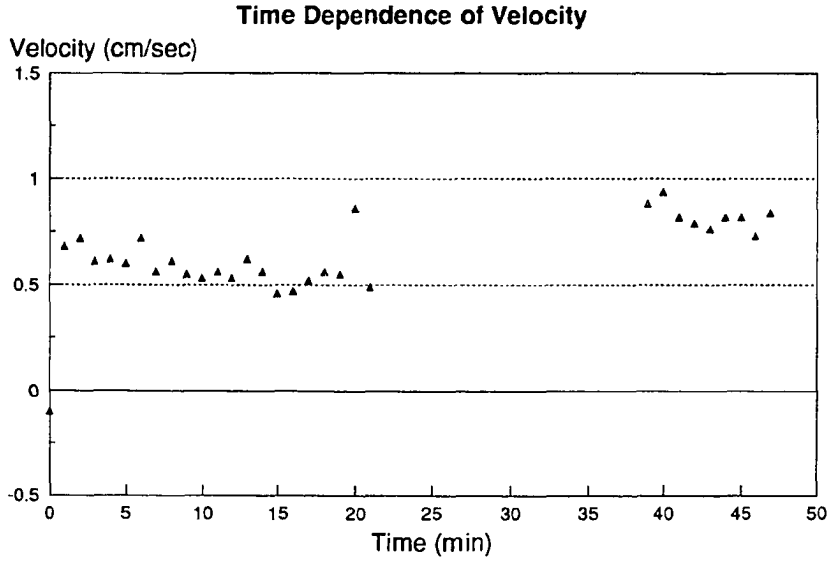

Figure 5-15 Time Dependence of Velocity at a Fixed Height

Numerous other sets of similar data were taken at various locations and showed that the flow remains essentially constant, apart from the fluctuations which occur, possibly due to turbulent fluctuations. The data do, however, consistently show a gradual upward trend in velocity as the experiment goes on. This appears to be related to the fact that the tank temperature profile changes gradually with time. This was unavoidable due to heat losses from the walls and surface along with the heat flux input through the inclined foil. Returning to the noisiness of the signal, it is worth mentioning that while the velocities plotted are the result of averaging 20-30 individual measurements, the standard deviation was nevertheless so large that in some cases it exceeded the magnitude of the actual mean velocity measured, particularly in the regions of low velocity.

Although the basic characteristics of the velocity profiles and their qualitative features mirror the Prandtl model's behavior, further analysis of the data brings out key differences. The maximum velocities observed and the depth of the slope flow layer were determined for each of seven experiments.

A log-log plot of maximum velocity versus dT/dz resulted in a best fit line with a slope of -0.61 while a similar plot of layer depth versus dT/dz gave a slope of -0.84 for the best fit line as shown in Figure 5-16 and Figure 5-17. These can be compared the Prandtl model predictions of -0.5 and -0.25 for these slopes. It is clear that at least for the prediction of maximum velocities, the Prandtl predictions seem to be an adequate representation of the trends observed. However, the Prandtl model appears to underestimate the variation of depth with stability quite significantly.

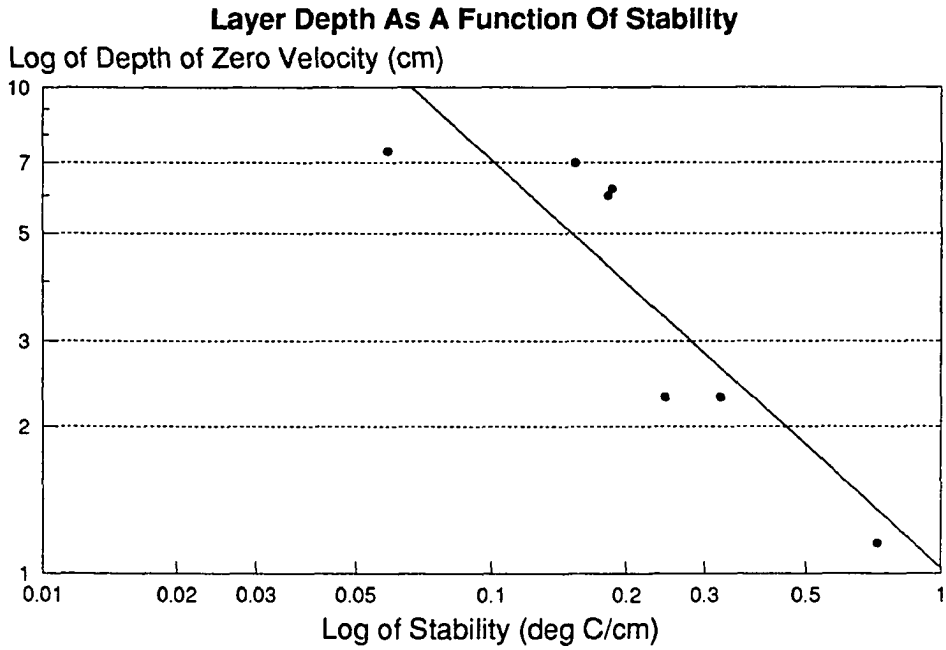

Figure 5-16 Layer Depth versus Stability

Log-log plot of layer depth versus dT/dz. Best fit line had slope of -0.84 (solid line). Prandtl model predicts slope of -0.25 (not shown).

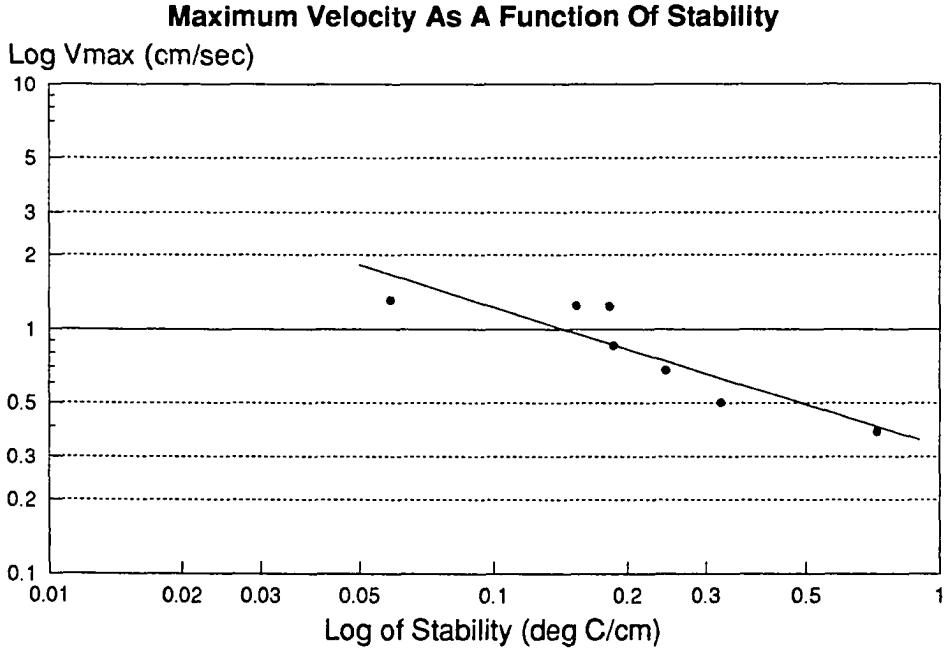

Figure 5-17 Maximum Velocity versus Stability

Log-log plot of maximum velocity versus dT/dz. Best fit line had slope of -0.61 (solid line). Prandtl model predicts slope of -0.5 (not shown).

The Prandtl model can be shown to predict a maximum velocity at depth of $y_{maxu}=\pi l/4$. The length scale l can thus be determined from the depth at which the maximum velocity is observed. The slope flow layer is generally confined to a layer of depth πl. Therefore, the Prandtl model predicts a layer depth of $4y_{maxu}$.

The predicted depths and actual depths measured are summarized in the table below and as can be seen the actual slope flow depth consistently exceeds the predicted depth by a large margin. A similar result has been noted by Defant as described by Sutton (1953) for atmospheric flows, with the typical slope flow depth ranging from 100-200m as compared to the predicted value of about 100m.

Table 5-1 Comparison of Prandtl Model Predictions to Experimental Model

Stability (°C/cm)	Depth of V_{max} (cm)	Depth for V=0 (predicted)	Depth for V=0 (actual)
0.059	1.0	4.0	7.4
0.154	1.0	4.0	7.0
0.182	1.0	4.0	6.0
0.186	1.2	4.8	6.2
0.244	1.0	4.0	2.3
0.325	0.5	2.0	2.3
0.725	0.1	0.4	1.15

One interesting feature of the velocity profiles is the elevated velocity peak which was often found in the region just above the area of negative velocity on the preceding figures. Two possible explanations for this observation follow.

The first possibility is that the small positive along slope velocity is due to occasional vertical penetration of strongly buoyant plumes outside the slope flow layer into a region of normally zero velocity resulting in a mean positive along slope velocity. The effect of these plumes would be to decrease the magnitude of the mean along slope velocity in the negative velocity region and hence the effect would be masked there except for an increase in standard deviation. This would imply that the velocity measured is unrelated to any sort of recirculation zone of the type shown in Figure 5-18.

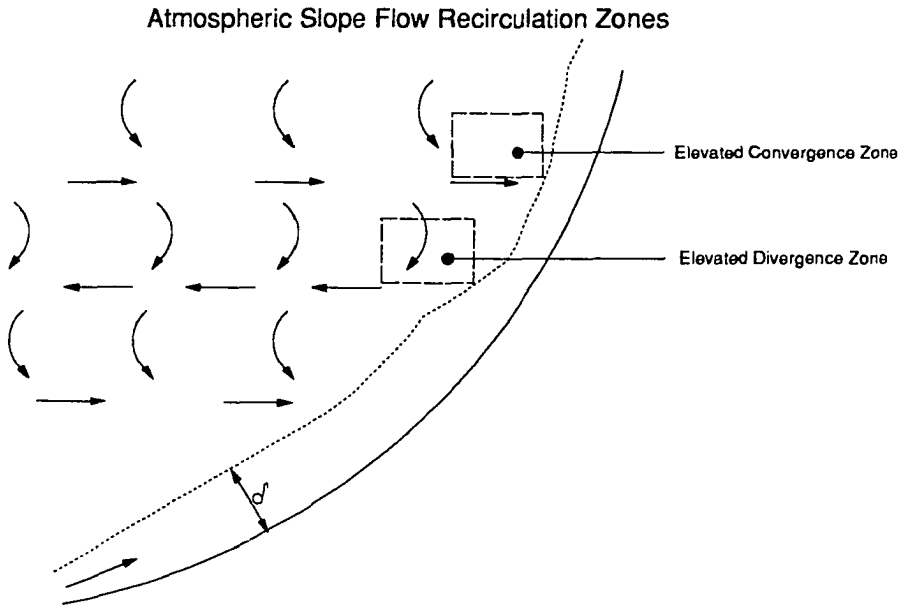

Figure 5-18 Influence of External Recirculation Patterns on Velocities Above the Boundary Layer

The second possibility is that the positive velocity reflects the presence of a region of convergence towards the boundary layer resulting in an enhanced along slope velocity component. This region would be expected if there were an entrainment into the slope flow layer in the less stable regions as depicted in the figure.

The height at which the elevated velocity peak occurs is generally well above the upper edge of the stable layer as determined from the temperature profile in the tank far away from the inclined surface. Nevertheless, it is reasonable to accept either of the possibilities above as feasible explanations based on the evidence at hand, since it is likely that the isotherms in the tank are distorted upward near the heated surface.

A third possibility is that the velocity peak is a spurious one which further experiments would show to be of no particular significance. This seems unlikely in spite of the relatively small data set, because of the ubiquity of this feature. However, without further data it was impossible to positively identify the mechanism at work here. This behavior can be better understood by looking at the more detailed sets of data discussed in section below which presents measurements made of the horizontal and vertical components of the turbulent velocity.

5.3.2 Measurements of Turbulent Horizontal and Vertical Velocity Components

In the sections below, the results of measurements taken from King and Reible (1986b) are summarized briefly. The velocity profiles presented differ from those described in the sections above in that measurements

were made for two components (horizontal and vertical) rather than a single along-slope component. In addition, data acquisition was partially automated in the interim so that profiles could be measured with more detail.

5.3.2.1 Experimental

During these experiments the current was again kept at 100 amps with a voltage of 7.5 volts resulting in a heating rate of 750 watts for a surface heat flux in excess of 16000 W/m^2, well within the range required to insure turbulent convection. The foil was mounted in the tank at an angle of 45 degrees (as before) with the bottom edge of the foil 10 cm from the bottom of the tank.

Two types of measurements were made during the experiments reported here. First, the ambient temperature profile was determined at four locations evenly spaced along the plate, from the leading edge to the trailing edge. Second, the turbulent velocity was measured at various heights throughout the free convection boundary layer, again at several locations along the plate.

Tank temperatures were measured using fine gage thermistors calibrated to an accuracy within 0.1°C. The time constant of the thermistors was less than 0.2 sec. Thermistor positions were monitored by counting drive pulses sent to a stepper motor by a separate controller.

Velocity measurements differ from the previous section in that the entire laser optics and traverser assembly was mounted on rails to provide a second dimension of travel. The laser's vertical position was monitored by the microcomputer. The velocity measured at each height is again an average of a number of instantaneous values. This time averaging was performed over a period of about 5 seconds. As mentioned above, the dominant frequencies of this type of turbulent convective flow have been determined to be of the order of a few seconds or less, which is of the same order as the averaging time used. Reliability of the average velocities was verified by comparing to measurements performed with an averaging period of 30-45 seconds. The results remained consistent.

Velocity profiles were measured for varying stabilities and at various distances along the plate. Measurements were made (separately) for vertical and horizontal components of the velocity. In all cases, the velocity profiles were begun at a distance ranging from 0.1-0.3 cm above the surface of the inclined surface depending on the angle of the beam crossing relative to the angle of the plate. The LDV was then traversed upwards away from the surface while measuring the selected velocity component.

5.3.2.2 Horizontal and Vertical Velocity Profiles

Figure 5-19 shows a typical ambient temperature profile. The sensors were affixed in a staggered rake shape so that they could traverse upward from the heated surface in a unified manner. Sensors were located every 10 cm along the length of a 30 cm long plate. The plots in the figure show three regions. With the vertical height defined to be 0 at the depth of the leading edge there are seen to be three regions as follows.

A) 0-11 cm : uniform temperature fluid.
B) 11-26 cm : stable layer.
C) 26-41 cm : uniform temperature fluid.

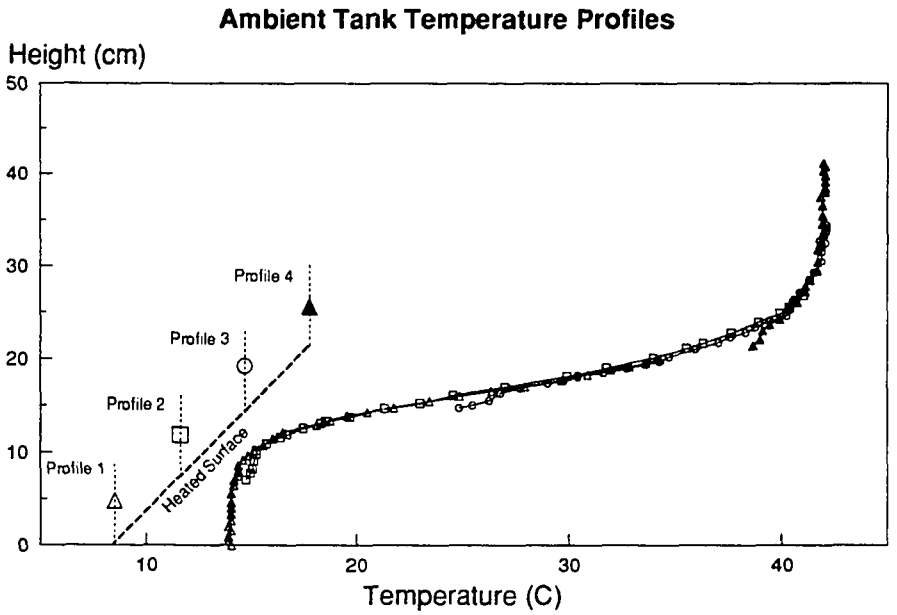

Figure 5-19 Ambient Temperature Profiles
Temperature profiles measured simultaneously on four sensors (staggered rake configuration) traversed through ambient fluid above a 45° inclined surface.

It also appears that the presence of the plate generated a temperature disturbance in the fluid immediately adjacent to the surface even while not heated. Conduction of heat along the plate and supporting metal structures is probably responsible for this deviation.

Figure 5-20 presents the horizontal velocity profiles which correspond to the temperature profiles described above. Velocity profiles were taken at horizontal distances of 3 cm, 7 cm, 11 cm, 15 cm, and 19 cm; thus spanning a distance of 22.6 cm along the length of the plate. The turbulent intensity was estimated by determining the magnitude of the standard deviation in the velocity at a given height. The velocity profiles

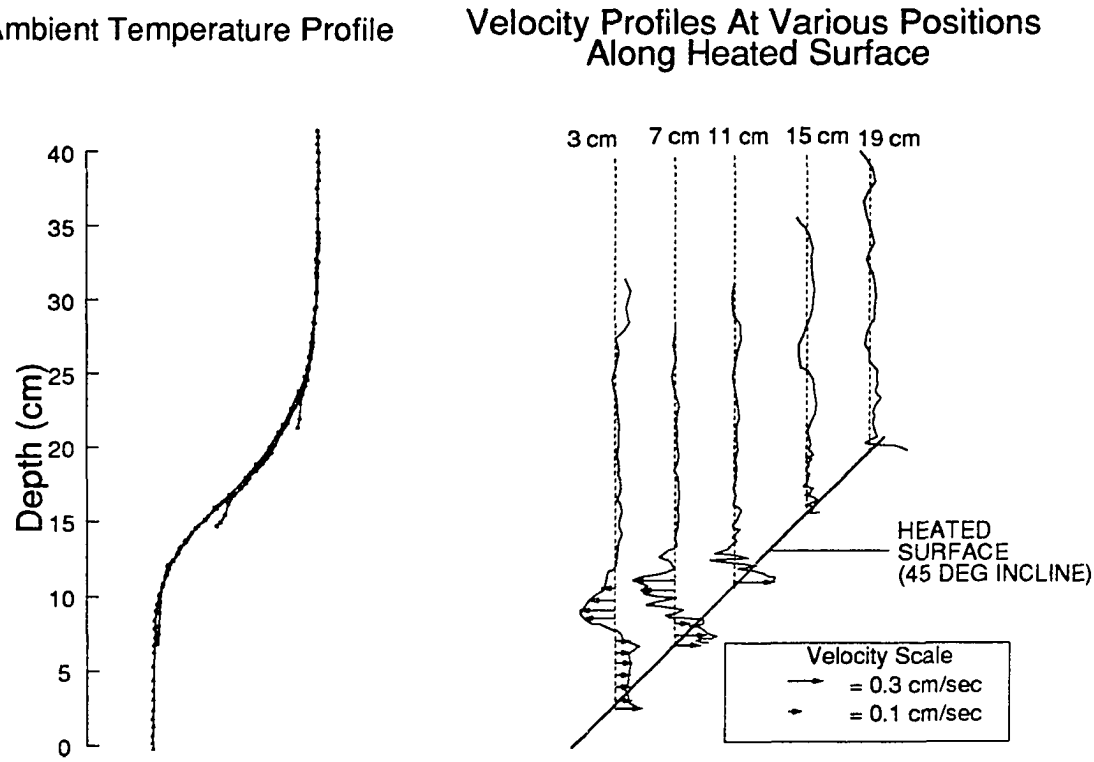

Figure 5-20 Elevated Horizontal Divergence Zone in Recirculating Slope Flows
Horizontal component of velocity, positive values indicate flow toward plate, negative values indicate divergence. Profiles measured sequentially at 5 locations evenly spaced from the vicinity of the leading edge to the vicinity of the trailing edge. Relative positions of heated plate and profiles are as indicated on figure.

in this figure were depicted along a 45° line representing the heated surface to clarify the interrelationships amongst the individual velocity profiles and the ambient temperature profile. The turbulent intensities of the velocities did not vary significantly along the profile and are not shown on this plot.

It is clear that there is a positive velocity (fluid moving toward the plate) in the region adjacent to the plate. This corresponds to the boundary layer flow along the plate. Unfortunately, it is also apparent that the fine structure of the velocity profile in the neighborhood of the plate is not easily discernable using the available LDV system. It is, however, possible to discern the flow patterns in the recirculating regions above and outside the near wall region. An important feature is the region of large negative velocity which is found around the height of 10 cm. This corresponds well to the beginning of region B) and is attributed to a capping effect of the stable layer. There appear to be only slight indications of a tendency to have an inflow in the elevated region between 25 and 30 cm as was described in the previous section. This is attributed to the fact that the heated plate did not extend into region C. (Vertical height of the 30 cm plate is 21.2 cm because of the 45° inclination.)

Figure 5-21 shows a second ambient temperature profile. The plots again show three regions. This time the depths are as follows.

A) 0-15 cm : linear stable layer.
B) 15-20 cm : slightly less stable layer.
C) 20-41 cm : uniform temperature fluid.

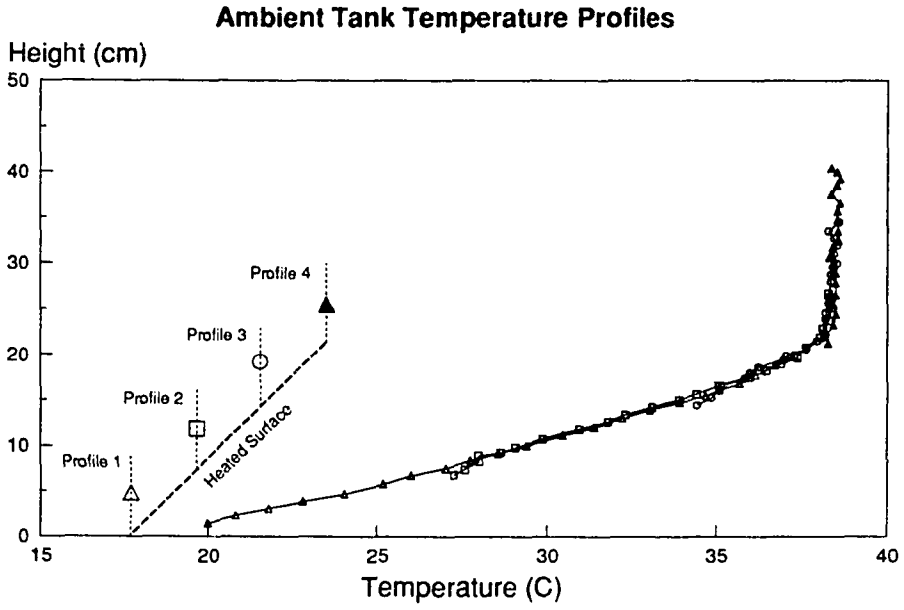

Figure 5-21 Ambient Temperature Profiles
Temperature profiles measured simultaneously on four sensors (staggered rake configuration) traversed through ambient fluid above a 45° inclined surface.

Figure 5-22 presents the horizontal velocity profiles which correspond to the temperature profiles described above. Velocity profiles were taken at horizontal distances of 3 cm, 7 cm, 15 cm, and 19 cm.

The ubiquitous elevated velocity peak shown in Figure 5-2 was again noted for the horizontal component. With this additional data it now becomes apparent that there is good evidence for a region of enhanced entrainment at the transition to a region with less stable fluid, in this case occurring above a height of approximately 15 cm. It is also of interest that the negative velocities below the stable layer, while present, are not nearly as pronounced under the conditions depicted here and may correspond to a parallel downslope subsidence rather than a horizontal recirculation. It is also apparent that there is a circulation above the level of the heated surface which may indicate velocities influenced by the large scale motions in the tank. Standard deviations of the measured velocities (not shown) indicated that the horizontal turbulent intensity remained relatively flat with some enhancement of the turbulence in the region immediately adjacent to the heated plate.

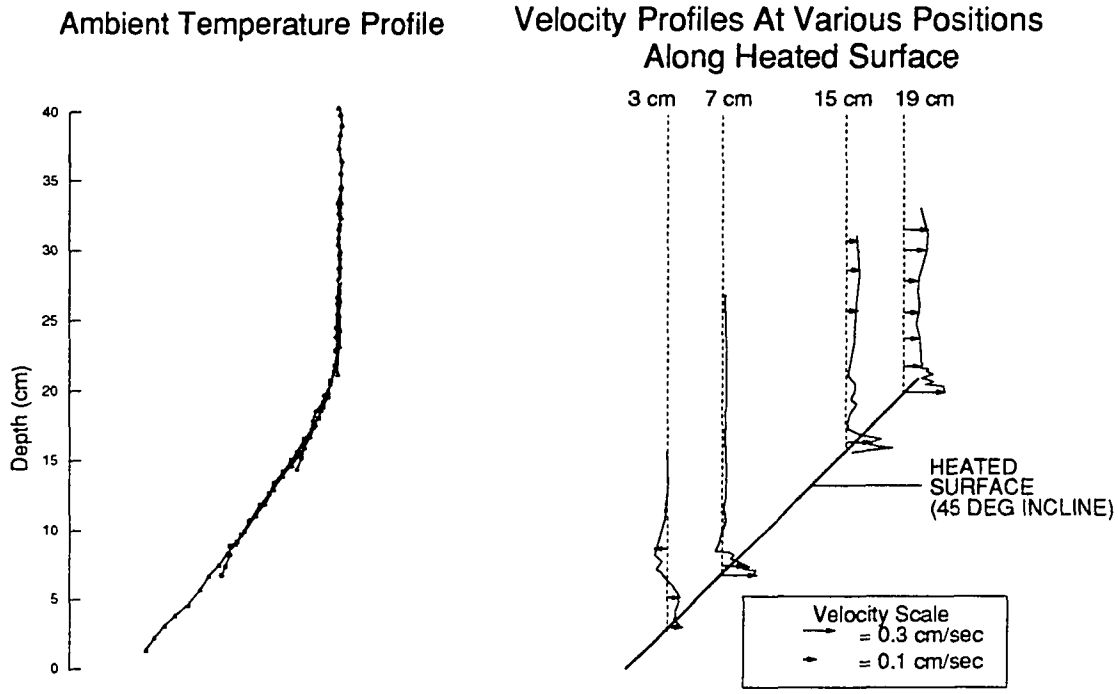

Figure 5-22 Elevated Convergence Zone in Recirculating Slope Flows
Horizontal component of velocity, positive values indicate converging flow toward plate, negative values indicate divergence. Profiles measured sequentially at 4 locations spaced between the vicinity of the leading edge and the vicinity of the trailing edge. Relative positions of heated plate and profiles are as indicated on figure.

The vertical velocities (not shown) did not lend themselves as easily to generalizations as the horizontal velocities did. There were local regions of strong upward flow immediately above the heated plate as expected but little other coherent information could be derived from the velocity profiles. While relatively straightforward, the feature of the vertical velocity profiles which was probably most significant was that the intensity of the turbulence as indicated by standard deviations was damped in the presence of a stable layer and increased markedly at the upper depths when the damping effect of the stability gradient was no longer present. This probably indicates that the turbulent exchange of kinetic energy provides a significant means by which momentum is transferred from the vertical and along slope components to diverging recirculations.

To be thorough, Figure 5-23 shows the velocity profile measured in a nominally quiescent tank. As can be seen, when the velocity profile is shown on the same scale as the previous figures in this section, only minute deviations from zero velocity are observable. On a 10× smaller scale, it can be seen that there are some deviations from zero velocity, which may be due to actual circulations within the tank or some other

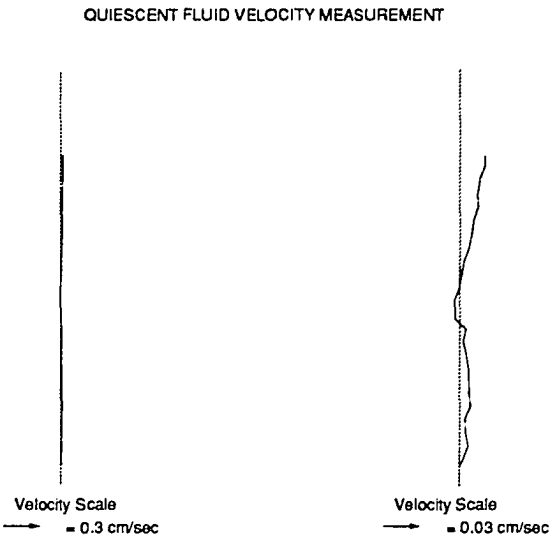

Figure 5-23 Baseline Velocity Measurement in Quiescent Tank
Left hand profile is on identical scale as previous velocity plots in this section. Right hand profile velocities are scaled up by a factor of 10.

source of inaccuracy inherent to the LDV setup. In any case, we conclude by comparison with this figure that the velocities measured and shown on the previous figures can be regarded as significantly greater than the noise threshold for the experiment.

5.4 Summary and Conclusions

In summary, the results of the laboratory experiments designed to duplicate the atmospheric slope flow on a laboratory scale gave results which agreed qualitatively with many of the basic behaviors predicted by Prandtl type models. The shape of the along slope velocity profiles was consistent with the predicted exponentially decaying sine wave and the strength and depth of the flow were shown to have an inverse dependence on stability. Quantitatively, log-log plots of velocity and depth against stability gave best fit slopes of -0.61 and -0.84 compared to the values of -0.5 and -0.25 predicted by Prandtl type models. The Prandtl predictions appeared to be acceptable for velocity profiles but depths were underestimated quite significantly on the model. This result, which agrees with atmospheric observations, may be a result of the neglect of entrainment and/or detrainment in Prandtl type models.

Measurements of turbulent horizontal and vertical velocity components gave profiles consistent with regions of convergence and divergence to the slope flow layer governed by ambient stability layers. The vertical turbulent fluctuations were damped strongly in the presence of capping stable layers, suggesting that models using equal values of K_M for vertical and horizontal components of velocity may not be well formulated for calculating separation due to highly stable layers.

The quantitative results indicated that the Prandtl model should provide a useful starting for describing slope flows. The assumed constant values for K_M and K_H in this model are one likely area for improvements to be made. Initial steps have been taken in this area by incorporating K values dependent on height from the surface, based on known atmospheric K profile measurements (after McRae (1981)). The equations can then solved numerically.

The Prandtl model is not capable of predicting diverging recirculations due to stability gradients since it assumes a one-dimensional velocity profile. In light of the quantitative data supporting the stability dependence of velocity profiles of one-dimensional Prandtl type models and qualitative data showing the frequent occurrence of horizontal extrusions it would appear the two dimensional theory of Egger may be the best starting point for pursuing model development. Egger's extrusion was found to develop as a result of a temperature disturbance at the surface. However, at present, this surface temperature disturbance is only hypothetical and no experimental data exists to support a relationship between such a disturbance of surface temperature and horizontal outflows from atmospheric slope flows. With the experimental evidence which has been compiled linking horizontal outflows to stability gradients it would be desirable to explore carefully the possibility of extending the theory of Egger to cover these conditions.

Chapter 6

Summary and Conclusions

Motivated by a need to assess pollutant transport by upslope flows, an investigation has been conducted into the fundamentals of natural convection flow over inclined surfaces. Particular attention was focused on the influence of ambient fluid stability.

Field studies were performed using tracer gas releases into the upslope flow over a Southern California mountain range. The field studies served to reveal the presence of a split slope flow recirculation and demonstrated the impact of this recirculation on the transport of pollutants from a valley.

In order to pursue a controlled investigation of the phenomena found in the field work, a laboratory model was developed using water as a working fluid. Extensive dye studies demonstrated the presence of this recirculation to varying degrees in nearly every configuration with a stable layer present. These results may be somewhat unexpected to heat transfer researchers who apparently have not observed this extrusion previously.

Heat transfer experiments conducted with the laboratory model served to refine and validate the experimental equipment used by enabling comparison with existing theoretical and empirical predictions. Existing correlations for inclined surfaces were extended to two orders of magnitude lower in Rayleigh number. Measurements made for 75° from vertical and for a horizontal surface constitute apparently the first measurements at these inclinations for uniform flux plates. Transition ranges and laminar and turbulent heat transfer correlations are expressed for these and other inclinations. Overall correlations are also reported with apparently far less scatter of data than for any previously reported research with inclined surfaces.

Experimentation with stratified ambient fluid resulted in the observation that, with turbulent flow, the stratification could apparently be disregarded and heat transfer simply calculated from local conditions. Laminar data was much more difficult to reconcile because of the strong influence of upstream conditions on conditions along the length of the plate. Further experimentation would be desirable to confirm the turbulent behavior for a variety of ambient temperature profiles and inclinations. However, in light of the fact that turbulent heat transfer becomes independent of position for uniform ambient temperatures, it appears that the mechanism for turbulent heat transfer is that of a local mixing circulation which is largely decoupled from any upstream conditions. Thus the observation for turbulent flow under stratified conditions will likely hold true under a wide range of situations.

The observed heat transfer characteristics for turbulent flow lend support to a simplifying assumption made by Prandtl in treating slope flows. An analytic solution for slope flows is then available. However, quantitative laboratory results show that Prandtl's one dimensional theory underpredicted the layer depths

observed. Similar results have been noted in the atmosphere. Two dimensional modeling techniques, such as Egger's (1981) model hold promise for future modeling efforts directed towards improving the Prandtl model's shortfalls.

Bibliography

Acharya, S. Natural convection in an inclined enclosure containing internal energy sources and cooled from below. Int. J. Heat and Fluid Flow, 113-121. 1985.

Adrian, R. J. Estimation of LDA signal strength and signal-to-noise ratio. TSI Quarterly, v. IV, issue 1, 3-8. 1978.

Agarwal, J. K. and Keady, P. Theoretical calculation and experimental observation of laser velocimeter signal quality. TSI Quarterly, v. VI, issue 1, 3-10. 1980.

Ahmad, T. and Faeth, G. M. An investigation of the laminar overfire region along upright surfaces. Journal of Heat Transfer, v. 100, 112-119. 1978.

Andreev, V. and Gannev, K. Model of convective heat exchange due to isolated thermals in the atmospheric boundary layer. Bound. Lay. Met., v. 20, 331-339. 1981.

Antonia, R. A. Conditional sampling in turbulence measurement. Ann. Rev. Fluid Mech., v. 13, 131-156. 1981.

Bejan, A. Convection heat transfer. John Wiley and Sons, New York. 1984.

Berkowicz, R. and Prahm, L. P. Note on turbulent scaling parameters for the convective planetary layer. Bound. Lay. Met., v. 21, 215-222. 1981.

Bever, M. (ed.) Encyclopedia of Materials Science and Engineering, v. 6, R-S. MIT Press, Cambridge. 1986.

Black, W. Z. and Norris, J. K. The thermal structure of free convection turbulence from inclined isothermal surfaces and its influence on heat transfer. Int. J. Heat Mass Transfer, v. 18, 43-50. 1975.

Bowers, C. G., Jr., Willits, D. H. and Bowen, H. D. Criteria for determining buoyancy effects on turbulent forced convection in an asymmetrically heated horizontal channel. Transactions of the ASAE, v. 29(2), 550-555. 1986.

Brehm, M. Hangwindexperiment Innsbruck, 1978. Gebirgswindsystem und Inversionsauflosung. Diplomarbeit, Meteorologisches Institut Univ. Munchen. 1981.

Briggs, G. A. Comments on 'Similarity model for maximum ground-level concentration in a freely convective atmospheric boundary layer'. Bound. Lay. Met., v. 21, 531-533. 1981.

Broadwell, J. E. and Breidenthal, R. E. A simple model of mixing and chemical reaction in a turbulent shear layer. J. Fluid Mech., v. 125, 397-410. 1982.

Buettner and Thyer. Valley winds in Mt. Rainier National Park. Weatherwise, 4/62, 63-67. 1962.

Busse, F. H. Bounds for turbulent shear flow. J. Fluid Mech., v. 41, Part 1, 219-240. 1970.

Cairnie, L. R. and Harrison, A. J. Natural convection adjacent to a vertical isothermal hot plate with a high surface-to-ambient temperature difference. Int. J. Heat Mass Transfer, v. 25, no. 7, 925-934. 1982.

Carruthers, D. J. and Choularton, T. W. Airflow over hills of moderate slope. Quart. J. R. Met. Soc., v. 108, 603-624. 1982.

Caughey, S. J. Observed characteristics of the atmospheric boundary layer. From 'Atmospheric turbulence and air pollution modelling,' Nieuwstadt and van Dop, (ed.) Reidel Publishing Company, Dolbrecht, Holland. 1982.

Cermak, J. E. Applications of fluid mechanics to wind engineering - a Freeman Scholar Lecture. J. Fluids Eng., 97, 9-38. 1975.

Cermak, J. E. Wind tunnel design for physical modeling of atmospheric boundary layers. Proc. A.S.C.E. Engineering Mechanics Div., v. 107, p. 623. 1981.

Chandraskekhara, B. C. and Namboodiri, P. M. S. Influence of variable permeability on combined free and forced convection about inclined surfaces in porous media. Int. J. Heat Mass Transfer, v. 28, no. 1, 199-206. 1985.

Cheesewright, R. Natural convection from a plane, vertical surface in non-isothermal surroundings. Int. J. Heat Mass Transfer, v. 10, 1847-1859. 1967.

Cheesewright, R. and Ierokiopitis, E. Velocity measurements in a turbulent natural convection boundary layer. Proc. 7th Intl. H.T. Conf., v. 2, 305-309, Munich, F.R.G. 1982.

Chen, C. and Eichorn, R. Natural convection from a vertical surface to a thermally stratified fluid. J. Heat Transfer, Trans. ASME, Series C, v. 98, 446-451. 1976.

Chen, T. S. and Yuh, C. F. Combined heat and mass transfer in natural convection on inclined surfaces. Numerical Heat Transfer, v. 2, 233-250. 1979.

Chen, T. S., Tien, H.C., and Armaly, B. F. Natural convection on horizontal, inclined, and vertical plates with variable surface temperature or heat flux. Int. J. of Heat and Mass Transfer, v. 29, 1465-1478. 1986.

Childress, W. S. and Spiegel, E. A. Archimedian instabilities in two-phase flows. SIAM Rev., v. 17, p. 136. 1975.

Clausing, A. M. Natural convection correlations for vertical surfaces including influences of variable properties. Journal of Heat Transfer, v. 105, 138-143. 1983.

Davis, P. A. and Reimer, A. Short-range atmospheric dispersion over a heterogeneous surface - I. lateral dispersion. Atmospheric Environment, v. 20, no. 1, 41-50. 1986.

de Lemos, M. J. S. and Sesonske, A. Turbulence modeling in combined convection in mercury pipe flow. Int. J. Heat Mass Transfer, v. 28, no. 6, 1067-1088. 1985.

Deardorff, J. W. Numerical investigation of neutral and unstable planetary boundary layers. J. Atmos. Sci., v. 29, 91-115. 1972.

Deardorff, J. W. Convective velocity and temperature scales for the unstable planetary boundary layer and for Rayleigh convection. J. Atmos. Sci., v. 27, 1211-1213. 1970.

Deardorff, J. W. and Willis, G. E. Ground-level concentrations due to fumigation into an entraining mixed layer. Atm. Env., v. 16, 1159-1170. 1982.

Deardorff, J. W. and Willis, G. E. A parameterization of diffusion into the mixed layer. J. Appl. Met., v. 14, p. 1451-1458. 1975.

Deardorff, J. W., Willis, G. E. and Stockton, B. H. Laboratory studies of the entrainment zone of a convectively mixed layer. J. Fluid Mech., v. 100, 41-64. 1980.

Defant, F. Local Winds, in Compendium of Meteorology, T. Malone ed. American Met. Soc., Boston. 1951.

Devi, C. and Nath, G. Unsteady nonsimilar natural convection over a vertical flat plate in a thermally stratified fluid. Int. J. Heat Mass Transfer, v. 27, 1424-1427. 1984.

Drivas, P. J. Investigation of atmospheric dispersion problems by means of a tracer technique. PhD Thesis, Calif. Inst. Tech., Pasadena, Calif. 1975.

Durox, D. and Baritaud, T. Statistical bias in LDA measurements. Dantec Information No. 04 1987.

Durst, F., Melling, and Whitelaw. Principles and practice of laser doppler velocimetry. 2nd ed., New York, Academic Press, 1981.

Dutton, J. The ceaseless wind. McGraw Hill. 1976.

Eatontown Signal Laboratory Group. Local winds: mountain and valley winds, land and sea breezes. Report 982, Weather Division, Headquarters Army Air Forces. 1945.

Eckert, E. R. G. The application of interferometry to time varying flow conditions. From Symposium on Flow Visualization A. S. M. E. Presentation Summaries, Section 12. 1960.

Eckert, E.R.G. and Drake, R.M. Heat and mass transfer. McGraw Hill, New York. 1959.

Eckert, E.R.G. and Drake, R.M. Analysis of heat and mass transfer. McGraw-Hill Book Co., New York. 1972.

Egger, J. On the linear two dimensional theory of thermally induced slope winds. Contrib. Atm. Phys., v. 54, 465-481. 1981.

Eichorn, R. Natural convection in a thermally stratified fluid. Progress in Heat and Mass Transfer, v. 2. 1969.

Fingerson, L. M. Relating light scattering theory to actual laser velocimeter systems. TSI Quarterly, v. VI, issue 4, 3-7. 1980.

Fujii, T. and Imura, H. Natural convection heat transfer from a plate with arbitrary inclination. Int. J. Heat Mass Transfer, v. 15, 755. 1972.

Fukui, K., Nakajima, M., and Ueda, H. A laboratory experiment on momentum and heat transfer in the stratified surface layer. Quart. J. R. Met. Soc., v. 109, 661-676. 1983.

Fussey, D. E. and Warneford, I. P. Free convection from a downward facing inclined flat plate. Int. J. Heat Mass Transfer, v. 21, 119. 1978.

Gal-Chen, T. and Somerville, R. C. J. Numerical solution of the Navier-Stokes equations with topography. J. Comp. Phys., v. 17, 276-310. 1975.

Gebhart, B. and Mahajan, R. L. Instability and transition in buoyancy-induced flows. Advances in Applied Mechanics, v. 22, 231-315. 1982.

Goldstein, R. J. and Wang, Q.J. An interferometric study of the natural convection in an inclined water layer. Int. J. Heat Mass Transfer, v. 27, 1445-1453. 1984.

Goodman, J. Ambient temperature stratification effects in laminar free convection. Int. J. Heat Mass Transfer, v. 16, 1949-1950. 1973.

Gray, D. D. and Giorgini, A. The validity of the Boussinesq approximation for liquids and gases. Int. J. Heat Mass Transfer, v. 19, 545-551. 1976.

Haaland, S.E. and Sparrow, E.M. Vortex instability of natural convection flow on inclined surfaces. Int. J. Heat Mass Transfer, v. 16, 2355-2367. 1973.

Hasan, M. and Mujumdar, A. S. Effect of finite normal interfacial velocity on free convection heat and mass transfer rates from an inclined plate. Int. Comm. Heat Mass Transfer, v. 10, 477-490. 1983.

Hassan, K. and Mohamed, S. A. Natural convection from isothermal flat surfaces. Int. J. Heat Mass Transfer, v. 13, 1873. 1970.

Heuss, J.M. etal. An analysis of factors contributing to Los Angeles oxidant and NO2 air quality. Report GMR-3230 ENV #74, GM Research Lab., Env. Sci. Dept. 1980.

Himasekhar, K. and Sarma, P. K. Laminar combined convection from a rotating cone to a thermally stratified environment. Journal of Heat Transfer, v. 108, 973-976. 1986.

Hindman, E. Air currents in a mountain valley deduced from the breakup of a stratus deck. Mon. Weather Rev., v. 101, 195. 1973.

Hinds, W. T. Diffusion over coastal mountains of Southern California. Atm. Env., v. 2, 149-165. 1970.

Hinze, J. O. Turbulence. McGraw Hill Book Co., Inc., New York. 1975.

Holman, J.P. Heat transfer. McGraw-Hill Book Co., Inc., New York. 1976.

Humphrey, J. A. C. and To, W. M. Numerical simulation of buoyant, turbulent flow - II. Free and mixed convection in a heated cavity. Int. J. Heat Mass Transfer, v. 29, 593-610. 1986.

Hunt, J. C. R. Diffusion in the stable boundary layer. From 'Atmospheric turbulence and air pollution modelling.' Nieuwstadt, F. T. and van Dop, H.(ed.) Reidel Publishing Company, Dordrecht, Holland. 1982.

Hunt, J. C. and Fernholz, H. Wind tunnel simulation of the atmospheric boundary layer: a report on Euromech 50. J. Fluid Mech., v. 70, 543. 1975.

Hwang, B. B. Investigation of the diffusion in turbulent shear flow. PhD Thesis, Rutger University. 1977.

Hyun, J. M. Adjustment of thermally-stratified fluid in a container with vertical through-flow. Int. J. of Heat Mass Transfer, v. 29, no. 10, 1487-1493. 1986.

Inaba, H. Experimental study of natural convection in an inclined air layer. Int. J. Heat Mass Transfer, v. 27, 1127-1139. 1984.

Inaba, H. Natural convection in an inclined rectangular channel heated from the bottom surface. Trans. ASME, v. 108, pp. 764-769. 1986.

Jackson, P. S. and Hunt, J. C. R. Turbulent wind flow over a low hill. Quart. J. R. Met. Soc., v. 101, 929-955. 1975.

Jaluria, Y. Natural convection heat and mass transfer. - (HMT, the science and applications of heat and mass transfer; v. 5). Pergamon Press Inc., New York. 1980.

Jaluria, Y. and Gebhart, B. Stability and transition of buoyancy-induced flows in a stratified medium. J. Fluid Mech., v. 66, 593-612. 1974.

Jang, D. S., Jetli, R. and Acharya, S. Comparison of the piso, simpler, and simplec algorithms for the treatment of the pressure-velocity coupling in steady flow problems. Numerical Heat Transfer, v. 10, 209-228. 1986.

Jirka, G. and List, J. E. Third international symposium on stratified flows. Journal of Hydraulic Engr., v. 14, 125-134. 1988.

Johnson, D. E. and Hilburn, J. L. Rapid practical designs of active filters. John Wiley and Sons, New York. 1975.

Joshi, Y. and Gebhart, B. Vertical transient natural convection flows in cold water. Int. J. Heat Mass Transfer, v. 27, 1573-1582. 1984.

Kaimal et al. Turbulence structure in the convective boundary layer. J. Atmos. Sci., v. 33, 2152-2169. 1976.

Kantha, L. H., Phillips O. M. and Azad, R. S. On turbulent entrainment at a stable density interface. J. Fluid Mech., v. 79, 753. 1977.

Karlekar, B.V. and Desmond, R.M. Engineering heat transfer. West Publishing Co., New York. 1977.

Kato, H., Nishiwaki, N. and Hirata, M. On the turbulent heat transfer by free convection from a vertical plate. Int. J. Heat Mass Transfer, v. 11, 1117-1125. 1968.

Kell, G.S. Effects of isotropic composition, temperature, pressure, and dissolved gases on the density of liquid water. J. of Physical and Chemical Reference Data, v. 6, 1115. 1977.

Kennedy, K. J. and Zebib, A. Combined free and forced convection between horizontal parallel planes: some case studies. Int. J. Heat Mass Transfer, v. 26, 471-474. 1983.

Kerman, B. R. Effective stratification for plume rise and boundary layer growth computations. Atm. Env., v. 17, 235-238. 1983.

Kierkus, W. T. An analysis of laminar free convection flow and heat transfer about an inclined isothermal plate. Int. J. Heat Mass Transfer, v. 11, 241. 1968.

Kim, S. and Chen, Y. A finite element computation of turbulent boundary layer flows with an algebraic stress turbulence model. Computer methods in applied mechanics and engineering, v. 66, 45-63 1988.

King, J. A. and Reible, D. D. Pollutant transport by slope winds. Presented at the AIChE Meeting, New Orleans, LA, 4/86. 1986.

King, J. A. and Reible, D. D. Laboratory simulation of pollutant transport by buoyancy driven slope flows. Presented at the Annual AIChE Meeting, Miami, FL, 11/86. 1986.

King, J. A., Shair, F. H. and Reible, D. D. The influence of atmospheric stability on pollutant transport by slope winds. Atm. Env., v. 21, 53-59. 1987.

Konrad, J. H. An experimental investigation of mixing in two-dimensional turbulent shear flows with applications to diffusion limited chemical reactions. Technical Report CIT-8-PU, Project Squid, Dept. of Navy. 1977.

Kulkarni, A.K., Jacobs, H.R. and Hwang, J.J. Similarity solution for natural convection flow over an isothermal vertical wall immersed in thermally stratified medium. Int. J. Heat Mass Transfer, v. 30, no. 4, 691-698. 1987.

Kutateladze, S. and Berdnikov, V. Structure of thermogravitational convection in flat variously oriented layers of liquid and on a vertical wall. Int. J. Heat Mass Transfer, v. 27, 1595-1611. 1984.

Lamb, B.K. Development and application of dual atmospheric tracer techniques for the characterization of pollutant transport and dispersion. PhD Thesis, Calif. Inst. Tech., Pasadena, Calif. 1978.

Leahey, D.M. and Hansen, M.C. Influences of terrain on plume level winds in the Athabasca oilsands area. Atm. Env., v. 16, 2489. 1982.

Lenschow, D.H., Stankov, B.B. and Mahrt, L. The rapid morning boundary layer transition. J. Atmos. Sci., v. 36, 2108-2124. 1979.

Liburdy, J.A. and Faeth, G.M. Heat transfer and mean structure of a turbulent thermal plume along a vertical isothermal wall. Journal of Heat Transfer, v. 100, 177-183. 1978.

Linden, P.F. The deepening of a mixed layer in a stratified fluid. J. Fluid Mech., v. 71, 385. 1975.

Lloyd, J.R. and Sparrow, E.M. On the instability of natural convection flow on inclined plates. J. Fluid Mech., v. 42, 465-470. 1970.

Lloyd, J.R., Sparrow, E.M. and Eckert, E.R.G. Laminar, transition and turbulent natural convection adjacent to inclined and vertical surfaces. Int. J. Heat Mass Transfer, v. 15, 457-473. 1972.

Lund, K.O. and Bush, W.B. Asymptotic analysis of plane turbulent Couette-Poiseuille flows. J. Fluid Mech., v. 96, 81-104. 1980.

Mahrt, L. Penetrative convection at the top of a growing boundary layer. Quart. J. Roy. Met. Soc., v. 105, 469-485. 1979.

Manins, P.C. and Sawford, B.L. Katabatic winds: a field case study. Quart. J. Roy. Met. Soc., v. 105, 1011-1025. 1979.

Markatos, N.C. Transient flow and heat transfer of liquid sodium coolant in the outlet plenum of a fast nuclear reactor. Int. J. Heat Mass Transfer, v. 21, 1565-1579. 1978.

Markatos, N.C. and Pericleous, K.A. Laminar and turbulent natural convection in an enclosed cavity. Int. J. Heat Mass Transfer, v. 27, 755-772. 1984.

McAdams, W.H. Heat transmission. (3rd ed.) McGraw-Hill Book Co., New York, 1954.

McLaughlin, S.B. Effects of air pollution on forests: a critical review. J.A.P.C.A., v. 35, pp. 511-534. 1985.

McNider, R. and Pielke, R. Diurnal boundary layer development over sloping terrain. J. Atmos. Sci., v. 38, 2198. 1981.

McRae, G.J. Mathematical modeling of photochemical air pollution. PhD thesis, Calif. Inst. Tech., Pasadena, Calif. 1981.

McRae, G., and Seinfeld, J. Development of a second generation mathematical model for urban air pollution - II. Evaluation of model performance. Atm. Env., v. 17, 501-522. 1983.

Meroney, R.N., Cermak, J.E., and Yang, B.T. Modeling of atmospheric transport and fumigation at shoreline sites. Bound. Lay. Met., v. 9., 69. 1975.

Miller, Paul R., etal. Photochemical oxidant air pollutant effects on a mixed conifer forest ecosystem - A progress report. EPA-600/3-77-104, U.S. EPA, Office of R&D, Ecol. Rsch. Ser. 1977.

Miller, P.R., McCutchan, M.H. and Milligam, H.P. Oxidant air pollution in the Central Valley, Sierra Nevada foothills and Mineral King Valley of California. Atmospheric Environment, 6, 622-633. 1972.

Miller, R.M. and Gebhart, B. An experimental study of the natural convection flow over a heated ridge in air. Int. J. Heat Mass Transfer, v. 21, 1229-1239. 1978.

Minkowycz, W.J., Sparrow, E.M., Schneider, G.E., and Pletcher, R.H. Handbook of numerical heat transfer. John Wiley and Sons, Inc., New York. 1988.

Miyamoto, M., Kajino, H., Kurima, J., or Takanami, I. Development of turbulence characteristics in a vertical free convection boundary layer. Proc. 7th Intl. H.T. Conf., v. 2, 323-328, Munich, F.R.G. 1982.

Mizuno, T. and Yokoyama, O. On the vertical diffusion from a ground level source in a developing mixing layer. Atmospheric Environment, v. 20, no. 1, 21-27. 1986.

Mollendorf, J.C., Arif, H. and Ajiniran, E.B. Developing flow and transport above a suddenly heated horizontal surface in water. Int. J. Heat Mass Transfer, v. 27, 273-289. 1984.

Moore, M.J. and Long, R.R. An experimental investigation of turbulent shearing flow. J. Fluid Mech., v. 49, 635-655. 1971.

Nagashima, A. Viscosity of water substance -- new international formulation and its background. J. of Physical and Chemical Reference Data, v. 6, 1159-1160. 1977.

Nakayama, A. and Koyama, H. An approximate solution procedure for laminar free and forced convection heat transfer problems. Int. J. Heat Mass Transfer, v. 26, no. 11, 1721-1726. 1983.

Neiburger, M. The role of meteorology in the study and control of air pollution. Bull. Amer. Met. Soc., v. 50, 957. 1969.

Nieuwstadt, F.T.M. and de Haan, B.J. An analytic solution of the one-dimensional diffusion equation in a non-stationary boundary layer with an application to inversion rise fumigation. Atmospheric Environment, v. 15, 845-851. 1981.

Odell, G.M. and Kovasznay, L.S.G. A new type of water channel with density stratification. J. Fluid Mech., v. 59, 535. 1971.

Ogawa, Y., Diosey, P.G., Uehara, K. and Ueda, H. A wind tunnel for studying the effects of thermal stratification in the atmosphere. Atm. Env., v. 15, 807-821. 1981.

Ogawa, Y., Griffiths, R. and Hoydysh, W.G. A wind-tunnel study of sea breeze effects. Bound. Lay. Met., v. 8, 141-161. 1975.

Orville, H. On mountain upslope winds. J. Atmos. Sci., v. 21, 622-633. 1964.

Ostrach, S. An analysis of laminar free-convection flow and heat transfer about a flat plate parallel to the direction of the generating body force. NACA TR 1111 1953.

Patankar, S.V. Numerical heat transfer and fluid flow. Hemisphere Publishing Corp., McGraw Hill Book Co., New York. 1980.

Patrick, M.A., Wragg, A.A. and Pargeter, D.M. Mass transfer by free convection during electrolysis at inclined electrodes. Can. J. Chem. Eng., v. 55, 432. 1977.

Pera, L. and Gebhart, B. Natural convection boundary layer flow over horizontal and slightly inclined surfaces. Int. J. Heat Mass Transfer, v. 16, 1131-1146. 1973.

Peyret, R. and Taylor, T. Computational methods for fluid flow. Springer-Verlag, New York. 1983.

Pielke, R. Note: The relationship between numerical and physical models of atmospheric flow. Environmental Software, v. 3, 39-41. 1988.

Powell, G.M. The structure of velocity and density interfaces in a weakly turbulent stratified shear flow. PhD thesis, University of Florida. 1980.

Prandtl, L. Stromungslehre. Braunschweig, Vieweg und Sohn. 1942.

Prandtl, L. Essentials of fluid dynamics. Blackie and Son Ltd., London. 1952.

Press, W. et al. Numerical recipes: the art of scientific computing. Cambridge University Press, New York, 1986.

Pronos, J., Vogler, D.R. and Smith, R.S. An evaluation of ozone injury to pines in the southern Sierra Nevada. Report 78-1, USDA Forest Service, San Francisco, CA. 1978.

Qureshi, Z.H. and Gebhart, B. Transition and transport in a buoyancy driven flow in water adjacent to a vertical uniform flux surface. Int. J. Heat Mass Transfer, v. 21, 1467-1479. 1978.

Rahm, L. On the thermal adjustment of an almost-enclosed fluid region with through-flow. Int. J. Heat Mass Transfer, v. 29, no. 10, 1479-1485. 1986.

Rees, D.A.S. and Riley, D.S. Free convection above a near horizontal semi-infinite heated surface embedded in a saturated porous medium. Int. J. Heat Mass Transfer, v. 28, no. 1, 183-190. 1985.

Reible, D.D. Investigations of transport in complex atmospheric flows. Ph.D. Dissertation. California Inst. of Technology. 1982.

Reible, D.D., Shair, F.H. and Aris, R. A two-layer model of the atmosphere indicating the effects of mixing between the surface layer and the air aloft. Atm. Env., v. 17, 25-33. 1983.

Rich, B.R. An investigation of heat transfer from an inclined flat plate in free convection. Trans. ASME, v. 75, 489-498. 1953.

Riley, N. Note on a paper by Kierkus. Int. J. Heat Mass Transfer, v. 18, 991-993. 1975.

Roberts, T.M. Effects of air pollutants on agriculture and forestry. Atmos. Env., v. 18, 629-652. 1984.

Rohsenow, W.M., Hartnett, J.P., and Ganic, E.N. (eds.) Handbook of heat transfer applications. (2nd edition) McGraw-Hill Book Co., New York. 1985.

Ruiz, R. Natural convection heat transfer in partially enclosed configurations. Ph. D. Dissertation. University of Minnesota. 1986.

Ryan, B. A mathematical model for diagnosis and prediction of surface winds in mountainous terrain. J. Appl. Met., v. 16, 571-584. 1977.

Schmidt, E. Schlierenaufnahmen des Temperaturfeides in der Nahe Warmeabgebender Korper. Forsch. Geb. IngWes, 3, 181-189. 1932.

Schreiber, W.C. and Singh, S.N. Natural convection from a flat plate oriented at an arbitrary angle in an infinite medium. Chem. Eng. Comm., v. 56, 149-168. 1987.

Sedahmed, G.H. and Shemilt, L.W. Natural convection mass transfer at cylinders in different positions. Chem. Eng. Sci., v. 37, 159. 1982.

Seinfeld, J.H. Air pollution: physical and chemical fundamentals. McGraw Hill, Inc., New York. 1975.

Shaukatullah, H. and Gebhart, B. An experimental investigation of natural convection flow on an inclined surface. Int. J. Heat Mass Transfer, v. 21, 1481-1490. 1978.

Shenoy, A.V. Laminar-mixed convection heat transfer from an isothermal inclined flat plate to power law fluids. AIChE J., v. 30, 824-826. 1984.

Simpson, J.E. Gravity currents in the laboratory, atmosphere, and ocean. Ann. Rev. Fluid Mech., v. 14, 213-234. 1982.

Singh, P. and Liburdy, J.A. Effect of plate inclination on natural convection from a plate to its cylindrical enclosure. Journal of Heat Transfer, v. 108, 770-775. 1986.

Sivertsen, B., Lamb, B. and Gronskei, K.E. A tracer study of pollutant transport in a deep, fjord valley. Atm. Env., v. 17, 1915-1922. 1983.

Smalley, C. A study of air flow patterns in the San Francisco Bay Area. Information Bull. 6-15-70 Technical Services Division. Bay Area APCD, San Francisco, Calif. 1970.

Smedman, A. and Hogstrom, U. The height of the convective layer. Boundary Layer Meterology, v. 25, 271-287. 1983.

Snyder, W.H. and Hunt, J.C. Turbulent diffusion from a point source in stratified and neutral flows around a three-dimensional hill--II. Laboratory measurements of surface concentration. Atm. Env., v. 18, 1969-2002. 1984.

Sorbjan, Z. Rossby-number similarity in the atmospheric boundary layer over a slightly inclined terrain. J. Atmos. Sci., v. 40, 718-728. 1983.

Sorbjan, Z. Effects of baroclinity on resistance laws for the atmospheric boundary layer over a slightly inclined terrain. J. Atmos. Sci., v. 40, 729-737. 1983.

Sorbjan, Z. A model study of the stably stratified steady-state atmospheric boundary layer over a slightly inclined terrain. J. of the Atmospheric Sciences, v. 41, 1863-1874. 1984.

Spalding, D.B. A general purpose computer program for multi-dimensional one- and two-phase flow. Mathematics and Computers in Simulation, v. 23, 267-276. 1981.

Sparrow, E.M. and Gregg, J.L. Laminar free convection from a vertical plate with uniform surface heat flux. Transactions of the ASME, v. 78, 435-440. 1956.

Sparrow, E.M. and Prakash, C. Interaction between internal natural convection in an enclosure and an external natural convection boundary-layer flow. Int. J. Heat Mass Tranfer, v. 24, 895-907. 1981.

Sparrow, E.M. and Tao, W.Q. Buoyancy-driven fluid flow and heat transfer in a pair of interacting vertical parallel channels. Numerical Heat Transfer, v. 5, 39-58. 1982.

Start, G.E., Dickson, C.R. and Ricks, N.R. Effluent dilutions over mountainous terrain and within mountain canyons. Symposium on Atmospheric Diffusion and Air Pollution, American Meteorological Society, Boston, Mass. 1974.

Strada, M. and Heinrich, J.C. Heat transfer rates in natural convection at high Rayleigh numbers in rectangular enclosures: a numerical study. Numerical Heat Transfer, v. 5, 81-93. 1982.

Surma Devi, C.D. and Nath, G. Unsteady nonsimilar natural convection over a vertical flat plate in a thermally stratified fluid. Int. J. Heat Mass Tranfer, v. 27, 1424-1427. 1984.

Sutton, O.G. Micrometeorology. McGraw Hill; New York. 1953.

TSI Inc. Instruction Manual: Model 1980 Counter Type Signal Processor for Laser Velocimeter. TSI Inc.; St. Paul. 1980.

TSI Inc. System 9100-3 General Purpose Helium-Neon LDV System Instruction Manual (Revision A). TSI Inc.; St. Paul. 1980.

TSI Inc. Two Component, Polarization System 9100-9 Preliminary. TSI Inc.; St. Paul. 1980.

TSI Inc. Model 9180 Frequency Shift System Instruction Manual (Revision B). TSI Inc.; St. Paul. 1979.

TSI Inc. Laser Velocimetry Systems Catalog. TSI Inc.; St. Paul. 1979.

Taulbee, D.B. and Shabbir, A. Evaluation of turbulence models for predicting buoyant flows. NSF Grant ATM-8023699 Report. 1987.

Taylor, G.I. Statistical theory of turbulence. Proc. Royal Soc. London, Series A, v. 151, 421. 1935.

Tennekes, H. Similarity relations, scaling laws and spectral dynamics. From 'Atmospheric turbulence and air pollution modelling' Nieuwstadt and van Dop, (ed.) Reidel Publishing Company, Dolbrecht, Holland. 1982.

Tennekes, H. and Lumley, J.L. A first course in turbulence. MIT Press; Cambridge, Massachusetts, 1972.

To, W.M. and Humphrey, J.A.C. Numerical simulation of buoyant, turbulent flow - I. Free convection along a heated, vertical, flat plate. Int. J. Heat Mass Transfer, v. 29, pp. 573-592. 1986.

Touloukian, Y.S. and Makita, T. Thermophysical properties of matter - specific heat. v. 6, IFI/Plenum, New York. 1981.

Touloukian, Y.S., Liley, P.E. and Saxena, S.C. Thermophysical Properties of Matter-Conductivity. v. 3, IFI/Plenum, New York. 1981.

Tritton, D.J. Transition to turbulence in the free convection boundary layers on an inclined plate. J. Fluid Mech., v. 16, 417. 1963.

Tsuji, T. and Nagano, Y. Characteristics of a turbulent natural convection boundary layer along a vertical flat plate. Int. J. Heat Mass Transfer, v. 31, no. 8, 1723-1734. 1988.

Turner, J.S. Buoyancy effects in fluids. Cambridge University Press; London. 1973.

Tzuoo, K.L., Chen, T.S. and Armaly, B.F. Wave instability of natural convection flow on inclined surfaces. Journal of Heat Transfer, v. 107, 107-111. 1985.

Ueda, H., Mitsumoto, S. and Komori, S. Buoyancy effects on the turbulent transport processes in the lower atmosphere. Quart. J. R. Met. Soc., v. 107, 561-578. 1981.

Van Valin, C.C., Pueschel, R.F., Barrett, E.W. and Williams, G. Field observations of stratified atmospheric flow above an obstacle. Bound. Lay. Met., v. 24, 331-343. 1982.

Venkatachala, B. and Nath, G. Nonsimilar laminar natural convection in a thermally stratified fluid. Int. J. Heat Mass Transfer, v. 24, 1848-1850. 1981.

Vergeiner, I. Eine energetische theorie der hangwinde. Annalen der Meteorologie, Offenbach a./M., n.s., #19, 189-193. 1982.

Vliet, G.C. Natural convection local heat transfer on constant-heat-flux inclined surfaces. J. Heat Transfer, v. 91, 511. 1969.

Vliet, G.C. and Ross, D.C. Turbulent natural convection on upward and downward facing inclined constant heat flux surfaces. J. Heat Transfer, ASME Trans. Series C, v. 97, 549-555. 1975.

Vliet, G.C., and Liu, C.K. An experimental study of turbulent natural convection boundary layers. J. Heat Transfer, v. 91C, 517-531. 1969.

Walin, G. Contained non-homogeneous flow under gravity or how to stratify a fluid in the laboratory. J. Fluid Mech. v. 48, 647-672. 1971.

Warner, C.Y. and Arpaci, V.S. An experimental investigation of turbulent natural convection in air at low pressure along a vertical heated flat plate. Int. J. Heat Mass Transfer, v. 11, 397. 1968.

Weast, R.C. (ed.) CRC handbook of chemistry and physics (55th edition). Chemical Rubber Publishing Company, Ohio. 1974.

Welty, J.R., Wicks, C.E., Wilson, R.E. Fundamentals of momentum, heat, and mass transfer. John Wiley and Sons, Inc., New York. 1984.

Whaley, H., Lee, G.K., and Gainer, J.G. The behavior of buoyant merging plumes in the rocky mountain foothills. J.A.P.C.A., v. 30, 782-786. 1980.

Whiteman, C.D. and McKee, T.B. Observations of vertical atmospheric structure in a deep mountain valley. Arch. Meteor. Geophys. Bioklim., A26, 39-50. 1977.

Whiteman, C.D. and McKee, T.B. Air pollution implications of inversion descent in mountain valleys. Atmos. Environ., 12, 2151-2158. 1978.

Wilkinson, D. and Wood, I. The formation of an intermediate layer by horizontal convection in two layer shear flow. J. Fluid Mech., v. 105, 1983.

Williams, W.T., Brady, M., and Willison, S.C. Air pollution damage to the forests of the Sierra Nevada Mountains of California. J.A.P.C.A., 27, 3, 230-234. 1977.

Willis, G.E. and Deardorff, J.W. A laboratory model of the unstable planetary boundary layer. J. Atmos. Sci., v. 31, 1297-1307. 1974.

Willis, G.E. and Deardorff, J.W. A laboratory model of diffusion into the convective planetary boundary layer. Quart. J. Roy. Met. Soc., v. 102, 427-445. 1976.

Willis, G.E. and Deardorff, J.W. A laboratory study of dispersion from an elevated source within a modeled convective planetary boundary layer. Atm. Env., v. 12, 1305-1311. 1978.

Willis, G.E. and Deardorff, J.W. A laboratory study of dispersion from a source in the middle of the convectively mixed layer. Atm. Env., v. 15, 109-117. 1981.

Willson, R., Shair, F., Reynolds, B. and Greene, W. Characterization of the transport and dispersion of pollutants in a narrow mountain valley region by means of an atmospheric tracer. Atm. Env., v. 17, 1633-1647. 1983.

Yang, K. Possible similarity solutions for laminar free convection on vertical plates and cylinders. Journal of Applied Mechanics, v. 27, 230-236. 1960.

Yang, K.T., Novotny, J.L. and Cheng, Y.S. Laminar free convection from a nonisothermal plate immersed in a temperature stratified medium. Int. J. Heat Mass Transfer, v. 15, 1097-1109. 1972.

Yang, K. and Jerger, E.W. First-order perturbations of laminar free-convection boundary layers on a vertical plate. Trans. ASME J. Heat Transfer, v. 86, 107-115. 1964.

Yung, Y.C. and Oetting, R.B. Free convection heat transfer from an inclined heated flat plate in air. Trans. ASME, 192. 1969.

Zaric, Z.P. (ed.) Structure of turbulence in heat and mass transfer. Hemisphere Publishing Co., Washington. 1982.

Zariffeh, E.K. and Daguenet, M. Laminar free convection on an inclined flat plate or a vertical cylinder with prescribed wall heat flux. Int. J. Heat Mass Transfer, v. 24, no. 6, 1071-1075. 1981.

Zeman, O. and Lumley, J.L. Modeling buoyancy driven mixed layers. J. Atmos. Sci., v. 33, 1974-1988. 1976.

Zeman, O. and Lumley, J.L. Buoyancy effects in entraining turbulent boundary layers: a 2nd order closure study. 'Turbulent shear flow (v. 1)' Durst etal. (ed.) 1977.

Nomenclature

α - thermal diffusivity

β - thermal expansion coefficient

$\delta\theta$ - potential temperature perturbation

π - dimensionless scaled pressure, $\pi = C_p/(P/1000mb)^{R/Cp}$ where P is pressure in millibars

ϕ - inclination of slope (from horizontal)

ρ - density

ρ_0 - density of reference state [kg/m^3]

τ - response time of thermistor (time for indicated temperature to reach 63.2% of correct value)

φ - inclination from horizontal (degrees)

θ - inclination from vertical (degrees)

θ_0 - potential temperature of reference state

θ - potential temperature (Section 5.1)

θ" - fluctuating temperature (Section 5.1)

θ - temperature deviation for Prandtl model ($T-T\infty$) (Section 5.3, Appendix 5)

ν - kinematic viscosity

μ - viscosity

Ω - rotation rate [rad/s]

B - constant ambient temperature gradient

C - empirical constant

C_p - specific heat [J/kgK]

e_{si} - measure of subgrid scale velocity correlations that can be estimated from the mean subgrid scale kinetic energy so that $e_{si}=[u_i"^2/2]^{0.5}$

g - acceleration of gravity

Gr_x^* - modified local Grashof number ($=Gr_xNu_x$)

Gr_x - local Grashof number

h - heat transfer coefficient (Chapter 4)

H - mixed layer depth (Section 5.1)

h_v - vertical height (Section 5.3)

h_x - local heat transfer coefficient (Section 5.3)

k - thermal conductivity (Chapter 4)

k_θ - thermal conductivity [w/mK] (Section 5.1)

K_H - turbulent exchange coefficient for heat (Section 5.3)

K_M - turbulent exchange coefficient for momentum (Section 5.3)

l - Prandtl model length scale (Section 5.3)

L - plate length (Chapter 4)

L - representative length scale (Section 5.1)

$-L_{MO}$ - Monin Obukhov length scale $=\rho u_*^3/(g\rho' w')$ (Section 5.1)

m - empirical constant (Chapter 4)

Nu_{av} - overall average Nusselt number (Chapter 4)

Nu_x - local Nusselt number (Chapter 4)

P_{diss} - power dissipated (Chapter 3)

Pr - Prandtl number (Chapter 4)

q_w - wall heat flux (Chapter 4)

R - ideal gas constant (Section 5.1)

R - resistance of plate (Chapter 4)

Ra_x^* - modified local Rayleigh number (Chapter 4)

Ra_x - local Rayleigh number (Chapter 4)

Re - Reynolds number (Section 5.1)

Ri_b - bulk Richardson number (Section 5.1)

R_l - load resistance (~124kΩ) (Chapter 3)

Ro - Rossby number (Section 5.1)

R_t - thermistor resistance (Chapter 3)

S - representative velocity scale (Section 5.1)

S_θ - source/sink term for energy equation (Section 5.1)

T - temperature

T_∞ - ambient fluid temperature (Section 5.3)

δ_T - thickness of thermal boundary layer (Chapter 4)

t - time

T_b - bulk temperature (Chapter 4)

T_f - film temperature (Chapter 4)

T_w - wall temperature (Chapter 4)

u - velocity (x - component)

u_i - ith velocity component, (dimensionless with a ^, overbar designates an averaged quantity) (Section 5.1)

$u_j"u_j"$ - fluctuating velocity covariance (Section 5.1)

U - gradient wind speed (Section 5.1)

v - component of velocity in y direction

V_0 - battery voltage (Chapter 3)

V_i - voltage on channel i (Chapter 3)

w - component of velocity in z direction

w^* - fluctuating vertical velocity scale for penetrative free convection (Section 5.1)

x,y,z - spatial coordinates (inclined coordinate system for Prandtl model) (Section 5.3)

X - body force term (Section 5.3)

x - distance along length of heated surface

x_j - dimensional coordinate (dimensionless with a ^) (Section 5.1)

Appendices

Appendix 1

Physical Properties of Water

Density of Water

Density can be expressed as a function of temperature (t) using polynomials of the following form, according to Kell (1977):

$$P_n(t) = a_0 + a_1 t + a_2 t^2 + \ldots + a_n t^n \tag{A1-1}$$

$$\rho = R_{nm}(t) = \frac{P_n(t)}{1 + b_1 t + b_2 t^2 + \ldots + b_n t^n} \tag{A1-2}$$

The polynomial R_{51} is chosen as the optimal form to represent the volume properties of water, so that the density of water is fit to the following function:

$$\rho = R_{51} = \frac{P_5(t)}{1 + b_1 t} = \frac{a_0 + a_1 t + a_2 t^2 + a_3 t^3 + a_4 t^4 + a_5 t^5}{1 + b_1 t} \tag{A1-3}$$

The coefficients are given as:

$a_0 = 999.84252$
$a_1 = 16.945227$
$a_2 = -7.9870641 \times 10^{-3}$
$a_3 = -46.1706 \times 10^{-6}$
$a_4 = 105.56334 \times 10^{-9}$
$a_5 = -280.54337 \times 10^{-12}$
$b_1 = 16.879850 \times 10^{-3}$

Upon substituting the given coefficients into the polynomial, along with the temperature t in °K, the density can be calculated with units of kg/m^3.

Thermal Expansion Coefficient of Water

In order to calculate the thermal expansion coefficient, we note that, by definition,

$$\beta = -\frac{d(\ln \rho)}{dt} \tag{A1-4}$$

If we take the derivative with respect to time of the polynomial $R_{51}(t)$ used in the previous section, we obtain,

$$\beta = -\frac{a_1 + 2a_2 t + 3a_3 t^2 + 4a_4 t^3 + 5a_5 t^4}{a_0 + a_1 t + a_2 t^2 + a_3 t^3 + a_4 t^4 + a_5 t^5} + \frac{b_1}{b_1 t + 1} \tag{A1-5}$$

The units of the thermal expansion coefficient calculated from the above equation are 1/°K and the temperature (t) used is in °K.

Viscosity of Water

The viscosity of water was calculated using a relation given by Nagashima (1977) to account for the temperature dependence of viscosity. The viscosity is given in dimensions of Pascal-sec by the equation

$$\mu = D_1 \exp\left(\frac{1.0 + D_2 T}{D_3 T + D_4 T^2}\right) \tag{A1-6}$$

where T is the temperature in °K and the constants are given by

$D_1 = 1.2571873 \times 10^{-5}$
$D_2 = -5.8064362 \times 10^{-3}$
$D_3 = 1.1309108 \times 10^{-3}$
$D_4 = -5.7239520 \times 10^{-6}$

Kinematic Viscosity of Water

Kinematic viscosity is defined as the viscosity divided by the density, that is,

$$\nu = \frac{\mu}{\rho} \tag{A1-7}$$

Thus the kinematic viscosity of water is easily calculated using the values found above for the viscosity and density. The kinematic viscosity thereby obtained has units of m^2/sec.

Thermal Conductivity of Water

A relationship for the variance of thermal conductivity with temperature from Touloukian et al. (1981) was used to calculate values for thermal conductivity with the units of W/mK.

$$k = -0.5844 + 0.006376T - 8.0 \times 10^{-6} T^2 \tag{A1-8}$$

Specific Heat of Water

Specific heats were calculated using a formula obtained from Touloukian and Makita (1981). The equation used was:

$$C_p = 14948.5806 - 99.6832223T + 0.306832629T^2 - 0.000314017T^3 \tag{A1-9}$$

T is the temperature in °K and the dimensions obtained for the specific heat are J/kgK.

Thermal Diffusivity of Water

Thermal diffusivity is defined as:

$$\alpha = \frac{k}{\rho c_p} \tag{A1-10}$$

and can be calculated using the previously calculated values for thermal conductivity, density and specific heat.

Summary

The following table is compiled from values calculated by the Turbo Pascal unit PHYSPROP for quick estimates of properties. It can be seen that the values correspond reasonably well to similar sets of physical property data tabulated in heat transfer textbooks such as Welty et al. (1984).

Table A1-1 Physical Properties of Water as Calculated by PHYSPROP

T (K)	ρ (kg/m³)	c_p (J/kgK)	μ (Pa s) (×10⁶)	ν (m²/s) (×10⁶)	k (W/mK)	α (m²/s) (×10⁸)	Pr	β (1/K) (×10³)
293	998.2	4184	1006	1.008	0.597	0.143	7.02	0.207
313	992.2	4179	655	0.660	0.628	0.151	4.33	0.385
333	983.2	4183	468	0.476	0.652	0.158	2.94	0.523
353	971.8	4182	356	0.366	0.669	0.165	2.14	0.641

Appendix 2

Turbo Pascal Library Units and Programs

Appendix 2.1 PHYSPROP.TPU

```
Unit PhysProp;

Interface

Function ThermalExpansionCoeffH2O { 1 / K }
  (T:real) : real;
Function DensityH2O { kg / m3 }
  (T:real) : real;
Function ViscosityH2O { Pa sec }
  (T:real) : real;
Function KinematicViscosityH2O { m2 / sec }
  (T:real) : real;
Function ThermalConductivityH2O { W / m K }
  (T:real) : real;
Function ThermalDiffusivityH2O { m2 / sec }
  (T:real) : real;
Function SpecificHeatH2O { J / kg K }
  (T:real) : real;
Function PrandtlH2O
  (T:real) : real;
Function GrashofModH2O
  (T,Dist,Flux,Theta: real) : real;
Function GrashofH2O
  (T,Dist,Flux,DeltaT: real) : real;

Implementation

Function ThermalExpansionCoeffH2O;

{Reference: Kell (1977), Journal of Physical and Chemical Reference Data, v. 6, pg. 1115. Calculates thermal expansion coefficient
(1/deg) as a function of temperature (deg C)}

Var
  Numer,Denom : real;
  T2,T3,T4,T5 : real; {temperature raised to various powers}
Const
  A : array[0..5] of real = (999.84252, 16.945227, -7.9870641E-3,
    -46.1706E-6, 105.56334E-9, -280.54337E-12);
  B = 16.879850E-3;

Begin
  T2 := sqr(T);
  T3 := exp(3*ln(T));
  T4 := exp(4*ln(T));
  T5 := exp(5*ln(T));
  Numer := A[1] + 2*A[2]*T + 3*A[3]*T2 + 4*A[4]*T3 + 5*A[5]*T4;
  Denom := A[0] + A[1]*T + A[2]*T2 + A[3]*T3 + A[4]*T4 + A[5]*T5;
  ThermalExpansionCoeffH2O := -Numer/Denom + (B / (1 + B*T));
End; { function ThermalExpansionCoeffH2O }

Function DensityH2O;

{Reference: Kell (1977), Journal of Physical and Chemical Reference Data, v. 6, pg. 1115. Calculates density (kg/m3) as a function
of temperature (deg C)}

Var
  Num1,Num2 : real;
  T2,T3,T4,T5 : real;
Const
  A : array[0..5] of real = (999.84252, 16.945227, -7.9870641E-3,
    -46.1706E-6, 105.56334E-9, -280.54337E-12);
  B = 16.879850E-3;

Begin
  T2 := sqr(T);
  T3 := exp(3*ln(T));
  T4 := exp(4*ln(T));
  T5 := exp(5*ln(t));
  Num1 := A[0] + A[1]*T + A[2]*T2 + A[3]*T3 + A[4]*T4 + A[5]*T5;
  Num2 := 1 + B*T;
  DensityH2O := Num1/Num2;
{ DensityH2O := (Num1/Num2) * (0.999972)*(1000); Converts from g/ml to kg/m3}
End; { function DensityH2O }
```

```
Function ViscosityH2O;

{Reference: Nagashima (1977), Journal of Physical and Chemical Reference Data, v. 6, 1159. Calculates viscosity (Pa sec) as a function of temperature (deg C)}

Const
  D : array[1..4] of real
    = (1.2571873E-5, -5.8064362E-3, 1.1309108E-3, -5.7239520E-6);

Begin
  T := T + 273.17;
{ Num1 := (1.0 + D[2] * T)/(D[3]*T + D[4]*sqr(T));}
  ViscosityH2O := D[1] * exp ((1.0 + D[2]*T) / (D[3]*T + D[4]*sqr(T)));
End; {function ViscosityH2O }

Function KinematicViscosityH2O;

Begin
  KinematicViscosityH2O :=(ViscosityH2O(T)/DensityH2O(T));
End; { function KinematicViscosityH2O }

Function ThermalConductivityH2O;

{Reference: Touloukian, et al. (1981), Thermophysical properties of matter - Conductivity. v. 3. Calculates thermal conductivity (W/mK) as a function of temperature (deg C)}

Begin
T := T + 273.17;
ThermalConductivityH2O := -0.58443 + 0.006376*T - 8.0E-6*(sqr(T));
End;

Function ThermalDiffusivityH2O;

{Calculates thermal diffusivity coefficient for water (m2/s) as a function of temperature in degrees C}

Begin
  ThermalDiffusivityH2O := ThermalConductivityH2O(T)/
    (DensityH2O(T)*SpecificHeatH2O(T));
End; {function ThermalDiffusivityH2O }

Function SpecificHeatH2O;

{Reference: Touloukian and Makita (1981), Thermophysical properties of matter - Specific Heat. v. 6. Calculates specific heat for water (J/kgK) as a function of temperature in degrees C}

Var
  T2,T3: real;

Begin
T := T + 273.17;
T2 := sqr(T);
T3 := exp(3*ln(T));
SpecificHeatH2O := 14948.5806 - 99.6832223*T + 0.306832629*T2 - 0.00031401*T3;
End; {function SpecificHeatH2O}

Function PrandtlH2O;

Begin
  PrandtlH2O := KinematicViscosityH2O(T)/ThermalDiffusivityH2O(T);
End;

Function GrashofModH2O;

Const
  g = 9.81;
Var
  gCosTheta,Beta,L4,Nu,Kappa : real;

Begin
  gCosTheta := g * Cos((90-Theta)*Pi/180);
  Nu := KinematicViscosityH2O(T);
  Kappa := ThermalConductivityH2O(T);
  Beta := ThermalExpansionCoeffH2O(T);
  L4 := Sqr(Sqr(Dist));
  GrashofModH2O := gCosTheta*Beta*L4*Flux/Kappa/Sqr(Nu);
End;

Function GrashofH2O;
```

```
Const
  g = 9.81;
Var
  Beta,L3,Nu,Kappa : real;

Begin
  Nu := KinematicViscosityH2O(T);
  Kappa := ThermalConductivityH2O(T);
  Beta := ThermalExpansionCoeffH2O(T);
  L3 := Dist * Dist * Dist;
  GrashofH2O := g*Beta*DeltaT*L3/Sqr(Nu);
End;

End. {PhysProp Unit}
```

Appendix 2.2 THERMLIB.TPU

```
Unit ThermLib;

Interface

Procedure MeasureVoltage
  (Channel, Gain, NTimes : integer; Var Voltage : real);
Procedure CheckBattery
  (var Voltage : real);
Procedure CheckBatteryNoPrint
  (var Voltage : real);
Function CalibValue
  (Channel : integer; R : real) : real;
Procedure SampleThermistor
  (Channel : integer; V0 : real; var Ohms : real);
Procedure SampleThermistorNTimes
  (Channel : integer; V0 : real; var AvgOhms,StdDev : real; NTimes : Integer);
Procedure SampleThermistorNTimesNoSD
  (Channel : integer; V0 : real; var AvgOhms : real; NTimes : Integer);
Procedure SampleActiveThermistorsNTimes
  (V0 : Real; ActiveChannelNumbers : ChannelNumbers; NTimes : Integer; Var Temperature: Range1);
Procedure SampleActiveResistancesNTimes
  (V0 : Real; ActiveChannelNumbers : ChannelNumbers; NTimes : Integer; Var AvgOhms: Range1);

Implementation

Const
  RLoad : array[1..15] of real = (124510.0,124230.0,124220.0,124160.0,124300.0,
  124420.0,124040.0,124610.0,124590.0,124160.0,123930.0,124070.0,123440.0,
  124230.0,124040.0);

Procedure MeasureVoltage;
  { This procedure measures the voltage on a selected channel }

Var
  Sum : real;
  I : integer; { index for do loop }
  PGLGain : integer; { the actual gain which the signal is multiplied by }

Begin
  Sum:= 0;
  If Gain=0 Then PGLGain:=1;    { Allows user to select voltage range }
  If Gain=1 Then PGLGain:=10;   { for best accuracy.}
  If Gain=2 Then PGLGain:=100;
  If Gain=3 Then PGLGain:=500;
  Port[16]:= 4+Gain; { Select load enable and set gain }
  Port[18]:= Channel; { Select channel to measure }
  For I:= 1 To NTimes Do
  Begin
    { Measures analog voltage and translates digital signal }
    Port[20]:=0;       { Start the AD }
    While (Port[16] shr 7) <> 1 Do    { Wait for A/D done bit };
    Voltage:= Port[18] + (Port[20] shl 8);
    Voltage:= Voltage * 10 / PGLGain / 4096;
    Sum:= Sum + Voltage;
  End;
  Voltage:=Sum/NTimes;
End;

Procedure CheckBattery;
  { Check battery to make sure its turned on and not drained.}

Const
  Channel = 0; { Battery on Channel 0 }
  Gain = 0;   { Gain select = 00 for PGL gain of 1 (Tecmar p. 56) }
  NTimes = 500; { Number of times to sample and average }
Var
  Response : char;

Begin
  MeasureVoltage(Channel, Gain, NTimes, Voltage);
  While Voltage < 3.5 Do
  Begin
    { Informs user that voltage is low and allows him either to go on }
    { using the low battery or remedy the situation          }
    WriteLn ('Battery voltage = ',Voltage:8:4,' CAUTION Battery may be low or off');
    WriteLn ('Return to remeasure, H to halt, C to continue with low battery');
    ReadLn (Response);
    If Upcase(Response) = 'H' Then Halt;
    If Upcase(Response) = 'C' Then Exit;
```

```
  MeasureVoltage(Channel, Gain, NTimes, Voltage);
 End;
Writeln ('Battery voltage = ',Voltage:8:4);    { Prints operating voltage }
End;

Procedure CheckBatteryNoPrint;
 { Check battery to make sure its turned on and not drained.}

Const
 Channel = 0; { Battery on Channel 0 }
 Gain = 0;   { Gain select = 00 for PGL gain of 1 (Tecmar p. 56) }
 NTimes = 500; { Number of times to sample and average }
Var
 Response : char;

Begin
 { Informs user that the voltage is low and allows him either to go }
 { on using the low battery or to remedy the situation        }
 MeasureVoltage(Channel, Gain, NTimes, Voltage);
 While Voltage < 3.5 Do
 Begin
  WriteLn ('Battery voltage = ',Voltage:8:4,'  CAUTION Battery may be low or off');
  WriteLn ('Return to remeasure, H to halt, C to continue with low battery');
  ReadLn (Response);
  If Upcase(Response) = 'H' Then Halt;
  If Upcase(Response) = 'C' Then Exit;
  MeasureVoltage(Channel, Gain, NTimes, Voltage);
 End;
End;

Function CalibValue;
 { Takes the resistance of a thermistor and converts it to temperature in degrees C.  Uses Steinhart-Hart parameters A, B, and C. }

Const

{Data set RTEST40.FIT}
A: array [0..15] of real = (1.0298319E-03,
 7.3647985E-04, 8.2726543E-04, 8.2808364E-04,
 1.4201387E-03, 8.7610597E-04, 8.7873656E-04,
 1.0129269E-03, 1.0333116E-03, 1.0689520E-03,
 1.0249923E-03, 1.0245102E-03, 1.0208861E-03,
 3.1809743E-03, 1.0297611E-03, 1.0233735E-03);

B: array [0..15] of real = (2.3895518E-04,
 2.8126172E-04, 2.6550329E-04, 2.6509161E-04,
 2.4730216E-03, 2.6085531E-04, 2.5861219E-04,
 2.4148746E-04, 2.3895569E-04, 2.3079049E-04,
 2.4043990E-04, 2.3986652E-04, 2.4013186E-04,
-1.0143123E-04, 2.3973885E-04, 2.4022631E-04);

C: array [0..15] of real = (1.5767218E-07,
 2.9089411E-08, 9.3652916E-08, 1.0293511E-07,
-1.3091784E-04, 1.1026339E-07, 1.0548487E-07,
 1.4639219E-07, 1.5812079E-07, 1.9934162E-07,
 1.5169667E-07, 1.5182573E-07, 1.4977546E-07,
 1.3871376E-06, 1.5398385E-07, 1.5016379E-07);

Var
 LogR : real;

Begin
 If (R < 10) or (A[Channel] = 0.0E+00) Then
  CalibValue := 0.0
 Else
 Begin
  LogR := Ln(R);
  CalibValue := 1/( A [Channel] + B [Channel]*LogR +
  C [Channel]*LogR*LogR*LogR)-273.17;
 End;
End;

Procedure SampleThermistor;

Var
 Voltage : real;

Begin
 MeasureVoltage(Channel,1,25,Voltage);  { Find voltage to compute resistance }
 Ohms:= RLoad[Channel]*Voltage/(V0-Voltage);  { Computes resistance }
End;
```

```
Procedure SampleThermistorNTimes;

Var
 Voltage,Sum,SumDev : real;
 N : integer;
 Ohms : array [1..NumMeasurements] of real;

Begin
Sum:= 0.0;
SumDev:=0.0;
For N:= 1 to NTimes Do
Begin
 MeasureVoltage(Channel,1,25,Voltage); { Finds voltage to compute resistance }
 Ohms[N]:= RLoad[Channel]*Voltage/(V0-Voltage); { Computes resistance n times}
 Sum:= Sum + Ohms[N];
End;
AvgOhms:=Sum/NTimes;   { Takes average of resistances computed }
For N:=1 to NTimes Do
 SumDev:= SumDev + sqr (AvgOhms- Ohms [N]);
StdDev:= sqrt (SumDev/(NTimes - 1));
End;

Procedure SampleThermistorNTimesNoSD;

Var
 Voltage,Sum,SumDev : real;
 N : integer;

Begin
Sum:= 0.0;
SumDev:=0.0;
For N:= 1 to NTimes Do
Begin
 MeasureVoltage(Channel,1,25,Voltage); { Finds voltage to compute resistance }
 Sum := Sum + RLoad[Channel]*Voltage/(V0-Voltage); { Computes resistance n times}
End;
AvgOhms:=Sum/NTimes;   { Takes average of resistances computed }
End;

Procedure SampleActiveThermistorsNTimes;

Var
 Voltage,Sum,AvgOhms : Range1;
 N,Chan : Integer;

Begin
FillChar(Sum,SizeOf(Sum),0);
For N:= 1 to NTimes Do
 For Chan:= 1 to 15 Do
 If Chan IN ActiveChannelNumbers Then
 Begin
  MeasureVoltage(Chan,1,25,Voltage[Chan]);
  Sum[Chan]:= Sum[Chan] + Voltage[Chan];
 End;
For Chan:= 1 to 15 Do
 If Chan IN ActiveChannelNumbers Then
 Begin
  Voltage[Chan]:= Sum[Chan]/NTimes;
  AvgOhms[Chan]:= Voltage[Chan] / (V0 - Voltage[Chan]) * RLoad[Chan];
  Temperature[Chan]:= CalibValue(Chan,AvgOhms[Chan]);
 End;
End;

Procedure SampleActiveResistancesNTimes;

Var
 Voltage,Sum : Range1;
 N,Chan : Integer;

Begin
FillChar(Sum,SizeOf(Sum),0);
For N:= 1 to NTimes Do
 For Chan:= 1 to 15 Do
 If Chan IN ActiveChannelNumbers Then
 Begin
  MeasureVoltage(Chan,1,25,Voltage[Chan]);
  Sum[Chan]:= Sum[Chan] + Voltage[Chan];
 End;
For Chan:= 1 to 15 Do
 If Chan IN ActiveChannelNumbers Then
 Begin
```

```
    Voltage[Chan]:= Sum[Chan]/NTimes;
    AvgOhms[Chan]:= Voltage[Chan] / (V0 - Voltage[Chan]) * RLoad[Chan];
  End;
End;

End. { of thermlib unit }
```

Appendix 2.3 TRAVLIB.TPU

```
Unit TravLib;

Interface

Function MovementCompleted
 (CounterNum : integer) : boolean;
 { Check if traverser has completed it's motion and toggled off }
Function HexValue
 (Num : integer) : integer;
 { Converts decimal to hex eg. 1000 to 4096 or 97 to 151 }
Procedure RampTo
 (Speed : integer);
 { Allows traverser to accelerate gradually to top speed (% of 1 cm/sec) }
Procedure MoveThermUp
 (Dist : Real); { Dist = distance to travel in cm }
 { This procedure moves traverser 2 up a given distance }
Procedure MoveThermDown
 (Dist : Real); { Dist = distance to travel in cm }
 { This procedure moves traverser 2 down a given distance }
Procedure InitTraverser;
 { This procedure sets up counters 1 and 2 to move traverser 2 as clocked by counter 3. }

Implementation

Procedure InitTraverser;
{ This procedure sets up counters 1 and 2 to move traverser 2 as clocked by counter 3. }

Begin
 Port[30]:=255;  { master mode reset }
 Port[30]:=95;   { load all counters to clear }
 Port[30]:=23;   { set data pointer to master mode register }
 Port[28]:=0;    { lo byte of command to MM register }
 Port[28]:=208;  { hi byte of command to MM register }
 Port[30]:=1;    { set data pointer to counter mode register 1 }
 Port[28]:=18;   { set counter 1 to BCD count down on rising edge of SRC 1 }
 Port[28]:=1;    { TC toggled output, no special gating }
 Port[30]:=2;    { set data pointer to counter mode register 2 }
 Port[28]:=18;   { set counter 2 to BCD count down on rising edge of SRC 1, }
 Port[28]:=1;    { TC toggled output, no special gating }
End;

Function MovementCompleted;
 { Check if traverser has completed it's motion and toggled off }

Begin
 Port[30]:= 31;  { set data pointer to status register (00011111) }
 MovementCompleted:= Not Odd (Port[30] shr CounterNum); { read status byte and isolate bit }
End;

Function HexValue;
 { Converts decimal to hex eg. 1000 to 4096 or 97 to 151 }

Var
 D1,D2,D3,D4: integer; { representing 1's place, 10's place etc. }
Begin
 If (Num>9999) Then
 Begin
  WriteLn ('Cannot determine hex value for more than four digits');
  Halt
 End;
 D1:=Num mod 10;
 D2:=Num mod 100 div 10;
 D3:=Num mod 1000 div 100;
 D4:=Num div 1000;
 HexValue:= D4*4096 + D3*256 + D2*16 + D1;
End;

Procedure RampTo;
 { Allows traverser to accelerate gradually to top speed (% of 1 cm/sec) }

Var
 {Speed: integer;  - percentage of max speed (1 cm/s) }
 StepsPerSec: integer;  { - note 1 cm = 1000 steps }
 TerminalCount: integer; { - the number to count up to each second }
 I : integer;
```

```
Begin
 StepsPerSec:= 10;
 Port[30]:= 3;   { set data pointer to counter 3 mode register }
 Port[28]:= 49;  { send setup command to counter 3 mode register }
 Port[28]:= 12;  { send setup command to counter 3 mode register }
 Port[30]:= 11;  { set data pointer to counter 3 data register }
 While StepsPerSec < (Speed * 10) Do
 Begin { the ramping procedure }
  I:=0;
  Repeat I:=I+1 Until I = 1000;{Waste Some Time};
  StepsPerSec:= StepsPerSec + 1;
  TerminalCount:= Round(100000.0/StepsPerSec);
  Port[28]:= Lo (HexValue (TerminalCount));  { load TC value }
  Port[28]:= Hi (HexValue (TerminalCount));  { load TC value }
  Port[30]:= 100;  { load and arm counter 3 }
 End; { the ramping procedure }
End;

Procedure MoveThermUp;
{ This procedure moves traverser 2 up a given distance }

Var
 Steps: integer; { Distance to travel in steps }
Const
 Speed = 25;

Begin
 While (Dist>=9) Do
 Begin
  Dist:= Dist - 9;
  Steps:= Round(1000*9);
  Port[30]:=10; { set data pointer to load register counter 2 }
  Port[28]:=Lo(HexValue(Steps));
  Port[28]:=Hi(HexValue(Steps));
  Repeat     { pause until the status bit for out1 toggles off }
  Until MovementCompleted(2);
  Port[30]:=98; { load and arm counter 2 }
  Port[30]:=234;
  RampTo(Speed);
 End;
 Steps:= Round(1000*Dist);
 Port[30]:=10; { set data pointer to load register counter 2 }
 Port[28]:=Lo(HexValue(Steps));
 Port[28]:=Hi(HexValue(Steps));
 Repeat     { pause until the status bit for out1 toggles off }
 Until MovementCompleted(2);
 Port[30]:=98; { load and arm counter 2 }
 Port[30]:=234;
 RampTo(Speed);
 Repeat     { pause until the status bit for out1 toggles off }
 Until MovementCompleted(2);
End;

Procedure MoveThermDown;
{ This procedure moves traverser 2 down a given distance }

Var
 Steps: integer; { Distance to travel in steps }
Const
 Speed = 50;

Begin
 While (Dist>=9) Do {Hexvalue function can't handle numbers bigger than 9}
 Begin
  Dist:= Dist - 9;
  Steps:= Round(1000*9);
  Port[30]:=9; { set data pointer to load register counter 1 }
  Port[28]:=Lo(HexValue(Steps));
  Port[28]:=Hi(HexValue(Steps));
  Repeat     { pause until the status bit for out1 toggles off }
  Until MovementCompleted(1);
  Port[30]:=97; { load and arm counter 1 }
  Port[30]:=233;
  RampTo(Speed);
 End;
 Steps:= Round(1000*Dist);
 Port[30]:=9; { set data pointer to load register counter 1 }
 Port[28]:=Lo(HexValue(Steps));
 Port[28]:=Hi(HexValue(Steps));
 Repeat     { pause until the status bit for out1 toggles off }
 Until MovementCompleted(1);
```

```
  Port[30]:=97; { load and arm counter 1 }
  Port[30]:=233;
  RampTo(Speed);
  Repeat      { pause until the status bit for out1 toggles off }
  Until MovementCompleted(1);
End;

End. { TravLib Unit }
```

Appendix 2.4 LDVLIB.TPU

```
Unit LDVLib;

Interface

Uses TimerLib,Crt;

Procedure SampleDopplerFreq
  (var DopplerFreq : real);
Procedure MeasureVelocity
  (var Velocity : real);
Procedure SampleVelocityNTimes
  (var Velocity, StdDev : real; NTimes : integer);
Procedure SampleVelocityNSeconds
  (var Velocity, StdDev : real; SamplingPeriod : integer);

Implementation

Const
  Lambda : Real = 6.328E-07 ; { Wavelength of HeNe Laser }
  Kappa : Real = 0.06213 ; { Half angle of focusing lens as printed 4.701
    Corrected to radians & refraction of H2O  see TSI 9100-3 Manual p.24 }
  SinKappa : Real = 0.06209 ; { Sin of half angle on lens }

Procedure SampleDopplerFreq;

Var
  Low,High,OldValue : byte ;
  Exponent : byte ;
  Mantissa : integer ;
Const
  ln2 : Real = 6.93147181E-01 ;
  Cycles : Real = 8.0E09 ; { Value on front panel of LDV times E09 }
  FreqShift : Real = 10000.0 ; { Alter according to frequency shift desired }

Begin
  Low:= Not Port[$80];
  Repeat
    OldValue := Low;
    Low := Not Port[$80]; { Refer to p. 4-D of Tecmar 4PIO Manual for address }
    High := Not Port[$81];
  Until (Low <> OldValue) or Keypressed;
  Exponent := High Shr 4 ;
  Mantissa := (High Shl 12) Shr 4 + Low ;
  DopplerFreq := Cycles / ( Mantissa * EXP ((Exponent - 2)*ln2)) - FreqShift;
End;

Procedure MeasureVelocity;

Var
  DopplerFreq : real;

Begin
  SampleDopplerFreq (DopplerFreq);
  Velocity := (DopplerFreq * Lambda)/( 2 * SinKappa) * 100;
End;

Procedure SampleVelocityNTimes;

Var
  N : integer ;
  DopplerFreq : Array[1..500] of real;
  MeanFreq : real;
  SumFreq, SumDev : real;

Begin
  SumFreq := 0.0;
  SumDev := 0.0;
  For N := 1 to NTimes Do
  Begin
    SampleDopplerFreq ( DopplerFreq[N] );
    SumFreq := SumFreq + DopplerFreq[N];
  End;
  MeanFreq := SumFreq/NTimes;
  WriteLn('MeanFreq = ',MeanFreq);
  For N := 1 to NTimes Do
    SumDev := SumDev + Sqr(MeanFreq - DopplerFreq[N]);
  WriteLn('SumDev = ',SumDev);
  StdDev := Sqrt(SumDev / (NTimes-1));
```

```
 StdDev := (StdDev * Lambda)/( 2 * SinKappa) * 100; {Convert to cm/sec}
 Velocity := (MeanFreq * Lambda)/( 2 * SinKappa) * 100;
End;

Procedure SampleVelocityNSeconds

{ Uses TIMERLIB functions }

Var
 DopplerFreq : Array[1..5000] of real;
 MeanFreq : real;
 I : integer;
Const
 SumFreq : Real = 0.0;
 SumDev : Real = 0.0;
 NSamples : Integer = 0;
 Ans : Char = 'N';

Begin
NSamples := 0;
Repeat
 StartTimer;
 Repeat
  NSamples := NSamples + 1;
  SampleDopplerFreq (DopplerFreq[NSamples]);
  WriteLn('N = ',NSamples,' DF = ',DopplerFreq[NSamples]:7:0,'Sum = ',
  SumFreq,'Run Time = ',RunTimeSec:5:0);
  SumFreq := SumFreq + DopplerFreq[NSamples];
 Until RunTimeSec > SamplingPeriod;
 If NSamples < 50 Then
 Begin
  WriteLn('Time Sampled = ',RunTimeSec:5:0,' Number of Samples = ',NSamples);
  WriteLn('Enter Y to proceed with less than 50 samples');
  ReadLn(Ans);
 End;
Until (NSamples >50) or (Upcase(Ans) = 'Y');
MeanFreq := SumFreq/NSamples;
WriteLn('MeanFreq = ',MeanFreq);
For I := 1 to NSamples Do
 SumDev := SumDev + Sqr(MeanFreq - DopplerFreq[I]);
WriteLn('SumDev = ',SumDev);
StdDev := Sqrt(SumDev / (NSamples-1));
StdDev := (StdDev * Lambda)/( 2 * SinKappa) * 100; {Convert to cm/sec}
Velocity := (MeanFreq * Lambda)/( 2 * SinKappa) * 100;
End;

End. { Of LDVLIB Unit}
```

Appendix 2.5 TIMERLIB.TPU

```
Unit TimerLib;

Interface

Procedure PrintTime;
Function RunTime
 : real;
Function RunTimeSec
 : real;
Procedure StartTimer;
Procedure SetTimer
 (Hour, Min, Sec : Byte);

Implementation

Procedure PrintTime;
 {This procedure saves, inputs and prints the contents of the time of
day registers (counters 1, 2). The timer functions are performed by
the AM9513 chip on the PIO board, leaving the chip on the A/D board
to manage the traversers.}

Var
 A,B,C,D: byte; {variables to input values from counters}

Begin
 Port[$84]:=163; {Save counters 1 & 2}
 Port[$84]:=17; {Set data pointer to counter #1 hold register}
 A:=Port[$86]; {input tenths and hundreths-seconds}
 B:=Port[$86]; {input tens and ones-seconds}
 If ((A=0) and (B=0)) Then Port[$84]:=166; {Check for ripple carryover}
 Port[$84]:=18; {Set data pointer to counter #2 hold register}
 C:=Port[$86]; {input tens and ones-minutes}
 D:=Port[$86]; {input tens and ones-hours}
 {the values read above are in hex and must be transformed to decimal
 when printing them out}
 Writeln (C shr 4,C mod 16,':',B shr 4,B mod 16,':',A shr 4,A mod 16);
End;

Function RunTime : real;
 {This function saves, inputs and returns the contents of the time of
day registers (counters 1, 2).}

Var
 A,B,C,D: byte; {variables to input values from counters}

Begin
 Port[$84]:=163; {Save counters 1 & 2}
 Port[$84]:=17; {Set data pointer to counter #1 hold register}
 A:=Port[$86]; {input tenths and hundreths-seconds}
 B:=Port[$86]; {input tens and ones-seconds}
 If ((A=0) and (B=0)) Then Port[$84]:=166; {Check for ripple carryover}
 Port[$84]:=18; {Set data pointer to counter #2 hold register}
 C:=Port[$86]; {input tens and ones-minutes}
 D:=Port[$86]; {input tens and ones-hours}
 {the values read above are in hex and must be transformed to decimal
 when printing them out}
 RunTime:= D shr 4 * 36000 + D mod 16 * 3600 + C shr 4 * 600 + C mod 16 * 60
       + B shr 4 * 10 + B mod 16 + A shr 4 * 0.1 + A mod 16 * 0.01;
End;

Function RunTimeSec : real;
 {This function saves, inputs and returns the contents of the time of
day registers (counters 1, 2).}

Var
 A,B,C,D: byte; {variables to input values from counters}

Begin
 Port[$84]:=163; {Save counters 1 & 2}
 Port[$84]:=17; {Set data pointer to counter #1 hold register}
 A:=Port[$86]; {input tenths and hundreths-seconds}
 B:=Port[$86]; {input tens and ones-seconds}
 If ((A=0) and (B=0)) Then Port[$84]:=166; {Check for ripple carryover}
 Port[$84]:=18; {Set data pointer to counter #2 hold register}
 C:=Port[$86]; {input tens and ones-minutes}
 D:=Port[$86]; {input tens and ones-hours}
 {the values read above are in hex and must be transformed to decimal
```

```
  when printing them out}
  RunTimeSec:= C shr 4 * 600 + C mod 16 * 60 + B shr 4 * 10 + B mod 16;
End;

Procedure StartTimer;

Var
  Sec,Min,Hour: byte;

Begin
  Sec:=0;
  Min:=0;
  Hour:=0;
  Port[$84]:=255;
  Port[$84]:=23;
  Port[$86]:=255;
  Port[$86]:=138;
  Port[$84]:=1;
  Port[$86]:=57;
  Port[$86]:=15;
  Port[$86]:=0;
  Port[$84]:=Sec;
  Port[$84]:=2;
  Port[$86]:=61;
  Port[$86]:=0;
  Port[$86]:=Min;
  Port[$86]:=Hour;
  Port[$84]:=67;
  Port[$84]:=9;
  Port[$86]:=0;
  Port[$86]:=0;
  Port[$84]:=10;
  Port[$86]:=0;
  Port[$86]:=0;
  Port[$84]:=35; {Arm counters 1,2}
End;

Procedure SetTimer;

Begin
  Hour:= (Hour div 10)*16 + Hour mod 10;
  Min:= (Min div 10)*16 + Min mod 10;
  Sec:= (Sec div 10)*16 + Sec mod 10;
  Port[$84]:=255;
  Port[$84]:=23;
  Port[$86]:=255;
  Port[$86]:=138;
  Port[$84]:=1;
  Port[$86]:=57;
  Port[$86]:=15;
  Port[$86]:=0;
  Port[$84]:=Sec;
  Port[$84]:=2;
  Port[$86]:=61;
  Port[$86]:=0;
  Port[$86]:=Min;
  Port[$86]:=Hour;
  Port[$84]:=67;
  Port[$84]:=9;
  Port[$86]:=0;
  Port[$86]:=0;
  Port[$84]:=10;
  Port[$86]:=0;
  Port[$86]:=0;
  Port[$84]:=35; {Arm counters 1,2}
End;

End. {of TIMERLIB Unit}
```

Appendix 2.6 NEVAL3.PAS

```
Program NEval3;  {Version 3 Written By John King 6-16-89}
Uses Dos,ThermLib,PhysProp,MathLib,Printer;
{$M 65520,8192,65520}
{Use with N300+ series data sets}

Function CalibValue (Channel : integer; R : real) : real;
{ Takes the resistance of a thermistor and converts it to temperature
  in degrees C using the fit parameters A, B, and C. }

Const
{Data set RTEST16x.FIT                    }
A: array [0..15] of real = (1.0298319E-03,
 7.3573620E-04, 7.3413462E-04, 7.4910402E-04,
 7.3586443E-04, 7.5353934E-04, 7.4914679E-04,
 7.4350201E-04, 7.4498860E-04, 7.3098493E-04,
 7.1904906E-04, 7.4217674E-04, 4.3103056E-03,
 4.3103056E-03, 1.0348636E-03, 1.0247458E-03);

B: array [0..15] of real = (2.3895518E-04,
 2.7945533E-04, 2.7926602E-04, 2.8071517E-04,
 2.7907546E-04, 2.8014352E-04, 2.8090726E-04,
 2.8097121E-04, 2.7921782E-04, 2.8003333E-04,
 2.8083715E-04, 2.7691546E-04,-2.1540146E-04,
-2.1540146E-04, 2.3797494E-04, 2.3994974E-04);

C: array [0..15] of real = (1.5767218E-07,
 3.7976102E-08, 4.8161165E-08, 3.6745502E-08,
 4.2639016E-08, 3.5807018E-08, 3.4687195E-08,
 3.3403515E-08, 3.7229367E-08, 3.5269075E-08,
 3.4782948E-08, 4.2317218E-08,-7.9701222E-05,
-7.9701222E-05, 1.6258873E-07, 1.5265612E-07);

Var
 LogR : real;

Begin
 If (R < 10) or (A[Channel] = 0.0E+00) Then
   CalibValue := 0.0
 Else
 Begin
   LogR := Ln(R);
   CalibValue := 1/( A [Channel] + B [Channel]*LogR +
   C [Channel]*LogR*LogR*LogR)-273.17;
 End;
End;

Type
 FileTags = Array [1..999] of Boolean;
 DataStorageR = Array[1..200] of real;
 DataStorageI = Array[1..200] of integer;
 Range4 = Array[1..6] of real;

Const
 Dist : Range4 = (0.025,0.075,0.125,0.175,0.225,0.275);
      {Sensor distance from leading edge (m)}
 Length = 0.3048; {Plate length (m)}
 Width = 0.1524; {Plate Width (m)}
 Path = '\DATA\N';
 Extension = '.DAT';

Var
 I,K,Chan : integer;
 Temp : Range2;
 Time : Range3;
 NumData : integer; {Total number of data points in data set}
 FileNum,FirstFileNum,LastFileNum : integer;
 FilePresent : FileTags;
 PlotDataFile,PrnFile,InputFile : text;
 TableFile : text;
 FileName : string;
 CurrentMillivolts,Theta : real;
 Flux : real;
 InitialNumData : integer; {Number of data points prior to power on}
 FinalNumData : integer; {Number of data points after stabilized}
 DeltaT,Tfilm : Range1;
 NuExptl,GrPr : Range1;
 GrPrS,NuExptlS,DeltaTS,ThetaS,FluxS,TfilmS,DistS : DataStorageR;
 FileNumS,ChanS : DataStorageI;
 NumExperiments : integer;  {Total number of files processed}
```

```
  NumValues : integer;      {Total number of nusselt data pts found}
  MinXToFit,MaxXToFit : real;{Min/Max laminar GrPr (must plot to see)}
  XData,YData : Range3;     {Data arrays for line fits}
  A,B,R2 : real;            {Best fit line parameters}
  PercentDev : real;

{-------------------------------------------------------------------------}
Procedure InputDataFileNumbers
{.........................................................................}
 (Var FirstFileNum,LastFileNum: integer);
Begin
WriteLn('First and last filenumbers to process?');
ReadLn(FirstFileNum,LastFileNum);
End;

{-------------------------------------------------------------------------}
Procedure SetupOutputDataFiles
{.........................................................................}
 (FirstFileNum,LastFileNum : integer;
  Var PlotDataFile,PrnFile : text;
  Path : string);
Var
  FirstString,LastString : string[3];
  FileName : string;
Begin
Str(FirstFileNum,FirstString);
Str(LastFileNum,LastString);
FileName := Path+FirstString+'-'+LastString+'.OUT';
Assign(PlotDataFile,FileName);
Rewrite(PlotDataFile);
WriteLn('Writing plotfile output to ',FileName);
Filename := Path+FirstString+'-'+LastString+'.TAB';
Assign(TableFile,FileName);
Rewrite(TableFile);
WriteLn('Writing data tables to: ',FileName);
End;

{-------------------------------------------------------------------------}
Procedure OpenInputFile
{.........................................................................}
 (Var FileNum : integer;
  Var InputFile : text;
  Path,Extension : string);
Var
  Attr : word;
  FileNumString : string;
  FileName : string;
Begin
  Str(FileNum,FileNumString);
  FileName := Path+FileNumString+Extension;
  Assign(InputFile,FileName);
  Reset(InputFile);
  WriteLn('Processing file number ',FileNum);
End;

{-------------------------------------------------------------------------}
Procedure CheckForMissingFiles
{.........................................................................}
 (Var FilePresent : FileTags;
  FirstFileNum,LastFileNum : integer;
  Path,Extension : string);
Var
  FileNumString,FileName : string;
  InputFile : text;
  Attr : word;
  FileNum,I : integer;
Begin
For I := 1 to 999 Do
  FilePresent[I] := True;
Write('Missing files: None');
For I := 1 to 4 Do
Write(#8); {Backspaces to write over the None if file not found}
For FileNum := FirstFileNum to LastFileNum Do
Begin
  Str(FileNum,FileNumString);
  FileName := Path+FileNumString+Extension;
  Assign(InputFile,FileName);
  GetFAttr(InputFile,Attr);
  If (DosError=2) Then
  Begin
    FilePresent[FileNum] := False;
```

```
  Write(FileNum,' ');
 End;
End;
WriteLn('');
End;

{-------------------------------------------------------------------------}
Procedure ReadInData
{.........................................................................}
 (Var Theta : real;                {Angle-Degrees from horizontal}
  Var CurrentMilliVolts : real;       {Multimeter reading for current (mV)}
  Var Temp : range2; Var Time : range3; {Data arrays for temperature and time}
  Var NumData,InitialNumData,FinalNumData : integer; {Data point counts}
  Var InputFile : text);
Var
 Res : Array[1..15] of real;
 I,Chan : integer;
Begin
ReadLn(InputFile,Theta);
ReadLn(InputFile,CurrentMilliVolts);
ReadLn(InputFile,InitialNumData);
ReadLn(InputFile,FinalNumData);
I := 0;
While Not(EOF(InputFile)) Do
Begin
 I := I + 1;
 ReadLn(InputFile,Res[1],Res[2],Res[3],Res[4],Res[5],Res[6],Res[7],Res[8],
 Res[9],Res[10],Res[11],Res[12],Res[13],Res[14],Res[15],Time[I]);
 For Chan := 1 to 15 Do
  Temp[Chan,I] := CalibValue(Chan,Res[Chan]);
 End;
NumData := I;
Close(InputFile);
End;

{-------------------------------------------------------------------------}
Procedure HeatFlux
{.........................................................................}
 (Var Flux : real;                { W/m2 }
  CurrentMilliVolts,Length,Width : real;  { mV; m }
  DeltaT,Tfilm : range1);
Var
 SurfaceArea : real; {m2}
 Resistance : real; {ohms}
 CurrentAmps : real; {amps}
 Power : real; {watts}
 AvgTemp : real;  {the average plate temperature}
 Chan : integer;
Const
 Resistivity = 8.178E-7; {ohms-m}
 TempCoeff = 0.00075;   {change / deg C}
 CrossSection = 3.87096E-6; {m2}
Begin
 AvgTemp := 0;
 For Chan := 1 to 6 Do
  AvgTemp := AvgTemp + DeltaT[Chan]/2 + Tfilm[Chan];
 AvgTemp := AvgTemp / 6;
 SurfaceArea := Length * Width;
 Resistance := (Resistivity + Resistivity * TempCoeff * (AvgTemp-20))
  * Length / CrossSection;
 CurrentAmps := CurrentMilliVolts * 4;
 Power := Sqr(CurrentAmps) * Resistance;
 Flux := Power/SurfaceArea;
End;

{-------------------------------------------------------------------------}
Procedure LineFit       {Fits data to eqn Y = AX + B; R2=Correlation Coeff}
{.........................................................................}
 (Var A,B,R2 : real;
 X,Y : Range3;
 NumData : integer;
 MinXToFit,MaxXToFit : real);
Var
 N,I : Integer;
 SumX,SumY,SumXY,SumX2,SumY2,M1,M2,P : Real;
Begin
 N := 0;
 SumX := 0;
 SumY := 0;
 SumXY := 0;
 SumX2 := 0;
```

```
 SumY2 := 0;
 For I := 1 to NumData Do
 If (X[I] < MaxXToFit) and (X[I] > MinXToFit) Then
 Begin
  Inc(N);
  SumX := SumX + X[I];
  SumY := SumY + Y[I];
  SumXY := SumXY + X[I] * Y[I];
  SumX2 := SumX2 + Sqr(X[I]);
  SumY2 := SumY2 + Sqr(Y[I]);
 End;
 { WriteLn('N ',N);}
 M1 := N * SumX2 - Sqr(SumX);
 M2 := N * SumY2 - Sqr(SumY);
 P := N * SumXY - SumX * SumY;
 A := P / M1;                    {Slope}
 B := (M1 * SumY - P * SumX) / (N * M1); {Intercept}
 R2 := Sqr(P) / (M1 * M2);       {Linear Correlation Coefficient}
{  WriteLn('InRoutine: ',(B+A*Time[NumData]):8:3);   }
End;

{-------------------------------------------------------------------------}
Procedure LineFitInt   {Fits data to eqn Y = AX + B; R2=Corr. Coeff.}
                {A is fixed externally}
{.........................................................................}
 (Var A,B,R2 : real;
 X,Y : Range3;
 NumData : integer;
 MinXToFit,MaxXToFit : real);
Var
 N,I : Integer;
 SumB : Real;
Begin
 N := 0;
 SumB := 0;
 For I := 1 to NumData Do
 If (X[I] < MaxXToFit) and (X[I] > MinXToFit) Then
 Begin
  Inc(N);
  B := Y[I] - (A * X[I]);
  SumB := SumB + B;
 End;
 B := SumB/N;
 { WriteLn('InRoutine: ',(B+A*Time[NumData]):8:3);   }
End;

{-------------------------------------------------------------------------}
Procedure DetermineInitialOffset
{.........................................................................}
 (InitialNumData : integer;
  Temp : Range2;
  Time : Range3;
  Var InitialOffset : Range1;
  Var TBulkInitial : real);  {The bulk temperature at startup time by least
                squares fit to the initial data}
Const
 MinXToFit = 0;
 MaxXToFit = 100;
Var
 X,Y : Range3;
 I : integer;
Begin
For I := 1 to InitialNumData Do
Begin
 X[I] := Time[I];
End;
For I := 1 to InitialNumData Do
 Y[I] := Temp[7,I];
LineFit(A,B,R2,X,Y,InitialNumData,MinXToFit,MaxXToFit);
TBulkInitial := (B + Time[InitialNumData]*A);
For Chan := 1 to 6 Do
Begin
 For I := 1 to InitialNumData Do
 Begin
  Y[I] := Temp[Chan,I];
 End;
 LineFit(A,B,R2,X,Y,InitialNumData,MinXToFit,MaxXToFit);
 InitialOffset[Chan] := (B + Time[InitialNumData]*A)-TBulkInitial;
End;
End;
```

```
{-------------------------------------------------------------------------}
Procedure DeltaTCalc
{.........................................................................}
 (InitialNumData,FinalNumData,NumData : integer;
  Temp : Range2;
  Time : Range3;
  Var DeltaTAvg,Tfilm : Range1);
Var
  DeltaT : Range2;
  DeltaTSum,TBulkSum,TBulkFin : real;
  I : integer;
  TBulk : Range3;
  TBulkInitial : real;
  InitialOffset : Range1;
Begin
For I := 1 to NumData Do
Begin
  TBulk[I] := Temp[7,I];
  For Chan := 1 to 6 Do
    DeltaT[Chan,I] := Temp[Chan,I]-TBulk[I];
End;
{...Correction for initial offset}
DetermineInitialOffset(InitialNumData,Temp,Time,InitialOffset,TBulkInitial);
For I := (NumData-(FinalNumData-1)) to NumData Do
  For Chan := 1 to 6 Do
    DeltaT[Chan,I] := DeltaT[Chan,I] - InitialOffset[Chan];
{...Correction for change in bulk temp}
For I := (NumData-(FinalNumData-1)) to NumData Do
  For Chan := 1 to 6 Do
    DeltaT[Chan,I] := DeltaT[Chan,I] - (TBulk[I] - TBulkInitial);
{WriteLn('Delta T: ',DeltaT[1,I]:8:3,DeltaT[2,I]:8:3,DeltaT[3,I]:8:3,
  DeltaT[4,I]:8:3,DeltaT[5,I]:8:3,DeltaT[6,I]:8:3);
WriteLn('Offset: ',InitialOffset[1]:8:3,InitialOffset[2]:8:3,
  InitialOffset[3]:8:3,InitialOffset[4]:8:3,InitialOffset[5]:8:3,
  InitialOffset[6]:8:3);
WriteLn('TBulk Corr: ',(TBulk[I] - TBulkInitial):8:3,
  (TBulk[I] - TBulkInitial):8:3,(TBulk[I] - TBulkInitial):8:3,
  (TBulk[I] - TBulkInitial):8:3,(TBulk[I] - TBulkInitial):8:3,
  (TBulk[I] - TBulkInitial):8:3);}
For Chan := 1 to 6 Do
Begin
  DeltaTSum := 0;
  For I := (NumData-(FinalNumData-1)) to NumData Do
    DeltaTSum := DeltaTSum+DeltaT[Chan,I];
  DeltaTAvg[Chan] := DeltaTSum / FinalNumData;
End;
TBulkSum := 0;
For I := (NumData-(FinalNumData-1)) to NumData Do
  TBulkSum := TBulkSum + TBulk[I];
TBulkFin := TBulkSum / FinalNumData;
For Chan := 1 to 6 Do
Begin
  DeltaTSum := 0;
  For I := (NumData-(FinalNumData-1)) to NumData Do
    DeltaTSum := DeltaTSum+DeltaT[Chan,I];
  DeltaTAvg[Chan] := DeltaTSum / FinalNumData;
  TFilm[Chan] := TBulkFin + DeltaTAvg[Chan]/2;
End;
End;

{-------------------------------------------------------------------------}
Procedure  CalculateNuExptl
{.........................................................................}
 (Var NuExptl : Range1;
  Dist : Range4; DeltaT : Range1;
  TFilm : Range1;
  Flux : real);
Var
  Kappa : real;
  hexptl : real;
  Chan : integer;
Begin
For Chan := 1 to 6 Do
Begin
  If DeltaT[Chan] = 0.0 Then DeltaT[Chan] := 0.00001; {To prevent div by 0}
  Kappa := ThermalConductivityH2O(Tfilm[Chan]);
  hexptl := Flux / DeltaT[Chan];
  NuExptl[Chan] := hexptl * Dist[Chan] / Kappa;
End;
End;
```

```
{-------------------------------------------------------------------------}
Procedure CalculateGrPr
{.........................................................................}
 (Var GrPr : Range1;
  Dist : Range4;
  DeltaT,TFilm : Range1;
  Flux,Theta : real);
Var
  Kappa : real;
  hexptl : real;
  Chan : integer;
Begin
For Chan := 1 to 6 Do
Begin
  GrPr[Chan] := GrashofModH2O(Tfilm[Chan],Dist[Chan],Flux,Theta) *
    PrandtlH2O(Tfilm[Chan]);
End;
If Theta = 0 Then
For Chan := 1 to 6 Do
Begin
  GrPr[Chan] := GrashofH2O(Tfilm[Chan],Dist[Chan],Flux,DeltaT[Chan]) *
    PrandtlH2O(Tfilm[Chan]);
End;
End;

{-------------------------------------------------------------------------}
Procedure StoreData
{.........................................................................}
 (Var GrPrS,NuExptlS,DeltaTS : DataStorageR;
  Var FileNumS,ChanS : DataStorage1;
  Var ThetaS,FluxS,TfilmS,DistS : DataStorageR;
  GrPr,NuExptl,DeltaT: Range1;
  FileNum : integer;
  Var Theta,Flux : real;
  Var Tfilm: Range1;
  Var Dist : Range4;
  Var I : integer);
Var
  Chan : integer;
Begin
For Chan := 1 to 6 Do
Begin
  Inc(I);
  DeltaTS[I] := DeltaT[Chan];
  GrPrS[I] := GrPr[Chan];
  NuExptlS[I] := NuExptl[Chan];
  FileNumS[I] := FileNum;
  ChanS[I] := Chan;
  ThetaS[I] := Theta;
  FluxS[I] := Flux;
  TfilmS[I] := Tfilm[Chan];
  DistS[I] := Dist[Chan];
End;
End;

{-------------------------------------------------------------------------}
Procedure DetermineRangeToFit
{.........................................................................}
  (Var MinXToFit,MaxXToFit : real;
  Theta : real);
Begin
MinXToFit := 0;
MaxXToFit := 14;  {Default}
If(Theta=90) Then MaxXToFit := 12.8;
If(Theta=75) Then MaxXToFit := 12;
If(Theta=60) Then MaxXToFit := 10;
If(Theta=45) Then MaxXToFit := 9;
If(Theta=30) Then MaxXToFit := 8;
If(Theta=15) Then MaxXToFit := 7.1;
If(Theta=0)  Then MaxXToFit := 7;
End;

{.........................................................................}
Begin
InputDataFileNumbers(FirstFileNum,LastFileNum);
CheckForMissingFiles(FilePresent,FirstFileNum,LastFileNum,Path,Extension);
SetUpOutputDataFiles(FirstFileNum,LastFileNum,PlotDataFile,PrnFile,Path);
I := 0;
For FileNum := FirstFileNum to LastFileNum Do
If FilePresent[FileNum] Then
Begin
```

```
  OpenInputFile(FileNum,InputFile,Path,Extension);
  ReadInData(Theta,CurrentMillivolts,Temp,Time,NumData,InitialNumData,
    FinalNumData,InputFile);
  If (Theta = 0) Then
  Begin
  WriteLn('NOTE: Theta = 0, reset distances to characteristic length');
   For K := 1 to 6 Do
     Dist[K] := (Length*Width) / (2*(Length+Width));
  End;
  DeltaTCalc(InitialNumData,FinalNumData,NumData,Temp,Time,DeltaT,Tfilm);
  HeatFlux(Flux,CurrentMilliVolts,Length,Width,DeltaT,Tfilm);
  CalculateNuExptl(NuExptl,Dist,DeltaT,Tfilm,Flux);
  CalculateGrPr(GrPr,Dist,DeltaT,Tfilm,Flux,Theta);
  StoreData(GrPrS,NuExptlS,DeltaTS,FileNumS,ChanS,ThetaS,FluxS,TfilmS,DistS,
    GrPr,NuExptl,DeltaT,FileNum,Theta,Flux,Tfilm,Dist,I);
End;
NumValues := I;
For I := 1 to NumValues Do
Begin
  XData[I] := Log(GrPrS[I]);
  YData[I] := Log(NuExptlS[I]);
End;
DetermineRangeToFit(MinXToFit,MaxXToFit,Theta);
LineFit(A,B,R2,XData,YData,NumValues,MinXToFit,MaxXToFit);
WriteLn('Best Fit Line:  Nu =',Pow(10,B):10:3,'(GrPr)^',A:6:3);
WriteLn('Fit Range: ',Log(GrPrS[1]):5:2,' < GrPr < ',MaxXToFit:5:2);
WriteLn('Correlation: R2 = ',R2:6:4);

{Statements added June 1989}
WriteLn(TableFile,'Angle: ',Theta:4:0,' degrees');
Write(TableFile,'Data files:');
For FileNum := FirstFileNum to LastFileNum Do
If FilePresent[FileNum] Then
  Write(TableFile,FileNum:4);
WriteLn(TableFile,' ');
WriteLn(TableFile,'Best Fit Line:  Nu =',Pow(10,B):10:3,'(GrPr)^',A:6:3);
WriteLn(TableFile,'Fit Range: ',Log(GrPrS[1]):5:2,' < GrPr < ',MaxXToFit:5:2);
WriteLn(TableFile,'Correlation: R2 = ',R2:6:4);
WriteLn(TableFile,' ');
WriteLn(TableFile,'Exp',' #','      x',' th','     Flux',' DelT',' TBulk',
  ' TFilm','     GrPr','      Nu',' LogGrPr',' LogNu');
WriteLn(TableFile,' ');
For I := 1 to NumValues Do
  WriteLn(TableFile,FileNumS[I]:3,ChanS[I]:2,DistS[I]:8:3,ThetaS[I]:3:0,
    FluxS[I]:10:2,DeltaTS[I]:7:3,(TfilmS[I]-DeltaTS[I]/2):6:2,TfilmS[I]:6:2,
    GrPrS[I]:10,NuExptlS[I]:10,Log(GrPrS[I]):8:3,Log(NuExptlS[I]):7:3);
Close(TableFile);
{.....}
For I := 1 to NumValues Do
 WriteLn(PlotDataFile,FileNumS[I]:3,ChanS[I]:2,GrPrS[I]:10,NuExptlS[I]:10,
   Log(GrPrS[I]):8:3,Log(NuExptlS[I]):8:3);
Close(PlotDataFile);
End.
```

Appendix 3

Similarity Solution for Uniform Flux Vertical Plate

In this appendix we set forth the similarity solution for a uniform flux vertical plate with uniform bulk temperature. The similarity transformation and equations used are those originally described by Sparrow and Gregg (1956). Here we will obtain solutions for Prandtl numbers in the range of interest for the experiments performed with uniform bulk temperature.

For the coordinate system drawn in Figure 4-1, the basic equations of motion reduce to:

continuity
$$\frac{\partial u}{\partial x}+\frac{\partial v}{\partial y}=0 \tag{A3-1}$$

momentum
$$u\frac{\partial u}{\partial x}+v\frac{\partial u}{\partial y}=g\beta(t-t_\infty)+\nu\frac{\partial^2 u}{\partial y^2} \tag{A3-2}$$

energy
$$u\frac{\partial t}{\partial x}+v\frac{\partial t}{\partial y}=\alpha\frac{\partial^2 t}{\partial y^2} \tag{A3-3}$$

Define a stream function,

$$u=\frac{\partial \Psi}{\partial y} \qquad v=-\frac{\partial \Psi}{\partial x} \tag{A3-4}$$

and similarity variables,

$$\eta=C_1 y/x^{\frac{1}{5}} \tag{A3-5}$$

$$F(\eta)=\Psi/C_2 x^{\frac{4}{5}} \tag{A3-6}$$

$$\theta=\frac{C_1(t_\infty-t)}{x^{\frac{1}{5}}q/k} \tag{A3-7}$$

$$C_1=\left(\frac{g\beta q}{5k\nu^2}\right)^{\frac{1}{5}} \qquad C_2=\left(\frac{5^4 g\beta q\nu^3}{k}\right)^{\frac{1}{5}} \tag{A3-8}$$

Then,

$$u=C_1C_2x^{\frac{3}{5}}F' \tag{A3-9}$$

$$v=\frac{C_2}{5x^{\frac{1}{5}}}(\eta F'-4F) \tag{A3-10}$$

and the momentum equation becomes,

$$F'''-3F'^2+4FF''-\theta=0 \tag{A3-11}$$

$$\theta''+\mathrm{Pr}\,(4F\theta''-F'\theta)=0 \tag{A3-12}$$

Boundary conditions for the constant heat flux plate are:

$$\text{At } y=0 \quad u=v=0 \text{ and } -k\left(\frac{\partial T}{\partial y}\right)=q \tag{A3-13}$$

$$\text{At } y=\infty \quad u=0 \text{ and } t=t_{\infty} \tag{A3-14}$$

Thus,

$$\text{At } \eta=0 \quad \{F'=0, F=0, \theta'=1\} \tag{A3-15}$$

$$\text{At } \eta=\infty \quad \{F'=0, \theta=0\} \tag{A3-16}$$

We are left with two ODE's and 5 boundary conditions. Solution of the ODE's was performed using a numerical solver (LSODE) which solves ODE's of the form

$$\frac{DY}{DT}=F(T,Y) \tag{A3-17}$$

For multiple ODE's the equations must be expressed in the form

$$\frac{DY(I)}{DT}=F(I)=F(I,T,Y(1),Y(2),\ldots,Y(NEQ)) \tag{A3-18}$$

Therefore, we need to rewrite the two ODE's as a set of linked 1st order ODE's. Define

$$\begin{aligned} Y_1&=F'' \\ Y_2&=F' \\ Y_3&=F \\ Y_4&=\theta' \\ Y_5&=\theta \end{aligned} \tag{A3-19}$$

We can now write five ODE's:

$$\begin{aligned} Y_1'&=3Y_2^2-4Y_3Y_1+Y_5 \\ Y_2'&=Y_1 \\ Y_3'&=Y_2 \\ Y_4'&=\Pr(-4Y_4Y_3+Y_5Y_2) \\ Y_5'&=Y_4 \end{aligned} \tag{A3-20}$$

The boundary conditions are applied to the newly defined variables so that,

$$\text{At } \eta=0 \quad \{F'=0, F=0, \theta'=1\} \tag{A3-21}$$

$$\Rightarrow\{Y_2=0, Y_3=0, Y_4=1\}$$

$$\text{At } \eta=\infty \quad \{F'=0, \theta=0\} \tag{A3-22}$$

$$\Rightarrow\{Y_2=0, Y_5=0\}$$

Only 3 of the 5 boundary conditions are given at η=0. Accordingly, the program uses a shooting method to arrive at the final solution to the set of equations. Therefore, we guess values for $\theta(0)$ and $F''(0)$, and calculate the solution to the set of equations to find if a solution has been found which gives $\theta(\infty) = 0$ and $F'(\infty) = 0$. Powell's method of conjugate directions was used to adjust the initial guesses and minimize the calculated values of θ and F'.

With this equation solver in place, the program was used to establish theoretical predictions for the heat transfer correlations. The Nusselt number is defined as

$$\mathrm{Nu}_x = \frac{h_x x}{k} = \frac{q}{(t_w - t_\infty)} \frac{x}{k} \tag{A3-23}$$

In terms of θ we can write,

$$\mathrm{Nu}_x = -\frac{1}{5^{\frac{1}{5}}\theta(0)} \mathrm{Gr}_x^{*1/5} \tag{A3-24}$$

Thus heat transfer correlations were developed from similarity theory by obtaining values for $\theta(0)$ for the range of Prandtl numbers of interest.

The program listing follows. Since the set of differential equations was stiff, the full Jacobian for the set of equations was required by LSODE and is included in a separate subroutine.

```
C
C
C*************************** ABSTRACT ****************************
C
C  THIS PROGRAM USES POWELL'S METHOD OF CONJUGATE DIRECTIONS TO
C  MINIMIZE THE CALCULATED VALUES OF VELOCITY AND TEMPERATURE (BOTH
C  SHOULD BE 0) AT INFINITY AWAY FROM A VERTICAL CONSTANT FLUX PLATE
C
C************************** NOMENCLATURE *************************
C
      DOUBLE PRECISION SOLVE, GUESS(2),WX1(2),WX2(2),S(2),A(2,2)
      COMMON IFLAG
      EXTERNAL SOLVE
C
C       IFLAG=1 - DON'T PRINT SOLUTION DURING SHOOTING ALGORITHM
C       IFLAG=2 - PRINT SOLUTION AFTER FINAL GUESSES FOR U,T FOUND
C
      IFLAG=1
      N=2
      GUESS(1)=0.5
      GUESS(2)=-1
      EPSLS=0.000000001
      CRIT=0.0000001
      LTYPE=1
      MAXI=100
      CALL PCD(GUESS,WX1,WX2,S,A,SOLVE,N,EPSLS,CRIT,LTYPE,MAXI)
C
C       OPTIMUM FOUND - PRINT SOLUTION
C
      IFLAG=2
      WRITE (6,*)
      WRITE (6,*)
      WRITE (6,*) ' SOLUTION FOR VELOCITY AND TEMPERATURE AS F(ETA)'
      WRITE (6,*)
      END=SOLVE(GUESS)
      STOP
      END
C
      FUNCTION SOLVE (GUESS)
C
C       THIS FUNCTION USES LSODE, AN IVP SOLVER, TO SOLVE
C       SPARROW AND GREGG PROBLEM VIA SHOOTING METHODS
C       LSODE PARAMETERS DEFINED IN LSODE MANUAL
C
      DOUBLE PRECISION SOLVE, GUESS(2),PR
      DOUBLE PRECISION ATOL, RWORK, RTOL, T, TOUT, Y
      DIMENSION Y(5), ATOL(5), RWORK(92), IWORK(25)
      COMMON IFLAG
      EXTERNAL FJAC
      NEQ=5
      Y(1)=GUESS(1)
      Y(2)=0.D0
      Y(3)=0.D0
      Y(4)=1.D0
      Y(5)=GUESS(2)
      T=0.D0
      ITOL=2
      RTOL=1.D-4
      ATOL(1)=1.D-6
      ATOL(2)=1.D-6
      ATOL(3)=1.D-6
      ATOL(4)=1.D-6
      ATOL(5)=1.D-6
      ITASK=1
      ISTATE=1
      IOPT=0
      LRW=92
      LIW=25
C
C       LSODE METHOD 21 USED - USER SUPPLIED JACOBIAN
C
      MF=21
      IF (IFLAG.EQ.2) THEN
        TOUT = 0.1D0
        DO 50 IOUT=1,50
          CALL LSODE(F,NEQ,Y,T,TOUT,ITOL,RTOL,ATOL,ITASK,ISTATE,
     &          ICPT,RWORK,LRW,IWORK,LIW,JAC,MF)
          WRITE (6,10) T,Y(2),Y(5)
   10     FORMAT(10H AT ETA = ,E12.4,7H  F' = ,E14.6, 7H  TH = ,
     &          E14.6)
          IF (ISTATE.LE.0) WRITE (6,*) 'ERROR - ISTATE =',ISTATE
```

```
 50   TOUT=TOUT+0.1D0
      ELSE
      TOUT=20
        CALL LSODE(F,NEQ,Y,T,TOUT,ITOL,RTOL,ATOL,ITASK,ISTATE,
     &          ICPT,RWORK,LRW,IWORK,LIW,JAC,MF)
C
C       OBJECTIVE FUNCTION TO MINIMIZE
C       SUM OF SQUARES OF FINAL VELOCITY AND TEMPERATURE (ETA=20)
C
        SOLVE=Y(2)*Y(2)+Y(5)*Y(5)
      ENDIF
      RETURN
      END
      SUBROUTINE F (NEQ,T,Y,DYDT)
      DOUBLE PRECISION T, Y, DYDT,PR
      DIMENSION Y(NEQ),DYDT(NEQ)
C
C     SET OF FIVE FIRST ORDER DIFFERENTIAL EQNS EQUIVALENT TO
C     THE ORIGINAL SET OF TWO NONLINEAR HIGHER ORDER EQUATIONS
C
C     PRANDTL NUMBER = 4.84 CASE
C
      PR=4.84D0
      DYDT(1)=3.D0*Y(2)*Y(2)-4.D0*Y(3)*Y(1)+Y(5)
      DYDT(2)=Y(1)
      DYDT(3)=Y(2)
      DYDT(4)= -PR*(4.D0*Y(4)*Y(3)-Y(5)*Y(2))
      DYDT(5)=Y(4)
      RETURN
      END
      SUBROUTINE JAC(NEQ,T,Y,ML,MU,PD,NROWPD)
      DOUBLE PRECISION T, Y,PR,PD
      DIMENSION Y(NEQ),PD(NROWPD,NEQ)
C
C     USER SUPPLIED JACOBIAN
C
      PR=4.84D0
      PD(1,1)=-4.D0*Y(3)
      PD(1,2)=2.D0*3.D0*Y(2)
      PD(1,3)=-4.D0*Y(1)
      PD(1,4)=0.D0
      PD(1,5)=1.0D0
      PD(2,1)=1.0D0
      PD(2,2)=0.D0
      PD(2,3)=0.D0
      PD(2,4)=0.D0
      PD(2,5)=0.D0
      PD(3,1)=0.D0
      PD(3,2)=1.D0
      PD(3,3)=0.D0
      PD(3,4)=0.D0
      PD(3,5)=0.D0
      PD(4,1)=0.D0
      PD(4,2)=PR*Y(5)
      PD(4,3)= -PR*4.D0*Y(4)
      PD(4,4)= -PR*4.D0*Y(3)
      PD(4,5)= PR*Y(2)
      PD(5,1)=0.D0
      PD(5,2)=0.D0
      PD(5,3)=0.D0
      PD(5,4)=1.D0
      PD(5,5)=0.D0
      RETURN
      END
```

Appendix 4

Tabulated Heat Transfer Data

Appendix 4.1 Uniform Bulk Temperature Heat Transfer Data

Angle: 90 degrees
Data files: 311 312 313 314 315 316 321 322 323 324 326
Best Fit Line: Nu = 0.563(GrPr)^ 0.199
Fit Range: 5.44 < GrPr < 12.80
Correlation: R2 = 0.9993

Expt Numb	Pt#	x cm	θ deg	Flux w/m²	ΔT °C	TBulk °C	TFilm °C	GrPr	Nu	LogGrPr	LogNu
311	1	0.025	90	27.45	0.167	21.17	21.25	2.761E+05	6.839E+00	5.441	0.835
311	2	0.075	90	27.45	0.206	21.17	21.27	2.239E+07	1.665E+01	7.350	1.221
311	3	0.125	90	27.45	0.230	21.17	21.29	1.729E+08	2.485E+01	8.238	1.395
311	4	0.175	90	27.45	0.245	21.17	21.29	6.646E+08	3.274E+01	8.823	1.515
311	5	0.225	90	27.45	0.248	21.17	21.29	1.816E+09	4.162E+01	9.259	1.619
311	6	0.275	90	27.45	0.262	21.17	21.30	4.055E+09	4.801E+01	9.608	1.681
312	1	0.025	90	150.69	0.661	21.17	21.50	1.540E+06	9.505E+00	6.188	0.978
312	2	0.075	90	150.69	0.812	21.17	21.57	1.253E+08	2.320E+01	8.098	1.365
312	3	0.125	90	150.69	0.900	21.17	21.62	9.698E+08	3.490E+01	8.987	1.543
312	4	0.175	90	150.69	0.957	21.17	21.65	3.732E+09	4.595E+01	9.572	1.662
312	5	0.225	90	150.69	1.002	21.17	21.67	1.021E+10	5.637E+01	10.009	1.751
312	6	0.275	90	150.69	1.056	21.17	21.70	2.283E+10	6.539E+01	10.359	1.816
313	1	0.025	90	617.81	2.051	21.17	22.19	6.596E+06	1.253E+01	6.819	1.098
313	2	0.075	90	617.81	2.483	21.17	22.41	5.414E+08	3.103E+01	8.734	1.492
313	3	0.125	90	617.81	2.731	21.17	22.53	4.209E+09	4.702E+01	9.624	1.672
313	4	0.175	90	617.81	2.933	21.17	22.63	1.627E+10	6.127E+01	10.211	1.787
313	5	0.225	90	617.81	3.062	21.17	22.70	4.463E+10	7.546E+01	10.650	1.878
313	6	0.275	90	617.81	3.228	21.17	22.78	1.001E+11	8.746E+01	11.000	1.942
314	1	0.025	90	2373.28	5.895	21.17	24.11	2.838E+07	1.666E+01	7.453	1.222
314	2	0.075	90	2373.28	7.082	21.17	24.71	2.376E+09	4.155E+01	9.376	1.619
314	3	0.125	90	2373.28	7.761	21.17	25.05	1.868E+10	6.313E+01	10.271	1.800
314	4	0.175	90	2373.28	8.343	21.17	25.34	7.288E+10	8.214E+01	10.863	1.915
314	5	0.225	90	2373.28	8.685	21.17	25.51	2.010E+11	1.014E+02	11.303	2.006
314	6	0.275	90	2373.28	9.139	21.17	25.74	4.539E+11	1.177E+02	11.657	2.071
315	1	0.025	90	5266.38	10.839	21.18	26.60	7.192E+07	1.998E+01	7.857	1.301
315	2	0.075	90	5266.38	12.950	21.18	27.65	6.139E+09	5.003E+01	9.788	1.699
315	3	0.125	90	5266.38	14.180	21.18	28.27	4.880E+10	7.603E+01	10.688	1.881
315	4	0.175	90	5266.38	15.205	21.18	28.78	1.920E+11	9.914E+01	11.283	1.996
315	5	0.225	90	5266.38	15.825	21.18	29.09	5.324E+11	1.224E+02	11.726	2.088
315	6	0.275	90	5266.38	16.626	21.18	29.49	1.210E+12	1.422E+02	12.083	2.153
316	1	0.025	90	9262.32	16.467	21.19	29.42	1.449E+08	2.296E+01	8.161	1.361
316	2	0.075	90	9262.32	19.617	21.19	31.00	1.259E+10	5.760E+01	10.100	1.760
316	3	0.125	90	9262.32	21.425	21.19	31.90	1.010E+11	8.770E+01	11.004	1.943
316	4	0.175	90	9262.32	22.943	21.19	32.66	4.003E+11	1.145E+02	11.602	2.059
316	5	0.225	90	9262.32	23.820	21.19	33.10	1.114E+12	1.416E+02	12.047	2.151
316	6	0.275	90	9262.32	24.608	21.19	33.50	2.525E+12	1.673E+02	12.402	2.224
321	1	0.025	90	5.79	0.051	20.03	20.05	5.371E+04	4.741E+00	4.730	0.676
321	2	0.075	90	5.79	0.059	20.03	20.06	4.352E+06	1.234E+01	6.639	1.091
321	3	0.125	90	5.79	0.066	20.03	20.06	3.359E+07	1.832E+01	7.526	1.263
321	4	0.175	90	5.79	0.076	20.03	20.06	1.291E+08	2.243E+01	8.111	1.351
321	5	0.225	90	5.79	0.076	20.03	20.06	3.527E+08	2.871E+01	8.547	1.458
321	6	0.275	90	5.79	0.081	20.03	20.07	7.872E+08	3.291E+01	8.896	1.517
322	1	0.025	90	50.75	0.276	20.04	20.17	4.750E+05	7.698E+00	5.677	0.886
322	2	0.075	90	50.75	0.332	20.04	20.20	3.855E+07	1.917E+01	7.586	1.283
322	3	0.125	90	50.75	0.371	20.04	20.22	2.978E+08	2.861E+01	8.474	1.457
322	4	0.175	90	50.75	0.404	20.04	20.24	1.145E+09	3.675E+01	9.059	1.565
322	5	0.225	90	50.75	0.423	20.04	20.25	3.132E+09	4.517E+01	9.496	1.655
322	6	0.275	90	50.75	0.446	20.04	20.26	6.995E+09	5.231E+01	9.845	1.719
323	1	0.025	90	393.18	1.437	20.05	20.76	3.830E+06	1.143E+01	6.583	1.058
323	2	0.075	90	393.18	1.734	20.05	20.91	3.133E+08	2.840E+01	8.496	1.453
323	3	0.125	90	393.18	1.916	20.05	21.00	2.432E+09	4.282E+01	9.386	1.632
323	4	0.175	90	393.18	2.064	20.05	21.08	9.389E+09	5.564E+01	9.973	1.745
323	5	0.225	90	393.18	2.160	20.05	21.13	2.574E+10	6.837E+01	10.411	1.835
323	6	0.275	90	393.18	2.261	20.05	21.18	5.762E+10	7.983E+01	10.761	1.902
324	1	0.025	90	37578.51	45.103	20.20	42.75	9.704E+08	3.299E+01	8.987	1.518
324	2	0.075	90	37578.51	53.186	20.20	46.79	8.877E+10	8.324E+01	10.948	1.920
324	3	0.125	90	37578.51	57.393	20.20	48.89	7.269E+11	1.280E+02	11.861	2.107
324	4	0.175	90	37578.51	59.955	20.20	50.18	2.892E+12	1.712E+02	12.461	2.233
324	5	0.225	90	37578.51	54.450	20.20	47.42	7.322E+12	2.436E+02	12.865	2.387
324	6	0.275	90	37578.51	40.514	20.20	40.46	1.319E+13	4.059E+02	13.120	2.608
326	1	0.025	90	59264.03	61.635	20.86	51.67	1.977E+09	3.741E+01	9.296	1.573
326	2	0.075	90	59264.03	71.654	20.86	56.68	1.816E+11	9.569E+01	11.259	1.981
326	3	0.125	90	59264.03	77.300	20.86	59.51	1.497E+12	1.471E+02	12.175	2.168
326	4	0.175	90	59264.03	80.036	20.86	60.87	5.934E+12	1.985E+02	12.773	2.298
326	5	0.225	90	59264.03	69.431	20.86	55.57	1.432E+13	2.968E+02	13.156	2.472
326	6	0.275	90	59264.03	39.449	20.86	40.58	2.089E+13	6.573E+02	13.320	2.818

Angle: 75 degrees
Data files: 333 334 335 336 337 338 339 340 341 345 346 347
Best Fit Line: Nu = 0.565(GrPr)^ 0.199
Fit Range: 5.04 < GrPr < 12.00
Correlation: R2 = 0.9973

Expt Numb	Pt#	x cm	θ deg	Flux w/m²	ΔT °C	TBulk °C	TFilm °C	GrPr	Nu	LogGrPr	LogNu
333	1	0.025	75	11.86	0.093	20.56	20.61	1.105E+05	5.347E+00	5.043	0.728
333	2	0.075	75	11.86	0.118	20.56	20.62	8.956E+06	1.258E+01	6.952	1.100
333	3	0.125	75	11.86	0.124	20.56	20.62	6.912E+07	1.997E+01	7.840	1.300
333	4	0.175	75	11.86	0.132	20.56	20.63	2.656E+08	2.625E+01	8.424	1.419
333	5	0.225	75	11.86	0.144	20.56	20.63	7.260E+08	3.097E+01	8.861	1.491
333	6	0.275	75	11.86	0.153	20.56	20.64	1.621E+09	3.562E+01	9.210	1.552
334	1	0.025	75	22.26	0.148	20.57	20.64	2.078E+05	6.287E+00	5.318	0.798
334	2	0.075	75	22.26	0.182	20.57	20.66	1.685E+07	1.538E+01	7.227	1.187
334	3	0.125	75	22.26	0.203	20.57	20.67	1.301E+08	2.295E+01	8.114	1.361
334	4	0.175	75	22.26	0.213	20.57	20.67	4.999E+08	3.053E+01	8.699	1.485
334	5	0.225	75	22.26	0.221	20.57	20.68	1.366E+09	3.786E+01	9.136	1.578
334	6	0.275	75	22.26	0.240	20.57	20.69	3.051E+09	4.259E+01	9.484	1.629
335	1	0.025	75	37.63	0.200	20.59	20.69	3.523E+05	7.849E+00	5.547	0.895
335	2	0.075	75	37.63	0.256	20.59	20.72	2.859E+07	1.840E+01	7.456	1.265
335	3	0.125	75	37.63	0.279	20.59	20.73	2.208E+08	2.821E+01	8.344	1.450
335	4	0.175	75	37.63	0.299	20.59	20.74	8.488E+08	3.680E+01	8.929	1.566
335	5	0.225	75	37.63	0.312	20.59	20.75	2.320E+09	4.531E+01	9.366	1.656
335	6	0.275	75	37.63	0.332	20.59	20.76	5.181E+09	5.207E+01	9.714	1.717
336	1	0.025	75	62.11	0.312	20.59	20.74	5.836E+05	8.303E+00	5.766	0.919
336	2	0.075	75	62.11	0.391	20.59	20.78	4.739E+07	1.992E+01	7.676	1.299
336	3	0.125	75	62.11	0.428	20.59	20.80	3.661E+08	3.032E+01	8.564	1.482
336	4	0.175	75	62.11	0.461	20.59	20.82	1.408E+09	3.942E+01	9.149	1.596
336	5	0.225	75	62.11	0.478	20.59	20.83	3.850E+09	4.888E+01	9.585	1.689
336	6	0.275	75	62.11	0.508	20.59	20.84	8.600E+09	5.619E+01	9.935	1.750
337	1	0.025	75	150.03	0.651	20.59	20.91	1.426E+06	9.621E+00	6.154	0.983
337	2	0.075	75	150.03	0.800	20.59	20.99	1.161E+08	2.347E+01	8.065	1.371
337	3	0.125	75	150.03	0.885	20.59	21.03	8.980E+08	3.537E+01	8.953	1.549
337	4	0.175	75	150.03	0.952	20.59	21.06	3.457E+09	4.606E+01	9.539	1.663
337	5	0.225	75	150.03	0.996	20.59	21.09	9.461E+09	5.659E+01	9.976	1.753
337	6	0.275	75	150.03	1.051	20.59	21.11	2.115E+10	6.555E+01	10.325	1.817
338	1	0.025	75	433.77	1.545	20.59	21.36	4.244E+06	1.171E+01	6.628	1.068
338	2	0.075	75	433.77	1.888	20.59	21.53	3.476E+08	2.872E+01	8.541	1.458
338	3	0.125	75	433.77	2.089	20.59	21.63	2.699E+09	4.327E+01	9.431	1.636
338	4	0.175	75	433.77	2.241	20.59	21.71	1.042E+10	5.644E+01	10.018	1.752
338	5	0.225	75	433.77	2.344	20.59	21.76	2.856E+10	6.937E+01	10.456	1.841
338	6	0.275	75	433.77	2.472	20.59	21.82	6.400E+10	8.040E+01	10.806	1.905
339	1	0.025	75	1482.66	4.126	20.59	22.65	1.573E+07	1.493E+01	7.197	1.174
339	2	0.075	75	1482.66	5.004	20.59	23.09	1.308E+09	3.689E+01	9.117	1.567
339	3	0.125	75	1482.66	5.527	20.59	23.35	1.025E+10	5.563E+01	10.011	1.745
339	4	0.175	75	1482.66	5.942	20.59	23.56	3.984E+10	7.240E+01	10.600	1.860
339	5	0.225	75	1482.66	6.203	20.59	23.69	1.097E+11	8.914E+01	11.040	1.950
339	6	0.275	75	1482.66	6.550	20.59	23.87	2.472E+11	1.031E+02	11.393	2.013
340	1	0.025	75	3440.03	7.978	20.60	24.59	4.080E+07	1.782E+01	7.611	1.251
340	2	0.075	75	3440.03	9.539	20.60	25.37	3.448E+09	4.463E+01	9.538	1.650
340	3	0.125	75	3440.03	10.503	20.60	25.85	2.729E+10	6.747E+01	10.436	1.829
340	4	0.175	75	3440.03	11.297	20.60	26.25	1.070E+11	8.772E+01	11.029	1.943
340	5	0.225	75	3440.03	11.747	20.60	26.47	2.959E+11	1.084E+02	11.471	2.035
340	6	0.275	75	3440.03	12.330	20.60	26.76	6.700E+11	1.261E+02	11.826	2.101
341	1	0.025	75	6206.29	12.679	20.62	26.96	8.340E+07	2.011E+01	7.921	1.303
341	2	0.075	75	6206.29	14.944	20.62	28.10	7.141E+09	5.103E+01	9.854	1.708
341	3	0.125	75	6206.29	16.367	20.62	28.81	5.698E+10	7.752E+01	10.756	1.889
341	4	0.175	75	6206.29	17.513	20.62	29.38	2.248E+11	1.013E+02	11.352	2.006
341	5	0.225	75	6206.29	18.304	20.62	29.78	6.254E+11	1.245E+02	11.796	2.095
341	6	0.275	75	6206.29	18.640	20.62	29.94	1.406E+12	1.493E+02	12.148	2.174
345	1	0.025	75	9164.73	17.094	20.80	29.35	1.381E+08	2.189E+01	8.140	1.340
345	2	0.075	75	9164.73	19.966	20.80	30.79	1.192E+10	5.602E+01	10.076	1.748
345	3	0.125	75	9164.73	21.738	20.80	31.67	9.557E+10	8.558E+01	10.980	1.932
345	4	0.175	75	9164.73	23.707	20.80	32.66	3.825E+11	1.096E+02	11.583	2.040
345	5	0.225	75	9164.73	23.156	20.80	32.38	1.033E+12	1.444E+02	12.014	2.159
345	6	0.275	75	9164.73	21.243	20.80	31.42	2.215E+12	1.928E+02	12.345	2.285
346	1	0.025	75	21023.19	30.216	21.14	36.25	4.204E+08	2.794E+01	8.624	1.446
346	2	0.075	75	21023.19	35.429	21.14	38.86	3.737E+10	7.107E+01	10.573	1.852
346	3	0.125	75	21023.19	38.499	21.14	40.39	3.037E+11	1.086E+02	11.482	2.036
346	4	0.175	75	21023.19	40.015	21.14	41.15	1.196E+12	1.461E+02	12.078	2.165
346	5	0.225	75	21023.19	33.694	21.14	37.99	2.937E+12	2.246E+02	12.468	2.351
346	6	0.275	75	21023.19	19.415	21.14	30.85	4.958E+12	4.845E+02	12.695	2.685
347	1	0.025	75	38686.67	43.815	22.62	44.53	1.019E+09	3.483E+01	9.008	1.542
347	2	0.075	75	38686.67	51.681	22.62	48.46	9.256E+10	8.790E+01	10.966	1.944
347	3	0.125	75	38686.67	55.574	22.62	50.41	7.532E+11	1.357E+02	11.877	2.133
347	4	0.175	75	38686.67	51.835	22.62	48.54	2.749E+12	2.045E+02	12.439	2.311
347	5	0.225	75	38686.67	40.900	22.62	43.07	6.396E+12	3.368E+02	12.806	2.527
347	6	0.275	75	38686.67	12.121	22.62	28.68	8.272E+12	1.436E+03	12.918	3.157

Angle: 60 degrees
Data files: 363 364 365 366 367 368 370
Best Fit Line: Nu = 0.539(GrPr)^ 0.201
Fit Range: 5.76 < GrPr < 10.00
Correlation: R2 = 0.9982

Expt Numb	Pt#	x cm	θ deg	Flux w/m²	ΔT °C	TBulk °C	TFilm °C	GrPr	Nu	LogGrPr	LogNu
363	1	0.025	60	70.07	0.368	20.30	20.48	5.800E+05	7.950E+00	5.763	0.900
363	2	0.075	60	70.07	0.453	20.30	20.52	4.712E+07	1.939E+01	7.673	1.288
363	3	0.125	60	70.07	0.501	20.30	20.55	3.641E+08	2.922E+01	8.561	1.466
363	4	0.175	60	70.07	0.530	20.30	20.56	1.400E+09	3.867E+01	9.146	1.587
363	5	0.225	60	70.07	0.562	20.30	20.58	3.830E+09	4.691E+01	9.583	1.671
363	6	0.275	60	70.07	0.584	20.30	20.59	8.554E+09	5.511E+01	9.932	1.741
364	1	0.025	60	313.43	1.263	20.30	20.93	2.674E+06	1.036E+01	6.427	1.016
364	2	0.075	60	313.43	1.535	20.30	21.07	2.185E+08	2.556E+01	8.340	1.408
364	3	0.125	60	313.43	1.718	20.30	21.16	1.696E+09	3.807E+01	9.229	1.581
364	4	0.175	60	313.43	1.766	20.30	21.18	6.527E+09	5.183E+01	9.815	1.715
364	5	0.225	60	313.43	1.918	20.30	21.26	1.792E+10	6.133E+01	10.253	1.788
364	6	0.275	60	313.43	1.595	20.30	21.10	3.958E+10	9.021E+01	10.597	1.955
365	1	0.025	60	813.42	2.662	20.31	21.64	7.266E+06	1.273E+01	6.861	1.105
365	2	0.075	60	813.42	3.253	20.31	21.94	5.996E+08	3.123E+01	8.778	1.495
365	3	0.125	60	813.42	3.673	20.31	22.15	4.687E+09	4.607E+01	9.671	1.663
365	4	0.175	60	813.42	3.178	20.31	21.90	1.773E+10	7.461E+01	10.249	1.873
365	5	0.225	60	813.42	2.891	20.31	21.76	4.802E+10	1.055E+02	10.681	2.023
365	6	0.275	60	813.42	2.828	20.31	21.73	1.069E+11	1.318E+02	11.029	2.120
366	1	0.025	60	2890.80	6.938	20.46	23.93	2.962E+07	1.725E+01	7.472	1.237
366	2	0.075	60	2890.80	8.544	20.46	24.73	2.510E+09	4.194E+01	9.400	1.623
366	3	0.125	60	2890.80	9.400	20.46	25.16	1.982E+10	6.347E+01	10.297	1.803
366	4	0.175	60	2890.80	7.600	20.46	24.26	7.247E+10	1.102E+02	10.860	2.042
366	5	0.225	60	2890.80	7.577	20.46	24.25	1.979E+11	1.421E+02	11.296	2.152
366	6	0.275	60	2890.80	6.674	20.46	23.80	4.305E+11	1.974E+02	11.634	2.295
367	1	0.025	60	9531.05	16.364	21.12	29.30	1.284E+08	2.378E+01	8.109	1.376
367	2	0.075	60	9531.05	18.981	21.12	30.61	1.103E+10	6.132E+01	10.043	1.788
367	3	0.125	60	9531.05	14.399	21.12	28.32	7.667E+10	1.355E+02	10.885	2.132
367	4	0.175	60	9531.05	14.143	21.12	28.19	2.928E+11	1.932E+02	11.467	2.286
367	5	0.225	60	9531.05	14.269	21.12	28.25	8.024E+11	2.461E+02	11.904	2.391
367	6	0.275	60	9531.05	13.625	21.12	27.93	1.763E+12	3.153E+02	12.246	2.499
368	1	0.025	60	20860.95	30.031	21.22	36.23	3.737E+08	2.790E+01	8.573	1.446
368	2	0.075	60	20860.95	31.593	21.22	37.01	3.115E+10	7.942E+01	10.493	1.900
368	3	0.125	60	20860.95	23.928	21.22	33.18	2.076E+11	1.763E+02	11.317	2.246
368	4	0.175	60	20860.95	27.138	21.22	34.78	8.496E+11	2.168E+02	11.929	2.336
368	5	0.225	60	20860.95	25.185	21.22	33.81	2.235E+12	3.011E+02	12.349	2.479
368	6	0.275	60	20860.95	16.782	21.22	29.61	4.174E+12	5.579E+02	12.621	2.747
370	1	0.025	60	58811.51	60.840	22.09	52.51	1.736E+09	3.755E+01	9.240	1.575
370	2	0.075	60	58811.51	49.748	22.09	46.97	1.209E+11	1.392E+02	11.082	2.144
370	3	0.125	60	58811.51	49.062	22.09	46.62	9.238E+11	2.354E+02	11.966	2.372
370	4	0.175	60	58811.51	47.938	22.09	46.06	3.491E+12	3.377E+02	12.543	2.529
370	5	0.225	60	58811.51	49.150	22.09	46.67	9.710E+12	4.230E+02	12.987	2.626
370	6	0.275	60	58811.51	14.085	22.09	29.13	1.151E+13	1.876E+03	13.061	3.273

Angle: 45 degrees
Data files: 382 383 384 385 386 388 389 392 395
Best Fit Line: Nu = 0.502(GrPr)^ 0.203
Fit Range: 5.26 < GrPr < 9.00
Correlation: R2 = 0.9891

Expt Numb	Pt#	x cm	θ deg	Flux w/m²	ΔT °C	TBulk °C	TFilm °C	GrPr	Nu	LogGrPr	LogNu
382	1	0.025	45	24.58	0.186	21.86	21.96	1.828E+05	5.490E+00	5.262	0.740
382	2	0.075	45	24.58	0.222	21.86	21.98	1.483E+07	1.380E+01	7.171	1.140
382	3	0.125	45	24.58	0.244	21.86	21.99	1.145E+08	2.095E+01	8.059	1.321
382	4	0.175	45	24.58	0.262	21.86	22.00	4.401E+08	2.735E+01	8.644	1.437
382	5	0.225	45	24.58	0.279	21.86	22.00	1.203E+09	3.302E+01	9.080	1.519
382	6	0.275	45	24.58	0.230	21.86	21.98	2.681E+09	4.890E+01	9.428	1.689
383	1	0.025	45	51.17	0.322	21.86	22.02	3.821E+05	6.610E+00	5.582	0.820
383	2	0.075	45	51.17	0.385	21.86	22.05	3.101E+07	1.660E+01	7.492	1.220
383	3	0.125	45	51.17	0.426	21.86	22.07	2.396E+08	2.501E+01	8.379	1.398
383	4	0.175	45	51.17	0.476	21.86	22.09	9.219E+08	3.134E+01	8.965	1.496
383	5	0.225	45	51.17	0.478	21.86	22.10	2.519E+09	4.008E+01	9.401	1.603
383	6	0.275	45	51.17	0.399	21.86	22.06	5.608E+09	5.868E+01	9.749	1.769
384	1	0.025	45	145.60	0.706	21.85	22.20	1.100E+06	8.586E+00	6.041	0.934
384	2	0.075	45	145.60	0.873	21.85	22.28	8.953E+07	2.080E+01	7.952	1.318
384	3	0.125	45	145.60	0.975	21.85	22.33	6.930E+08	3.106E+01	8.841	1.492
384	4	0.175	45	145.60	0.936	21.85	22.32	2.659E+09	4.529E+01	9.425	1.656
384	5	0.225	45	145.60	0.721	21.85	22.21	7.218E+09	7.562E+01	9.858	1.879
384	6	0.275	45	145.60	0.835	21.85	22.26	1.616E+10	7.980E+01	10.209	1.902
385	1	0.025	45	576.28	2.049	21.84	22.87	4.532E+06	1.168E+01	6.656	1.068
385	2	0.075	45	576.28	2.619	21.84	23.15	3.734E+08	2.739E+01	8.572	1.438
385	3	0.125	45	576.28	2.080	21.84	22.88	2.835E+09	5.753E+01	9.453	1.760
385	4	0.175	45	576.28	1.960	21.84	22.82	1.085E+10	8.549E+01	10.036	1.932
385	5	0.225	45	576.28	1.827	21.84	22.76	2.954E+10	1.179E+02	10.470	2.072
385	6	0.275	45	576.28	2.188	21.84	22.94	6.663E+10	1.203E+02	10.824	2.080
386	1	0.025	45	2231.32	5.075	22.24	24.78	1.958E+07	1.816E+01	7.292	1.259
386	2	0.075	45	2231.32	6.567	22.24	25.53	1.651E+09	4.203E+01	9.218	1.624
386	3	0.125	45	2231.32	5.428	22.24	24.96	1.236E+10	8.487E+01	10.092	1.929
386	4	0.175	45	2231.32	4.691	22.24	24.59	4.652E+10	1.376E+02	10.668	2.139
386	5	0.225	45	2231.32	4.320	22.24	24.40	1.258E+11	1.923E+02	11.100	2.284
386	6	0.275	45	2231.32	4.881	22.24	24.68	2.852E+11	2.078E+02	11.455	2.318
388	1	0.025	45	5228.77	11.152	22.02	27.60	5.308E+07	1.923E+01	7.725	1.284
388	2	0.075	45	5228.77	9.472	22.02	26.76	4.124E+09	6.807E+01	9.615	1.833
388	3	0.125	45	5228.77	8.228	22.02	26.14	3.082E+10	1.308E+02	10.489	2.117
388	4	0.175	45	5228.77	10.652	22.02	27.35	1.259E+11	1.410E+02	11.100	2.149
388	5	0.225	45	5228.77	9.810	22.02	26.93	3.369E+11	1.971E+02	11.527	2.295
388	6	0.275	45	5228.77	10.313	22.02	27.18	7.612E+11	2.290E+02	11.881	2.360
389	1	0.025	45	9144.49	16.296	22.33	30.48	1.061E+08	2.285E+01	8.026	1.359
389	2	0.075	45	9144.49	12.595	22.33	28.63	7.899E+09	8.910E+01	9.898	1.950
389	3	0.125	45	9144.49	12.189	22.33	28.43	6.037E+10	1.535E+02	10.781	2.186
389	4	0.175	45	9144.49	13.735	22.33	29.20	2.404E+11	1.904E+02	11.381	2.280
389	5	0.225	45	9144.49	15.198	22.33	29.93	6.793E+11	2.208E+02	11.832	2.344
389	6	0.275	45	9144.49	13.962	22.33	29.31	1.474E+12	2.942E+02	12.168	2.469
392	1	0.025	45	20709.10	31.172	22.44	38.02	3.232E+08	2.657E+01	8.509	1.424
392	2	0.075	45	20709.10	24.613	22.44	34.74	2.320E+10	1.017E+02	10.365	2.007
392	3	0.125	45	20709.10	23.933	22.44	34.40	1.766E+11	1.745E+02	11.247	2.242
392	4	0.175	45	20709.10	25.260	22.44	35.07	6.962E+11	2.311E+02	11.843	2.364
392	5	0.225	45	20709.10	25.599	22.44	35.24	1.915E+12	2.931E+02	12.282	2.467
392	6	0.275	45	20709.10	16.630	22.44	30.75	3.560E+12	5.573E+02	12.551	2.746
395	1	0.025	45	36853.81	44.964	23.33	45.81	7.387E+08	3.225E+01	8.868	1.509
395	2	0.075	45	36853.81	35.843	23.33	41.25	5.196E+10	1.225E+02	10.716	2.088
395	3	0.125	45	36853.81	34.182	23.33	40.42	3.902E+11	2.145E+02	11.591	2.331
395	4	0.175	45	36853.81	36.608	23.33	41.64	1.559E+12	2.797E+02	12.193	2.447
395	5	0.225	45	36853.81	37.412	23.33	42.04	4.317E+12	3.515E+02	12.635	2.546
395	6	0.275	45	36853.81	16.429	23.33	31.55	6.555E+12	1.002E+03	12.817	3.001

Angle: 30 degrees
Data files: 401 402 403 404 405 406 407 409 410 413
Best Fit Line: Nu = 0.472(GrPr)^ 0.207
Fit Range: 4.58 < GrPr < 8.00
Correlation: R2 = 0.9923

Expt Numb	Pt#	x cm	θ deg	Flux w/m²	ΔT °C	TBulk °C	TFilm °C	GrPr	Nu	LogGrPr	LogNu
401	1	0.025	30	6.68	0.064	23.36	23.39	3.831E+04	4.331E+00	4.583	0.637
401	2	0.075	30	6.68	0.083	23.36	23.40	3.105E+06	1.007E+01	6.492	1.003
401	3	0.125	30	6.68	0.082	23.36	23.40	2.396E+07	1.679E+01	7.379	1.225
401	4	0.175	30	6.68	0.088	23.36	23.40	9.204E+07	2.206E+01	7.964	1.344
401	5	0.225	30	6.68	0.105	23.36	23.41	2.516E+08	2.372E+01	8.401	1.375
401	6	0.275	30	6.68	0.103	23.36	23.41	5.615E+08	2.968E+01	8.749	1.472
402	1	0.025	30	24.14	0.191	23.34	23.43	1.388E+05	5.246E+00	5.142	0.720
402	2	0.075	30	24.14	0.240	23.34	23.46	1.126E+07	1.254E+01	7.052	1.098
402	3	0.125	30	24.14	0.252	23.34	23.46	8.692E+07	1.987E+01	7.939	1.298
402	4	0.175	30	24.14	0.220	23.34	23.45	3.336E+08	3.188E+01	8.523	1.504
402	5	0.225	30	24.14	0.222	23.34	23.45	9.117E+08	4.061E+01	8.960	1.609
402	6	0.275	30	24.14	0.245	23.34	23.46	2.036E+09	4.491E+01	9.309	1.652
403	1	0.025	30	107.59	0.590	23.32	23.61	6.252E+05	7.563E+00	5.796	0.879
403	2	0.075	30	107.59	0.748	23.32	23.69	5.087E+07	1.787E+01	7.706	1.252
403	3	0.125	30	107.59	0.542	23.32	23.59	3.902E+08	4.111E+01	8.591	1.614
403	4	0.175	30	107.59	0.591	23.32	23.61	1.501E+09	5.281E+01	9.176	1.723
403	5	0.225	30	107.59	0.640	23.32	23.64	4.108E+09	6.265E+01	9.614	1.797
403	6	0.275	30	107.59	0.706	23.32	23.67	9.184E+09	6.950E+01	9.963	1.842
404	1	0.025	30	402.72	1.620	23.31	24.12	2.408E+06	1.029E+01	6.382	1.012
404	2	0.075	30	402.72	1.547	23.31	24.08	1.947E+08	3.233E+01	8.289	1.510
404	3	0.125	30	402.72	1.343	23.31	23.98	1.494E+09	6.208E+01	9.174	1.793
404	4	0.175	30	402.72	1.337	23.31	23.98	5.737E+09	8.727E+01	9.759	1.941
404	5	0.225	30	402.72	1.468	23.31	24.04	1.573E+10	1.022E+02	10.197	2.009
404	6	0.275	30	402.72	1.659	23.31	24.14	3.530E+10	1.105E+02	10.548	2.043
405	1	0.025	30	1471.64	4.478	23.31	25.55	9.517E+06	1.355E+01	6.978	1.132
405	2	0.075	30	1471.64	4.329	23.31	25.47	7.678E+08	4.206E+01	8.885	1.624
405	3	0.125	30	1471.64	3.660	23.31	25.14	5.819E+09	8.299E+01	9.765	1.919
405	4	0.175	30	1471.64	3.713	23.31	25.17	2.239E+10	1.145E+02	10.350	2.059
405	5	0.225	30	1471.64	4.050	23.31	25.33	6.173E+10	1.349E+02	10.791	2.130
405	6	0.275	30	1471.64	4.252	23.31	25.43	1.385E+11	1.570E+02	11.141	2.196
406	1	0.025	30	5361.38	11.813	23.33	29.23	4.158E+07	1.854E+01	7.619	1.268
406	2	0.075	30	5361.38	8.606	23.33	27.63	3.122E+09	7.665E+01	9.494	1.884
406	3	0.125	30	5361.38	9.825	23.33	28.24	2.481E+10	1.117E+02	10.395	2.048
406	4	0.175	30	5361.38	10.619	23.33	28.64	9.710E+10	1.446E+02	10.987	2.160
406	5	0.225	30	5361.38	10.276	23.33	28.46	2.632E+11	1.922E+02	11.420	2.284
406	6	0.275	30	5361.38	10.811	23.33	28.73	5.948E+11	2.231E+02	11.774	2.348
407	1	0.025	30	14339.38	20.150	23.60	33.68	1.345E+08	2.875E+01	8.129	1.459
407	2	0.075	30	14339.38	17.626	23.60	32.42	1.035E+10	9.890E+01	10.015	1.995
407	3	0.125	30	14339.38	18.954	23.60	33.08	8.205E+10	1.530E+02	10.914	2.185
407	4	0.175	30	14339.38	20.382	23.60	33.79	3.244E+11	1.989E+02	11.511	2.299
407	5	0.225	30	14339.38	20.315	23.60	33.76	8.852E+11	2.566E+02	11.947	2.409
407	6	0.275	30	14339.38	17.644	23.60	32.43	1.871E+12	3.623E+02	12.272	2.559
409	1	0.025	30	28596.21	29.354	23.72	38.40	3.197E+08	3.893E+01	8.505	1.590
409	2	0.075	30	28596.21	29.036	23.72	38.24	2.575E+10	1.181E+02	10.411	2.072
409	3	0.125	30	28596.21	31.179	23.72	39.31	2.062E+11	1.829E+02	11.314	2.262
409	4	0.175	30	28596.21	32.834	23.72	40.14	8.145E+11	2.427E+02	11.911	2.385
409	5	0.225	30	28596.21	33.317	23.72	40.38	2.244E+12	3.074E+02	12.351	2.488
409	6	0.275	30	28596.21	19.317	23.72	33.38	3.879E+12	6.584E+02	12.589	2.818
410	1	0.025	30	58536.04	44.500	25.63	47.88	8.804E+08	5.154E+01	8.945	1.712
410	2	0.075	30	58536.04	45.602	25.63	48.43	7.243E+10	1.507E+02	10.860	2.178
410	3	0.125	30	58536.04	46.389	25.63	48.82	5.650E+11	2.468E+02	11.752	2.392
410	4	0.175	30	58536.04	48.472	25.63	49.86	2.233E+12	3.300E+02	12.349	2.519
410	5	0.225	30	58536.04	49.446	25.63	50.35	6.184E+12	4.155E+02	12.791	2.619
410	6	0.275	30	58536.04	13.076	25.63	32.17	7.557E+12	1.997E+03	12.878	3.300
413	1	0.025	30	57258.65	42.401	26.77	47.97	8.634E+08	5.291E+01	8.936	1.724
413	2	0.075	30	57258.65	47.940	26.77	50.74	7.545E+10	1.396E+02	10.878	2.145
413	3	0.125	30	57258.65	47.213	26.77	50.37	5.765E+11	2.365E+02	11.761	2.374
413	4	0.175	30	57258.65	49.567	26.77	51.55	2.285E+12	3.147E+02	12.359	2.498
413	5	0.225	30	57258.65	49.893	26.77	51.71	6.271E+12	4.018E+02	12.797	2.604
413	6	0.275	30	57258.65	8.811	26.77	31.17	7.088E+12	2.905E+03	12.851	3.463

Angle: 15 degrees
Data files: 421 422 423 424 425 426 429 430 431
Best Fit Line: Nu = 0.288(GrPr)^ 0.233
Fit Range: 4.28 < GrPr < 7.10
Correlation: R2 = 0.9185

Expt Numb	Pt#	x cm	θ deg	Flux w/m²	ΔT °C	TBulk °C	TFilm °C	GrPr	Nu	LogGrPr	LogNu
421	1	0.025	15	6.04	0.097	24.58	24.63	1.925E+04	2.579E+00	4.284	0.411
421	2	0.075	15	6.04	0.112	24.58	24.64	1.560E+06	6.688E+00	6.193	0.825
421	3	0.125	15	6.04	0.117	24.58	24.64	1.204E+07	1.069E+01	7.081	1.029
421	4	0.175	15	6.04	0.106	24.58	24.64	4.623E+07	1.653E+01	7.665	1.218
421	5	0.225	15	6.04	0.101	24.58	24.63	1.263E+08	2.214E+01	8.101	1.345
421	6	0.275	15	6.04	0.111	24.58	24.64	2.819E+08	2.475E+01	8.450	1.394
422	1	0.025	15	22.80	0.238	24.55	24.67	7.278E+04	3.964E+00	4.862	0.598
422	2	0.075	15	22.80	0.283	24.55	24.69	5.902E+06	9.989E+00	6.771	1.000
422	3	0.125	15	22.80	0.234	24.55	24.67	4.548E+07	2.014E+01	7.658	1.304
422	4	0.175	15	22.80	0.241	24.55	24.67	1.748E+08	2.733E+01	8.242	1.437
422	5	0.225	15	22.80	0.245	24.55	24.67	4.776E+08	3.456E+01	8.679	1.539
422	6	0.275	15	22.80	0.263	24.55	24.68	1.066E+09	3.934E+01	9.028	1.595
423	1	0.025	15	84.57	0.598	24.50	24.80	2.720E+05	5.842E+00	5.434	0.767
423	2	0.075	15	84.57	0.549	24.50	24.78	2.200E+07	1.911E+01	7.342	1.281
423	3	0.125	15	84.57	0.534	24.50	24.77	1.697E+08	3.271E+01	8.230	1.515
423	4	0.175	15	84.57	0.561	24.50	24.78	6.523E+08	4.357E+01	8.814	1.639
423	5	0.225	15	84.57	0.578	24.50	24.79	1.783E+09	5.444E+01	9.251	1.736
423	6	0.275	15	84.57	0.623	24.50	24.82	3.984E+09	6.163E+01	9.600	1.790
424	1	0.025	15	360.65	1.712	24.49	25.34	1.194E+06	8.693E+00	6.077	0.939
424	2	0.075	15	360.65	1.274	24.49	25.12	9.559E+07	3.506E+01	7.980	1.545
424	3	0.125	15	360.65	1.347	24.49	25.16	7.391E+08	5.524E+01	8.869	1.742
424	4	0.175	15	360.65	1.454	24.49	25.21	2.847E+09	7.165E+01	9.454	1.855
424	5	0.225	15	360.65	1.548	24.49	25.26	7.800E+09	8.649E+01	9.892	1.937
424	6	0.275	15	360.65	1.572	24.49	25.27	1.742E+10	1.041E+02	10.241	2.018
425	1	0.025	15	1442.55	4.414	24.48	26.69	5.123E+06	1.343E+01	6.710	1.128
425	2	0.075	15	1442.55	3.826	24.48	26.40	4.088E+08	4.653E+01	8.612	1.668
425	3	0.125	15	1442.55	3.849	24.48	26.41	3.156E+09	7.709E+01	9.499	1.887
425	4	0.175	15	1442.55	3.954	24.48	26.46	1.216E+10	1.050E+02	10.085	2.021
425	5	0.225	15	1442.55	4.195	24.48	26.58	3.343E+10	1.273E+02	10.524	2.105
425	6	0.275	15	1442.55	4.400	24.48	26.68	7.499E+10	1.482E+02	10.875	2.171
426	1	0.025	15	5235.59	7.777	24.51	28.40	2.022E+07	2.755E+01	7.306	1.440
426	2	0.075	15	5235.59	8.039	24.51	28.53	1.648E+09	7.994E+01	9.217	1.903
426	3	0.125	15	5235.59	10.314	24.51	29.67	1.340E+10	1.035E+02	10.127	2.015
426	4	0.175	15	5235.59	10.165	24.51	29.59	5.131E+10	1.471E+02	10.710	2.168
426	5	0.225	15	5235.59	10.306	24.51	29.66	1.407E+11	1.865E+02	11.148	2.271
426	6	0.275	15	5235.59	10.760	24.51	29.89	3.171E+11	2.183E+02	11.501	2.339
429	1	0.025	15	15116.00	15.113	24.75	32.31	6.940E+07	4.054E+01	7.841	1.608
429	2	0.075	15	15116.00	17.936	24.75	33.72	5.953E+09	1.021E+02	9.775	2.009
429	3	0.125	15	15116.00	18.436	24.75	33.97	4.639E+10	1.655E+02	10.666	2.219
429	4	0.175	15	15116.00	19.841	24.75	34.67	1.832E+11	2.150E+02	11.263	2.332
429	5	0.225	15	15116.00	21.729	24.75	35.61	5.189E+11	2.518E+02	11.715	2.401
429	6	0.275	15	15116.00	15.776	24.75	32.64	1.030E+12	4.269E+02	12.013	2.630
430	1	0.025	15	28443.73	22.911	26.51	37.96	1.621E+08	4.967E+01	8.210	1.696
430	2	0.075	15	28443.73	29.942	26.51	41.48	1.479E+10	1.131E+02	10.170	2.054
430	3	0.125	15	28443.73	29.511	26.51	41.26	1.133E+11	1.914E+02	11.054	2.282
430	4	0.175	15	28443.73	30.602	26.51	41.81	4.430E+11	2.581E+02	11.646	2.412
430	5	0.225	15	28443.73	30.742	26.51	41.88	1.213E+12	3.303E+02	12.084	2.519
430	6	0.275	15	28443.73	9.269	26.51	31.14	1.820E+12	1.372E+03	12.260	3.137
431	1	0.025	15	57266.67	41.052	28.18	48.70	4.563E+08	5.458E+01	8.659	1.737
431	2	0.075	15	57266.67	44.720	28.18	50.54	3.885E+10	1.498E+02	10.589	2.175
431	3	0.125	15	57266.67	44.312	28.18	50.33	2.981E+11	2.520E+02	11.474	2.401
431	4	0.175	15	57266.67	47.418	28.18	51.89	1.194E+12	3.288E+02	12.077	2.517
431	5	0.225	15	57266.67	48.250	28.18	52.30	3.297E+12	4.151E+02	12.518	2.618
431	6	0.275	15	57266.67	7.176	28.18	31.76	3.763E+12	3.563E+03	12.576	3.552

Angle: 0 degrees
Data files: 602 603 604 605 606 607 608 609 613 614
Best Fit Line: $Nu_{x} = 0.164(Ra_{L})^{0.327}$
Fit Range: 6.8 < GrPr < 9.00
Correlation: R2 = 0.5849

Expt Numb	Pt#	x cm	θ deg	Flux w/m²	ΔT °C	TBulk °C	TFilm °C	Ra_L	Nu_x	LogGrPr	LogNu
602	1	0.051	0	1.52	0.076	29.56	29.60	2.451E+05	1.665E+00	5.389	0.221
602	2	0.051	0	1.52	0.083	29.56	29.60	2.685E+05	1.520E+00	5.429	0.182
602	3	0.051	0	1.52	0.079	29.56	29.60	2.560E+05	1.594E+00	5.408	0.203
602	4	0.051	0	1.52	0.077	29.56	29.60	2.494E+05	1.637E+00	5.397	0.214
602	5	0.051	0	1.52	0.082	29.56	29.60	2.656E+05	1.537E+00	5.424	0.187
602	6	0.051	0	1.52	0.062	29.56	29.59	2.005E+05	2.035E+00	5.302	0.309
603	1	0.051	0	6.07	0.154	29.49	29.57	4.977E+05	3.276E+00	5.697	0.515
603	2	0.051	0	6.07	0.181	29.49	29.59	5.866E+05	2.781E+00	5.768	0.444
603	3	0.051	0	6.07	0.156	29.49	29.57	5.065E+05	3.219E+00	5.705	0.508
603	4	0.051	0	6.07	0.181	29.49	29.59	5.863E+05	2.783E+00	5.768	0.444
603	5	0.051	0	6.07	0.167	29.49	29.58	5.414E+05	3.013E+00	5.733	0.479
603	6	0.051	0	6.07	0.165	29.49	29.58	5.349E+05	3.049E+00	5.728	0.484
604	1	0.051	0	23.59	0.317	29.44	29.60	1.028E+06	6.168E+00	6.012	0.790
604	2	0.051	0	23.59	0.321	29.44	29.60	1.042E+06	6.089E+00	6.018	0.785
604	3	0.051	0	23.59	0.320	29.44	29.60	1.039E+06	6.105E+00	6.017	0.786
604	4	0.051	0	23.59	0.297	29.44	29.59	9.637E+05	6.578E+00	5.984	0.818
604	5	0.051	0	23.59	0.283	29.44	29.58	9.160E+05	6.918E+00	5.962	0.840
604	6	0.051	0	23.59	0.320	29.44	29.60	1.039E+06	6.106E+00	6.017	0.786
605	1	0.051	0	91.64	0.740	29.38	29.75	2.418E+06	1.027E+01	6.383	1.011
605	2	0.051	0	91.64	0.557	29.38	29.66	1.811E+06	1.365E+01	6.258	1.135
605	3	0.051	0	91.64	0.673	29.38	29.72	2.194E+06	1.129E+01	6.341	1.053
605	4	0.051	0	91.64	0.661	29.38	29.71	2.156E+06	1.149E+01	6.334	1.060
605	5	0.051	0	91.64	0.593	29.38	29.68	1.932E+06	1.280E+01	6.286	1.107
605	6	0.051	0	91.64	0.782	29.38	29.78	2.559E+06	9.707E+00	6.408	0.987
606	1	0.051	0	577.90	1.636	29.35	30.17	5.452E+06	2.924E+01	6.737	1.466
606	2	0.051	0	577.90	1.853	29.35	30.27	6.205E+06	2.582E+01	6.793	1.412
606	3	0.051	0	577.90	1.967	29.35	30.33	6.604E+06	2.432E+01	6.820	1.386
606	4	0.051	0	577.90	2.063	29.35	30.38	6.944E+06	2.318E+01	6.842	1.365
606	5	0.051	0	577.90	1.622	29.35	30.16	5.404E+06	2.949E+01	6.733	1.470
606	6	0.051	0	577.90	1.963	29.35	30.33	6.590E+06	2.437E+01	6.819	1.387
607	1	0.051	0	2290.64	4.296	29.34	31.49	1.521E+07	4.400E+01	7.182	1.643
607	2	0.051	0	2290.64	4.769	29.34	31.72	1.707E+07	3.962E+01	7.232	1.598
607	3	0.051	0	2290.64	5.070	29.34	31.87	1.826E+07	3.725E+01	7.262	1.571
607	4	0.051	0	2290.64	5.517	29.34	32.10	2.007E+07	3.422E+01	7.303	1.534
607	5	0.051	0	2290.64	4.886	29.34	31.78	1.753E+07	3.866E+01	7.244	1.587
607	6	0.051	0	2290.64	4.456	29.34	31.57	1.583E+07	4.242E+01	7.200	1.628
608	1	0.051	0	9192.30	11.896	29.39	35.34	4.961E+07	6.319E+01	7.696	1.801
608	2	0.051	0	9192.30	12.679	29.39	35.73	5.371E+07	5.923E+01	7.730	1.773
608	3	0.051	0	9192.30	14.209	29.39	36.49	6.203E+07	5.277E+01	7.793	1.722
608	4	0.051	0	9192.30	14.577	29.39	36.68	6.410E+07	5.141E+01	7.807	1.711
608	5	0.051	0	9192.30	14.201	29.39	36.49	6.199E+07	5.279E+01	7.792	1.723
608	6	0.051	0	9192.30	11.182	29.39	34.98	4.597E+07	6.728E+01	7.662	1.828
609	1	0.051	0	20652.34	21.275	29.60	40.23	1.067E+08	7.852E+01	8.028	1.895
609	2	0.051	0	20652.34	23.187	29.60	41.19	1.203E+08	7.189E+01	8.080	1.857
609	3	0.051	0	20652.34	24.265	29.60	41.73	1.283E+08	6.862E+01	8.108	1.836
609	4	0.051	0	20652.34	24.061	29.60	41.63	1.267E+08	6.922E+01	8.103	1.840
609	5	0.051	0	20652.34	24.789	29.60	41.99	1.322E+08	6.713E+01	8.121	1.827
609	6	0.051	0	20652.34	10.102	29.60	34.65	4.096E+07	1.675E+02	7.612	2.224
613	1	0.051	0	37163.32	31.485	29.68	45.42	1.880E+08	9.444E+01	8.274	1.975
613	2	0.051	0	37163.32	35.485	29.68	47.42	2.254E+08	8.347E+01	8.353	1.922
613	3	0.051	0	37163.32	35.947	29.68	47.65	2.299E+08	8.236E+01	8.362	1.916
613	4	0.051	0	37163.32	36.002	29.68	47.68	2.305E+08	8.223E+01	8.363	1.915
613	5	0.051	0	37163.32	36.873	29.68	48.11	2.392E+08	8.022E+01	8.379	1.904
613	6	0.051	0	37163.32	5.628	29.68	32.49	2.083E+07	5.437E+02	7.319	2.735
614	1	0.051	0	58010.16	43.107	30.59	52.14	3.141E+08	1.063E+02	8.497	2.027
614	2	0.051	0	58010.16	45.414	30.59	53.29	3.416E+08	1.007E+02	8.534	2.003
614	3	0.051	0	58010.16	46.469	30.59	53.82	3.546E+08	9.831E+01	8.550	1.993
614	4	0.051	0	58010.16	44.101	30.59	52.64	3.258E+08	1.038E+02	8.513	2.016
614	5	0.051	0	58010.16	43.948	30.59	52.56	3.240E+08	1.042E+02	8.511	2.018
614	6	0.051	0	58010.16	1.107	30.59	31.14	3.858E+06	4.328E+03	6.586	3.636

Appendix 4.2 Stratified Bulk Temperature Heat Transfer Data

Angle: 0 degrees (Vertical)
Data file: NS90_07
Stratified Ambient Fluid

Expt Numb	P#	x cm	θ deg	Flux w/m²	ΔT °C	TBulk °C	TFilm °C	GrPr	Nu	LogGrPr	LogNu
7	1	0.037	90	207.61	0.810	23.24	23.65	1.099E+07	1.552E+01	7.041	1.191
7	2	0.081	90	207.61	0.961	22.90	23.38	2.617E+08	2.901E+01	8.418	1.463
7	3	0.149	90	207.61	1.030	23.13	23.65	3.069E+09	4.985E+01	9.487	1.698
7	4	0.227	90	207.61	0.873	23.46	23.90	1.656E+10	8.922E+01	10.219	1.950
7	5	0.303	90	207.61	0.618	24.68	24.99	5.608E+10	1.680E+02	10.749	2.225
7	6	0.381	90	207.61	0.616	26.33	26.64	1.533E+11	2.111E+02	11.186	2.324
7	1	0.037	90	835.63	2.440	23.29	24.51	4.647E+07	2.068E+01	7.667	1.316
7	2	0.081	90	835.63	2.905	22.90	24.36	1.114E+09	3.853E+01	9.047	1.586
7	3	0.149	90	835.63	3.210	23.16	24.76	1.315E+10	6.421E+01	10.119	1.808
7	4	0.227	90	835.63	3.192	23.51	25.11	7.127E+10	9.795E+01	10.853	1.991
7	5	0.303	90	835.63	2.704	24.72	26.07	2.391E+11	1.541E+02	11.379	2.188
7	6	0.381	90	835.63	2.356	26.37	27.55	6.456E+11	2.217E+02	11.810	2.346
7	1	0.037	90	1840.45	4.525	23.37	25.63	1.088E+08	2.449E+01	8.036	1.389
7	2	0.081	90	1840.45	5.404	22.92	25.62	2.628E+09	4.546E+01	9.420	1.658
7	3	0.149	90	1840.45	6.004	23.18	26.18	3.124E+10	7.532E+01	10.495	1.877
7	4	0.227	90	1840.45	6.188	23.57	26.66	1.703E+11	1.108E+02	11.231	2.045
7	5	0.303	90	1840.45	5.777	24.79	27.68	5.711E+11	1.582E+02	11.757	2.199
7	6	0.381	90	1840.45	5.310	26.37	29.03	1.525E+12	2.158E+02	12.183	2.334

Angle: 45 degrees
Data files: NS45_10, NS45_11, NS45_12
Stratified Ambient Fluid

Expt Numb	Pt#	x cm	θ deg	Flux w/m²	ΔT °C	TBulk °C	TFilm °C	GrPr	Nu	LogGrPr	LogNu
10	1	0.030	45	150.14	1.002	15.54	16.04	1.529E+06	7.664E+00	6.184	0.884
10	2	0.144	45	150.14	0.830	17.01	17.42	9.027E+08	4.409E+01	8.956	1.644
10	3	0.221	45	150.14	0.713	19.39	19.75	5.858E+09	7.787E+01	9.768	1.891
10	4	0.297	45	150.14	0.660	22.14	22.47	2.293E+10	1.123E+02	10.360	2.050
10	5	0.373	45	150.14	0.630	24.85	25.16	6.673E+10	1.468E+02	10.824	2.167
10	6	0.449	45	150.14	0.570	27.81	28.09	1.629E+11	1.939E+02	11.212	2.288
10	7	0.487	45	150.14	0.560	29.11	29.39	2.396E+11	2.134E+02	11.380	2.329
11	1	0.030	45	664.79	2.780	15.85	17.24	7.511E+06	1.219E+01	6.876	1.086
11	2	0.144	45	664.79	2.520	17.37	18.63	4.394E+09	6.408E+01	9.643	1.807
11	3	0.221	45	664.79	2.300	19.54	20.69	2.767E+10	1.066E+02	10.442	2.028
11	4	0.297	45	664.79	2.060	22.16	23.19	1.060E+11	1.590E+02	11.025	2.201
11	5	0.373	45	664.79	2.000	24.83	25.83	3.061E+11	2.044E+02	11.486	2.310
11	6	0.449	45	664.79	1.950	27.52	28.49	7.350E+11	2.507E+02	11.866	2.399
11	7	0.487	45	664.79	1.900	28.57	29.52	1.067E+12	2.784E+02	12.028	2.445
11	1	0.030	45	1378.22	6.150	15.85	18.92	1.777E+07	1.137E+01	7.250	1.056
11	2	0.144	45	1378.22	4.650	17.37	19.69	9.846E+09	7.177E+01	9.993	1.856
11	3	0.221	45	1378.22	4.190	19.54	21.63	6.102E+10	1.210E+02	10.785	2.083
11	4	0.297	45	1378.22	4.010	22.16	24.16	2.325E+11	1.689E+02	11.366	2.228
11	5	0.373	45	1378.22	3.860	24.83	26.76	6.657E+11	2.190E+02	11.823	2.340
11	6	0.449	45	1378.22	3.580	27.52	29.31	1.583E+12	2.825E+02	12.199	2.451
11	7	0.487	45	1378.22	3.630	28.51	30.32	2.294E+12	3.015E+02	12.361	2.479
12	1	0.030	45	30208.20	47.780	15.85	39.74	1.065E+09	3.043E+01	9.027	1.483
12	2	0.144	45	30208.20	34.890	17.37	34.81	4.675E+11	2.016E+02	11.670	2.305
12	3	0.221	45	30208.20	34.900	19.54	36.99	2.759E+12	3.064E+02	12.441	2.486
12	4	0.297	45	30208.20	31.720	22.16	38.02	9.375E+12	4.524E+02	12.972	2.656
12	5	0.373	45	30208.20	31.020	24.83	40.34	2.531E+13	5.784E+02	13.403	2.762

Appendix 5

Development of Prandtl Model

The full Navier-Stokes equation is written

$$\rho\left(\frac{\partial u}{\partial t}+u\frac{\partial u}{\partial x}+v\frac{\partial u}{\partial y}+w\frac{\partial u}{\partial z}\right)=\mu\left(\frac{\partial^2 u}{\partial x^2}+\frac{\partial^2 u}{\partial y^2}+\frac{\partial^2 u}{\partial z^2}\right)-\frac{\partial P}{\partial x}+\rho X \tag{A5-1}$$

where X is the body force term:

$$X = g\beta(T-T_\infty) \tag{A5-2}$$

In this instance, we utilize a coordinate system inclined parallel to the slope. Thus the body force term for the x momentum equation resolves to,

$$X = g\sin\phi\beta(T-T_\infty) \tag{A5-3}$$

where φ is the angle from horizontal. Also, define $\theta=T-T_\infty$, so that

$$X = g\sin\phi\beta\theta \tag{A5-4}$$

Make the following simplifying assumptions: steady state ⇒ du/dt = 0; 1-dimensional ⇒ v=w=0; and u is a function only of y. In addition neglect pressure effects. The N-S equation reduces to

$$v\frac{\partial^2 u}{\partial y^2}+g\sin\phi\beta\theta=0 \tag{A5-5}$$

where φ is the angle of inclination from horizontal and β is the coefficient of thermal expansion.

The energy equation is

$$\rho c_p\left(u\frac{\partial T}{\partial x}+v\frac{\partial T}{\partial y}+w\frac{\partial T}{\partial z}\right)=k\left(\frac{\partial^2 T}{\partial x^2}+\frac{\partial^2 T}{\partial y^2}+\frac{\partial^2 T}{\partial z^2}\right) \tag{A5-6}$$

Take v=w=0 and regard the second derivatives in the x and z directions as small, so that this reduces to

$$u\frac{\partial T}{\partial x}=\frac{k}{\rho c_p}\frac{\partial^2 T}{\partial y^2} \tag{A5-7}$$

Now, if h_v is the vertical height or elevation, a linear temperature gradient in the ambient atmosphere can be expressed in terms of constants A and B as,

$$T_\infty = A + Bh_v \tag{A5-8}$$

Note that,

$$h_v = x\sin\phi + y\cos\phi \tag{A5-9}$$

Thus,

$$\theta = T - T_\infty = T - (A + Bh_v) \tag{A5-10}$$

$$\frac{\partial\theta}{\partial x}=\frac{\partial T}{\partial x}-B\sin\phi \tag{A5-11}$$

$$u\frac{\partial T}{\partial x}=u\left(\frac{\partial \theta}{\partial x}+B\sin\phi\right)=uB\sin\phi \tag{A5-12}$$

Note that dθ/dx is zero in the above equation because ΔT is assumed to be constant along the slope. Using the above relation, we can transform the equation of energy to

$$\alpha\frac{\partial^2\theta}{\partial y^2}-uB\sin\phi=0 \tag{A5-13}$$

Differentiating twice gives,

$$\frac{\partial^2 u}{\partial y^2}=\frac{\alpha}{B\sin\phi}\frac{\partial^4\theta}{\partial y^4} \tag{A5-14}$$

This can then be combined with the equation of motion to eliminate u yielding,

$$\frac{\partial^4\theta}{\partial y^4}+\left(\frac{g\beta}{\alpha\nu}\right)B\sin^2\phi\theta=0 \tag{A5-15}$$

This is a fourth order homogeneous linear differential equation fitting the general form,

$$L(\theta)=\frac{d^4\theta}{dy^4}+P\theta=0 \text{ where } P=\frac{g\beta}{\alpha\nu}B\sin^2\phi \tag{A5-16}$$

This equation has the general solution,

$$\theta(y)=C_1\theta_1(y)+C_2\theta_2(y)+C_3\theta_3(y)+C_4\theta_4(y) \tag{A5-17}$$

where θ_i are the 4 independent solutions to the equation.

The characteristic equation is obtained by writing,

$$L(e^{ry})=(r^4+P)e^{ry}=0 \tag{A5-18}$$

yielding the characteristic equation,

$$r^4+P=0 \tag{A5-19}$$

$$\Rightarrow r^4=-P=(-1)P$$

Note that,

$$-1=e^{\pi i}=e^{3\pi i}=e^{5\pi i}=e^{7\pi i} \tag{A5-20}$$

This yields the four roots,

$$r_1=e^{i\frac{\pi}{4}}P^{\frac{1}{4}}=\left(\cos\frac{\pi}{4}+i\sin\frac{\pi}{4}\right)P^{\frac{1}{4}}=\frac{1}{\sqrt{2}}(1+i)P^{\frac{1}{4}} \tag{A5-21}$$

$$r_2=e^{i\frac{3\pi}{4}}P^{\frac{1}{4}}=\left(\cos\frac{3\pi}{4}+i\sin\frac{3\pi}{4}\right)P^{\frac{1}{4}}=-\frac{1}{\sqrt{2}}(1-i)P^{\frac{1}{4}} \tag{A5-22}$$

$$r_3=e^{i\frac{5\pi}{4}}P^{\frac{1}{4}}=\left(\cos\frac{5\pi}{4}+i\sin\frac{5\pi}{4}\right)P^{\frac{1}{4}}=-\frac{1}{\sqrt{2}}(1+i)P^{\frac{1}{4}} \tag{A5-23}$$

$$r_4 = e^{i\frac{7\pi}{4}} P^{\frac{1}{4}} = \left(\cos\frac{7\pi}{4} + i\sin\frac{7\pi}{4}\right) P^{\frac{1}{4}} = \frac{1}{\sqrt{2}}(1-i)P^{\frac{1}{4}} \tag{A5-24}$$

At this point we define $(P/4)^{-1/4} = l$. Also, note that r_3 and r_4 are the complex conjugates of r_2 and r_1 respectively. Thus,

$$e^{r_1 y} = e^{\frac{y}{l}}\left[\cos\frac{y}{l} + i\sin\frac{y}{l}\right] \tag{A5-25}$$

and,

$$e^{r_2 y} = e^{-\frac{y}{l}}\left[\cos\frac{y}{l} + i\sin\frac{y}{l}\right] \tag{A5-26}$$

are two complex valued solutions of the equation. This allows us to say that,

$$\theta_1(y) = e^{-\frac{y}{l}}\cos\frac{y}{l} \tag{A5-27}$$

$$\theta_2(y) = e^{\frac{y}{l}}\sin\frac{y}{l} \tag{A5-28}$$

$$\theta_3(y) = e^{-\frac{y}{l}}\cos\frac{y}{l} \tag{A5-29}$$

$$\theta_4(y) = e^{-\frac{y}{l}}\sin\frac{y}{l} \tag{A5-30}$$

are four real valued independent solutions of the ODE for the general solution which was expressed above. Now, as $y \to \infty$ we require $\theta(y) \to 0$, therefore, $C_1 = C_2 = 0$. Also, at $y = 0$, $\theta = \theta_0 \Rightarrow C_3 = \theta_0$. Finally, it can be shown that,

$$u|_{y=0} = \left(\frac{\partial^2 \theta}{\partial y^2}\right)_{y=0} = \frac{\alpha}{B\sin\phi}\left(-\frac{1}{l^2}\right)2C_4 = 0 \tag{A5-31}$$

$$\Rightarrow C_4 = 0 \tag{A5-32}$$

The final solution obtained is thus,

$$\theta = \theta_0 e^{\left(-\frac{y}{l}\right)}\cos\left(\frac{y}{l}\right) \tag{A5-33}$$

$$u = \theta_0\left(\frac{g\beta\alpha}{B\nu}\right)^{\frac{1}{2}} e^{\left(-\frac{y}{l}\right)}\sin\left(\frac{y}{l}\right) \tag{A5-34}$$

These results can be extended to the turbulent flow in the atmosphere through simple mixing length arguments. ν and α are replaced by turbulent exchange coefficients for momentum and heat, K_M and K_H,

which are assumed constant. It is supposed that $K_M \neq K_H$. Sutton (1953) describes the turbulent solution, and it can be seen that the equations and solutions are identical to the laminar case except for the replacement of α and ν by the appropriate eddy diffusivities.

Vita

John A. King was born September 2, 1960 in Moline, Illinois. Raised by missionary parents in Japan, he spent the first sixteen years of his life shuttling back and forth between Japan and the U.S. After graduating as valedictorian from the Canadian Academy in Kobe, Japan, John began his undergraduate studies at Caltech. During the next few years he sampled course offerings at U.C. Berkeley, Occidental College and Pasadena City College before finally buckling down and obtaining his B.S. in Energy Engineering from Caltech in 1982. While at Caltech, John coughed his way through four years of smoggy summer afternoon practices as a member of the Caltech soccer team. For his trouble he received a nifty letter jacket and a keen interest in studying the phenomena which underlie atmospheric pollution.

After arriving at LSU in 1982, John settled in and put an end to the migratory pattern of his undergraduate career. To his advisor's chagrin, however, John decided to broaden his horizons by leaving Baton Rouge to travel the world whenever allowed, by taking classes in business, music and dance performance, and by pursuing unauthorized research projects in the laboratory on weekends. Eventually, these halcyon days came to an end along with John's halftime assistantship, forcing him to take careful measure of his financial reserves. Nine months later, this dissertation appeared in the hands of the examining committee.

John will move on to a two month stint as a post doctoral researcher working with his ever patient Ph.D. advisor. Following this he will work for eight months with Professor R.G. Rice, also at LSU. His plans after that are to either assume a faculty position at another university or go to work as a corporate researcher.

DOCTORAL EXAMINATION AND DISSERTATION REPORT

Candidate: John A. King

Major Field: Chemical Engineering

Title of Dissertation: Natural Convection Above Heated Inclined Surfaces

Approved:

Major Professor and Chairman

Dean of the Graduate School

EXAMINING COMMITTEE:

Date of Examination:

October 17, 1989